NDOR Sponsoring Agency Contract No. DPU-STWD (94)

DEVELOPMENT OF A NEW ENERGY-ABSORBING ROADSIDE/MEDIAN BARRIER SYSTEM WITH RESTORABLE ELASTOMER CARTRIDGES

Submitted by

Jennifer D. Schmidt, Ph.D., E.I.T.
Post-Doctoral Research Associate

Ronald K. Faller, Ph.D., P.E.,
Research Associate Professor
MwRSF Director

Dean L. Sicking, Ph.D., P.E.
Emeritus Professor

John D. Reid, Ph.D.
Professor

Karla A. Lechtenberg, M.S.M.E., E.I.T.
Research Associate Engineer

Robert W. Bielenberg, M.S.M.E., E.I.T.
Research Associate Engineer

Scott K. Rosenbaugh, M.S.C.E., E.I.T.
Research Associate Engineer

Jim C. Holloway, M.S.C.E., E.I.T.
Test Site Manager

MIDWEST ROADSIDE SAFETY FACILITY
Nebraska Transportation Center
University of Nebraska-Lincoln
130 Whittier Research Center
2200 Vine Street
Lincoln, Nebraska 68583-0853
(402) 472-0965

Submitted to

NEBRASKA DEPARTMENT OF ROADS
1500 Nebraska Highway 2
Lincoln, Nebraska 68502

FEDERAL HIGHWAY ADMINISTRATION – Nebraska Division
100 Centennial Mall North – Room 220
Lincoln, Nebraska 68508

MwRSF Research Report No. TRP-03-281-13

July 16, 2013

TECHNICAL REPORT DOCUMENTATION PAGE

1. Report No. TRP-03-281-13	2.	3. Recipient's Accession No.	
4. Title and Subtitle Development of a New Energy-Absorbing Roadside/Median Barrier System with Restorable Elastomer Cartridges		5. Report Date July 16, 2013 6.	
7. Author(s) Schmidt, J.D., Faller, R.K., Sicking, D.L., Reid, J.D., Lechtenberg, K.A., Bielenberg, R.W., Rosenbaugh, S.K., and Holloway, J.C.		8. Performing Organization Report No. TRP-03-281-13	
9. Performing Organization Name and Address Midwest Roadside Safety Facility (MwRSF) Nebraska Transportation Center University of Nebraska-Lincoln 130 Whittier Research Center 2200 Vine Street Lincoln, Nebraska 68583-0853		10. Project/Task/Work Unit No. 11. Contract (C) or Grant (G) No. NDOR DPU-STWD (94)	
12. Sponsoring Organization Name and Address Nebraska Department of Roads 1500 Nebraska Highway 2 Lincoln, Nebraska 68502 Federal Highway Administration 100 Centennial Mall North – Room 220 Lincoln, Nebraska 68508.		13. Type of Report and Period Covered Final Report: 2010 – 2013 14. Sponsoring Agency Code	
15. Supplementary Notes Prepared in cooperation with U.S. Department of Transportation, Federal Highway Administration.			

16. Abstract (Limit: 200 words)

A *Manual for Assessing Safety Hardware* (MASH) Test Level 4 (TL-4) energy-absorbing, urban roadside/median barrier was developed to reduce lateral vehicle accelerations below those observed during similar crashes into permanent concrete barriers. Several types of energy absorbers were evaluated for use in this barrier. Elastic polymers, or elastomers, have superior restorability, reusability, compressibility, and resistance to environmental effects. Finite element analysis simulations were used to further study the energy absorption and deflection of conical-shaped, cylindrical-shaped, and shear fender elastomer shapes. Component tests were conducted on rubber cylinders and marine shear fenders.

The proposed design consisted of an open concrete rail with shear fender rubber posts that are anchored to a concrete foundation. The precast concrete beams measured 22 in. (559 mm) wide, 20 in. (508 mm) tall, and 20 ft (6.1 m) long and were spliced on top of 16-in. (406-mm) high, 14-in. (356-mm) wide, and 22-in. (559-mm) long shear fender posts, which were spaced at 10 ft (3 m) on center. Finite element analysis simulations also demonstrated that lateral vehicle accelerations were reduced by up to 33 percent for a MASH TL-4 small car impact into the new barrier as compared to a rigid concrete barrier. Simulations also demonstrated that the new barrier had adequate capacity to contain the MASH TL-4 single-unit truck. The cost of the barrier was estimated to be $175/ft ($574/m). The barrier should be further evaluated using finite element simulations and full-scale crash testing.

17. Document Analysis/Descriptors Highway Safety, Crash Test, Roadside Appurtenances, Compliance Test, MASH, Energy-Absorbing Barrier, Elastomers, Rubber		18. Availability Statement No restrictions. Document available from: National Technical Information Services, Springfield, Virginia 22161	
19. Security Class (this report) Unclassified	20. Security Class (this page) Unclassified	21. No. of Pages 236	22. Price

DISCLAIMER STATEMENT

This report was completed with funding from the Federal Highway Administration, U.S. Department of Transportation. The contents of this report reflect the views and opinions of the authors who are responsible for the facts and the accuracy of the data presented herein. The contents do not necessarily reflect the official views or policies of the Nebraska Department of Roads nor the Federal Highway Administration, U.S. Department of Transportation. This report does not constitute a standard, specification, regulation, product endorsement, or an endorsement of manufacturers.

UNCERTAINTY OF MEASUREMENT STATEMENT

The Midwest Roadside Safety Facility (MwRSF) has determined the uncertainty of measurements for several parameters involved in standard full-scale crash testing and non-standard testing of roadside safety features. Information regarding the uncertainty of measurements for critical parameters is available upon request by the sponsor and the Federal Highway Administration. Test nos. EPDM-1 through EPDM-12, HSF14-1 through HSF14-5, SFHC-1, and SFHT-1 were non-certified component tests conducted for research and development purposes only.

ACKNOWLEDGEMENTS

The authors wish to acknowledge several sources that made a contribution to this project: (1) the Federal Highway Administration and the Nebraska Department of Roads for sponsoring this project; (2) Maritime International, Inc. for donating shear fenders for dynamic testing; and (3) MwRSF personnel for constructing the systems and conducting the component tests.

Acknowledgement is also given to the following individuals who made a contribution to the completion of this research project.

Midwest Roadside Safety Facility

A.T. Russell, B.S.B.A., Shop Manager
K.L. Krenk, B.S.M.A., Maintenance Mechanic
S.M. Tighe, Laboratory Mechanic
D.S. Charroin, Laboratory Mechanic
C.S. Stolle, Ph.D., Post-Doctoral Research Associate
Undergraduate and Graduate Research Assistants

Nebraska Department of Roads

Phil TenHulzen, P.E., Design Standards Engineer
Jodi Gibson, Research Coordinator

Federal Highway Administration

John Perry, P.E., Nebraska Division Office
Danny Briggs, Nebraska Division Office

TABLE OF CONTENTS

LIST OF FIGURES

LIST OF TABLES

1 INTRODUCTION

1.1 Problem Statement

Concrete barriers have gained widespread application along our nation's highways and roadways, primarily as median barriers and bridge railings. Most of these barriers are largely maintenance free and can provide the capacity to contain high-energy truck impacts at much lower construction costs than metal barriers. However, accident data has shown that impacts with these barriers cause more fatalities than observed with flexible guardrails [1]. Vehicular impacts into rigid concrete barriers often impart high decelerations to vehicles and their occupants. Concrete barrier shapes, such as the New Jersey barrier, also increase the rate of rollovers [2]. Thus, there is a need for an energy-absorbing roadside/median barrier that lowers vehicle decelerations but still has the capacity to contain high-energy truck impacts without significant increases in cost.

The Steel And Foam Energy Reduction (SAFER) barrier was successfully developed for use in high-speed racetrack applications for the purpose of reducing the severity of race car crashes into outer, rigid concrete containment walls [3-12]. The barrier consists of a vertical-face, steel impact panel that is spaced away from a rigid concrete wall with discrete, energy-absorbing foam cartridges, as shown in Figure 1. Dynamic crush of the foam cartridges dissipates the impacting vehicle's kinetic energy. Prior to the installation of the SAFER barrier at all National Association for Stock Car Auto Racing (NASCAR) and Indy Racing League (IRL) racetracks, an average of 1½ deaths occurred per year during high-speed impacts with the outer rigid containment barriers which surrounded oval racetracks. No serious injury or fatal crashes involving outer wall impacts have been reported since the installation of the SAFER barrier. Vehicle decelerations were reduced by approximately 30 percent with the SAFER barrier, and

the maximum neck tensions and head injury criteria values were reduced by up to 75 percent during full-scale crash testing.

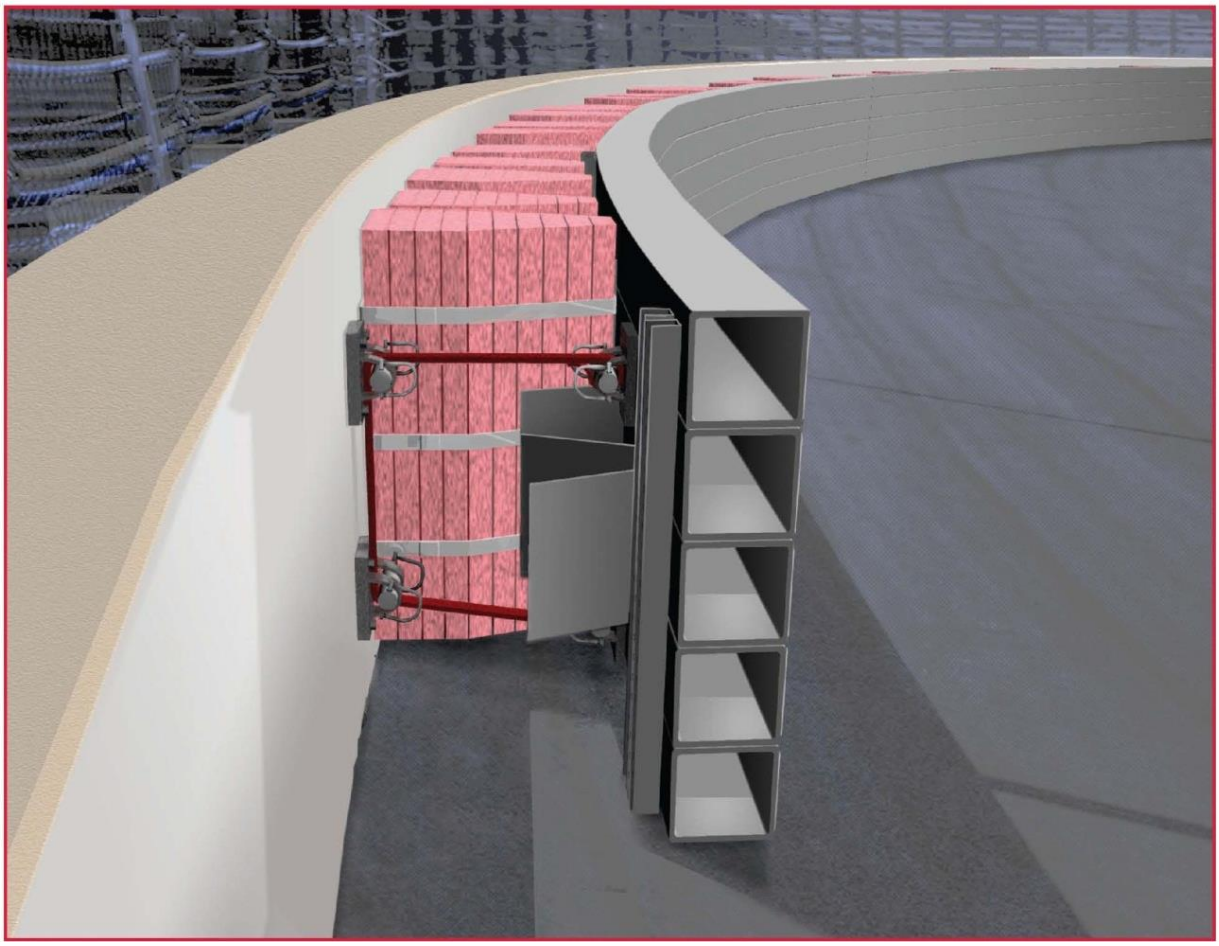

Figure 1. Cross-Section of the SAFER Barrier Installed on Rigid Concrete Wall

SAFER barrier technology could be used to reduce the severity of rigid concrete barrier impacts in highway applications by reducing vehicle decelerations and rollover rates. The current SAFER barrier was impacted by race cars weighing from 2,000 to 3,600 lb (910 to 1,630 kg), at speeds in excess of 150 mph (240 km/h), and at angles up to 25 degrees. The weight of highway vehicles is highly variable, ranging from 2,300-lb (1,040-kg) small cars to 80,000-lb (36,000-kg) tractor/trailer trucks. Highway vehicle crashes with rigid barriers would involve impact speeds around 60 mph (100 km/h) and at 25-degree angles.

Although the current SAFER barrier would absorb enough energy to reduce the severity of an impact with a rigid barrier in a highway application, there are several reasons why using the same system would not be practical. First, the current SAFER barrier has an initial cost that generally ranges from $300 to $400 per linear foot ($984 to $1,312/m), excluding the cost of the concrete wall or backup structure. Typical concrete median barriers cost as low as $35 per linear foot ($115/m). A benefit-cost analysis would be expected to show that it is not cost-effective to implement the current SAFER barrier in highway applications, unless a roadway is extremely dangerous. Also, the current foam cartridges would require replacement after severe crash events. Thus, the maintenance cost of the current SAFER barrier may also be too high for use in highway applications. A new barrier should be reusable and restorable, so that little maintenance is required after high-energy crash events and for the barrier to function properly. A restorable and reusable barrier saves on the overall cost of the system. And finally, the lateral deceleration experienced by a race car impacting a rigid barrier is significantly greater than that of a passenger vehicle impacting a rigid barrier. Thus, the adapted SAFER barrier for highway applications will not need to absorb as much energy as the current motorsports barrier system. The vertical steel impact panel can be reduced to a smaller section, and the foam cartridges can be replaced with a reusable and restorable material. Therefore, using SAFER barrier technology, a lower cost, energy-absorbing barrier can be designed to contain both passenger vehicles and high-energy truck impacts in highway applications.

1.2 Objectives

The objectives of the research study were to design and/or evaluate various reusable energy-absorbing materials for use in the design of an urban roadside/median barrier system adapted from the SAFER barrier technology. The adapted barrier design must provide an optimized energy management system that is compatible with highway vehicles, be less costly to

construct than other energy-absorbing barriers, be more damage resistant than flexible barrier systems, and require little routine maintenance.

1.3 Scope

The research objectives were accomplished with six tasks:

1.3.1 Design Objectives

Several design objectives were established to guide the development process of a completely new barrier. The SAFER barrier, crash testing standards, and previously-crash tested rigid barriers were examined to help determine the target test level, energy absorption capacity, system width, range in construction cost, system height, and redirective capacity. Based on static analysis and review of current barriers that withstand extreme impact events and/or absorb impact energy, a design barrier deflection was determined based on the desired reduction in occupant ridedown acceleration.

1.3.2 Energy-Absorbing Applications

Several crash cushions, existing roadside barriers, and other energy-absorbing applications were reviewed. A brief description of each system was provided along with the material and function of the energy-absorbing mechanism.

1.3.3 Design Concepts

The properties of energy-absorbing materials were compared to see which have superior restorability, reusability, compressibility, and resistance to environmental effects. Once the most feasible energy-absorbing material was selected, a shape study was conducted to identify the most efficient energy-absorbing shapes to further pursue.

The steel impact plate and the foam cartridges from the current SAFER barrier system both were to be modified and/or replaced for the new barrier. Many different concepts were

brainstormed for both retrofit applications (to be mounted on a rigid concrete parapet) and new construction (serve as a new, standalone design).

1.3.4 Material Modeling

Once the best energy-absorbing material was selected, the optimal size and shape of the energy absorber was determined using the LS-DYNA finite element analysis (FEA) software [13]. A review was conducted of the energy-absorbing material that was targeted for impact analysis with simulation. Material tests were used to obtain accurate material properties. The LS-DYNA material models and element formulations were investigated through FEA simulations of tension tests and other component tests. Dynamic and durability tests were conducted on the most promising energy absorbers. Component testing results were used to validate the FEA simulations. A summary of the elastomer modeling process and conclusions about LS-DYNA material models were provided.

1.3.5 Final Barrier Design

The energy absorber was incorporated into the final design concept. The best design concept was simulated using the test conditions published in the *Manual for Assessing Safety Hardware* (MASH) [14] in order to evaluate the safety performance of the barrier system. Simulated impacts into rigid concrete barriers were also performed using the same test conditions in order to provide a baseline condition for which to compare vehicle accelerations and stability. The simulations were modified and refined to provide the most accurate results. Design details of the new barrier were provided.

1.3.6 Recommendations and Conclusions

Conclusions were made as to the cost and safety performance of the new barrier as compared to a rigid concrete parapet. Several future needs were recommended for a complete barrier design, including (1) evaluating the effects of temperature on the barrier; (2) developing a

transition and end terminal; and (3) conducting a full-scale crash testing program according to the test conditions for MASH TL-4 longitudinal barriers.

2 DESIGN OBJECTIVES

First, the performance of the SAFER barrier was analyzed to help establish the design objectives. Then, objectives were set forth to guide the design of the new energy-absorbing roadside/median barrier including: 1) test level; 2) acceleration reductions; 3) barrier width; 4) construction cost; 5) maintenance cost; 6) barrier height; 7) lateral design load; and 8) lateral barrier deflection.

2.1 SAFER Barrier Analysis

The deflection and energy analysis of the current SAFER barrier was analyzed. In test no. IRL-24, a 3,606-lb (1,636-kg) NASCAR stock car impacted the curved SAFER barrier at a velocity of 133.1 mph (214.2 km/h) and at an angle of 26.9 degrees. The impact severity was 436.5 kip-ft (591.8 kJ). The maximum dynamic deflection of the barrier was 20 in. (508 mm), and eight foam blocks deflected at least 6.1 in. (155 mm). Other foam blocks deflected to a lesser extent and were not included in the analysis. Four foam blocks deflected an average of 83 percent of the maximum deflection, and the other four foam blocks deflected an average of 40 percent of the maximum deflection. Since the foam block energy absorbers were spaced at 67.2 in. (1,707 mm), the deformed foam blocks occurred over a span of 45 ft (13.7 m).

The force vs. deflection and energy vs. deflection curves of the one SAFER barrier foam block under a dynamic impact are shown in Figure 2. Based on the deflection of the eight foam blocks in test no. IRL-24, 103.3 kip-ft (140.1 kJ) energy, or 23.7 percent of the initial lateral component of the vehicle's kinetic energy, was absorbed specifically by the foam blocks. In test no. IRL-20, a 3,596-lb (1,631-kg) NASCAR stock car impacted a curved concrete wall at a velocity of 135.6 mph (218.2 km/h) and at an angle of 26.4 degrees. The impact severity was 436.5 kip-ft (591.8 kJ), which is the same as test no. IRL-24. The peak lateral acceleration was

reduced at least 12.5 percent in the SAFER barrier impact when compared to the curved concrete wall impact.

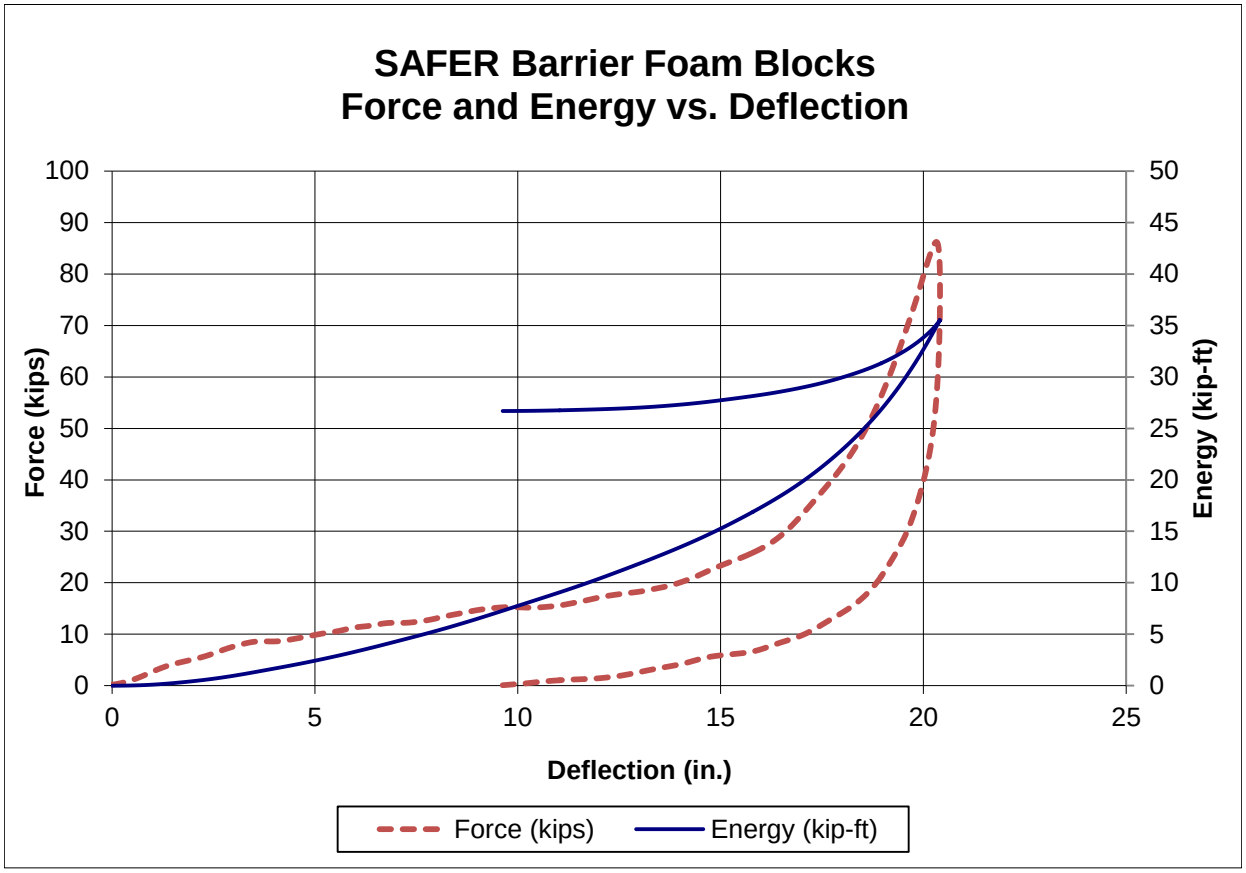

Figure 2. SAFER Barrier Foam Blocks – Force and Energy vs. Deflection

In test no. IRL-25, a 1,951-lb (885-kg) open-wheel IRL car impacted the curved SAFER barrier at a velocity of 150.9 mph (242.9 km/h) and at an angle of 27.5 degrees. The impact severity was 315.5 kip-ft (427.8 kJ). The maximum dynamic deflection of the barrier was 11.2 in. (284 mm), and seven foam blocks deflected at least 3.3 in. (81 mm). Other foam blocks deflected minimally and were not included in the analysis. Based on the deflection of the seven foam blocks in test no. IRL-25, 29.5 kip-ft (40.0 kJ) energy, or 9.4 percent of the initial lateral component of the vehicle's kinetic energy, was absorbed specifically by the foam blocks. In test no. IRL-26, a 2,021-lb (917-kg) open-wheel IRL car impacted a curved concrete wall at a

velocity of 146.1 mph (235.1 km/h) and at an angle of 28.9 degrees. The impact severity was 328.1 kip-ft (444.8 kJ), which is 4 percent higher than test no. IRL-25. The peak lateral acceleration was reduced 32 percent in the SAFER barrier impact when compared to the curved concrete wall impact, but some of the reduction is possibly due to the decrease in impact severity.

2.2 Test Level

The new barrier system was initially targeted for urban roadside/median applications as either a retrofit to existing rigid safety shape barriers or as a completely new barrier installation. The new barrier should provide acceptable safety performance according MASH Test Level 4 (TL-4) [14]; since, typical ratings for urban concrete roadside/median barriers range from Test Level 3 to Test Level 5.

According to TL-4 of MASH, longitudinal barrier systems must be subjected to three full-scale vehicle crash tests. The three full-scale crash tests are as follows:

1. Test Designation No. 4-10 consists of a 2,425-lb (1,100-kg) passenger car impacting the system at a nominal speed and angle of 62 mph (100 km/h) and 25 degrees, respectively.

2. Test Designation No. 4-11 consists of a 5,000-lb (2,268-kg) pickup truck impacting the system at a nominal speed and angle of 62 mph (100 km/h) and 25 degrees, respectively.

3. Test Designation No. 4-12 consists of a 22,046-lb (10,000-kg) single-unit truck impacting the system at a nominal speed and angle of 56 mph (90 km/h) and 15 degrees, respectively.

The test conditions of TL-4 longitudinal barriers are summarized in Table 1.

Evaluation criteria for full-scale vehicle crash testing are based on three appraisal areas: (1) structural adequacy; (2) occupant risk; and (3) vehicle trajectory after collision. Criteria for structural adequacy are intended to evaluate the ability of the median barrier to contain and redirect impacting vehicles. Occupant risk evaluates the degree of hazard to occupants in the

impacting vehicle. Vehicle trajectory after collision is a measure of the potential for the post-impact trajectory of the vehicle to result in secondary collisions with other vehicles or fixed objects, thereby increasing the risk of injury to the occupant of the impacting vehicle and to other vehicles. These evaluation criteria are summarized in Table 2 and defined in greater detail in MASH. Therefore, these test conditions and evaluation criteria were used to establish guidelines for designing the new barriers.

Table 1. MASH TL-4 Crash Test Conditions

Test Article	Test Designation No.	Test Vehicle	Impact Conditions			Evaluation Criteria [1]
			Speed		Angle (deg)	
			mph	km/h		
Longitudinal Barrier	4-10	1100C	62	100	25	A,D,F,H,I
	4-11	2270P	62	100	25	A,D,F,H,I
	4-12	10000S	56	90	15	A,D,G

[1] Evaluation criteria explained in Table 2

2.3 Acceleration Reductions

Vehicle decelerations were reduced up to 30 percent for racecar crashes with the SAFER barrier as compared to similar crashes into rigid concrete barriers. Thus, a similar reduction in vehicle deceleration was desired for the new roadside barrier. Since the majority of vehicular impacts with rigid concrete barriers correspond to passenger vehicles, the barrier should reduce peak vehicle decelerations by at least 30 percent for impact events associated with MASH test designation nos. 4-10 and 4-11.

MASH test designation no. 3-10 (equivalent to 4-10) is usually waived due to the large number of small car crash tests that were conducted years ago under the NCHRP Report No. 350 criteria [15]. Previously, one 1100C small car crash test was successfully conducted on a 32-in. (813-mm) high New Jersey-shaped concrete barrier under the MASH impact safety standards

[16]. The 10-msec average lateral acceleration trace from test no. 2214NJ-1 is shown in Figure 3. From this curve, the peak lateral acceleration was 37 g's.

Table 2. MASH Evaluation Criteria for Longitudinal Barriers

<table>
<tr><td>Structural Adequacy</td><td>A.</td><td colspan="3">Test article should contain and redirect the vehicle or bring the vehicle to a controlled stop; the vehicle should not penetrate, underride, or override the installation although controlled lateral deflection of the test article is acceptable.</td></tr>
<tr><td rowspan="5">Occupant Risk</td><td>D.</td><td colspan="3">Detached elements, fragments or other debris from the test article should not penetrate or show potential for penetrating the occupant compartment, or present an undue hazard to other traffic, pedestrians, or personnel in a work zone. Deformations of, or intrusions into, the occupant compartment should not exceed limits set forth in Section 5.3 and Appendix E of MASH.</td></tr>
<tr><td>F.</td><td colspan="3">The vehicle should remain upright during and after collision. The maximum roll and pitch angles are not to exceed 75 degrees.</td></tr>
<tr><td>G.</td><td colspan="3">It is preferable, although not essential, that the vehicle remain upright during and after collision.</td></tr>
<tr><td>H.</td><td colspan="3">Occupant Impact Velocities (OIV) (see Appendix A, Section A5.3 of MASH for calculation procedure) should satisfy the following limits:
<table>
<tr><td colspan="3">Occupant Impact Velocity Limits</td></tr>
<tr><td>Component</td><td>Preferred</td><td>Maximum</td></tr>
<tr><td>Longitudinal and Lateral</td><td>30 ft/s
(9.1 m/s)</td><td>40 ft/s
(12.2 m/s)</td></tr>
</table></td></tr>
<tr><td>I.</td><td colspan="3">The Occupant Ridedown Acceleration (ORA) (see Appendix A, Section A5.3 of MASH for calculation procedure) should satisfy the following limits:
<table>
<tr><td colspan="3">Occupant Ridedown Acceleration Limits</td></tr>
<tr><td>Component</td><td>Preferred</td><td>Maximum</td></tr>
<tr><td>Longitudinal and Lateral</td><td>15.0 g's</td><td>20.49 g's</td></tr>
</table></td></tr>
</table>

MASH designation test no. 3-11 (equivalent to 4-11) was conducted on a 36-in. (914-mm) high single-slope concrete barrier on a pan-formed bridge deck at the Texas Transportation

Institute (TTI) [17]. The 10-msec average lateral acceleration trace from test no. 420020-3 is shown in Figure 4. From this curve, the peak lateral acceleration was 28 g's.

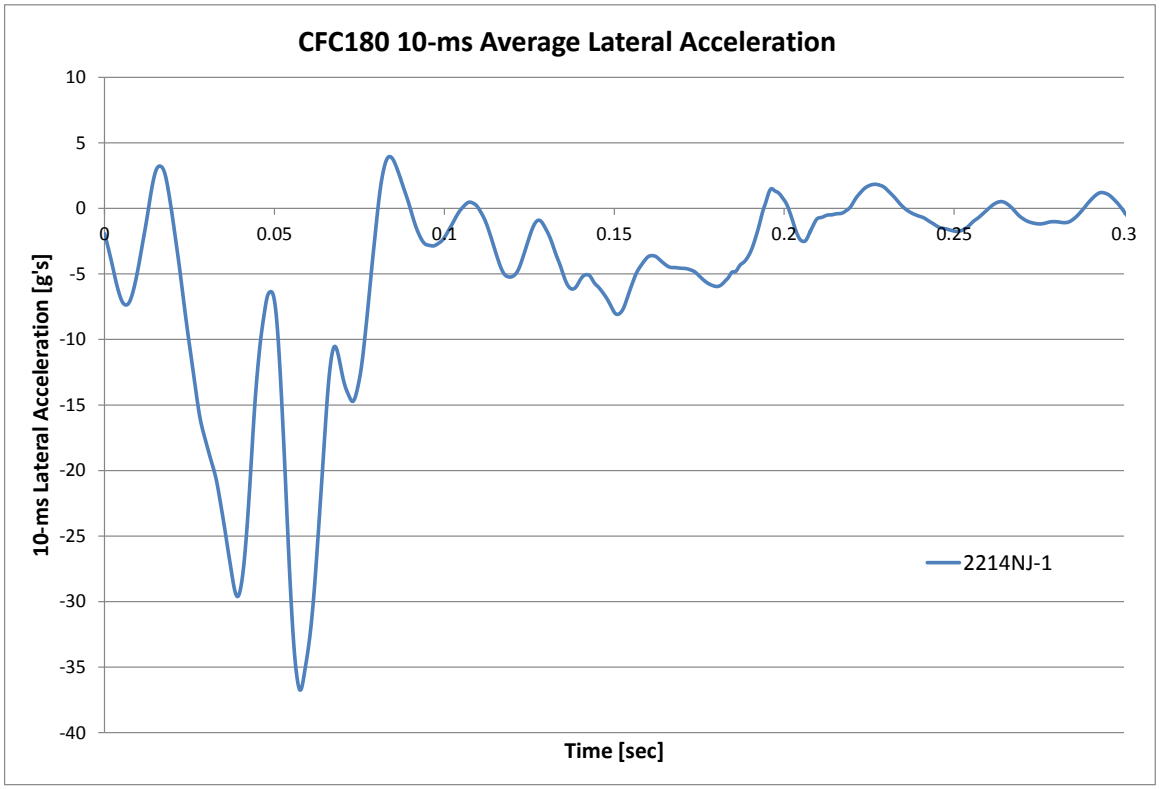

Figure 3. MASH Test No. 3-10 New Jersey Barrier Test – Lateral Accelerations [16]

2.4 Barrier Width

One of the targeted applications for the new barrier system was for urban medians, where rigid concrete parapets are typically used to divide two-way traffic. Typical TL-4 and TL-5 barrier shapes are vertical, single-slope, and safety-shaped (New Jersey- and F-shaped). The TL-5 New Jersey barrier is the widest barrier and has a base width of 32 in. (813 mm). Thus, it was desired that the new barrier width be less than or equal to 36 in. (914 mm) in order to fit within the special constraints of current urban medians.

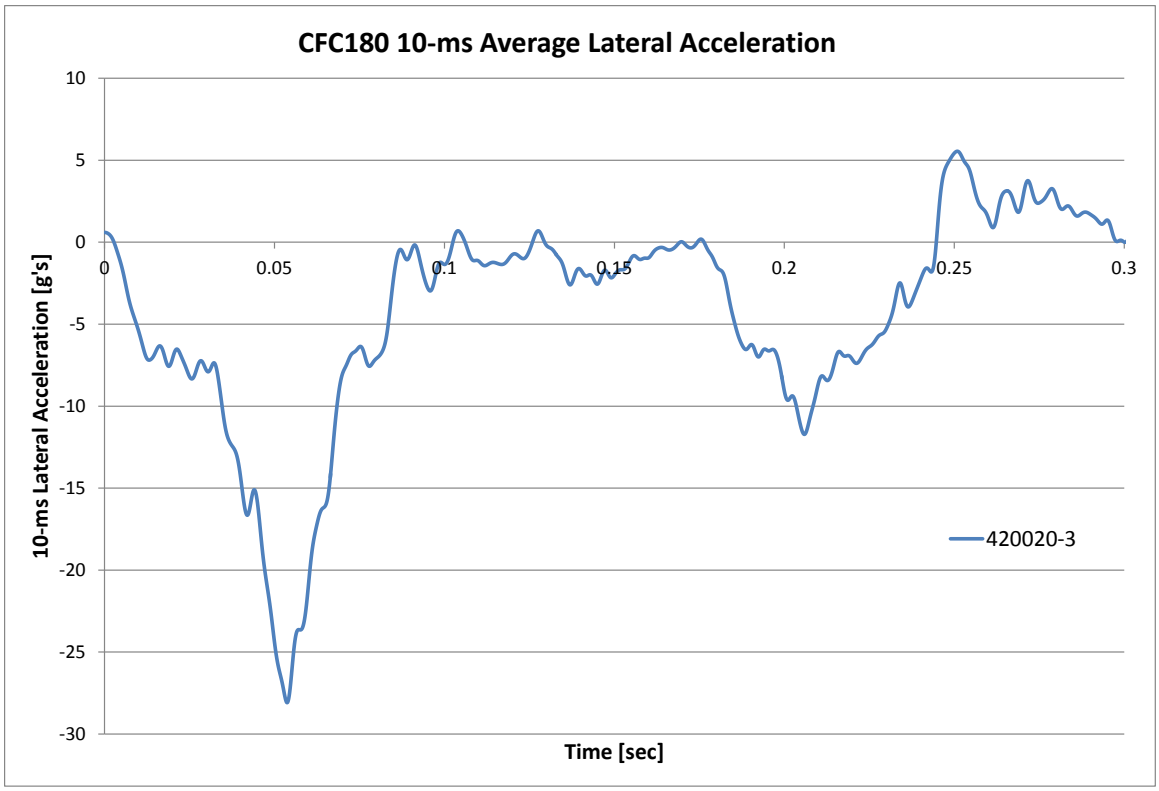

Figure 4. MASH Test No. 3-11 Single-Slope Barrier Test – Lateral Accelerations [17]

2.5 Construction Cost

In 2007, the initial construction costs of 32-in. (813-mm) tall TL-4 and 42-in. (1,067-mm) tall TL-5 concrete barriers were estimated on a price per linear foot basis [18]. The cost of materials and labor to slipform the concrete barriers with a foundation ranged from $40 to $60/ft ($131 to $197/m). Based on a recent survey of the Midwest Pooled Fund States, the installation cost of concrete median barriers can vary greatly, ranging from $35 to $274/ft ($115 to $899/m) for 32-in. (813-mm) and 42-in. (1,067-mm) tall concrete barriers. If only a short barrier segment is built or the barrier is constructed separate from the overall roadway construction, mobilization and labor costs can significantly inflate the price of the concrete median barrier. The cost of the foundation is generally not included in this price when the concrete slab or foundation is poured continuously with the roadway. However, the States' standard item costs do not distinguish the

foundation cost separate from the roadway cost. To be competitive with other concrete barriers currently found on the nation's roadsides, the targeted cost of the new barrier is approximately $200 per linear foot.

2.6 Maintenance Cost

The maintenance cost for the new barrier system should be virtually zero under normal impact conditions. The energy absorber should be restorable and reusable, and the rail element should be stiff enough to resist permanent deformation during passenger vehicle impacts. A minimal amount of damage is permissible with single-unit truck impact events. The energy absorber should also be resistant to environment effects, so that it has a long useable life.

2.7 Barrier Height

Multiple 32-in. (813-mm) tall TL-4 concrete barriers have been successfully crash tested according to the safety performance criteria found in NCHRP Report No. 350. In 2009, MASH replaced NCHRP Report No. 350 as the new crash standards, and the TL-4 crash standards for test designation no. 4-12 increased both the velocity and weight of the single-unit truck. Thus, there was a 56 percent increase in impact severity for test designation no. 4-12. Previous TL-4 bridge rails were recommended to have a minimum height of 32 in. (318 mm) according to the American Association of State Highway and Transportation Officials (AASHTO) *Load and Resistance Factor Design (LRFD) Bridge Design Specifications* [19]. Preliminary MASH testing showed the propensity for a 10000S single-unit truck to roll over a Federal Highway Administration (FHWA) accepted, TL-4 NCHRP Report No. 350 crash tested, 32-in. (813-mm) high, New Jersey shape concrete barrier. Therefore, the 32-in. (813-mm) high, New Jersey shape barrier would be unacceptable according to MASH standards [20].

A recent TTI study recommended a minimum height of 36 in. (914 mm) for TL-4 bridge rails [21]. A 36-in. (914-mm) high single-slope bridge rail was successfully crash-tested

according to test no. 4-12 of MASH. Thus, the top barrier height to meet TL-4 of MASH should be at least 36 in. (914 mm) to contain a single-unit truck.

A recent Midwest Roadside Safety Facility (MwRSF) study examined the maximum height of the Midwest Guardrail System (MGS) that could still contain a TL-3 1100C small car impact event [22]. A top rail mounting height of 34 in. (864 mm) and 36 in. (914 mm) both successfully passed test no. 3-10 of MASH. Since the rail element in these tests was W-beam corrugated rail, which is 12¼ in. (311 mm) tall, the lowest bottom height of the new rail element to adequately capture 1100C small cars is 22 to 24 in. (559 to 610 mm). However, the large deformations of the MGS guardrail allowed the Kia Rio to roll into the barrier, which helped to capture and redirect the car. Since it is desired that no permanent deformation occur to the new barrier system, a lower rail mounting height of 24 in. (610 mm) may not effectively capture the 1100C small car if there is no permanent deformation to the rail element. Therefore, the maximum bottom height of the new rail element should be 22 in. (559 mm) above the ground in order to capture the 1100C small car at the TL-3 impact conditions of MASH.

The MGS guardrail was blocked out so that the face of the post was offset 15.4 in. (390 mm) behind the front of the rail. The front bumper or wheels of passenger vehicles have the potential to snag on posts if the offset is less than 15.4 in. (390 mm). Due to targeted barrier width restrictions, this large offset may not be achieved. Therefore, the lower rail mounting height may need to be lower than 22 in. (559 mm) if there is potential for undesired vehicle interaction with posts.

2.8 Lateral Design Load – TL-4

As mentioned previously, the impact severity of the TL-4 single-unit truck impact increased 56 percent according to MASH guidelines compared to NCHRP Report No. 350. Therefore, the lateral load imparted to barriers will also increase. MwRSF used numerical

approximations, scaling of NCHRP Report No. 350 crash test results, and computer simulations to estimate the lateral design load for a MASH TL-4 concrete barrier [23]. These approximations varied from 75 to 98 kips (334 to 436 kN), thus the recommended design lateral load was 100 kips (445 kN).

In 2011, TTI recommended that a lateral design load of 80 kips (356 kN) be used to design TL-4 bridge rails [21]. This conclusion was based on FEA simulations performed on a 42-in. (1,067-mm) high TL-4 bridge rail. During the full-scale crash test on a 36-in. (914-mm) high single-slope concrete barrier with a single-unit truck, the barrier experienced a CFC60 50-ms average peak force over 90 kips (400 kN) including the mass of the entire vehicle. However, the single-unit truck does not function as a single unit, so only including the mass of the cargo box would decrease this force.

Thus, a lateral design load of 80 to 100 kips (356 to 445 kN) would be used for initially configuring the barrier using assumption that any dynamic barrier deflection would reduce peak lateral loading.

2.9 Lateral Barrier Deflection

The new median barrier system had not yet been designed and thus had unknown dimensions and materials. A lateral deflection analysis was conducted to determine the lateral displacement required to obtain a 30 percent reduction in peak lateral deceleration. First, a simplistic analysis using NCHRP Report No. 86 [24] was used to analyze the peak lateral decelerations for MASH test designation nos. 4-10 (1100C small car) and 4-11 (2270P pickup truck). Then, a comparative study was conducted to compare rigid barrier impacts to previously-developed, energy-absorbing barrier systems.

2.9.1 NCHRP Report No. 86 Method

A simplified analysis from NCHRP Report No. 86 was used to predict the average and peak lateral accelerations for given impact conditions and vehicle geometries. The following input variables were needed for the analysis:

L = length of vehicle

AL = distance from front of vehicle to longitudinal center of gravity (c.g.)

B = distance from the side of vehicle to lateral c.g.

θ = impact angle

V_i = impact velocity

D = deflection of barrier

The lateral change in velocity (ΔV_{lat}) and the lateral change in displacement (ΔS_{lat}) were computed using the change in time (Δt) from initial impact to when the vehicle was parallel to the barrier, or when the lateral component of the velocity is zero. The equation for lateral change in velocity is:

$$\Delta V_{lat} = V_i sin\theta$$

The equation for lateral change in displacement is:

$$\Delta S_{lat} = AL sin\theta - B(1 - cos\theta) + D$$

Since the final lateral velocity is zero, the average lateral velocity over this time frame is equal to one half of the initial lateral velocity. The change in time from initial impact to when the vehicle was parallel to the barrier is:

$$\Delta t = \frac{\Delta S_{lat}}{V_{lat,ave}} = \frac{\Delta S_{lat}}{\frac{1}{2} * V_i sin\theta}$$

The equation for the average lateral deceleration (G_{lat}) is:

$$G_{lat} = \frac{\Delta V_{lat}}{\Delta t * g}$$

The goal was to reduce the peak lateral deceleration ($G_{lat,peak}$). A dynamic magnification factor of 2 was applied to the average lateral deceleration, thus

$$G_{lat,peak} = 2 * G_{lat}$$

First, an analysis of test no. 4-10 into a rigid barrier (D = 0 in.) was conducted. Then, an analysis of test no. 4-10 into a flexible barrier of unknown deflection was conducted, assuming that the peak lateral deceleration was reduced by 30 percent over the rigid barrier case. The same procedure was repeated for an analysis of test no. 4-11. Dimensions for the 2270P and 1100C vehicles were taken from actual vehicles used in previous crash tests conducted at MwRSF.

For an analysis of test no. 4-10 into a rigid barrier,

L = 165¾ in. (4,210 mm)

AL = $72^{15}/16$ in. (1,853 mm)

B = 31¾ in. (806 mm)

θ = 25 degrees

V_i = 62 mph (100 km/h)

D = 0 in.

$G_{lat,ave} = 9.9$ g′s

$G_{lat,peak} = 19.8$ g′s

For an analysis of test no. 4-10 into a flexible barrier with $G_{lat,peak}$ reduced by 30 percent,

$G_{lat,peak} = 13.8$ g′s

$G_{lat,ave} = 6.9$ g′s

L = 165¾ in. (4,210 mm)

AL = $72^{15}/16$ in. (1,853 mm)

B = 31¾ in. (806 mm)

θ = 25 degrees

V_i = 62 mph (100 km/h)

D = 12 in. (305 mm)

For an analysis of test no. 4-11 into a rigid barrier,

L = 227 in. (5,766 mm)

AL = 91 in. (2,311 mm)

B = 38⅞ in. (987 mm)

θ = 25 degrees

V_i = 62 mph (100 km/h)

D = 0 in.

$G_{lat,ave} = 7.9$ g's

$G_{lat,peak} = 15.8$ g's

For an analysis of test no. 4-11 into a flexible barrier with $G_{lat,peak}$ reduced by 30 percent,

$G_{lat,peak} = 11.1$ g's

$G_{lat,ave} = 5.6$ g's

L = 227 in. (5,766 mm)

AL = 91 in. (2,311 mm)

B = 38⅞ in. (987 mm)

θ = 25 degrees

V_i = 62 mph (100 km/h)

D = 15 in. (381 mm)

Based on this analysis, the new barrier would need to deflect 12 in. (305 mm) for a 30 percent reduction in the 1100C small car's lateral deceleration. The new barrier would need to

deflect 15 in. (381 mm) for a 30 percent reduction in the 2270P pickup truck's lateral deceleration. Since these equations are derived from vehicle geometry and barrier displacement, they may not be accurate since vehicle crush is not considered with this method. In test no. IRL-25, the SAFER barrier deflected 11.2 in. (284 mm) with a 1,951-lb (885-kg) IRL car impacting at 150.9 mph (242.8 km/h) and 27.5 degrees [9]. Although the racecar was lighter than the 2,425-lb (1,100-kg) small car, the impact speed was much greater than 62 mph (100 km/h). Thus, a 12-in. (381-mm) and 15-in. (381-mm) lateral deflection may not be necessary to achieve a 30 percent reduction in lateral vehicle accelerations for the small car and pickup truck, respectively. Therefore, these lateral deflection estimates may be too high for 1100C and 2270P impact events.

2.9.2 Comparisons of Energy-Absorbing Barriers

During a study at TTI, the impact forces of several heavy vehicle impacts were into instrumented, rigid walls determined [25-26]. The impact conditions, impact severity, and resulting forces and accelerations are shown in Table 3. The impact conditions for a TL-4 2270P pickup truck test into a longitudinal barrier are at a velocity of 62 mph (100 km/h) and an angle of 25 degrees. Impact severity (IS) is the lateral component of kinetic energy and that portion often considered in the design of longitudinal barriers. When considering barriers of equivalent stiffness, strength, and deformation, it often is used to make comparisons for the severity of various impact events. IS can be calculated using the equation:

$$IS = \frac{1}{2} M(V sin\theta)^2$$

Where M = mass

V = initial velocity

θ = impact angle

Thus, the impact severity for the pickup truck test is 114.8 kip-ft (155.6 kJ), while the impact severity for the 1100C small car test is 55.7 kip-ft (75.5 kJ). Since it was desired to achieve at least a 30 percent reduction in lateral vehicle accelerations with the new barrier compared to a rigid barrier, energy-absorbing barriers with similar IS values as the instrumented wall tests were compared. The low-maintenance, energy-absorbing bridge rail had an axially-compressed, rubber energy absorber between a bridge rail and posts, as shown in Figure 5 [27]. The Collapsing Ring Bridge Rail System (CRBRS) had a lower tube rail with an axial collapsing ring attached to a post, as shown in Figure 6 [28].

One test with the low-maintenance, axial rubber energy-absorbing bridge rail was test no. 2417-2. Two of the tests with the CRBRS were test nos. CRBRS-7 and CRBRS-4. A summary of these barriers, impact conditions, impact severity, and resulting accelerations is shown in Table 3. Test no. 7046-1 and test no. 2417-2 have similar IS values. The low-maintenance, axial rubber bridge rail had a 29 percent reduction in lateral vehicle acceleration with 7.2 in. (183 mm) of lateral deflection compared to the rigid barrier. Therefore, the new energy-absorbing barrier system could reasonably be designed to achieve a 30 percent reduction in lateral vehicle acceleration with barrier displacements ranging from 7 to 10 in. (178 to 254 mm).

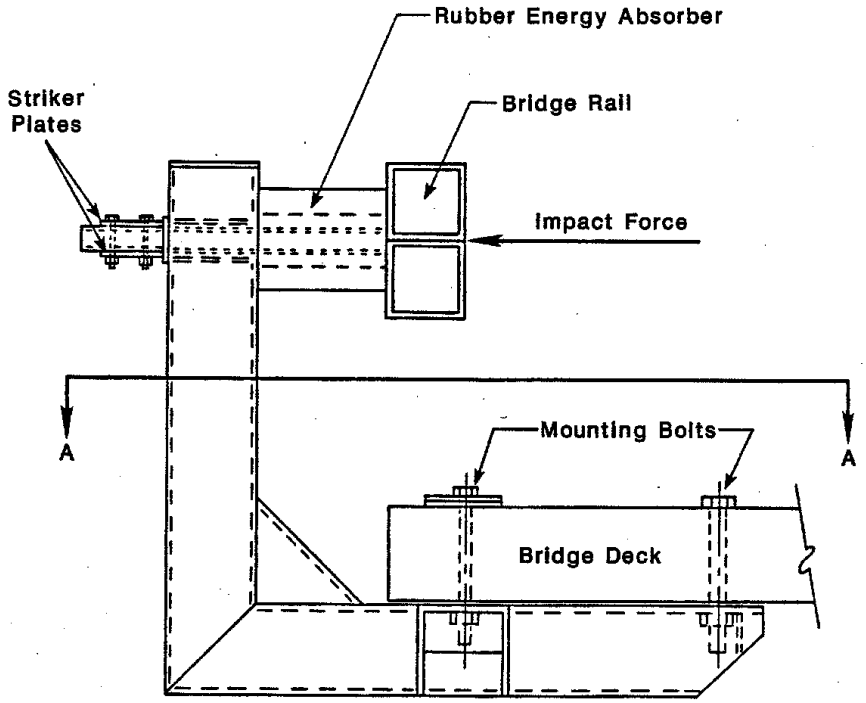

Figure 5. Low Maintenance Energy-Absorbing Bridge Rail [27]

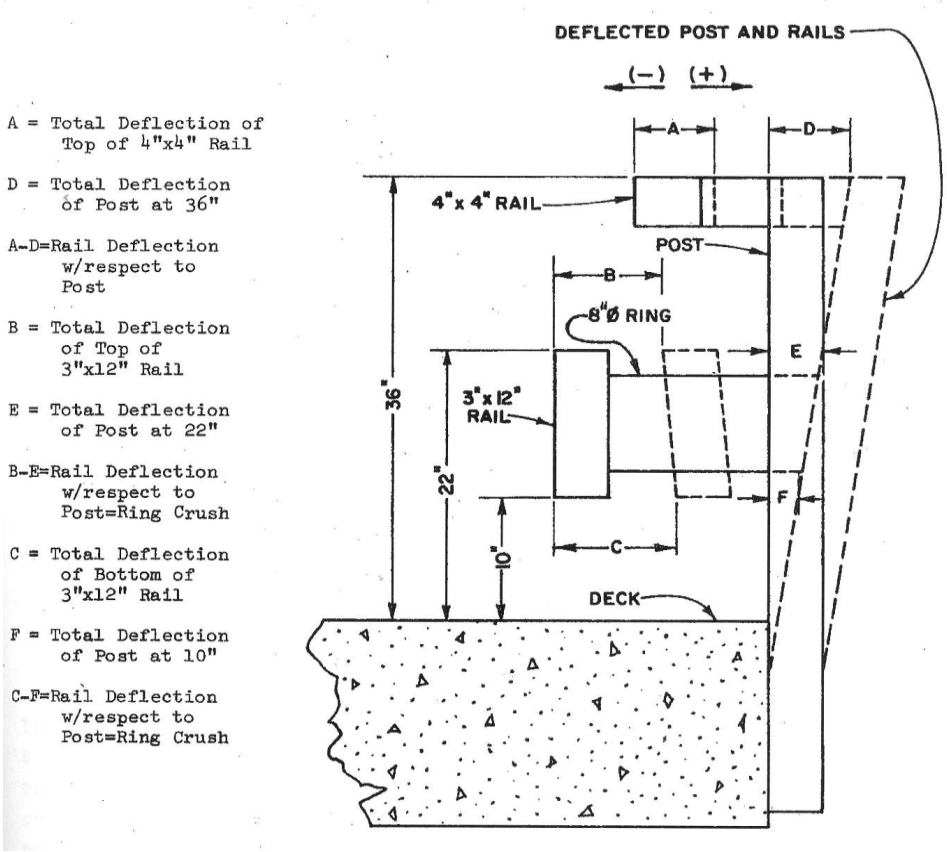

Figure 6. Collapsing Ring Bridge Railing System [28]

Table 3. Comparison of Rigid and Energy-Absorbing Barriers

Test No.	Vehicle Type	Weight	Velocity	Angle	Force [kips]	Max. Lateral Acceleration [g's]	IS [kip-ft]	Reduction in g's [%]	Deflection [in.]	Reference No.
INSTRUMENTED WALL TESTS										
7046-1	Sedan	4500	61.8	25.6	56	14	107	-	-	26
7046-2	Bus	40050	58.6	15.4	386	9.7	324	-	-	26
7046-3	Tractor Van-Trailer	80080	55	15.3	220	9.7	564	-	-	26
7046-4	Tractor Tank-Trailer	79900	54.8	16	408	12.3	609	-	-	26
7046-5	Pickup	5409	65.8	19.9	45	12.5	91	-	-	26
7046-6	Pickup	5432	46.8	19	32	10.7	42	-	-	26
7046-7	Suburban	5400	64.1	19.7	51	9.7	84	-	-	26
7046-8	Suburban	5350	44.7	19.5	28	7.4	40	-	-	26
7046-9	Tractor Van-Trailer	50000	50.4	14.6	150	6.8	270	-	-	26
7046-10	Single Unit Truck	18050	51.6	16.8	90	6.1	134	-	-	26
COMPARABLE ENERGY-ABSORBING SYSTEMS										
2417-2	Sedan	4500	61	25.5	-	10	104	28.6	7.2	27
CRBRS BR-7	Sedan	4230	56.7	29.1	-	8.2	107	41.4	30 [1]	28
CRBRS BR-4	Sedan	4097	60	25.9	-	6.6	94	52.9	15.6 [2]	28

[1] Most of the lateral deflection occurred from rail crushing and post displacement
[2] The rail ruptured and speared the vehicle

3 LITERATURE REVIEW

Numerous crash cushions, existing roadside barriers, and other energy-absorbing applications were reviewed and are discussed in this chapter. However, since a significant number of systems exist, the following list is not inclusive of all of those energy-absorbing devices and mechanisms.

3.1 Crash Cushions

3.1.1 Inertial Barriers

Inertial barriers transfer the momentum of an impacting vehicle into an expendable mass. The Fitch Universal Barrels [29], Sand-filled Recycled Tires [30], Energite III [31], and BigSandy [32] are sand-filled containers that vary in mass in order to decelerate a vehicle within acceptable ridedown limits. These inertial barriers are not designed to withstand multiple impacts without being re-set.

3.1.2 Sequential Cartridge Crushing

Several sequential crash cushions often utilize multiple bays to absorb a vehicle's kinetic energy through the crushing of energy-dissipating cartridges. These early crash cushions were developed and crash tested according to NCHRP Report No. 230 test standards [33]. The Hi-Dro Cell Sandwich [34] has water-filled cartridges that dissipate energy by expelling water during impact. The Hi-Dri Cell Sandwich [34] has concrete-filled cartridges that crush and dissipate energy. The Guard Rail Energy-Absorbing Terminal (GREAT) [35] and Hex-FOAM [35] are TL-3 redirective, non-gating crash cushions. The GREAT and Hex-FOAM both have HexFoam cartridges within each bay to absorb energy. The Low Maintenance Attenuator (LMA) is a redirective, non-gating crash cushion that has collapsible elastomeric cylinders within the sequential bays to dissipate energy [35].

Several crash cushions have crushable clustered cylinders. A 20-ft (6-m) long clustered, rubber-cylinder crash cushion was developed and successfully crash tested under the NCHRP Report No. 230 safety performance standards [36]. Eighteen 30-in. (762-mm) tall, 25-in. (635-mm) inner diameter cylinders had thicknesses varying from 1.5 to 3 in. (38 to 76 mm). The system performed acceptably with a 4,500-lb (2,043-kg) car impacting at 31.2 mph (50.2 km/h) and 47.9 mph (77.1 km/h). The system mostly restored, but significant cracking occurred at points of delamination between the layers of rubber. Insufficient bonding between the rubber layers in large diameter, thick-walled cylinders can be a problem in mandrel-wrapped cylinders. The system also performed acceptably with a 1,800-lb (817-kg) small car impacting at 24.6 mph (39.6 km/h) and 58.3 mph (93.8 km/h).

Many crash cushions were also developed and crash tested according to NCHRP Report No. 350 impact safety standards. The Connecticut Impact Attenuation System (CIAS) and the Narrow CIAS (NCIAS) are TL-3 redirective, gating crash cushions [37-38]. These systems have clustered steel cylinders with varying diameters, thicknesses, and struts to absorb an impacting vehicle's kinetic energy through deformation or crushing of cylinders.

The EASI-Cell [39], Reusable Energy-Absorbing Crash Terminal (REACT) [40], and Vanderbilt Truck Mounted Attenuator (VTMA) [41-44] have clustered crushable HDPE cylinders. The EASI-Cell is a TL-1 non-redirective, crash cushion with HDPE cylinders clustered together. The REACT is a TL-3 redirective, gating crash cushion with several HDPE cylinders that can be configured for narrow or wide objects. The VTMA is a TL-3 truck-mounted attenuator with HDPE cylinders. HDPE is reusable and can restore most of its original shape.

The QuadGuard family has many types of similar sequential cartridge crushing, energy-absorbing crash cushions [45-47]. The QuadGuard LMC has rubber cartridges and is mostly restorable and reusable, as shown in Figure 7. The QuadGuard Elite has HDPE cartridges and is

also mostly restorable and reusable. The QuadTrend is a TL-3 redirective, gating end treatment for concrete barriers with Quad-Beam panels, sand-filled boxes, and a redirective cable to absorb impact energy [48]. The TAU-II is a TL-3 redirective, non-gating crash cushion with polyethylene, energy-absorbing cartridges [49-50]. The QUEST and TRACC families are redirective, non-gating crash cushions with steel deformation for the sequential compressing bays [50-51]. The TRACC can be varied for a multitude of widths and lengths. The QUEST can also protect hazards of varying widths and is approved for impacts up to 70 mph (112.7 km/h). The SCI-100GM is a redirective, non-gating crash cushion with a shock-arresting cylinder that can be easily re-set after impact [52].

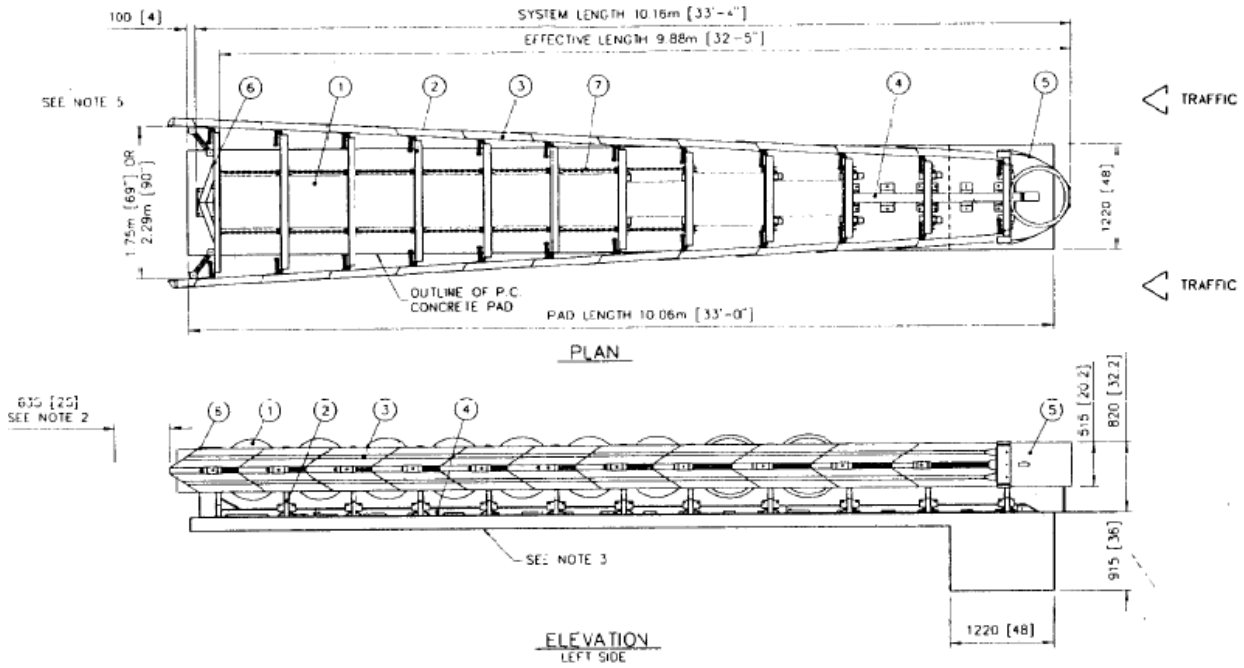

Figure 7. QuadGuard LMC [47]

Two other NCHRP Report No. 350 TL-3 crash cushions were noted to be reusable and restorable. The Hybrid Energy Absorbing Reusable Terminal (HEART) is a redirective, non-gating crash cushion, as shown in Figure 8 [53-54]. Variable-size, HDPE plates absorb energy when deflected, and the system self-restores to 95 percent of its original length. The Compressor

is a redirective, non-gating crash cushion [55]. Curved HDPE modules of varying sizes and thicknesses are compressed within bays to absorb energy, and the system self-restores almost completely.

Figure 8. HEART Crash Cushion System [53-54]

3.1.3 Water Expulsion Clusters

Several crash cushions use a combination of plastic deformation and water expulsion to absorb impact energy. The Hi-Dro Cell Cluster [34], ABSORB350 [56], SLED [57-58], and ACZ-350 [59-60] are examples of these systems. These crash cushions do not redirect errant vehicles and need to be replaced after impact. The Hi-Dro Cell Cluster is a cluster of water-filled cylinders that dissipate energy by expelling water during impact. The ABSORB350 is a TL-3 non-redirective, gating crash cushion that prevents errant vehicles from impacting the ends of

concrete barriers with reinforced plastic bays filled with water. The SLED and ACZ-350 systems are TL-3 gating, non-redirective end treatments for use in shielding the ends of concrete median barriers.

3.1.4 Crushable Concrete

The ADIEM [61] crash cushion absorbs energy by the sequential crushing of concrete elements. The concrete is ultra-low-strength and lightly reinforced, so it can easily crush and dissipate energy upon impact. The ADIEM is a TL-3 redirective, gating system that protects the vehicle from impacting the ends of a concrete barrier, bridge piers, and other rigid objects.

3.1.5 Aluminum Honeycomb

The N-E-A-T is a TL-2 non-redirective, temporary crash cushion [62]. An aluminum shell surrounds the aluminum cells, which dissipate energy when crushed.

3.1.6 Recycled Tires

A study evaluated tires and tire-derived rubber use in a low-cost, reusable crash cushion [63]. The as-tested, tire-derived rubber pads produced low deflections and high forces when crushed, which is not ideal for crash cushions. Horizontally-crushed tires showed the most promise, as shown in Figure 9a, although the deflections for each individual tire were low. Vertically-crushed tires may also be effective, as shown in Figure 9b, because the peak forces in horizontal and vertical compression were very similar. The deflection was also much greater in the vertical configuration, which would reduce accelerations but also increase the length of the crash cushion. The tires also did not fully restore when vertically compressed, so the crash cushion would not be reusable without some maintenance.

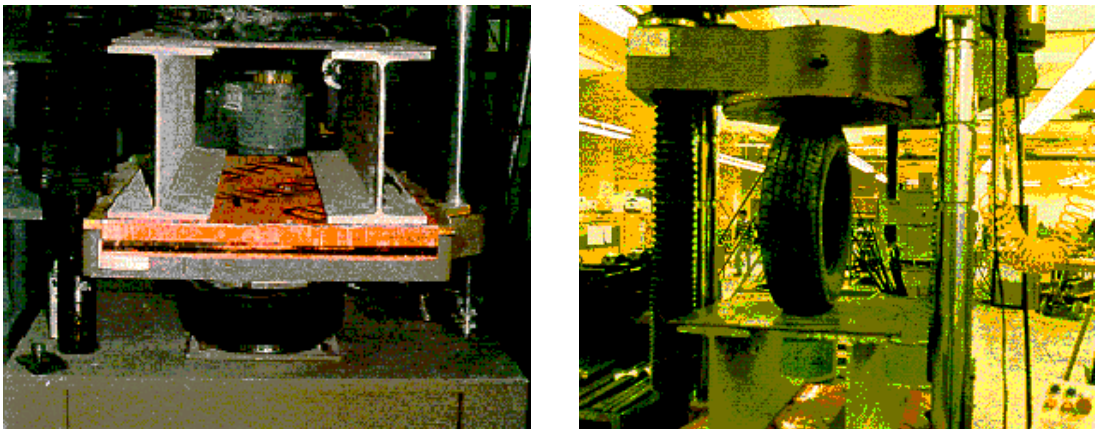

(a) Horizontally Compressed (b) Vertically Compressed

Figure 9. Horizontally and Vertically Crushed Tires for Use in a Crash Cushion [63]

3.1.7 Airfence

The Airfence IIs is a flexible and soft motorcycle racing barrier. Sections of heavy duty, reinforced PVC fabric, which are flexible and UV stabilized, are strapped together to fit any track [64]. A section of the Airfence is shown in Figure 10. Slightly-pressurized cells hold the barrier upright. Other cells under ambient air pressure build up and release pressure when impacted by a rider. The barrier resumes its original shape after impact and can take repeated impacts.

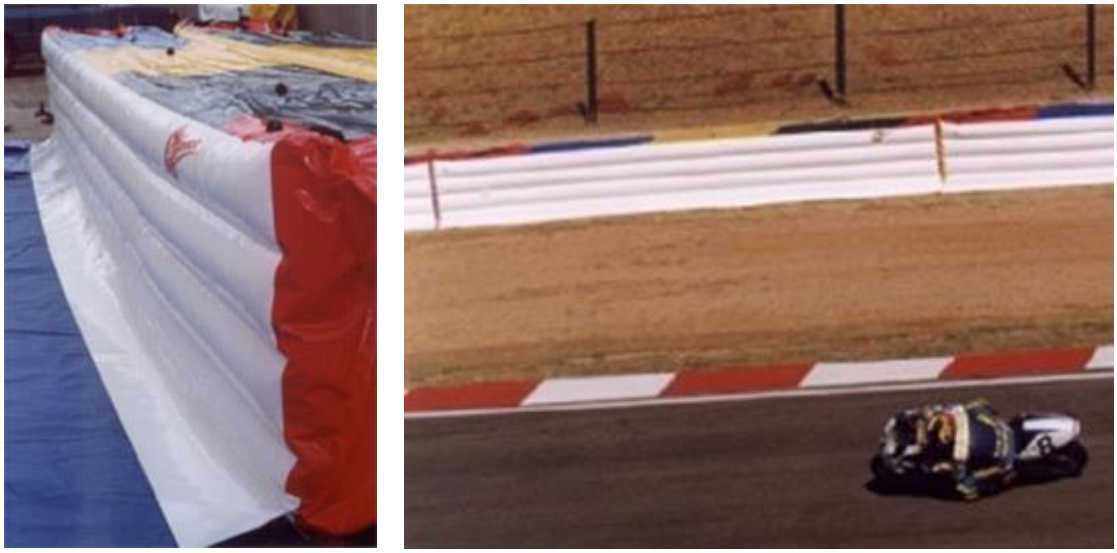

Figure 10. Airfence IIs Crash Cushion [64]

3.2 Roadside Barriers

Traditional semi-rigid (W-beam, thrie beam, box beam) and flexible (cable) guardrails primarily absorb impact energy through axial and bending deformations of the rail element, plastic post deformations, post fracture, and post rotation in soil. Of course, other losses may occur due to vehicle-to-barrier friction, vehicle crush, wheel drag in soil, and wheel contact with discrete support posts. So, all guardrails are generally considered energy-absorbing when compared to rigid barriers. Certain energy-absorbing guardrails have a specific built-in mechanism to absorb additional energy, as summarized hereafter.

3.2.1 Guardrail End Terminals

There are several energy-absorbing W-beam guardrail end terminals. The Combination Attenuator Terminal (CAT) is a TL-3 redirective, gating crash cushion that dissipates energy through shearing steel in telescoping, staged W-beam guardrail sections [65]. The safety barrier end treatment (SENTRE) is a NCHRP 230 redirective, gating terminal that absorbs energy through sand-filled cartridges through momentum transfer [66]. The Brakemaster is a NCHRP 350 TL-3 redirective, gating guardrail end treatment that uses friction to decelerate vehicles as the system telescopes downstream during end-on impacts [67].

Several end terminals have an extruder head that is pushed downstream when impacted end-on. For impacts downstream of the terminal end, tension is transmitted to an anchorage system. The BEST is a TL-3 end terminal that absorbs energy as an impact head is pushed downstream when impacted end-on and the W-beam is cut into four flat strips, bent, and redirected away from traffic [68]. The Sequential Kinking Terminal (SKT) [69] and the Flared Energy Absorbing Terminal (FLEAT) [70] are TL-3 terminals that absorb energy during end-on impacts when the impact head incrementally bends the W-beam rail into a deflector plate which

sequentially kinks the W-beam into segments and moves it away from traffic. The FLEAT and SKT are similar systems but have slightly different extruder heads.

The Beam-Bursting, Energy-Absorbing Terminal Single-Sided Crash Cushion (BEAT-SSCC) is a redirective, gating box-beam end terminal [71-72]. Energy is dissipated through the bursting of box-beam into four strips through two stages. The BEAT terminal is also available in a median bridge pier configuration (BEAT-BP) [72].

3.2.2 Energy Absorbing Bridge Rail (Fragmenting Tube)

A fragmenting tube energy-absorbing bridge rail was developed at the Texas Transportation Institute in 1970 [73]. A 6-in. x 6-in. (152-mm x 152-mm) box beam rail was supported by an aluminum fragmenting tube that fractures into small segments, absorbing energy, when forced into a die attached to the posts, as shown in Figure 11. Four crash tests were conducted. One of the crash tests had an impact severity of 84.6 kip-ft (114.8 kJ), and the barrier permanently deflected 14.8 in. (375 mm).

3.2.3 Reinforced Concrete with Open Box Guardrail and Polystyrene

Two reinforced concrete barriers, one with open box guardrail and one with polystyrene brackets, were crash tested and evaluated at the Transport and Road Research Laboratory in England in 1972 [74]. The reinforced concrete barrier with open box guardrail absorbed energy through the collapsing of the open box guardrail and the hexagonal brackets, as shown in Figure 12. Two full-scale crash tests were conducted. One crash test had an impact severity of 61.6 kip-ft (83.5 kJ), and the barrier permanently deflected 5.1 in. (130 mm). The other crash test had an impact severity of 145.3 kip-ft (197 kJ), and the barrier permanently deflected 7.3 in. (185 mm).

The reinforced concrete barrier with polystyrene brackets was similar to the open box guardrail barrier, but it had additional energy-absorbing polystyrene fill surrounding the lower hexagonal brackets, as shown in Figure 13. Two full-scale crash tests were conducted. One crash

test had an impact severity of 51.3 kip-ft (69.6 kJ), and the barrier dynamically deflected 12.1 in. (308 mm) and permanently deflected 4.5 in. (115 mm). The other crash test had an impact severity of 132.3 kip-ft (179.3 kJ), and the barrier permanently deflected 6 in. (152 mm).

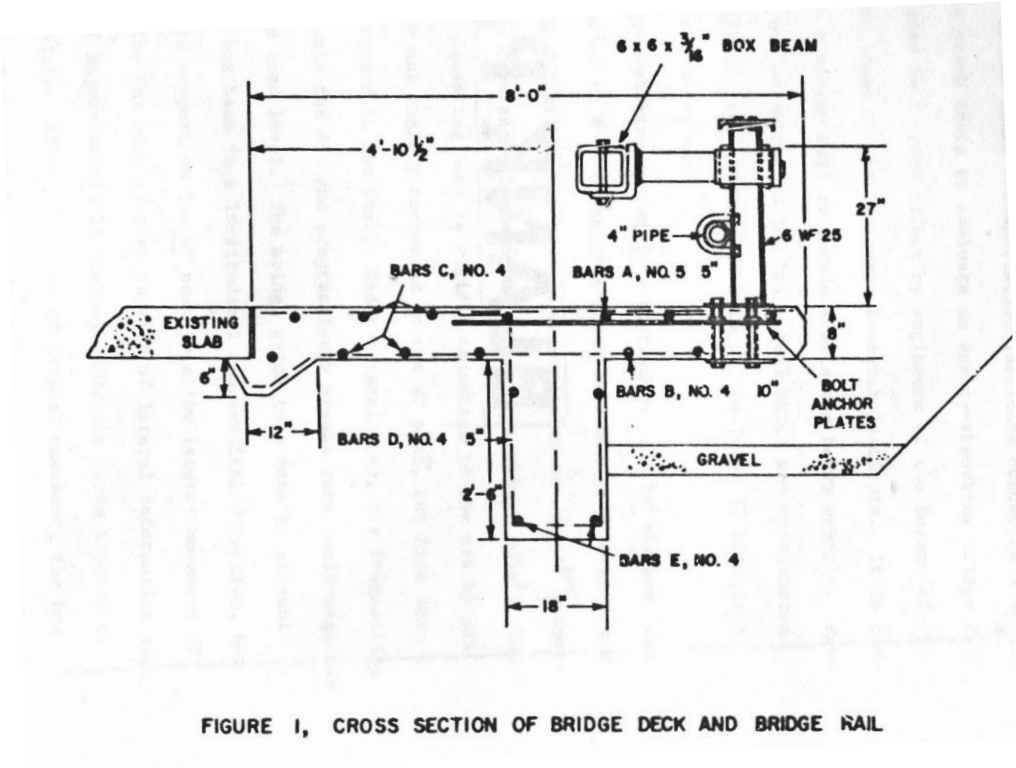

Figure 11. Fragmenting Tube Energy-Absorbing Bridge Rail [73]

3.2.4 Collapsing Ring

Two rail systems absorbed energy through crushing rings. The Collapsing Ring Bridge Railing System (CRBRS) was developed at the Southwest Research Institute in 1976 [28]. The bridge rail had a lower tube rail with an axial collapsing ring attached to a post, as shown in Figure 14. An upper rail contains impacts from large tractor/trailer trucks and buses. Several full-scale crash tests were conducted according to NCHRP Report No. 153 test standards [75]. One crash test had an impact severity of 84.4 kip-ft (144.5 kJ), and the barrier dynamically deflected 21 in. (533 mm). Another crash test had an impact severity of 311.4 kip-ft (422.3 kJ), and the barrier dynamically deflected 57.1 in. (1,458 mm).

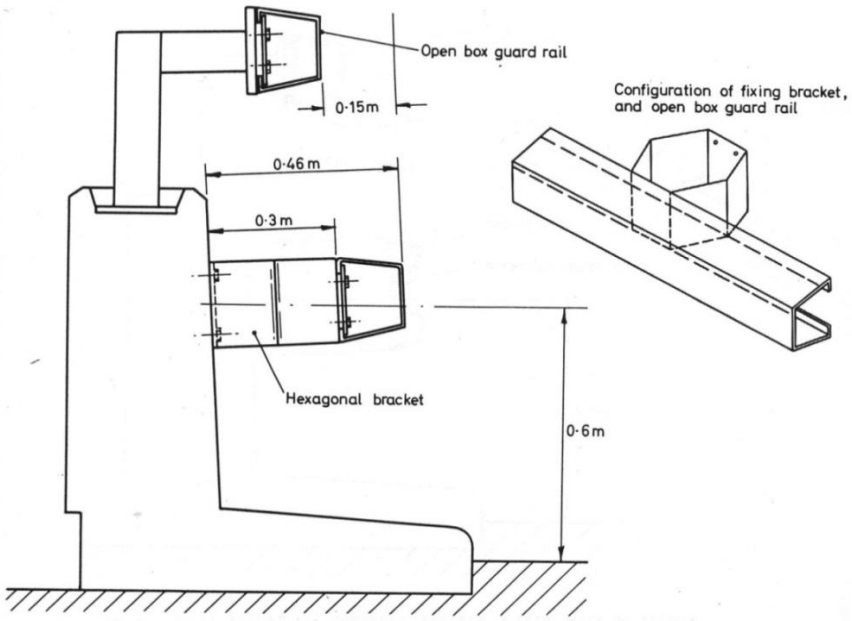

Fig. 2. CROSS SECTION OF CONCRETE PARAPET FITTED WITH STEEL BRACKETS AND OPEN BOX GUARDRAIL

Figure 12. Reinforced Concrete with Open Box Guardrail [74]

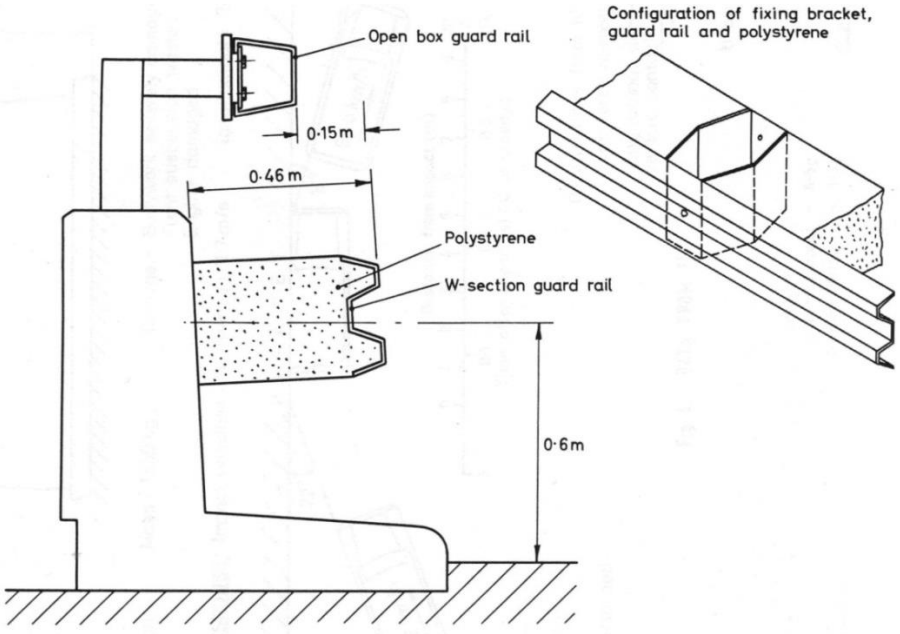

Fig. 3. CROSS SECTION OF CONCRETE PARAPET FITTED WITH W-SECTION GUARDRAIL AND POLYSTYRENE PADDING

Figure 13. Reinforced Concrete with Polystyrene Brackets [74]

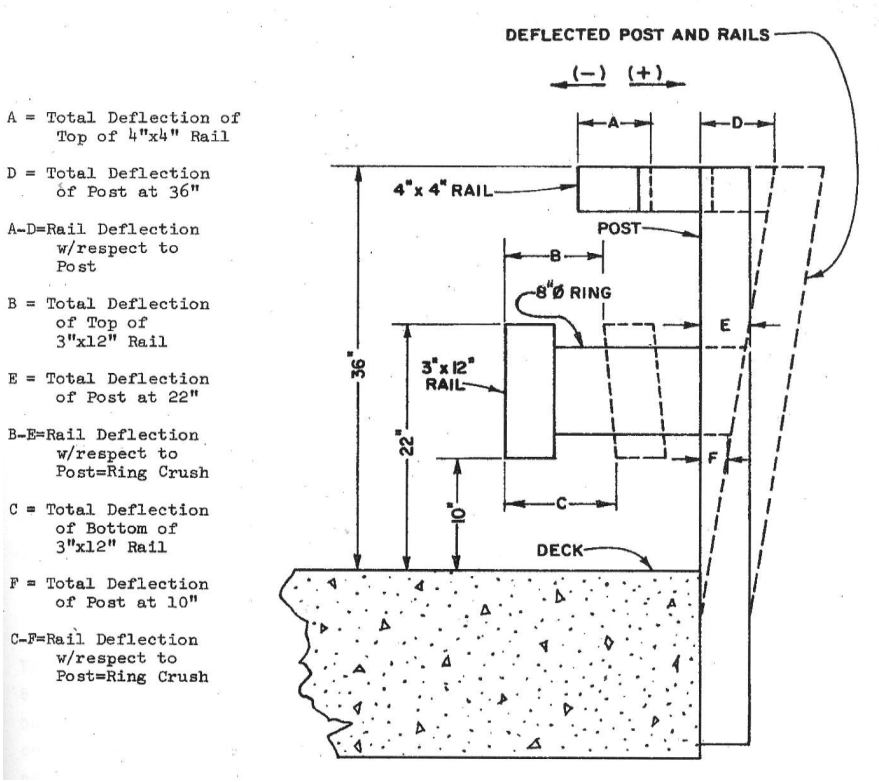

Figure 14. Collapsing Ring Bridge Railing System [28]

The Tubular Thrie Beam on a Concrete Baluster [76] and Tubular Thrie Beam Retrofit Bridge Rail [77] were developed at the Southwest Research Institute in 1976 and 1985, respectively. The tubular thrie beam on a concrete baluster had a laterally-loaded collapsing ring attached to a concrete baluster bridge rail, as shown in Figure 15. The barrier was tested according to NCHRP Report No. 153 crash standards. One of the crash tests had an impact severity of 98.6 kip-ft (133.7 kJ), and the barrier permanently deflected 5 in. (127 mm).

The tubular thrie beam retrofit bridge rail also contained a laterally-loaded collapsing ring attached to a steel and concrete bridge rail, as shown in Figure 16 [77]. The system was also modified to a 38 in. (965 mm) height. The barrier was crash tested according to NCHRP Report No. 230. One of the crash tests had an impact severity of 76.5 kip-ft (103.7 kJ), and the barrier permanently deflected 5.5 in. (140 mm).

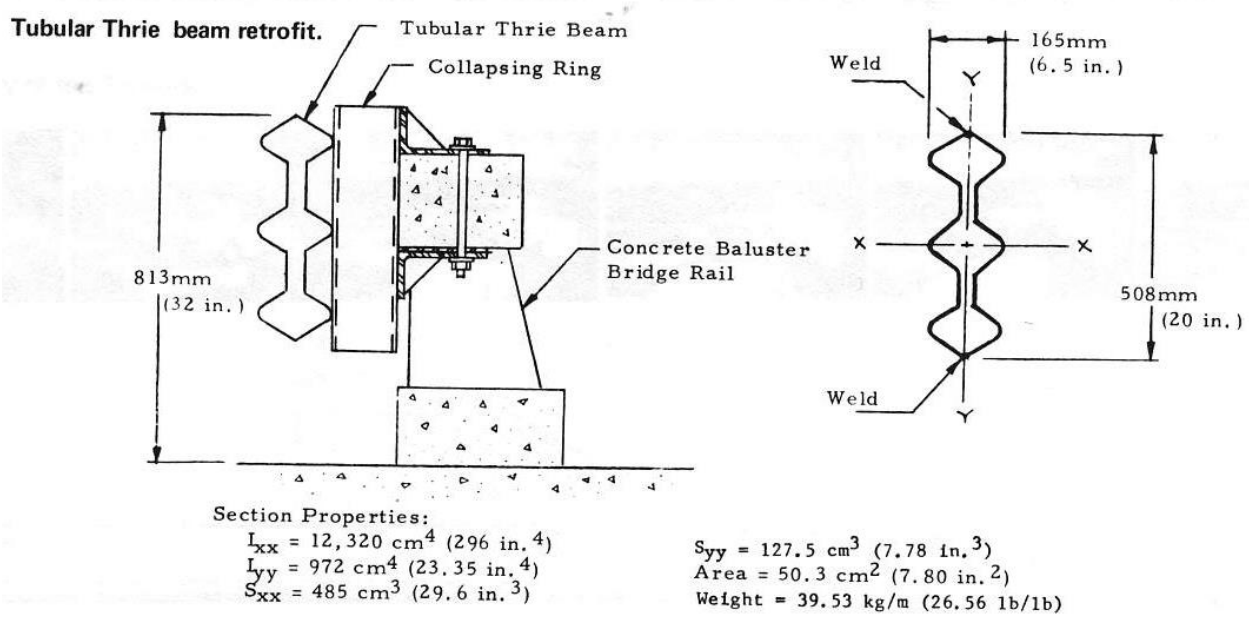

Figure 15. Tubular Thrie Beam on Concrete Baluster [76]

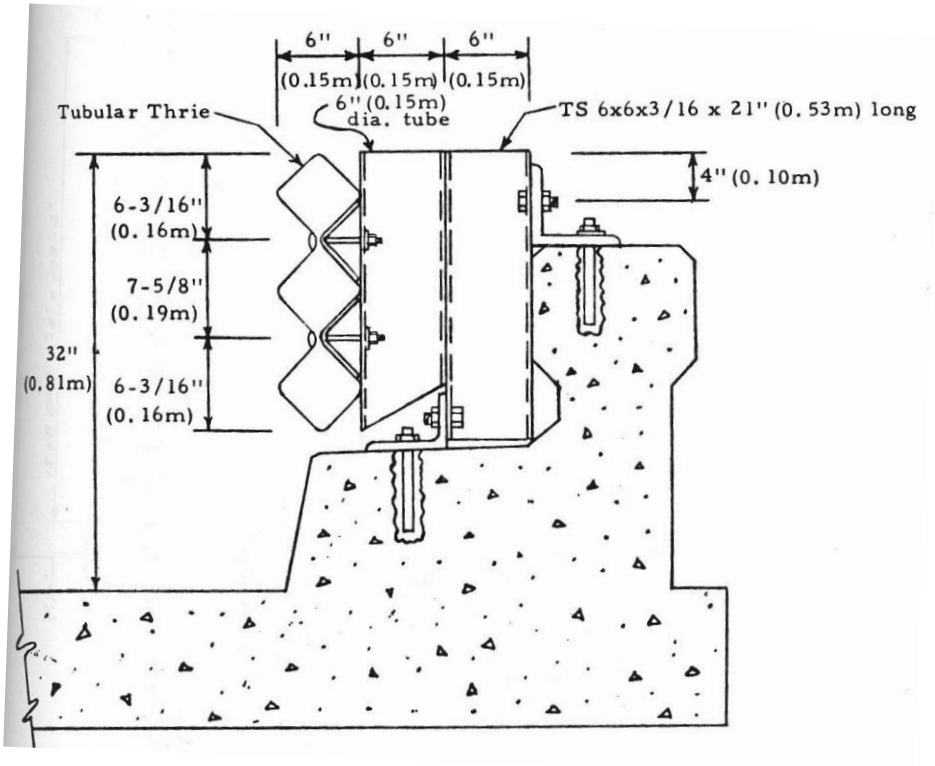

Figure 16. Tubular Thrie Beam on Retrofit Bridge Rail [77]

3.2.5 Low-Maintenance, Energy-Absorbing Bridge Rail

A low maintenance, energy-absorbing bridge rail was developed at TTI in 1986 [27]. The bridge rail had structural steel tube railings and posts and high-strength rubber energy absorbers, as shown in Figure 17. The rail was crash tested according to NCHRP Report No. 230 crash test standards. One crash test had an impact severity of 103.8 kip-ft (140.7 kJ), and the barrier dynamically deflected 7.2 in. (183 mm).

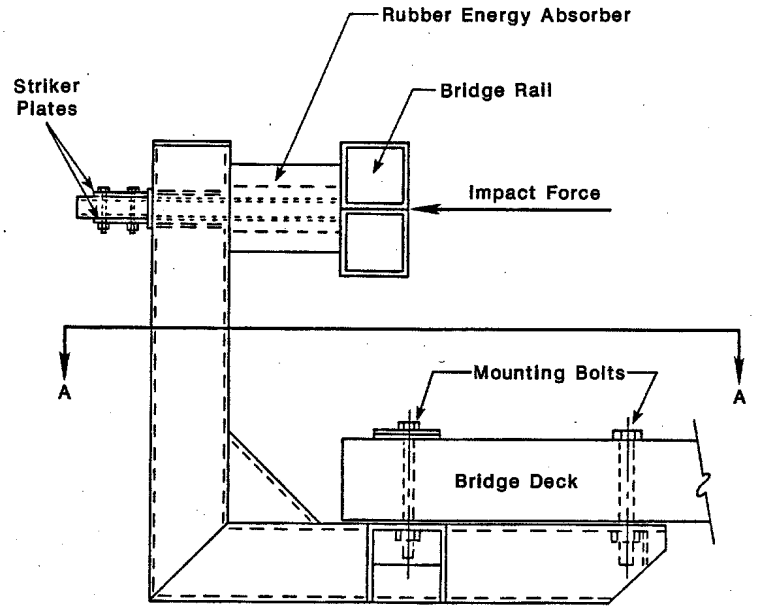

Figure 17. Low Maintenance Energy-Absorbing Bridge Rail [27]

3.2.6 SERB Bridge Rail Retrofit, Median Barrier, and Bridge Rail

The SElf-Restoring Barrier (SERB) family of barriers was developed at the Southwest Research Institute in 1987 [78]. The thrie beam rails pivot upward upon impact to absorb energy and then restore to their original position. The bridge rail and median barrier configurations are shown in Figure 18. The bridge rail retrofit was similar to the bridge rail configuration, only it was attached to a concrete parapet. Several full-scale crash tests were conducted according to NCHRP Report No. 230 test standards. One crash test had an impact severity of 98 kip-ft (132.9

kJ), and the barrier dynamically deflected 14.2 in. (361 mm). Another crash test had an impact severity of 262.9 kip-ft (356.4 kJ), and the barrier dynamically deflected 28.8 in. (732 mm).

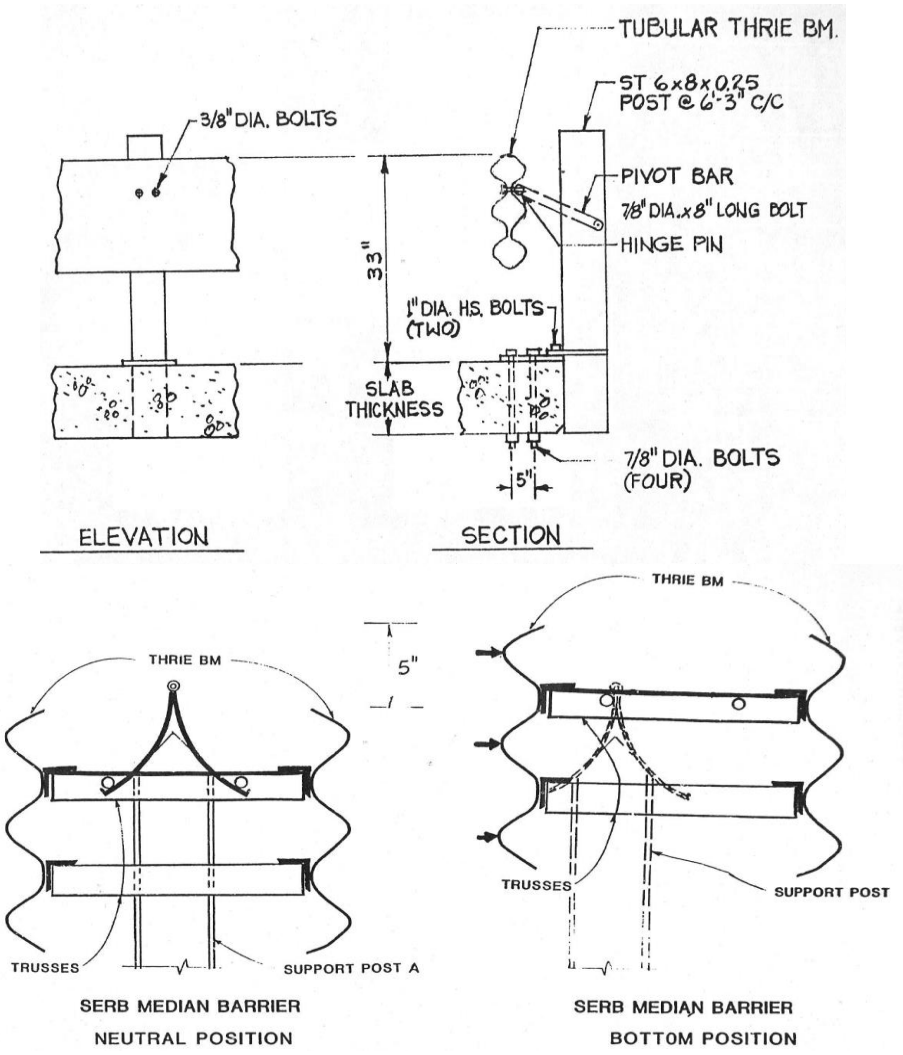

Figure 18. SERB Bridge Rail and Median Barrier [78]

3.2.7 Energy-Absorbing Bridge Rail

The Energy-Absorbing Bridge Rail was developed at the Texas Transportation Institute in 2010 [79]. The barrier contained two steel tube rails with a laterally-loaded collapsible steel pipe attached to a concrete parapet, as shown in Figure 19. Two full-scale crash tests were conducted according to MASH, only at higher speeds around 85 mph (137 km/h). One successful crash test with an 1100C small car had an impact severity of 110.6 kip-ft (150 kJ), and the barrier

dynamically deflected 7.5 in. (191 mm) and permanently deflected 5.3 in. (133 mm). One unsuccessful crash test with a 2270P pickup truck had an impact severity of 228 kip-ft (309.1 kJ), and the barrier permanently deflected 6.5 in. (165 mm). The dynamic deflection was unknown. The 2270P pickup truck was redirected and exited the system, and then subsequently rolled over two and one- half times.

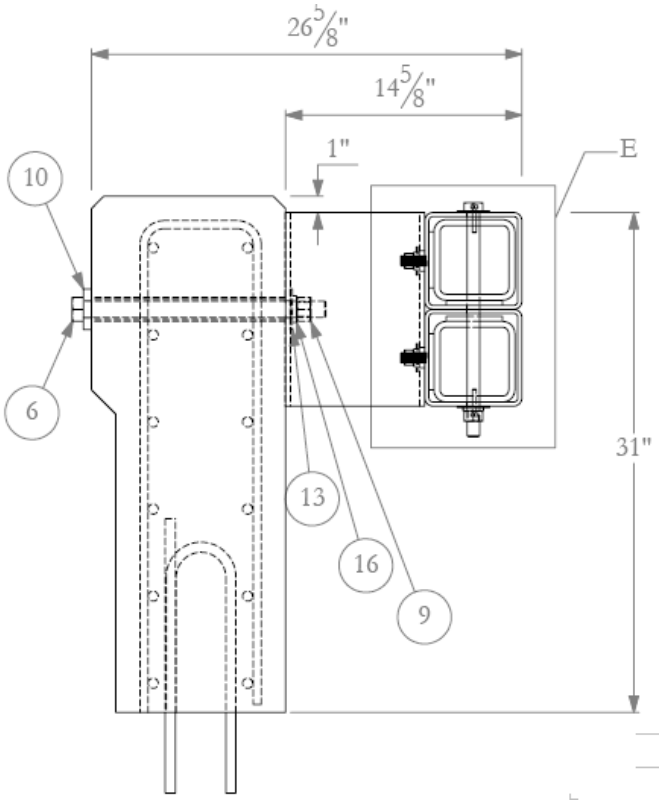

Figure 19. Energy-Absorbing Bridge Rail [79]

3.3 Bridge Bumpers

A bridge bumper, consisting of a stiff guard and energy-absorbing material attached to a reinforced concrete bridge girder, was developed to minimize damage from overheight vehicles driving underneath bridges, as shown in Figure 20 [80]. Four different types of the Last-A-Foam series of foams manufactured by General Plastics Manufacturing Company were explored for the energy-absorbing material. A small drop test experiment showed that the bridge bumper

decreased peak accelerations by up to 86 percent. Finite element simulations were validated by the experiments and used to optimize the bridge bumper for full-scale applications.

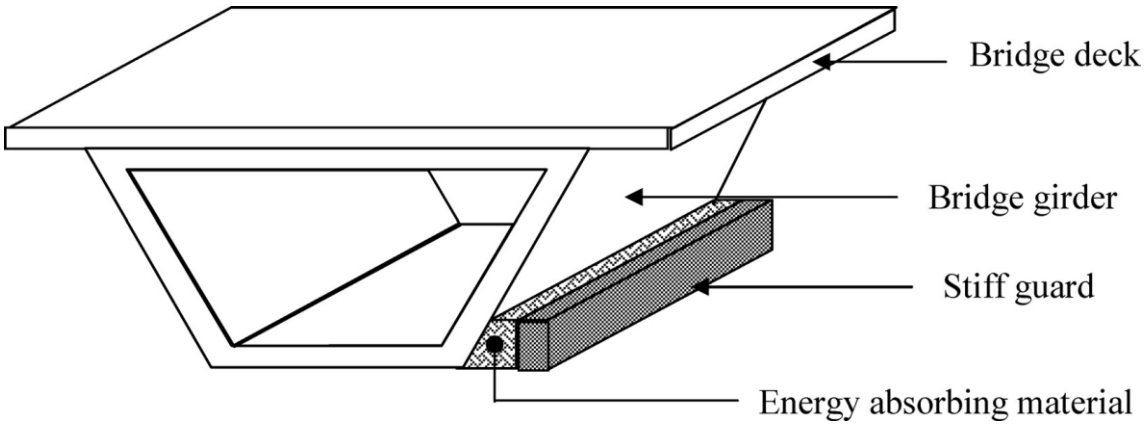

Figure 20. Energy-Absorbing Bridge Bumper [80]

3.4 Loading Dock Bumpers

Loading dock bumpers protect loading docks from damage when impacted by large trucks. Some dock bumpers can be made of laminated, recycled tire material and can absorb up to 80 percent of truck impacts [81], as shown in Figure 21a. Other dock bumpers are made of extruded 70-durometer rubber shapes with an impact resistance of 75 percent. Examples of some of the extruded shapes are shown in Figure 21b.

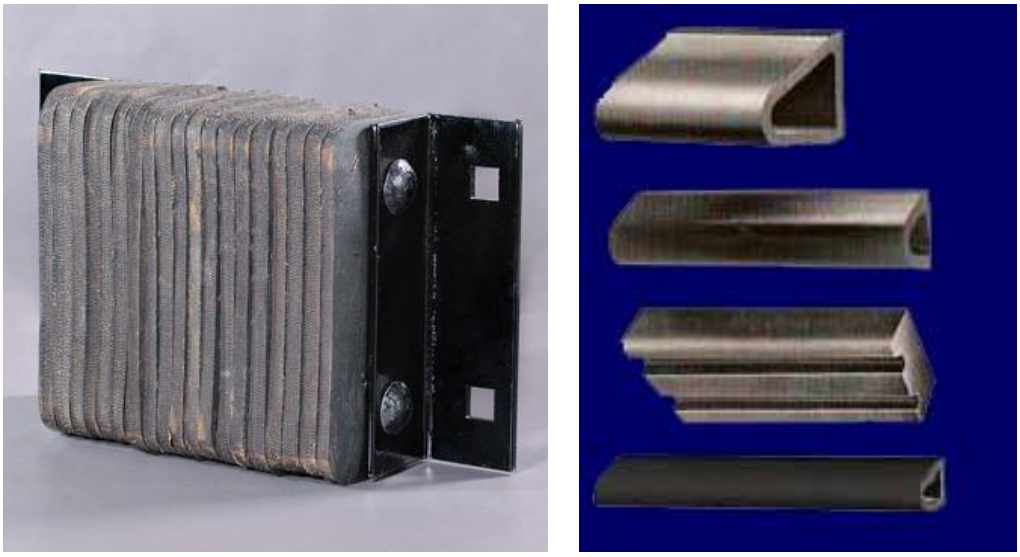

(a) Laminated Recycled Tire Bumper (b) Extruded Rubber Bumper

Figure 21. Loading Dock Bumpers [81]

3.5 Marine Fenders

Elastomeric marine fenders protect large port docks from impacts with berthing ships. Most deform primarily under shear or compressive loads but can also accept tensile loads. Marine fenders come in a wide variety of shapes and sizes. An extruded elastomer shape may extend the length of a dock, or single units with steel faces may be placed incrementally along the dock.

Figure 22. Marine Fenders [82]

3.6 Membrane Shock Absorber

Membrane shock absorbers are typically used to prevent boats from impacting docks, as shown in Figure 23 [83]. The force vs. deflection curve is nearly zero until it nears the maximum deflection, at which the force increases rapidly [84]. Membrane shock absorbers can have an initial air pressure to provide more resistance, but most have ambient air pressure.

Figure 23. Membrane Shock Absorber [83]

3.7 Buoys

Buoys are placed in waterways to provide light and direct vessels. Collision survivable buoys made by Urethane Technologies, Inc. are made of closed cell, cross-linked polyethylene foam with a polyurethane skin to protect them from environmental effects [85]. Buoys come in a large variety of sizes and shapes. Two examples of buoys are shown in Figure 24.

3.8 Automobile Absorbers and Bumpers

Automobile absorbers and bumpers reduce the dynamic loads applied to the vehicle on uneven road surfaces. They can be made from a wide variety of materials. One such example is the Enertrols Elastomeric Bumpers which are made from rubber, as shown in Figure 25 [86]. Enertrols Elastomeric Bumpers are engineered energy-absorption products that are used in a variety of applications, especially transportation vehicles. The bumpers are lightweight compared to some of the other rubber shapes. The Enertrol bumpers can have an energy capacity up to 1.4 kip-ft (1.9 kJ) in just over 2 in. (51 mm) of crush deflection. Many different sizes and shapes of

Enertrol bumpers can be utilized in varied applications. The bumpers also have a large temperature range of -30 F to 150 F (-34 C to 66 C).

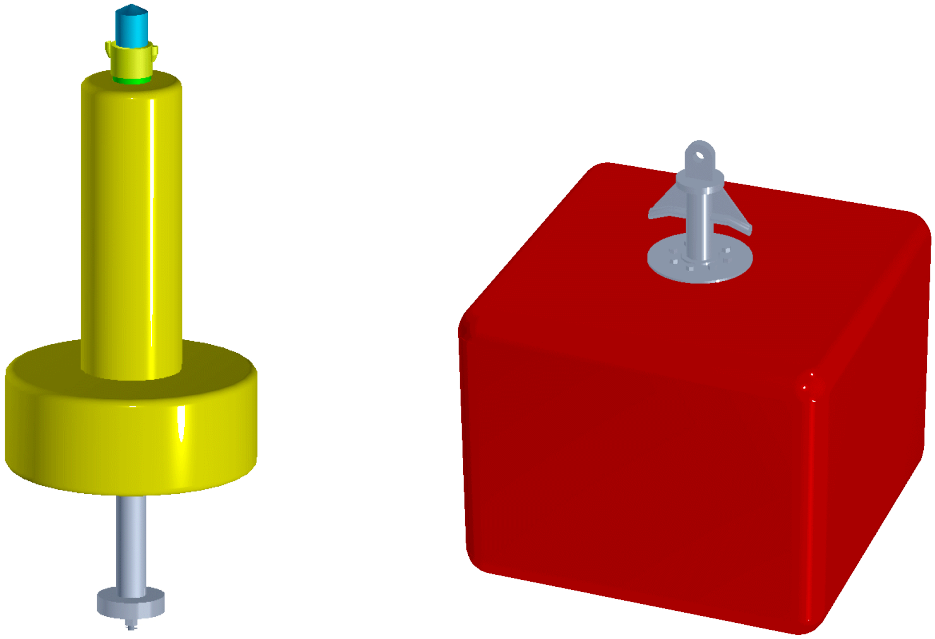

Figure 24. Collision Survivable Buoys [85]

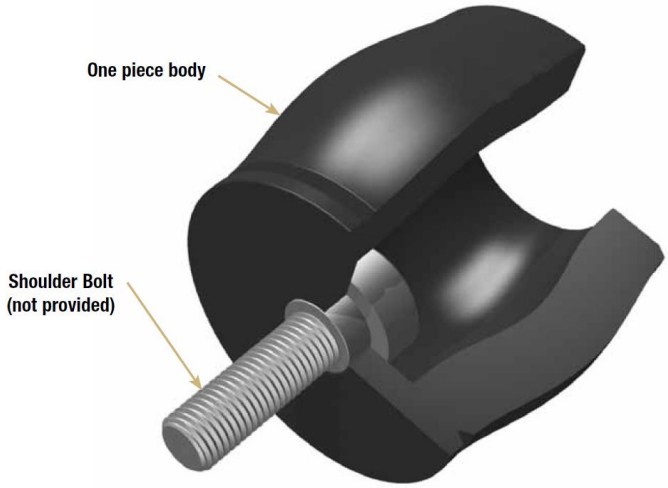

Figure 25. Enertrol Bumper [86]

3.9 Springs

Springs can elastically deform in systems to absorb energy. The deformation can either be through extension, compression, or torsion. One notable application is the use of coil springs

in an automobile suspension system. Springs reduce the motion of the vehicle caused by uneven roadway surfaces.

3.10 SAFER Barrier

The current SAFER barrier utilizes open-cell foam blocks. The blocks are manufactured from 15-psi (103-kPa) rated, extruded, polystyrene foam sheets which are bonded together [9]. The 22-in. (559-mm) deep x 40-in. (1,016-mm) tall foam blocks have a trapezoidal-shape front section with a 16-in. (406-mm) wide by 8-in. (203-mm) deep rectangular-shape rearward section. Foam cartridges are spaced at 67.2 in. (1,707-mm) on center. The foam blocks can be almost fully crushed, but they are not reusable after such a major impact event. In test no. IRL-24, a 3,606-lb (1,636-kg) NASCAR stock car impacted the curved SAFER barrier at a speed of 133.1 mph (214.2 km/h) and at an angle of 26.9 degrees, and the barrier dynamically deflected 20.0 in. (508 mm). The peak lateral deceleration decreased 12.4 percent compared to a similar impact with a rigid concrete wall. In test no. IRL-25, a 1,951-lb (885-kg) IRL car impacted the curved SAFER barrier at a speed of 150.9 mph (242.9 km/h) and at an angle of 27.5 degrees, and the barrier dynamically deflected 11.2 in. (284 mm). The peak lateral deceleration decreased 36 percent compared to a similar impact with a rigid concrete wall.

3.11 Sorbothane

Sorbothane is visco-elastic polymer with material properties that are similar to rubber [87]. Sorbothane is primarily used in shock absorption and vibration damping applications and is restorable with a long fatigue life. Sorbothane is used in small deflection energy-absorption applications, such as in shoe insoles and appliance vibration damping. An example of the damping response of Sorbothane, butyl rubber, and neoprene to a given impulse is shown in Figure 26.

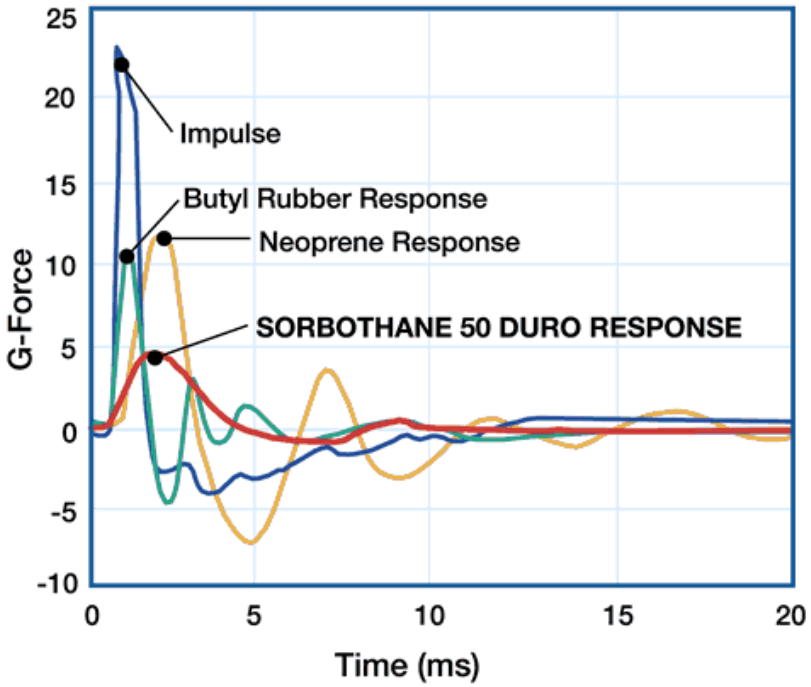

Figure 26. Time Delay Effect of Impulse (Shock) Response of Selected Materials [87]

4 DESIGN CONCEPTS

4.1 Energy Absorber Requirements

The most efficient energy absorber was sought to maximize the benefits of the new barrier system. Measures of energy-absorber efficiency include:

Average Force/Peak Force

Initial Length/Compressible Length

Energy/Unit Weight

Energy/Unit Length of Deflection

The ideal force versus deflection curve, which maximizes the average force to peak force ratio, is shown in Figure 27. However, materials that exhibit properties similar to the ideal curve do not usually fully restore. So, other force versus deflection curves were also acceptable as long as the energy absorber restores and adequately deflects without a large spike in force.

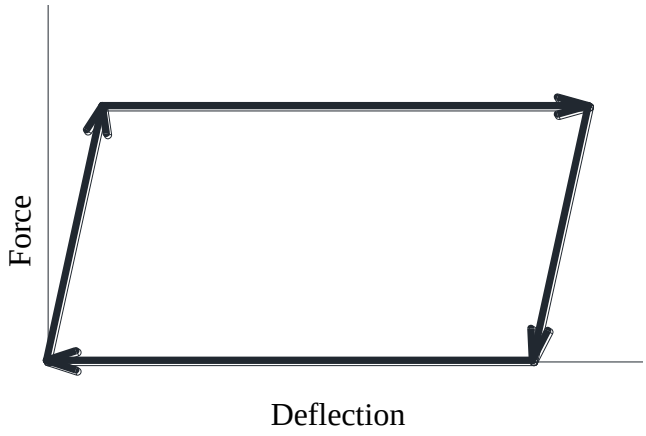

Figure 27. Ideal Force versus Deflection Curve

The compressible length, or stroke, was targeted to be a maximum of 10 in. (254 mm) for the MASH TL-4 2270P impact. An ideal energy absorber would have an initial length to compressible length of 1. The ideal energy/unit weight would be as high as possible, so that the energy absorber would be as lightweight as possible.

The capacity of an energy-absorbing system can be adjusted by adding additional elements and modifying the spacing. The desired energy per unit length of deflection is dependent on the spacing of the energy absorbers and continuity of the rail.

The new barrier system was designed to maximize absorption, and all the energy absorbers within a 40-ft (12.2-m) span were assumed to deflect at least 40 percent of the maximum deflection, similar to the results of test no. IRL-24. The SAFER barrier analysis demonstrated that there is not a direct relationship between energy absorbed by a barrier and the corresponding reduction in peak lateral acceleration. Considering that 24 percent of the lateral component of the 3,606-lb (1,636-kg) racecar's kinetic energy was absorbed specifically by the foam energy absorbers, it was estimated that 30 percent of the lateral kinetic energy of the larger pickup truck should be absorbed by the energy absorbers in the new barrier. However, this value could vary significantly between vehicles depending on the amount of vehicle crush that occurs. If 30 percent of the lateral kinetic energy in the 2270P TL-4 impact (35 kip-ft (47.4 kJ)) is absorbed by the energy absorbers, the energy absorption per linear foot of barrier is 0.88 kip-ft/ft (3.91 kJ/m).

Assuming half of the energy absorbers deflect 80 percent of the maximum deflection and half of the energy absorbers deflect 40 percent of the maximum deflection, a schematic of the barrier deflection is shown in Figure 28. Energy absorbers over a 40-ft (12.2-m) span deflect an average of 60 percent of the maximum deflection (10 in. (254 mm)). The combinations of spacing and force levels expected from each energy absorber could be estimated using the following equation for an ideal force versus deflection curve:

$$\frac{0.88\ k-ft}{ft} = \frac{F * 0.6(10\ in.) * \frac{1ft}{12\ in.}}{s}$$

Where *F* is the force required in kips and *s* is the spacing of energy absorbers in ft

The required peak force for an energy absorber that will deflect a maximum of 10 in. (254 mm) during a 2270P TL-4 impact compared to energy absorber spacing is shown in Figure 29. The energy required from each absorber is approximately 4.4 kip-ft (6.0 kJ) for 5 ft (1.5 m) spacing and 17.6 kip-ft (23.9 kJ) for 20 ft (6.1 m) spacing, based on the prior assumptions.

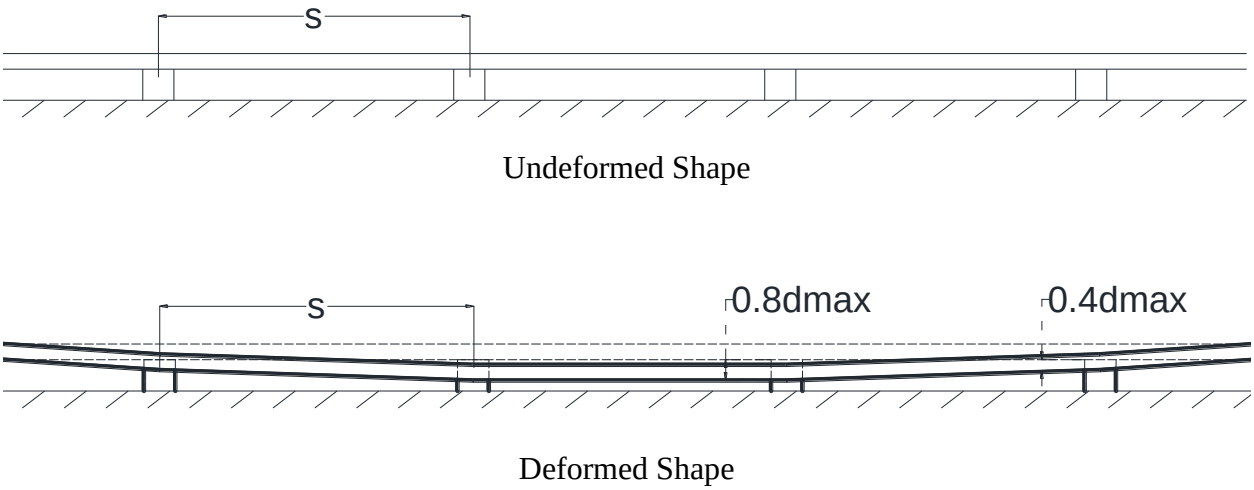

Figure 28. Schematic of Barrier Deflection

If the energy absorbers deflect more than 10 in. (254 mm), these force levels would decrease. If the energy absorber has a force versus deflection that is less than the ideal curve in Figure 27, the required force levels would increase.

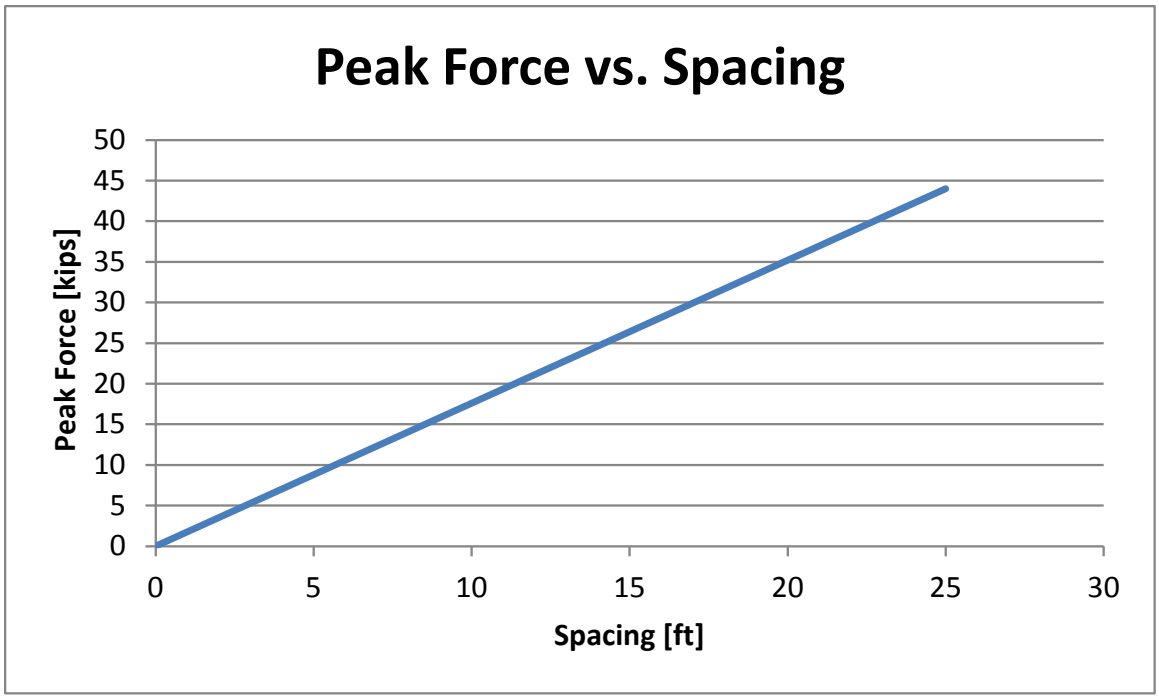

Figure 29. Energy Absorber Force vs. Spacing

4.2 Material Evaluation

The energy absorber must be restorable, reusable, and resistant to environmental effects. Several of the energy-absorbing applications previously discussed do not meet these criteria. The materials that could meet these criteria include: elastomeric shapes (including marine fenders, loading dock bumpers, Enertrols, and recycled tires), some foams, some air baffle systems, springs, Sorbothane, and HDPE.

4.2.1 HDPE

HDPE was the energy-absorbing material used in two restorable crash cushions (the Compressor and HEART). However, in an end-on impact, neither system restored completely, and a large deflection was required for those particular shapes to absorb a vehicle's impact energy. The energy-absorption properties of HDPE is highly dependent on the shape it is molded, and HDPE absorbs more energy in compression that tension. Due to this fact and the

results from some previous in-house component testing, HDPE was not further considered for use in this barrier system.

4.2.2 Foam

Many open-cell foams, such as the foam used in the SAFER Barrier, cannot take multiple impact events so are not recommend for use in a low-maintenance barrier. Molded polyurethane foams are often used in automotive applications such as seat cushions. Lower density foams are usually semi-recoverable, and can be almost fully recoverable at low strains. The higher density foams can take larger forces and absorb more energy than lower density foams; however, they deflect less and do not recover like the lower density foams. Foams are not resistant to environmental effects and thus would therefore require a protective membrane to be considered low maintenance. The foams and protective membrane could be susceptible to snagging by vehicle components.

4.2.3 Air-Baffles

Air-baffled systems have been successfully used in other energy-absorbing applications, such as the Airfence IIs crash cushion for motorcycle impacts. Since motorcycles have a much lower mass than passenger vehicles, motorcycle impacts have a lot lower impact severity. An air-baffled system would be difficult to adapt to a highway barrier, since the baffle membrane would need to be strong enough to resist damage and puncture from vehicle components, but weak enough to allow deformation to absorb impact energy. Air baffles were not further considered.

4.2.4 Sorbothane

Sorbothane is typically used in applications when very small deflections are expected, and no premade shapes would be practical for this application. Creating a custom-made Sorbothane shape would require a significant upfront investment and thus was not further explored for this project.

4.2.5 Coil Springs

Steel springs have already been used in a wide variety of energy absorbing applications. Design equations and variables for compression springs can be found in Shigley and Mischke [88]. A 15-in. (381-mm) long compression spring comprised of ½-in. (13-mm) diameter steel wire with 5 active 5-in. (127 mm) diameter coils absorbs 2.2 kip-ft (3 kJ) of energy over a maximum deflection of 11½ in (292 mm). Therefore, 16 springs that fully-deflect would be required to absorb 34.4 kip-ft (46.6 kJ) of energy. Increasing the wire diameter increases the energy absorbed by a compressed spring. However, it is difficult to manufacture coils with a small ratio of coil diameter to wire diameter, and increasing the coil diameter decreases the energy absorbed by a compressed spring. While compression springs could be configured to adequately absorb the energy required for a 30 percent reduction in 2270P kinetic energy, the size of the springs could become quite large. Compression springs are made to work in pure compression or tension only, so if the springs deform in shear or torsion, they might be permanently damaged. Therefore, since the barrier has width restrictions and there is a possibility for the springs to be permanently damaged, they were not further pursued.

4.2.6 Elastomers

Elastomers can be made from unlimited combinations of compounds. Elastomers are reusable and restorable and can be custom molded into any shape. It has been successfully used in crash cushions, for stabilizing vehicle motions, and marine dock applications. Marine fenders can absorb the kinetic energy from large berthing vessels moving at low velocities. The kinetic energy of passenger vehicles moving at high velocities can also involve significant levels. Thus, many current marine fenders may also be adequate for use in highway applications.

The properties of elastomer compounds from CLA-VAL [89] are shown in Table 4. All compounds, except for Polyurethane, have service temperatures that are well beyond

temperatures found in the United States. Four compounds (Chloro-Isobutylene Isoprene Rubber (CIIR), Chloro-Sulfonyl Polyethylene (CSM), Ethylene Propylene Diene Monomer (EPDM), and Tetrafluoro-ethylene Resin (AFMU)) had very good or excellent resistance to important environmental effects, such as oxidation, ozone, sunlight aging, heat aging, weather, and water. EPDM is a common elastomer and has been used in previous crash cushions, so it recommended for further evaluation. Elastomers have good resistance to important environmental effects, can be molded into any shape, and have been used successfully in other roadside safety applications; therefore, elastomers were further considered for this project.

4.3 Shape Study

Statically-loaded, force versus deflection information and other energy absorber properties were collected for a variety of rubber shapes. Most of the considered shapes are currently used in other applications, such as marine fenders for berthing ships or shock-absorbing elastomeric bumpers in transportation vehicles. Several different sizes of existing rubbers shapes were compared based on the four measures of efficiency:

1. Initial Length/Compressible Length
2. Average Force/Peak Force
3. Energy/Unit Length of Deflection
4. Energy/Unit Weight

Table 4. Properties of Elastomer Compounds

PHYSICAL PROPERTIES	CR	NBR	NR/PGR	CIIR	CSM	EPDM	FPM/FKM	AFMU	SI	AU/EU
Specific Gravity	1.23-1.25	0.98	0.92	0.92	1.11-1.28	0.86	1.4-1.95	117	1.1-1.6	1.23-1.28
Hardness, Durometer	30A-95A	30A-100A	30A-100A	30A-100A	40A-95A	30A-90A	40A-95A	510	20A-90A	62-64
Tensile Strength	500-3500	1000-3500	2500-4500	2000-3000	500-3500	500-3500	2000	3400	1500	4459-4870
Elongation %	100-800	400-600	500-700	300-800	100-700	100-700	150-450	350	10040	680-690
Compression Set %	20-60	5-20	10-30	25	35-80	20-60	20-25	-	0	-
Resilience %	50-80	-	80	30	30-70	40-75	40-70	-	10	-
Tear Resistance	Good	Good	Excellent	Good	Fair	Fair-Good	Fair	Good	Fair	Good
Abrasion Resistance	Excellent	Excellent	Excellent +	Good	Good	Good	Fair	Fair	Poor	Fair
ELECTRICALPROPERTIES										
Vol.Res. ohm-cm	2x10	3.5x10	-	2x10	1X10	2x10	2x10	-	1x10	-
Dielectric Str, v/mil	400.600	250	400-600	600-800	650	500-1000	500	430	400-700	510
THERMAL PROPERTIES										
Service Temp F										
Max.	230	240	180	250	250	300	400	450	500	320
Min.	-65	-65	-65	-65	-65	-40	-40	-120	-160	32
SPECIFIC RESISTANCE										
Oxidation	Excellent	Good	Good	Excellent	Excellent	Excellent	Excellent +	Excellent +	Excellent	Excellent
Ozone	Good	Fair	Poor	Excellent	Excellent	Excellent +	Excellent	Excellent +	Excellent +	Excellent +
Sunlight Aging	Very Good	Poor	Poor	Very Good	Excellent +	Excellent +	Good	Excellent +	Excellent	Fair
Heat Aging	Excellent	Good	Good	Excellent	Excellent	Excellent	Excellent +	Excellent +	Excellent +	Excellent
Flame	Excellent +	Poor	Poor	Fair	Excellent +	Poor	Excellent	Excellent +	Poor	Poor
Oil	Good	Very Good	Poor	Poor	Good	Poor	Excellent	Excellent +	Fair	Poor
Fuel	Fair	Good	Poor	Poor	Fair	Poor	Excellent	Excellent +	Poor	Poor
Ketone/Esters	Poor	Fair	Good	Excellent	Fair	Excellent	Poor	Excellent +	Fair	Fair
Aliphatic Hydrocarbons	Good	Excellent	Poor	Poor	Fair	Poor	Excellent	Excellent +	Poor	Poor
Aromatic Hydrocarbons	Fair	Good	Poor	Fair	Fair	Fair	Excellent	Excellent +	Poor	Poor
Weather	Excellent	Good	Fair	Excellent	Excellent	Excellent	Excellent	Excellent +	Excellent	Fair
Water	Good	Good	Excellent	Excellent	Very Good	Very Good	Very Good	Excellent +	Good	Excellent

Nomenclature: CR (Chloroprene Rubber), NBR (Nitrile Butadiene Rubber), NR (Natural Rubber), PGR (Pure Gum Rubber), CIIR (Chloro-Isobutylene Isoprene Rubber), CSM (Chloro-Sulfonyl Polyethylene), EPDM (Ethylene Propylene Diene Monomer), FPM/FKM (Fluorocarbon Elastomer), AFMU (Tetrafluoro-ethylene Resin), SI (Dimethyl Polysilicone), AU/EU (Polyurethane)

The compressible length was either provided by the manufacturer or taken from a force versus deflection curve at the maximum or near maximum deflection. The energy was either provided by the manufacturer or taken from the energy versus deflection at the maximum deflection. The forces were estimated from the force versus deflection curves. A limited database exists on rubber shapes, sizes, and compounds, thus the following shapes have significantly different capacities and should be compared with caution.

4.3.1 Shear Marine Fender

The shear marine fender primarily absorbs energy through shear deformation and compression. Similar shear fenders are manufactured by Maritime International, Inc. and Morse Rubber. The shear fender is shown in Figure 30. *W* varies from 10 to 24 in. (254 to 610 mm), *H* varies from 11⅝ to 27¾ in. (295 to 705 mm), and *L* varies from 15¾ to 37¾ in. (400 to 959 mm). The load vs. deflection curves for shear and compression have a similar shape and maximum load, as shown in Figures 31 and 32 for the Maritime International, Inc. type HSF14 shear fender. However, the maximum load in compression occurs at a smaller deflection; therefore, less energy is absorbed during the compression loading. The curves are similar shaped for other sizes as well.

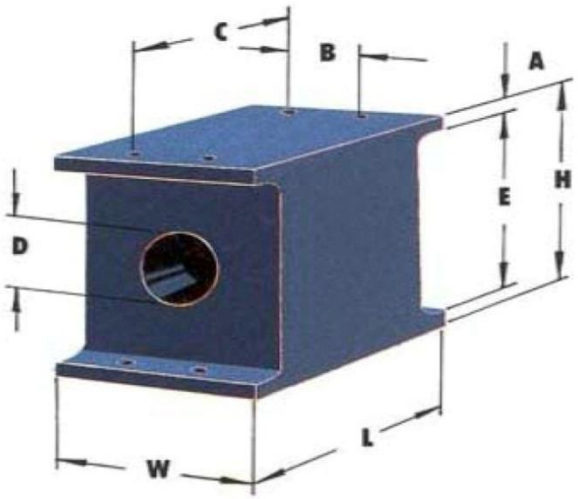

Figure 30. Shear Marine Fender

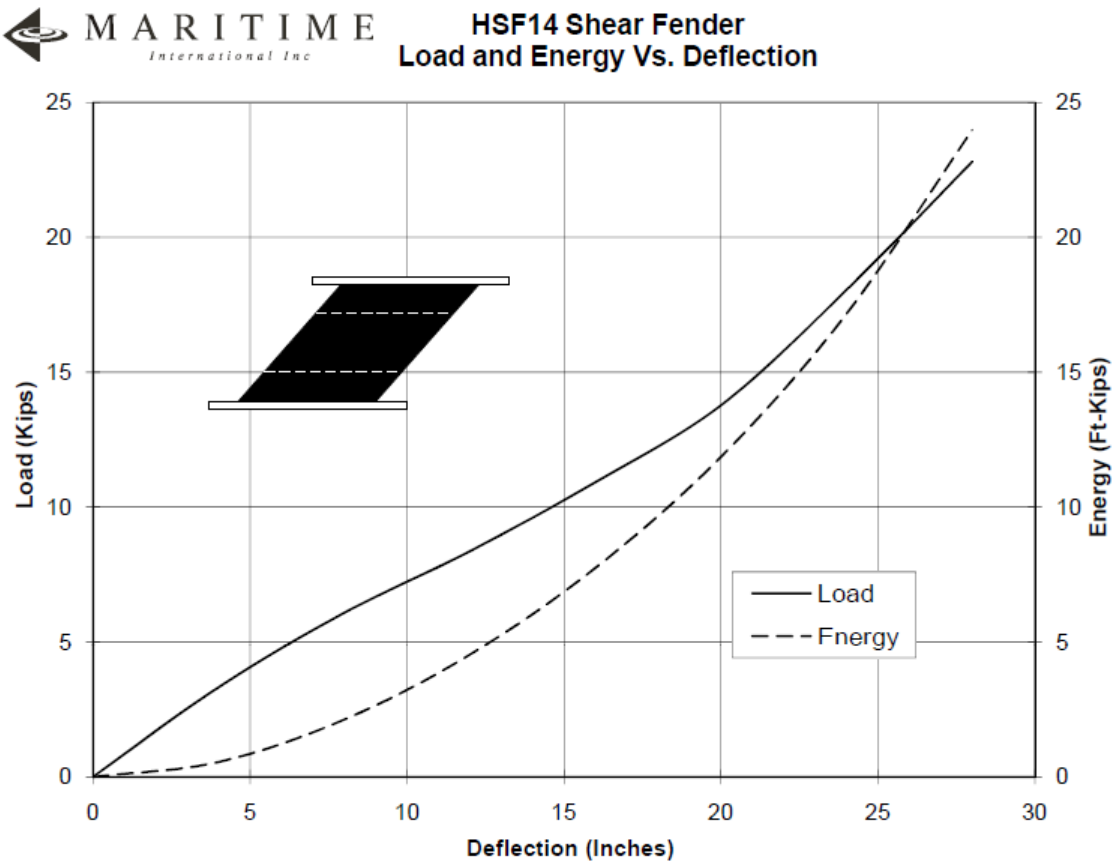

Figure 31. Shear Fender in Shear – Static Force vs. Deflection

The energy for shear marine fenders in shear varies from 9 kip-ft (12.2 kJ) to 125 kip-ft (169.5 kJ) per absorber. The efficiency measures for the shear fenders in shear are approximately:

1. Initial Length/Deformed Length = 0.43 to 0.49
2. Average Force/Peak Force = 0.54
3. Energy/Unit Length of Deflection = 0.55 to 2.5 kip-ft per inch (0.029 to 0.133 kJ per mm) of deflection
4. Energy/Unit Weight = 0.11 to 0.61 kip-ft per pound (0.33 kJ to 1.82 kJ per kg) of weight

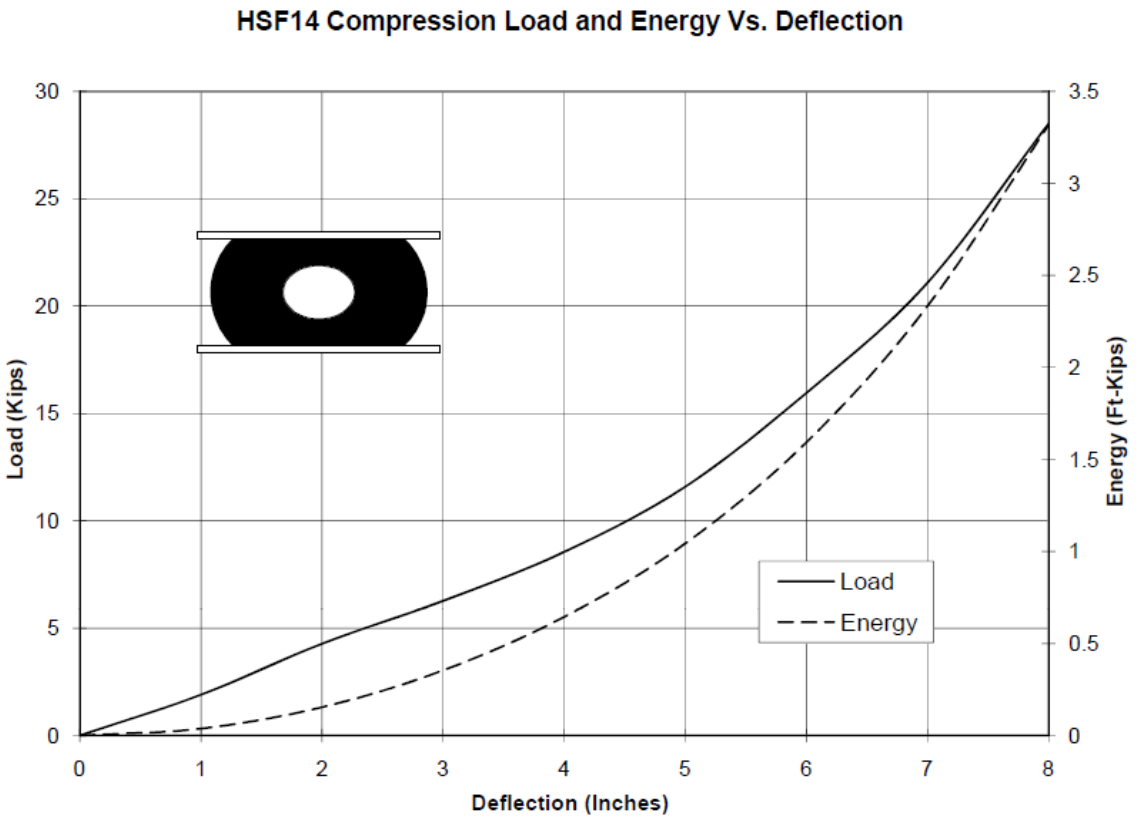

Figure 32. Shear Fender in Compression – Static Force vs. Deflection

The energy for shear fenders in compression varies from 2.8 kip-ft (3.8 kJ) to 24 kip-ft (32.5 kJ) per absorber. The efficiency measures for the shear fenders are approximately:

1. Initial Length/Compressible Length = 1.9 to 2.8
2. Average Force/Peak Force = 0.53 to 0.58
3. Energy/Unit Length of Deflection = 0.46 to 2.4 kip-ft per inch (0.025 to 0.128 kJ per mm) of deflection
4. Energy/Unit Weight = 0.03 to 2.4 kip-ft per pound (0.09 to 7.17 kJ per kg) of weight

4.3.2 Elastomeric Bumpers

The Enertrols elastomeric bumpers were discussed in Chapter 3. Since the bumpers are designed for vehicles, they are not that large nor do they have a large stroke. There are single, double, and triple stacked bumpers that were designed for high efficiency in compression.

The energy for Enertrols elastomeric bumpers varies from 0.0017 kip-ft (0.0023 kJ) to 9.4 kip-ft (12.7 kJ) per absorber. The efficiency measures for the Enertrols are approximately:

1. Initial Length/Compressible Length = 1.27 to 2.26
2. Average Force/Peak Force = NA (Peak Force = 0.18 to 192 k)
3. Energy/Unit Length of Deflection = 0.009 to 1.21 kip-ft per inch (0.0005 to 0.064 kJ per mm) of deflection
4. Energy/Unit Weight = 0.34 to 1.18 kip-ft per pound (1.02 to 3.53 kJ per kg) of weight

4.3.3 Cone-shaped marine fender

Trelleborg Marine Systems manufactures a variety of sizes of axially-loaded cone-shaped marine fenders, which is shown in Figure 33. *H* varies from 12 in. (300 mm) to 79 in. (2,000 mm), and ϕW varies from 20 in. (500 mm) to 126 in. (3,200 mm). The force vs. deflection and energy vs. deflection curves for the Trelleborg SCN300 marine fender are shown in Figure 34 [82]. The curves are similar shaped for other sizes as well.

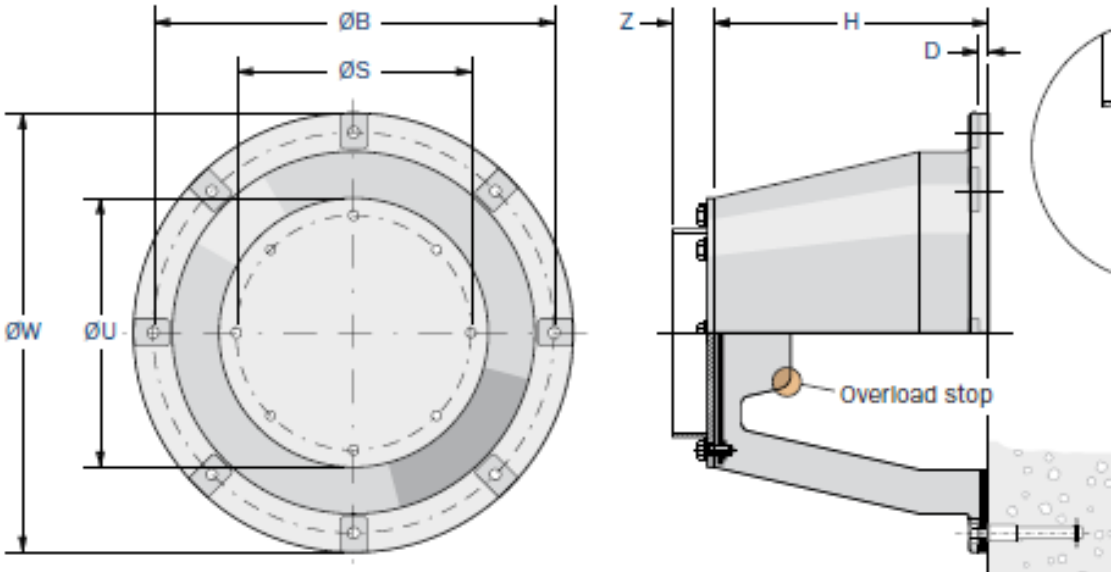

Figure 33. Cone-shaped Marine Fender [82]

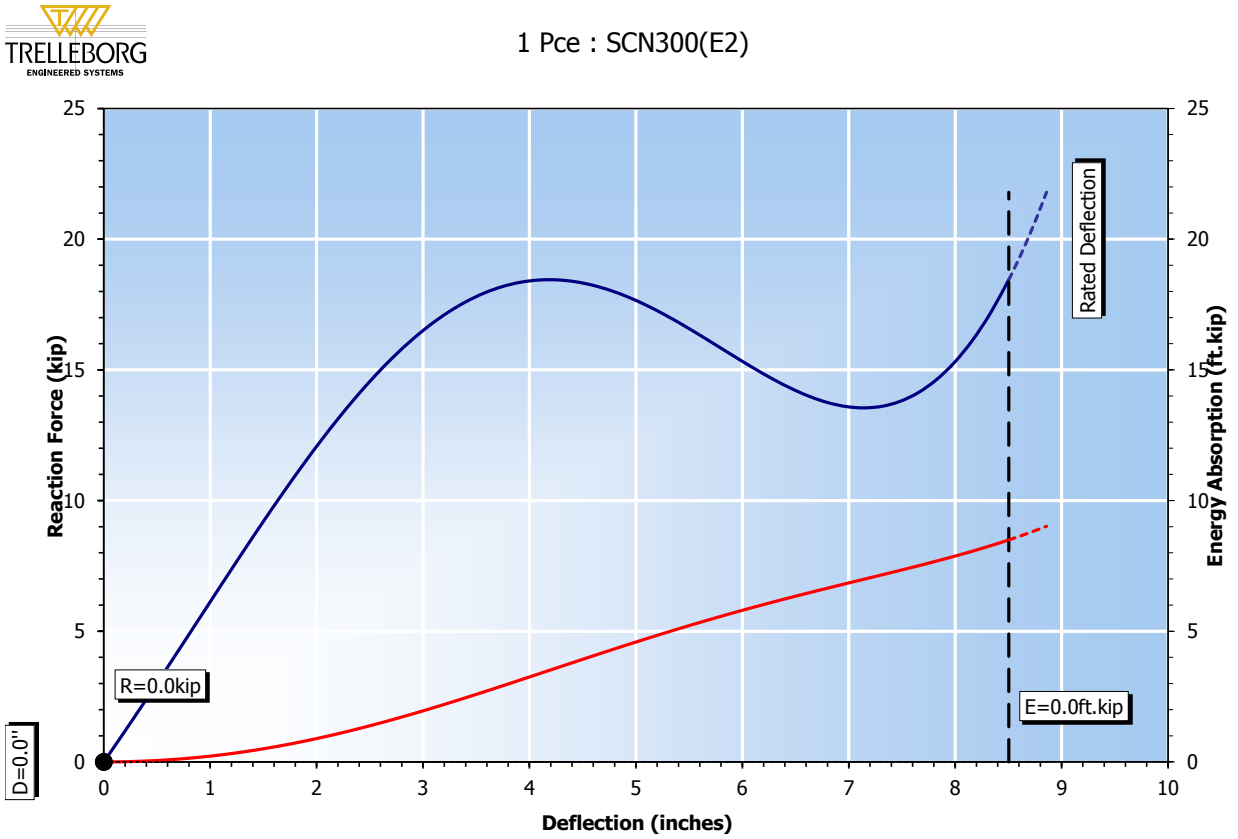

Figure 34. Cone-shaped Fender – Static Force and Energy vs. Deflection [82]

The energy for cone marine fenders varies from 8.5 kip-ft (11.5 kJ) to 2,804 kip-ft (3,802 kJ) per absorber. The efficiency measures for cone marine fenders for are approximately:

1. Initial Length/Compressible Length = 1.39
2. Average Force/Peak Force = 0.77 to 0.84
3. Energy/Unit Length of Deflection = 1 to 50 kip-ft per inch (0.05 to 2.7 kJ per mm) of deflection
4. Energy/Unit Weight = 0.10 to 0.13 kip-ft per pound (0.3 to 0.39 kJ per kg) of weight

4.3.4 Cylindrical Marine Fender

Several companies manufacture a variety of sizes of axially-loaded, cylindrical marine fenders. Trelleborg Marine Systems manufactures the elastomeric cylinders shown in Figure 35

[82]. *H* varies from 16 in. (400 mm) to 118 in. (3,000 mm), and ϕW varies from 26 in. (650 mm) to 132 in. (3,350 mm). The force vs. deflection and energy vs. deflection curves for the Trelleborg SCK400 marine fender are shown in Figure 36. The curves are similar shaped for other sizes as well.

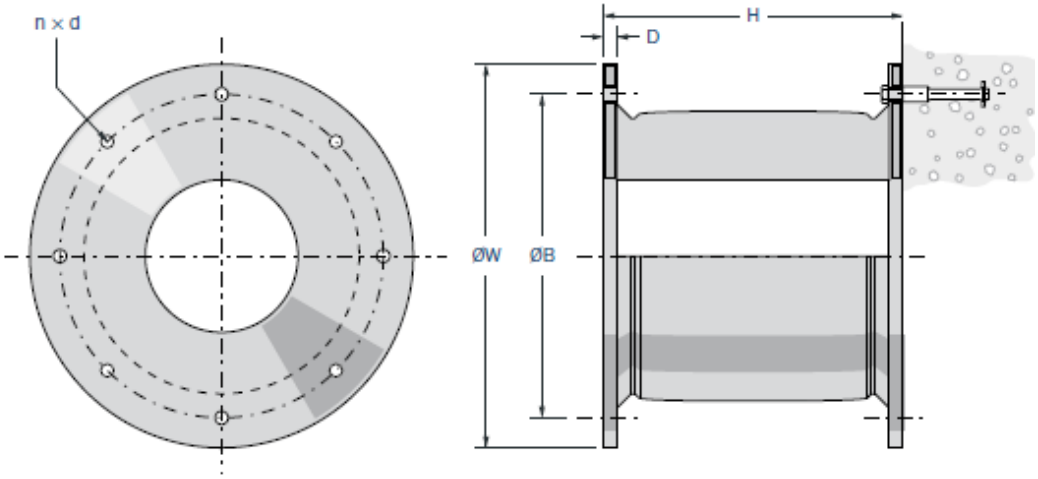

Figure 35. Cylindrical Marine Fender [82]

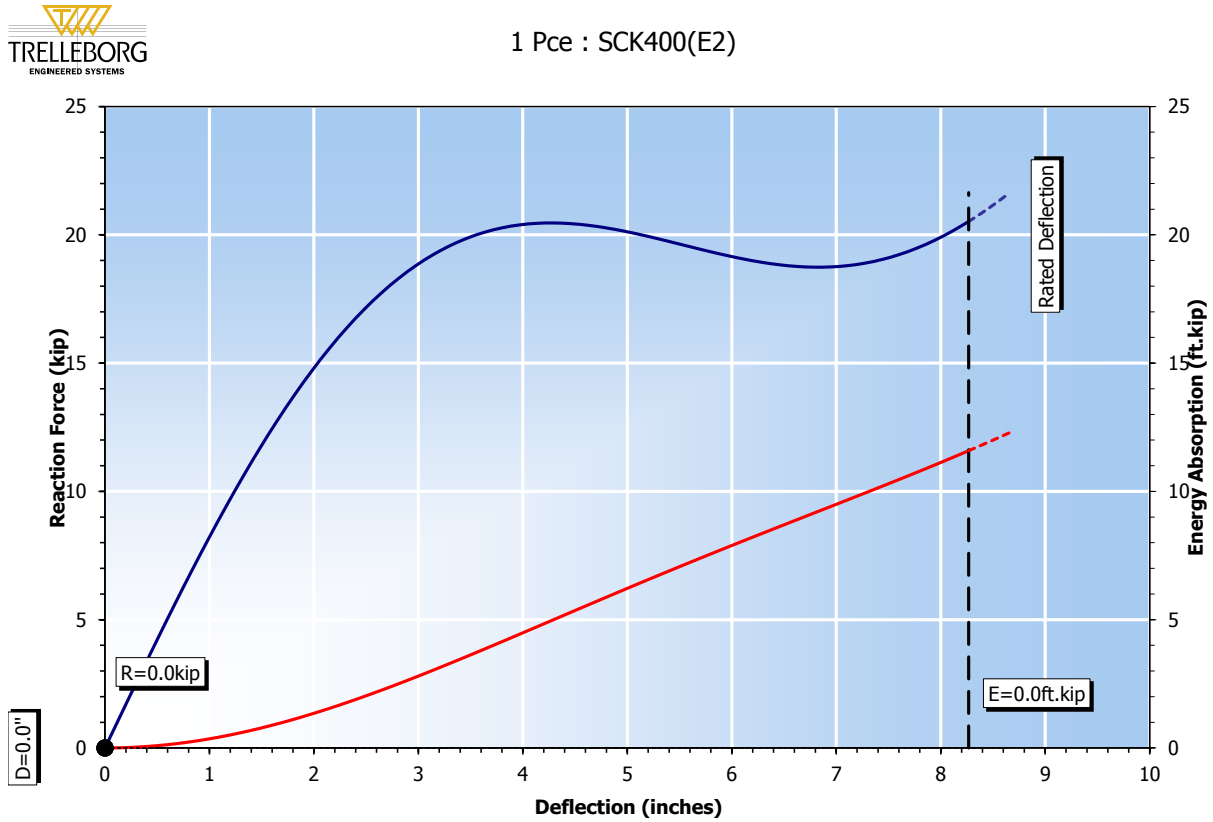

Figure 36. Cylindrical Fender – Static Force and Energy vs. Deflection [82]

The energy for cylindrical marine fenders varies from 11.6 kip-ft (15.7 kJ) to 3,191 kip-ft (4,326 kJ) per absorber. The efficiency measures for cylindrical marine fenders are approximately:

1. Initial Length/Compressible Length = 1.90 to 2.54
2. Average Force/Peak Force = 0.85 to 0.90
3. Energy/Unit Length of Deflection = 1.9 to 61.7 kip-ft per inch (0.10 to 3.29 kJ per mm) of deflection
4. Energy/Unit Weight = 0.07 to 0.08 kip-ft per pound (0.21 to 0.24 per kg) of weight

4.3.5 Unit Elements

Single trapezoidal-shaped unit element marine fenders are manufactured by Trelleborg Marine Systems, as shown in Figure 37 [82]. *H* varies from 10 in. (250 mm) to 63 in. (1,600 mm), and *W* varies from 9 in. (218 mm) to 44 in. (1,130 mm). The length of the unit element can vary from 24 in. (600 mm) to 110 in. (2800 mm). The force vs. deflection and energy vs. deflection curves for the Trelleborg UE300x600 marine fender are shown in Figure 38.

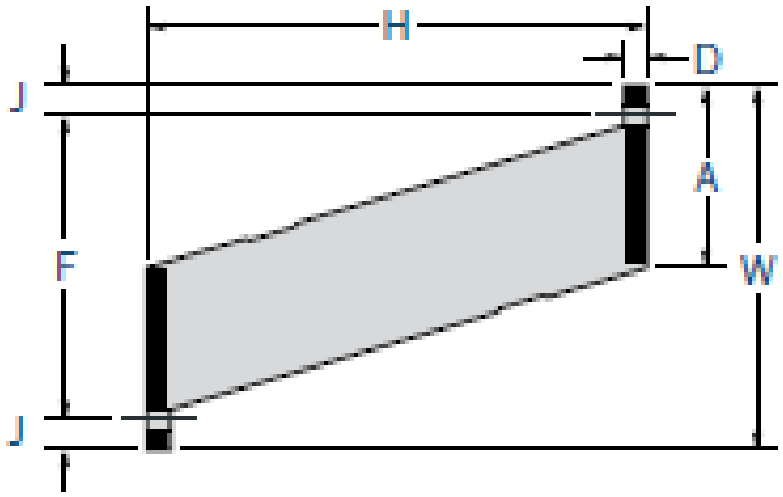

Figure 37. Marine Unit Element [82]

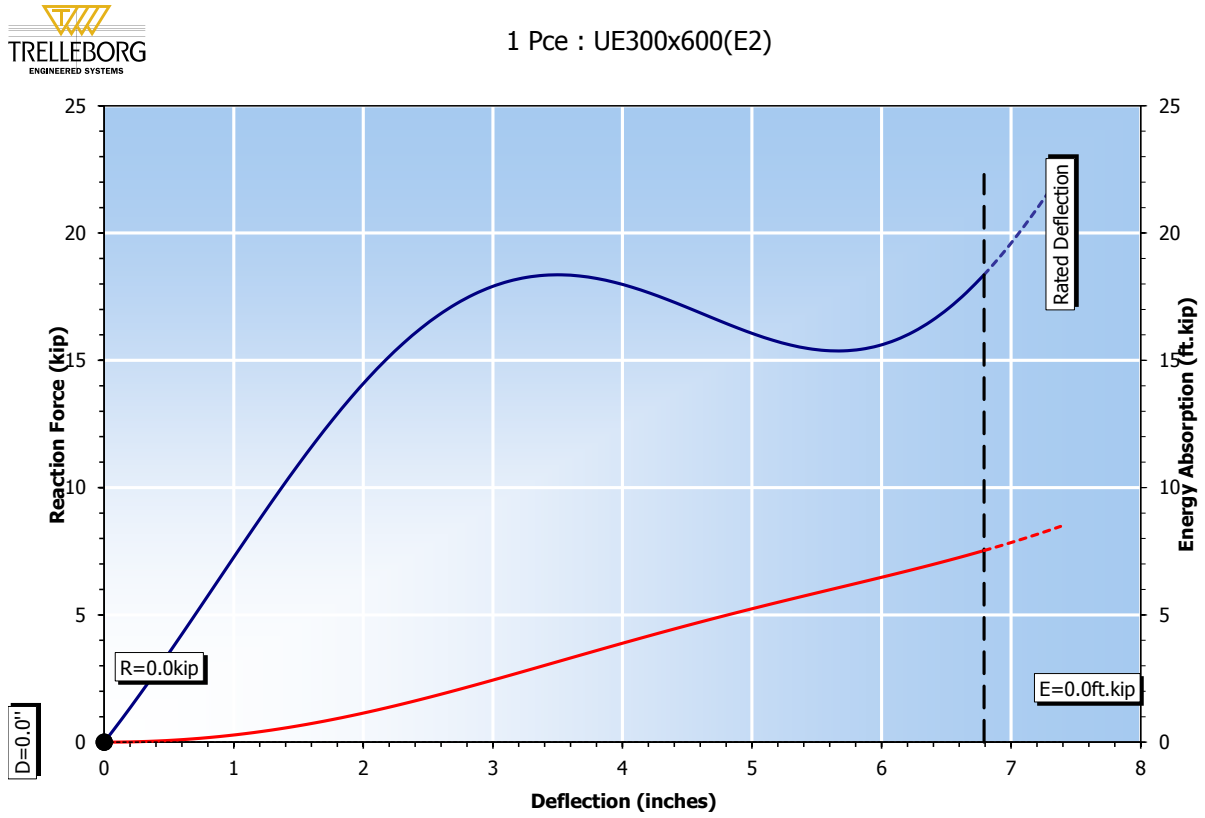

Figure 38. Unit Element – Static Force and Energy vs. Deflection [82]

The energy for unit element marine fenders varies from 5.3 kip-ft (7.2 kJ) to 357 kip-ft (484 kJ) per absorber. The efficiency measures for unit element marine fenders are approximately:

1. Initial Length/Compressible Length = 1.72 to 1.74
2. Average Force/Peak Force = 0.81 to 0.85
3. Energy/Unit Length of Deflection = 0.93 to 9.87 kip-ft per inch (05 to 0.53 kJ per mm) of deflection
4. Energy/Unit Weight = 0.06 to 0.13 kip-ft per pound (0.19 to 0.39 kJ per kg) of weight

4.3.6 Arch Marine Fenders

Arch marine fenders manufactured by Trelleborg Marine Systems are like two unit element fenders molded together, as shown in Figure 39 [82]. *H* varies from 6 in. (150 mm) to 39

in. (1,000 mm), and *W* varies from 13 in. (326 mm) to 73 in. (1,850 mm). The length of the unit element can vary from 39 in. (1,000 mm) to 138 in. (3,500 mm). The force vs. deflection and energy vs. deflection curves for the Trelleborg AN200x1000 marine fender are shown in Figure 40.

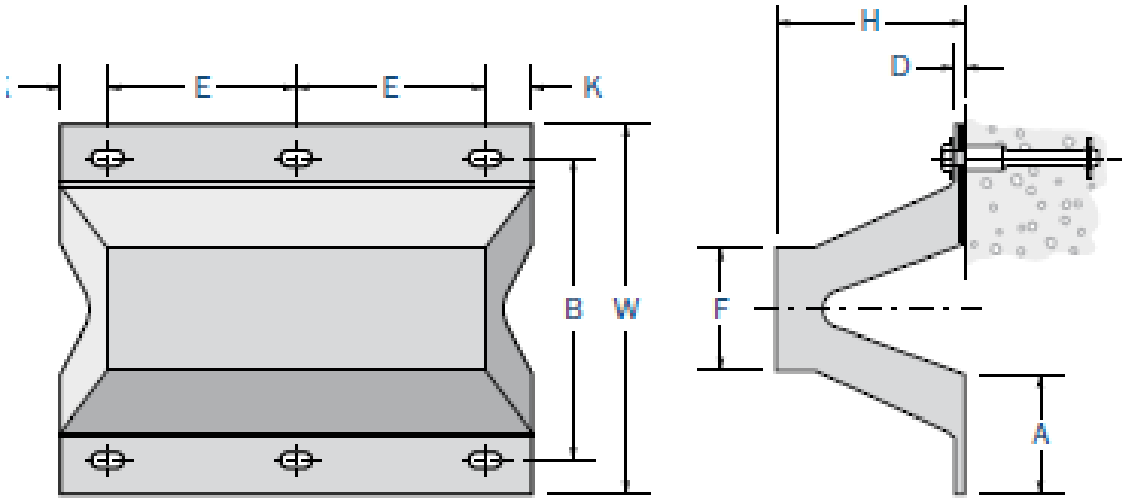

Figure 39. Arch Marine Fender [82]

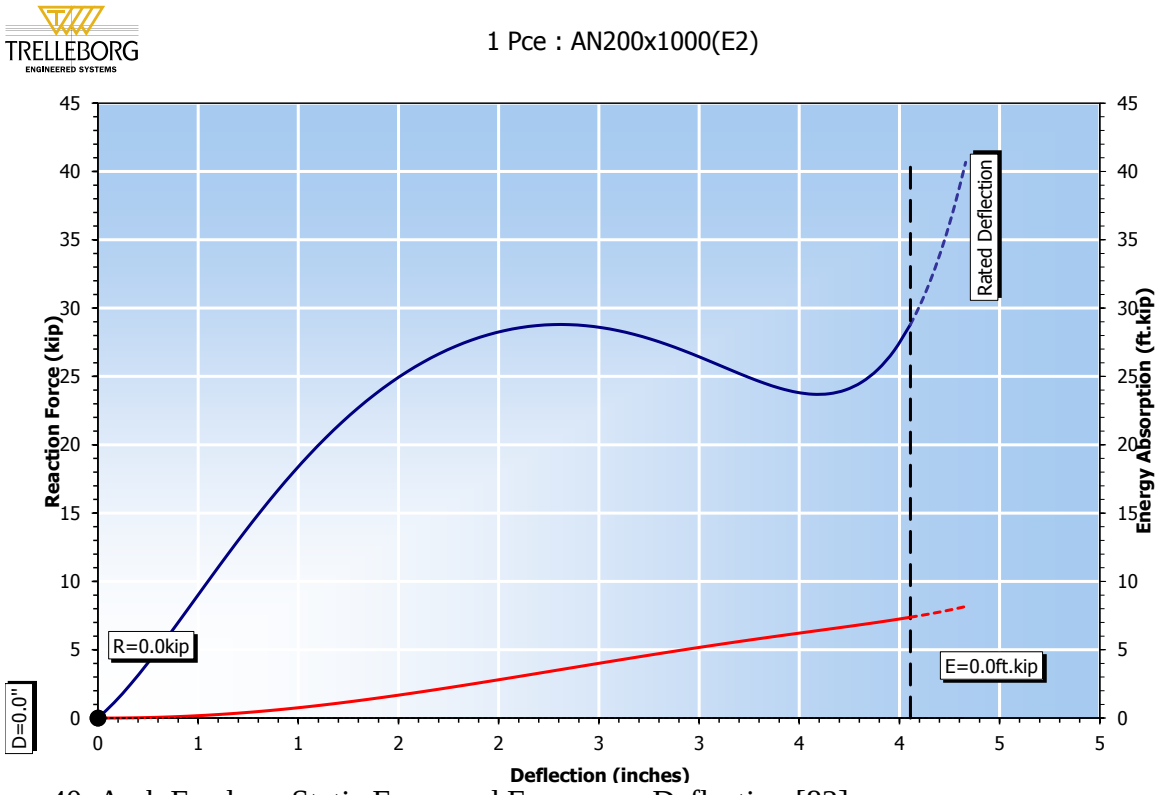

Figure 40. Arch Fender – Static Force and Energy vs. Deflection [82]

The energy for arch fender marine fenders varies from 4.1 kip-ft (5.6 kJ) to 554 kip-ft (750 kJ) per absorber. The efficiency measures for arch fender marine fenders are approximately:

1. Initial Length/Compressible Length = 1.94 to 1.97
2. Average Force/Peak Force = 0.83
3. Energy/Unit Length of Deflection = 1.37 to 27.3 kip-ft per inch (0.07 to 1.46 kJ per mm) of deflection
4. Energy/Unit Weight = 0.06 to 0.07 kip-ft per pound (0.18 to 0.21 kJ per kg) of weight

4.3.7 Cylinders Laterally Loaded

Elastomeric cylinders can be made from any type of rubber compound. Roschke et. al studied laterally-loaded natural rubber compound cylinders [90]. Circular and square elements composed of identical natural rubber compounds had a length of 4.8 in. (122 mm), a diameter of 4.8 in. (122 mm), and a wall thickness of 0.45 in. (11 mm). Irrecoverable damage was probably caused to the cylinders, thus the deflection where the shape could restore is not known. The compressible length was the maximum displacement shown in Figure 41. Other element sizes were not investigated in this study.

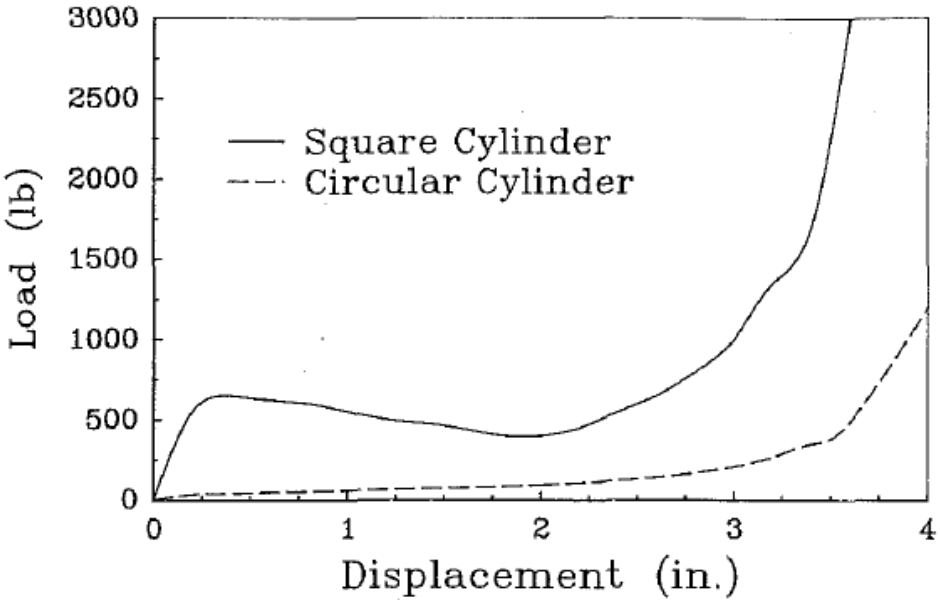

Figure 41. Laterally-loaded Cylinder – Static Force vs. Displacement [90]

The efficiency measures for the square cylinder are:

1. Initial Length/Compressible Length = 1.37
2. Average Force/Peak Force = 0.38
3. Energy/Unit Length of Deflection = 0.06 kip-ft per inch (0.003 kJ per mm) of deflection
4. Energy/Unit Weight = 0.14 kip-ft per pound (0.42 kJ per kg) of weight

The efficiency measures for the circular cylinder are:

1. Initial Length/Compressible Length = 1.2
2. Average Force/Peak Force = 0.33
3. Energy/Unit Length of Deflection = 0.02 kip-ft per inch (0.001 kJ per mm) of deflection
4. Energy/Unit Weight = 0.06 kip-ft per pound (0.18 kJ per kg) of weight

4.4 Summary and Recommendation for Energy Absorber Shape

The efficiency measures for all of the elastomeric shapes are shown in Table 5. The laterally-loaded circular cylinder had an initial/compressible length ratio closest to 1. The shear fender had an initial/compressible length ratio less than 1, since it does not compress but rather stretches in shear. The cylindrical marine fender had an average/peak force ratio closest to 1. All of the shapes met the minimum requirement for energy/unit length of deflection ratio, except the laterally-loaded square and circular cylinders. However, only one size of square and circular cylinders was tested, so if the dimensions were increased or the cylinders were stiffened, they might be a feasible option for the energy absorber. Some of the rubber shapes that had high energy/unit length of deflection ratios were also much larger in size than the new barrier would

allow. The elastomeric bumper had the highest energy/unit weight ratio. The shear fender followed by the cylindrical marine fender had the greatest total energy absorption per unit.

The laterally-loaded cylinders were eliminated from further evaluation; since, they did not meet the minimum energy required. The elastomeric bumper was also eliminated because the smaller sizes did not meet the minimum energy absorbed requirement, and the larger sizes had very large peak forces (up to 192 kip). The conical fender, cylindrical fender, and shear fender in shear were selected for further study.

Table 5. Efficiency Comparison of Rubber Energy Absorbers

Rubber Shape	Initial Length/ Compressible Length	Average Force/ Peak Force	Energy/ Unit Length of Deflection [kip-ft per in.]	Energy/ Unit Weight [kip-ft per lb]	Energy per Element [kip-ft]
Minimum Required	**1 (ideal)**	**1 (ideal)**	**0.44 to 1.76**	**NA**	**4.4 to 17.6**
Shear Fender - Shear	0.43 to 0.49	0.54	0.55 to 2.5	0.11 to 0.61	9 to 125
Shear Fender - Compression	1.9 to 2.8	0.53 to 0.58	0.46 to 2.4	0.03 to 2.4	2.8 to 24
Elastomeric bumper	1.27 to 2.26	NA	0.009 to 1.21	0.34 to 1.18	0.0017 to 9.4
Conical Marine Fender	1.39	.77 to .84	1 to 50	.10 to .13	8.5 to 2,804
Cylindrical Marine Fender	1.90 to 2.54	.85 to .90	1.9 to 61.7	.07 to .08	11.6 to 3,191
Unit Element - Axial Load	1.72 to 1.74	.81 to .85	.93 to 9.9	.10 to .13	5.3 to 357
Arch	1.94 to 1.97	0.83	1.37 to 27.3	.06 to .07	4.1 to 554
Square Cylinder - Lateral Load	1.37	0.38	0.06	0.14	0.2
Circular Cylinder - Lateral Load	1.2	0.33	0.02	0.06	0.07

4.5 Barrier Design Concepts

The ideal energy-absorbing barrier would feature attributes of both rigid and semi-rigid barriers. The desirable features of rigid, concrete barriers are that they prevent cross-median crashes (no penetrations), have little or no dynamic deflection (ideal for small urban medians), contain crashes with heavy trucks, can be configured to prevent vehicle snag, and do not require significant repair and maintenance. The desirable features of semi-rigid barriers are that vehicle accelerations are lower than those observed in rigid barrier crashes and they have a low initial installation costs. Therefore, the ideal energy-absorbing barrier needs to incorporate features of

both the rigid and semi-rigid barriers. Several barrier design concepts were studied to evaluate these features which would best accommodate the needs for the new barrier.

4.5.1 Retrofit Concept for Existing Concrete Barriers

The retrofit concept would attach to existing concrete barriers. This retrofit concept could be placed on a safety shape, single-slope, or vertical concrete wall, and the energy-absorber and rail system would reduce the high lateral accelerations normally imparted by rigid concrete barriers. The retrofit concept on safety-shaped barriers would help alleviate vehicle climb and reduce the potential for vehicle rollover due to the addition of an upper rail.

The retrofit barrier has a steel tubular rail positioned in front of axially-compressible energy absorbers that are mounted to a vertical concrete barrier, as shown in Figure 42. For a median barrier configuration, additional rails and energy absorbers would also be on the backside of the barrier. The rail element is shown as a single 6-in. x 6-in. x 3/16 in. (152-mm x 152-mm x 4.8-mm) steel tube, but prior experience and simulation work has shown that permanent deformations will occur during a TL-3 impact with a 2270P vehicle. Therefore, the rail element would likely need to be modified. The energy absorbers are shown as rubber cylinders in Figure 42, but these could be cylinders, cones, or any other compressible shape. It would be desirable that the rail face be taller to prevent snagging from occurring on the energy absorbers.

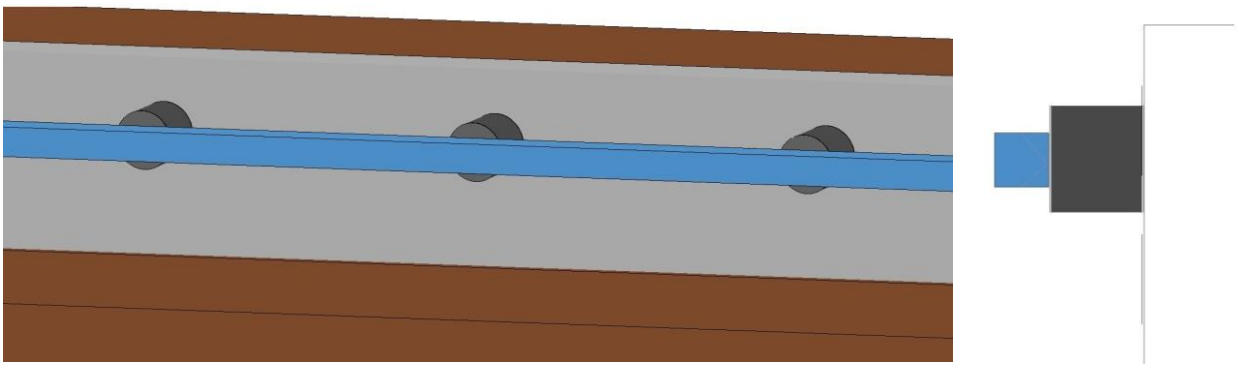

Figure 42. Axial Energy-Absorber Retrofit on a Vertical Concrete Wall

This barrier may not meet MASH TL-4 crash test performance criteria, depending on the height of the barrier on which it is installed. As previously discussed, current NCHRP 350 TL-4 concrete barriers which are 32 in. (813 mm) tall have not had a successfully safety performance with MASH criteria. Since the purpose of the retrofit is to enhance the safety performance of existing concrete barriers, the retrofit barrier would only need to be tested to MASH TL-3 criteria to reduce the accelerations of the 2270P and 1100C vehicles compared to existing rigid concrete barriers.

4.5.2 Sliding-Post Free-Standing Median Barrier Concept

A second concept consisted of a single free-standing system where the whole system absorbs energy during an impact event. One variation could utilize post-supported rails with energy absorbers at midspans, is shown in Figure 43. The posts are configured with domed base plates to allow the impact-side posts to slide backward upon impact. The non-impact side posts and rail would remain rigid with tethers angled toward the ground. As the impact-side rail deflects backward, energy absorbers are compressed against the rigid backside rail. Once again, the tube rail elements and the energy absorbers could be modified to other shapes. However, underriding vehicle parts could snag on the posts and tethers. C-shaped posts could be utilized to move the posts farther away from the roadway, as shown in Figure 44.

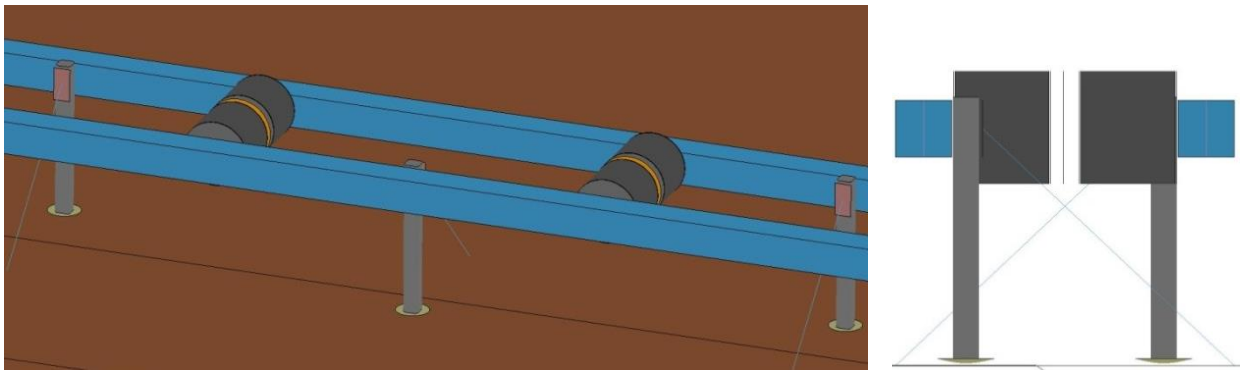

Figure 43. Sliding Domed-Post Open Median Barrier

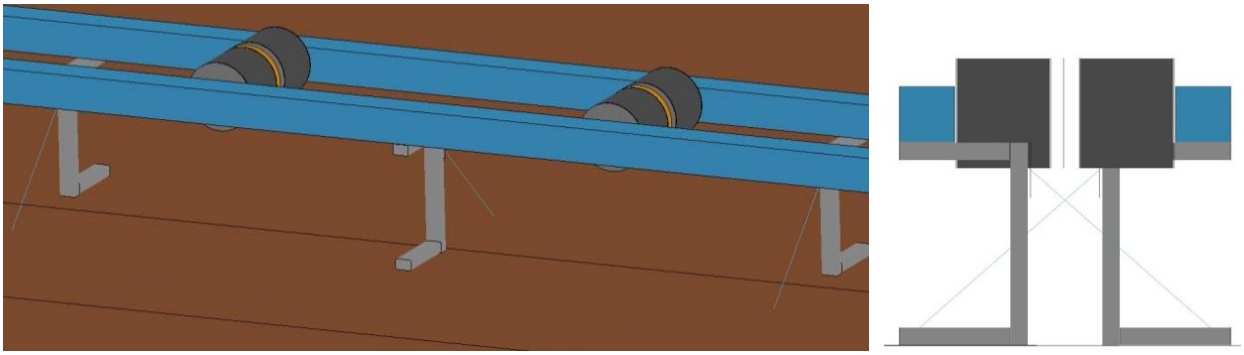

Figure 44. Sliding C-Post Open Median Barrier

Neither of the sliding post systems is anchored to the ground except by the tethers, which would make the system vulnerable to tipping over with its small inertia. The posts could be placed in guidance tracks to help control the deformation and movement of the system, but there would be more parts that are vulnerable to permanent deformation. The energy absorbers are also exposed to snagging and damage. The system also may not have enough capacity to survive a single-unit truck impact without a stronger base.

4.5.3 Plunger-Post Median Barrier Concept

The freestanding system was modified to have rigid center posts which were anchored to the ground, as shown in Figure 45. A double stroke is achieved with a plunger through the front-side cylinder that allows both the impact-side and non-impact side cylinders to compress equally. Posts would need to be very large to remain rigid. However, the rail needs to be taller to prevent the small car from underriding the rail and snagging on the rigid posts. The rail and energy absorber configuration could also be implemented through a concrete wall. However, several lateral holes would be required in the wall, and various components may be prone to deform during impact events. The energy absorbers are still exposed and could be snagged by a single-unit truck.

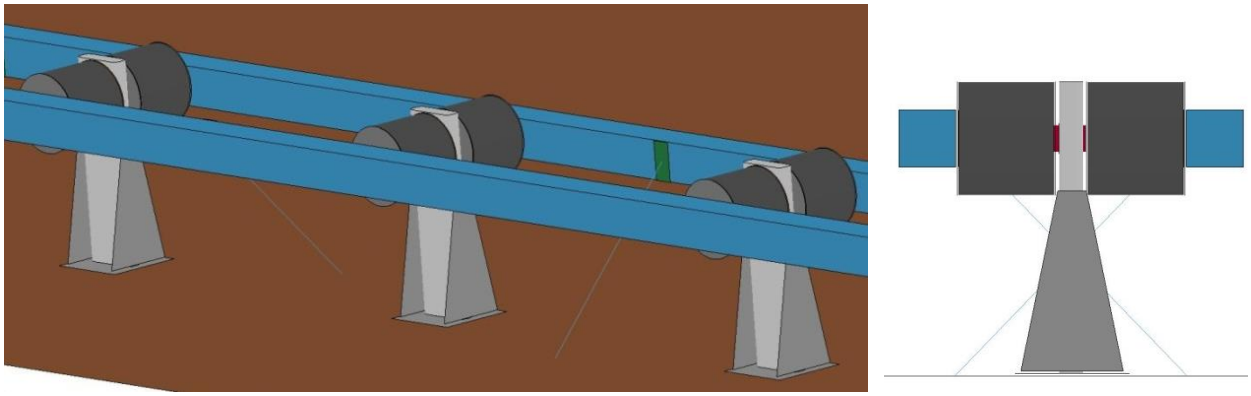

Figure 45. Plunger Post Median Barrier

4.5.4 Shear Fender with Extended Rail Concept

The shear fender concept has duality, if implemented into a barrier correctly, because it can work from either impact face of the barrier without having a second energy absorber on the backside. The shear fender energy absorber could be placed on a short concrete wall with a rail extended to either side, as shown in Figure 46. The shear fender concept may not work for single-unit truck crashes, as currently configured, because the heavy truck will lean on the rail and push it lower, thus increasing the potential for rollover, override, and cargo box penetration and snag within the interior region of the system. As such, additional rails may be needed above the system to contain and redirect heavy trucks. The upper and lower rail elements would need to capture a large range of passenger vehicles and heavy trucks. This system would work most efficiently if it deformed in pure shear (i.e. the load is applied perfectly lateral at the top of the shear fender). Pure shear will never be obtained given the height of the different vehicle loadings. A rail element that does not deform but which can capture a large range of vehicle heights on two sides of the barrier may be costly.

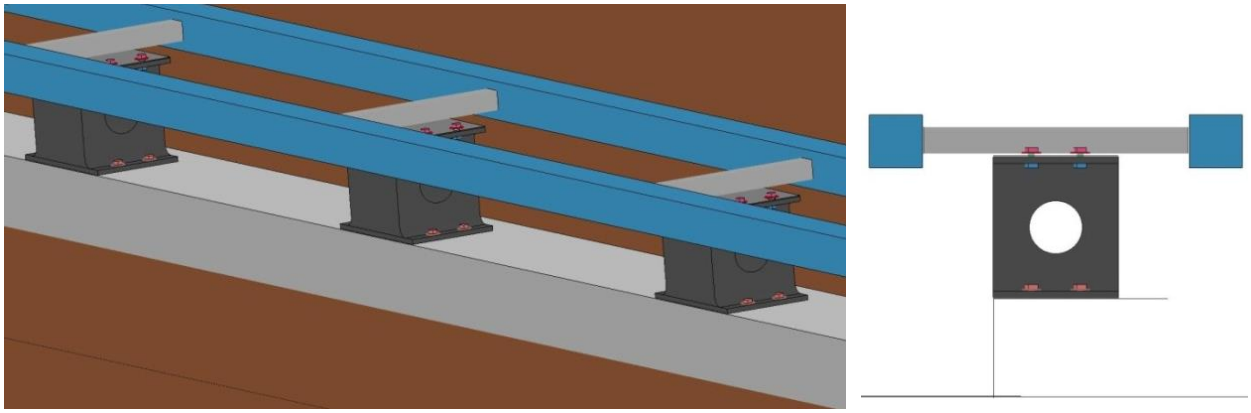
Figure 46. Shear Fender with Extended Rail Median Barrier Concept

4.5.5 Open Concrete Rail with Rubber Post Concept

The rail element on the shear fender barrier was modified to be less costly and adaptable to a wide range of vehicle impacts. This alternative barrier concept would be similar to an open concrete bridge rail, which is currently accepted for use as a TL-4 barrier under NCHRP Report No. 350 safety standards, except that the rigid concrete posts would be replaced with deformable shear fender posts, as shown in Figure 47.

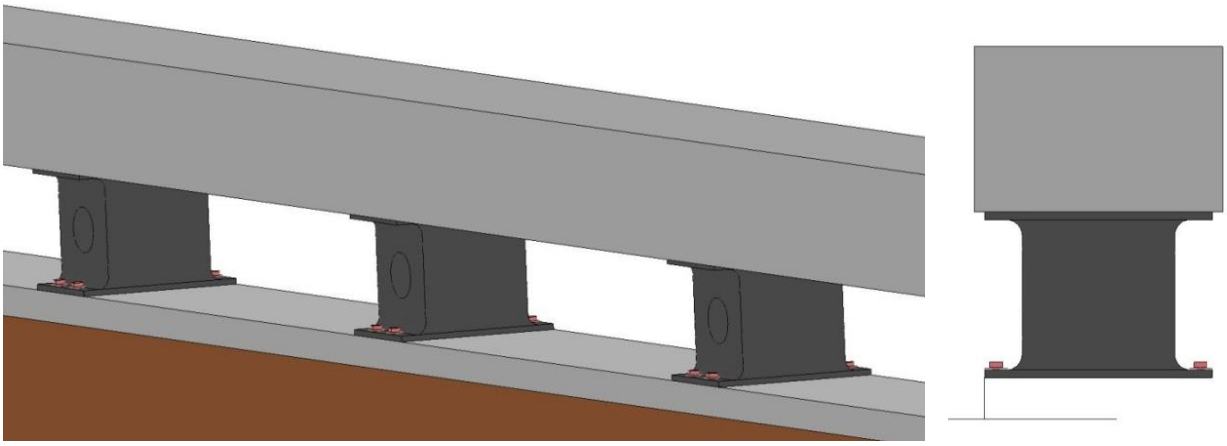
Figure 47. Open Concrete Rail with Rubber Post Concept

The shear fenders should provide adequate stiffness when compressed vertically, thus the top rail height should not be compromised for single-unit truck impact events. The shear fender would provide flexibility in the lateral direction, thus allowing the rail to deflect and absorb

energy when impacted by vehicles. However, the rail element may need to be lightweight, so that high accelerations are not imparted to the 1100C vehicle due to the inertia of the barrier.

4.6 Energy Absorber Implementation

Several energy absorbers were evaluated and design concepts were discussed. Before a barrier was designed, the behavior of rubber was studied and evaluated through finite element simulations. The most efficient shapes of energy absorbers to be further studied were determined to be cylindrical, conical, and the shear fender. With an idea of how the energy absorbers would be loaded based on the barrier concepts, the energy absorbers could be evaluated and optimized using finite element simulations.

5 ELASTOMER MODELING

Rubber material properties that are input in finite element analysis (FEA) software, such as LS-DYNA [13], have limited public availability. Since there are many rubber compounds and they widely vary in stiffness, finding material properties for a specific compound may be difficult. Finite element simulations of rubber in high-speed impact applications are also not highly published. Some companies, especially in the automobile industry, invest significant time and funding into creating accurate material models that fully depicts elastomeric behavior, including: nonlinear load-extension, time- and temperature-dependence, incompressibility, hysteresis effects, and contact with rigid parts. Many of these research studies included fatigue investigations of elastomer parts, which are not applicable to a barrier that may experience ten impacts during its life. Information about the nonlinear finite element analysis of elastomers is detailed in a MSC Software paper [91]. This simulation effort revealed accurate elastomeric models without fully characterizing elastomeric behavior which will save time and funding for future applications. Thus, the simulation techniques for investigating various elastomers in high-speed impact events were studied extensively and published herein.

5.1 Material Models

There are several rubber material formulation models in LS-DYNA Version 971 [13]. The models that were evaluated in this research study include:

MAT_BLATZ-KO_RUBBER (MAT_007)

MAT_MOONEY-RIVLIN_RUBBER (MAT_027)

MAT_FRAZER_NASH_RUBBER_MODEL (MAT_031)

MAT_HYPERELASTIC_RUBBER (MAT_077_H)

MAT_OGDEN_RUBBER (MAT_077_O)

MAT_CELLULAR_RUBBER (MAT_087)

MAT_ARRUDA_BOYCE_RUBBER (MAT_127)

MAT_SIMPLIFIED_RUBBER/FOAM (MAT_181)

MAT_SIMPLIFIED_RUBBER_WITH_DAMAGE (MAT_183)

The input parameters for each of the nine rubber material models are briefly discussed as follows. The specific constitutive equations can be found in Appendix A and the LS-DYNA Keyword User's Manual [13].

The most basic rubber model in LS-DYNA is Blatz-Ko. The only material properties that are input into this model are shear modulus (G) and mass density (ρ). This model assumes Poisson's ratio (ν) is 0.463.

The Mooney-Rivlin rubber material model includes mass density, Poisson's ratio, and curve fitting constants or tensile test data as inputs. The tensile test data was provided so that the software would do the curve fitting. Poisson's ratio was set to 0.495.

The Frazer-Nash rubber material model is a slightly compressible rubber model and includes mass density, Poisson's ratio, and curve fitting constants or tensile test data as inputs. The tensile test data was provided so that the software would do the curve fitting. Since Poisson's ratio was recommended to be between 0.49 and 0.50, 0.495 was selected. The Frazer-Nash model is only applicable to solid elements.

The Hyperelastic rubber material model includes mass density, Poisson's ratio, and curve fitting constants or tensile test data as inputs. Optional inputs include the shear modulus and limit stress for frequency independent damping, shear relaxation modulus, and decay constant. The tensile test data was provided so that the software would do the curve fitting. Poisson's ratio was set to 0.495.

The Ogden rubber material model includes mass density, Poisson's ratio, and curve fitting constants or experimental test data as inputs. Optional inputs include the shear modulus

and limit stress for frequency independent damping, shear relaxation modulus, and decay constant. Three types of experimental test data could be input: uniaxial tensile data; biaxial data; and pure shear data. The test data was provided so that the software would do the curve fitting. Poisson's ratio was set to 0.495.

The Cellular rubber model includes mass density, Poisson's ratio, initial air pressure, ratio of cellular rubber to rubber density, initial volumetric strain, and curve fitting constants or tensile test data. Optional inputs include shear relaxation modulus and decay constant. The Cellular rubber model is used when the rubber has air voids within the sample. The selected rubber for further testing and evaluation had no significant voids that could be measured, so this model was not used for simulations.

This Arruda-Boyce material model requires the input of the mass density, Poisson's ratio, shear modulus, and bulk modulus. Optional inputs include relaxation curve, shear relaxation modulus, and decay constant. As discussed previously, when $\nu = 0.5$, then K goes to infinity, which is not a realistic input for models. Therefore, several values of K were input to study the effects on the results. The Arruda-Boyce rubber model is only applicable to solid elements.

The Simplified Rubber/Foam material model includes mass density, bulk modulus, damping coefficient, and tensile test data as inputs. Optional inputs include the shear modulus and limit stress for frequency independent damping. Several optional parameters control how the rate effects are treated, and a family of curves at multiple strain rates can be input. Other optional parameters can be defined for material failure. The tensile test curve is input, but this material formulation does not use a strain energy density function to curve fit the data as is the case with all the other material formulations.

The Simplified Rubber/Foam with damage material model includes mass density, bulk modulus, damping coefficient, and loading and unloading tensile test data as inputs. Optional

inputs include the shear modulus and limit stress for frequency independent damping. Several optional parameters control how the rate effects are treated, and a family of curves at multiple strain rates can be input. Since unloading data was not obtained during all of the tension tests and material damage was not being evaluated, this model was not used.

Seven out of the nine rubber material formulations in LS-DYNA were evaluated for modeling rubber using both shell and solid elements.

5.2 Material Tests

Tension tests were conducted on 60-durometer and 80-durometer EPDM rubber samples. The EPDM rubber compound was chosen for its excellent performance with environmental effects, as previously shown in Table 4. The hardness of rubber is measured in units of durometer on a scale of 0 to 100. The 60-durometer is relatively soft, and the 80-durometer rubber is relatively stiff. The mass density (ρ) was 71.8 lb/ft^3 ($1.15x10^{-6}$ kg/mm^3).

The MTS 810 system stretched a 1.5-in. (38-mm) wide by 0.077-in. (1.96-mm) thick by 6-in. (152-mm) long, 60-durometer rectangular EPDM tensile test sample. The test setup is shown in Figure 48. At the ends of each sample, a 1-in. (25-mm) segment length was clamped, thus leaving a gauge length of 4 in. (102 mm). The testing rate was 2 in./min. (0.00085 mm/ms), and the sample stretched for 6 in. (152 mm) (150 percent strain). Another identical sample stretched 6 in. (152 mm) at 20 in./min. (0.0085 mm/ms) and then unloaded. To calculate the engineering strain, the initial length was assumed to be 4 in. (102 mm); since, the sample was clamped 1 in. (25 mm) at each end. The data was also filtered using a 20-point moving average. The resulting force vs. displacement and engineering stress vs. strain curves are shown in Figures 49 and 50. The stresses in the sample were approximately 6 percent higher at the 20 in./min. (0.0085 mm/ms) rate compared to the 2 in./min. (0.00085 mm/ms) rate.

Figure 48. Tension Test Setup

The MTS 810 system stretched a 1.5-in. (38-mm) wide by 0.092-in. (2.34-mm) thick by 6-in. (152-mm) long, 80-durometer rectangular EPDM tensile test sample. At the ends of each sample, a 1-in. (25-mm) segment length was clamped, thus leaving a gauge length of 4 in. (102 mm). The testing rate was 2 in./min. (0.00085 mm/ms), and the sample stretched 6 in. (152 mm) (150 percent strain) and then unloaded at the same rate. Another identical sample stretched 6 in. (152 mm) at 20 in./min. (0.0085 mm/ms) and then unloaded at the same rate. To calculate the engineering strain, the initial length was assumed to be 4 in. (102 mm); since, the sample was clamped 1 in. (25 mm) at each end. The data was also filtered using a 20-point moving average. The resulting force vs. displacement and engineering stress vs. strain curves are shown in Figures 51 and 52. The stresses in the sample were approximately 5 percent higher at the 20 in./min. (0.0085 mm/ms) rate compared to the 2 in./min. (0.00085 mm/ms) rate.

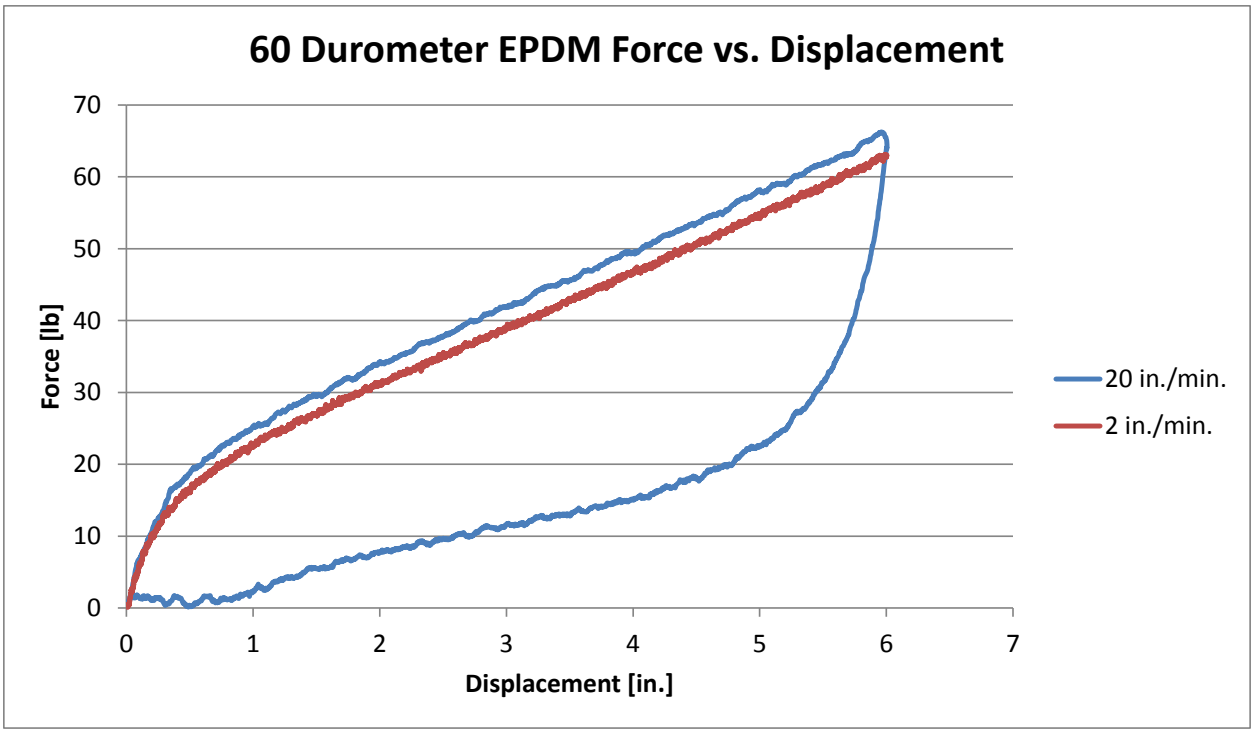

Figure 49. 60-Durometer EPDM Force vs. Displacement

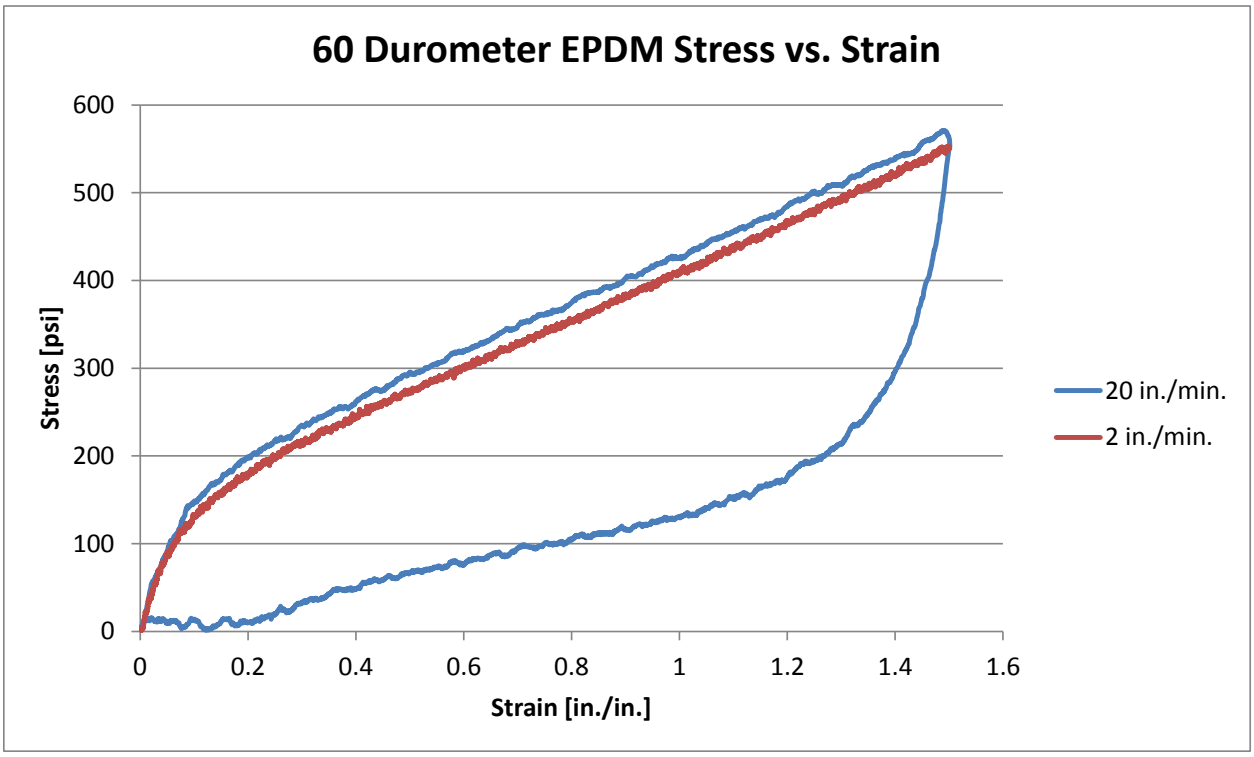

Figure 50. 60-Durometer EPDM Engineering Stress vs. Strain

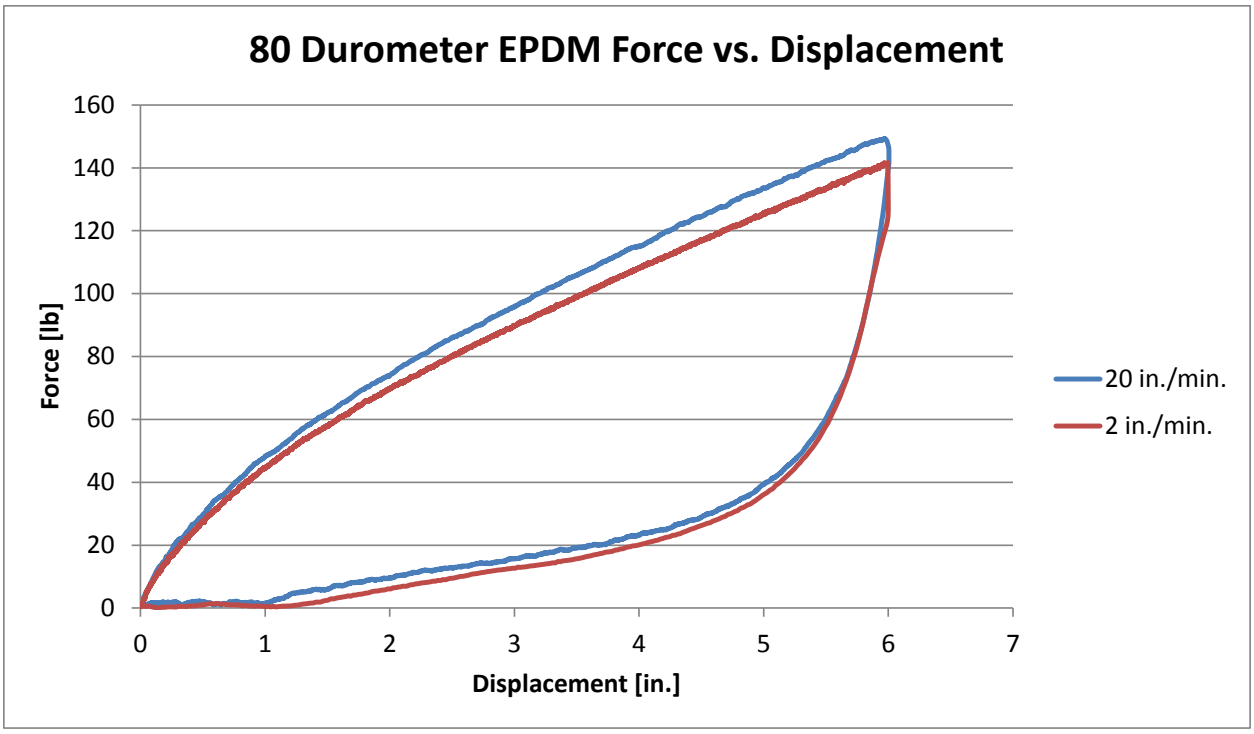

Figure 51. 80-Durometer EPDM Force vs. Displacement

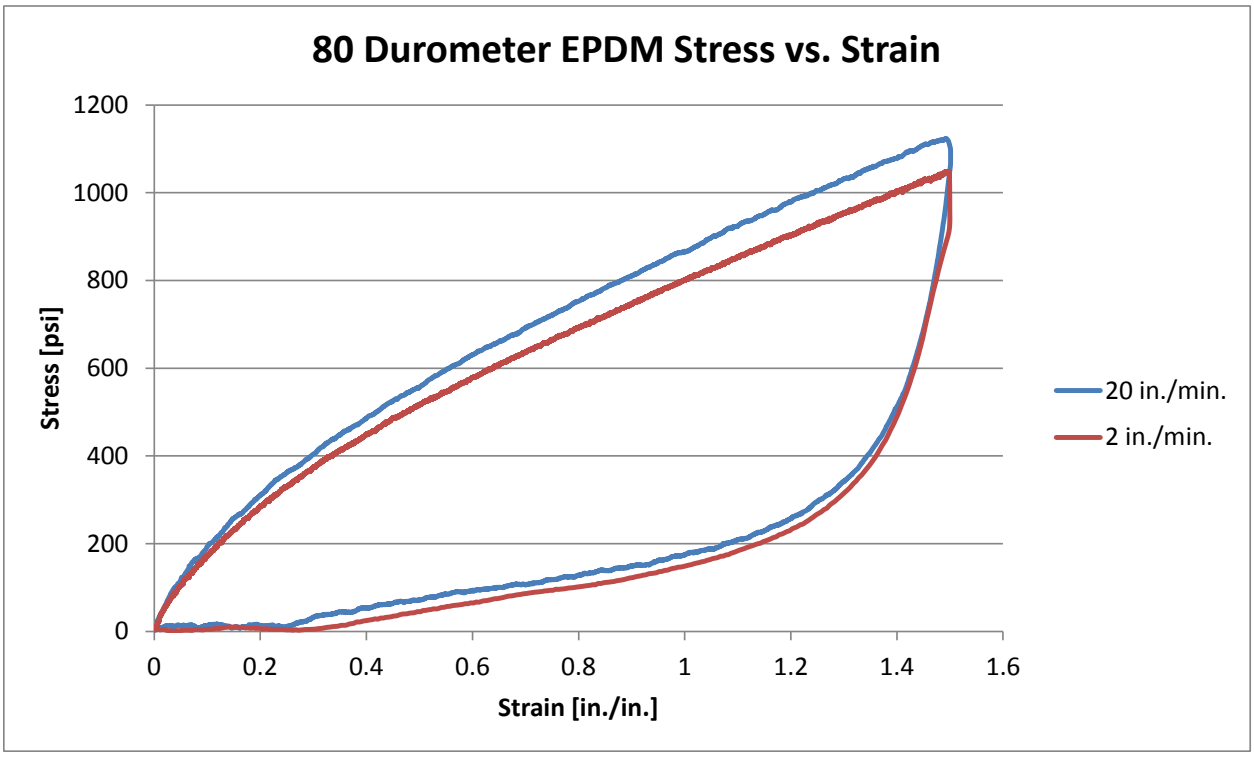

Figure 52. 80-Durometer EPDM Engineering Stress vs. Strain

Rubber does not follow Hooke's Law, and therefore it is difficult to calculate Young's modulus (*E*) since the tensile stress vs. strain curve does not have a linear elastic region. Due to the fact that rubber is an incompressible or nearly incompressible material, Poisson's ratio (ν) was assumed to be 0.5. The shear modulus (*G*) is an important property of rubber, which is the slope of the shear stress vs. strain curve. Since the shear test was not available, the shear modulus was calculated from the following equation:

$$G = \frac{E}{2(1+\nu)}$$

When ν = 0.5, *E* is three times *G*. The shear modulus varies with strain due to rubber's nonlinearity, so Gent recommended that the shear modulus is taken at the strain which is of interest for FEA simulations [92]. All the simulations had high strains, so Young's modulus was calculated from the tensile tests at larger strains. The 60-durometer rubber exhibited a linear region from 30 to 150 percent in which *E* was 276 psi (1.90 MPa). The shear modulus for the 60-durometer rubber is 92 psi (0.66 MPa). The 80-durometer rubber exhibited an approximately linear region from 60 percent to 150 percent in which *E* was 541 psi (3.73 MPa). The shear modulus for the 80-durometer rubber is 180 psi (1.24 MPa).

The bulk modulus (*K*) is calculated from the following equation:

$$K = \frac{E}{3(1-2\nu)}$$

When ν = 0.5, the bulk modulus increases to infinity, which demonstrates that the bulk modulus is much larger than the shear or Young's modulus. When Poisson's ratio is close to 0.5, *K* varies greatly. For the 60-durometer rubber, when ν = 0.495, *K* = 9,200 psi (63 MPa); when ν = 0.497, *K* = 15,333 psi (105 MPa); and when ν = 0.499, *K* = 46,000 psi (317 MPa).

5.2.1 Tension Test Simulation

The tensile tests were simulated using LS-DYNA. Ten points from the tensile test were input for the force versus deflection curve required for many of the material models. Single element tension test simulations and results are shown in Appendix B. The geometry was modeled using both shell and solid elements measuring approximately ⅜ in. x 5/16 in. (9.5 mm x 7.6 mm), as shown in Figure 53. Although the element sizes were large, they provided sufficient accuracy for the initial investigation of rubber material models.

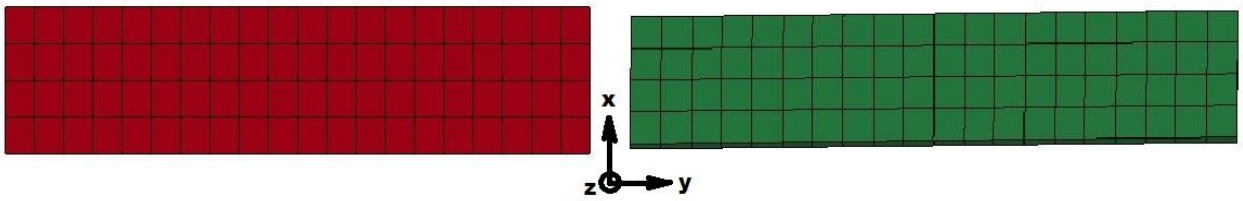

Figure 53. Shell (left) and Solid (right) Elements

From previous research, hourglass excitement in rubber models can be a significant problem. Over-constrained elastomeric elements can hourglass significantly, but unconstrained elements can also have hourglassing problems. The *BOUNDARY_SPC nodal constraints were used to model the boundary conditions where the sample was clamped. Neither x-, y-, or z-translations nor x-, y-, or z- rotations were observed in the clamped region. However, applying these boundary conditions, with a *BOUNDARY_PRESCRIBED_MOTION in the y-axis along the right clamp, caused many of the models to become unstable. The most important boundary condition was that a 1-in. (25-mm) segment (first 4 rows of nodes) at the left end of the sample did not move in the y-direction, while a 1-in. (25-mm) segment (last 4 rows of nodes) at the right end of the sample was subjected to motion in the y-direction. A planar cross-section orthogonal to the y-axis was placed at the center of the sample to measure forces.

5.2.2 Strain Rate Effects

The tension tests were conducted at much lower strain rates than what was expected from full-size energy absorbers impacted at 62 mph (100 km/h). The tension tests were conducted at constant strain rates of 0.0083/sec and 0.0833/sec. The strain rate effects in elastomers can be quite significant. The tension tests showed a 6 percent increase in stress for the 60-durometer EPDM and a 5 percent increase in stress for the 80-durometer EPDM with a 10 time increase in strain rate. Strain rate effects can only be implemented into the material models by inputting a family of tension test curves. Since the tension tests only investigated two low strain rates, it was not implemented into the model. The material properties at higher strain rates were desired, but due to the limited capabilities of the MTS, higher strain rates were not investigated. So, two constant strain rates (0.0083/sec and 0.833/sec) were used in the tension test simulations to evaluate any differences.

5.2.3 Shell Elements

The Blatz-Ko, Mooney-Rivlin, Hyperelastic, Ogden, and Simplified rubber material models were evaluated with shell elements. The Belytschko-Tsay shell elements were used for the initial explicit analysis of the elastomer material models. The force vs. displacement from the simulations at the two strain rates (0.0083/sec and 0.833/sec) were compared to the 60-durometer EPDM tensile tests, as shown in Figures 54 and 55, respectively. Most of the forces were not very accurate above 1 in. (25 mm) of displacement at both strain rates. Most of the simulations became unstable, especially at the lower strain rate.

The Blatz-Ko model deformed in a uniform manner at both strain rates that was consistent with the tensile test, as shown in Figure 56. There was no hourglass energy, and the internal energy at the final state was 115 k-in. (13 kJ) at both strain rates. The force vs. deflection curve was completely linear and did not match the tensile test, but it did have the same slope at

larger strains. Since the value of *G* was somewhat subjective as previously discussed, *G* could be modified to provide more accurate results at the strains of interest.

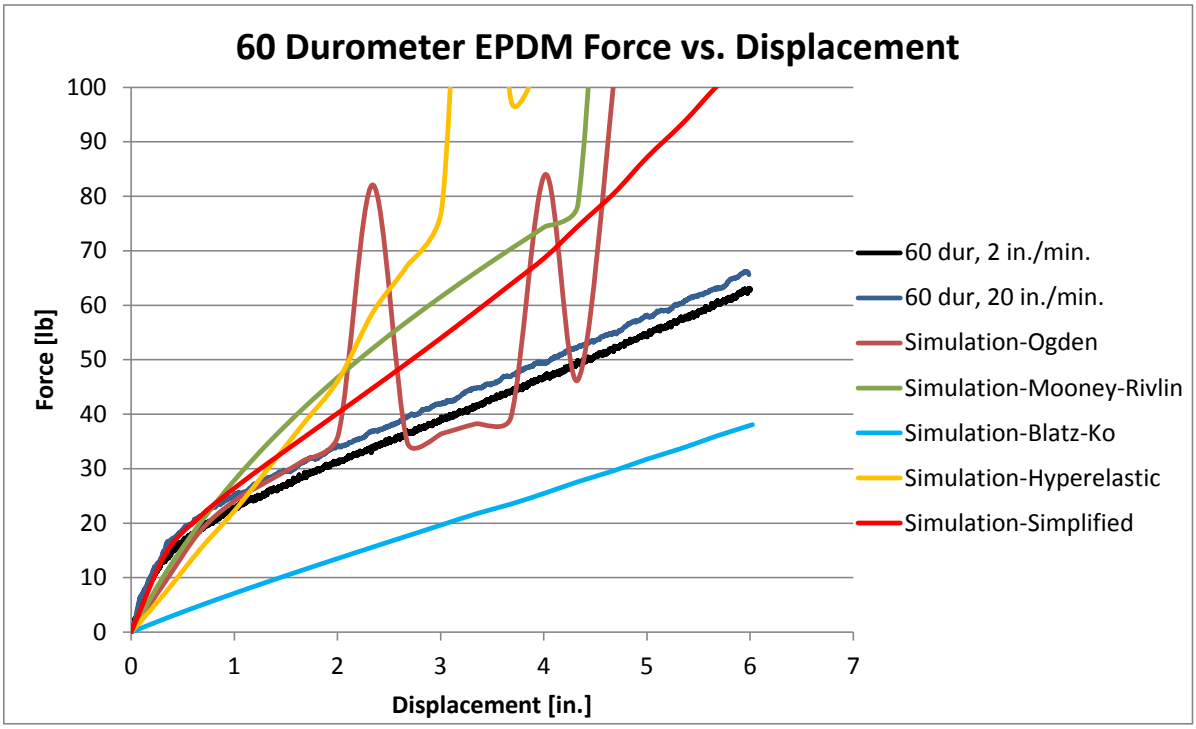

Figure 54. Comparison of Rubber Shell Elements – 60 Durometer – 0.0083/sec

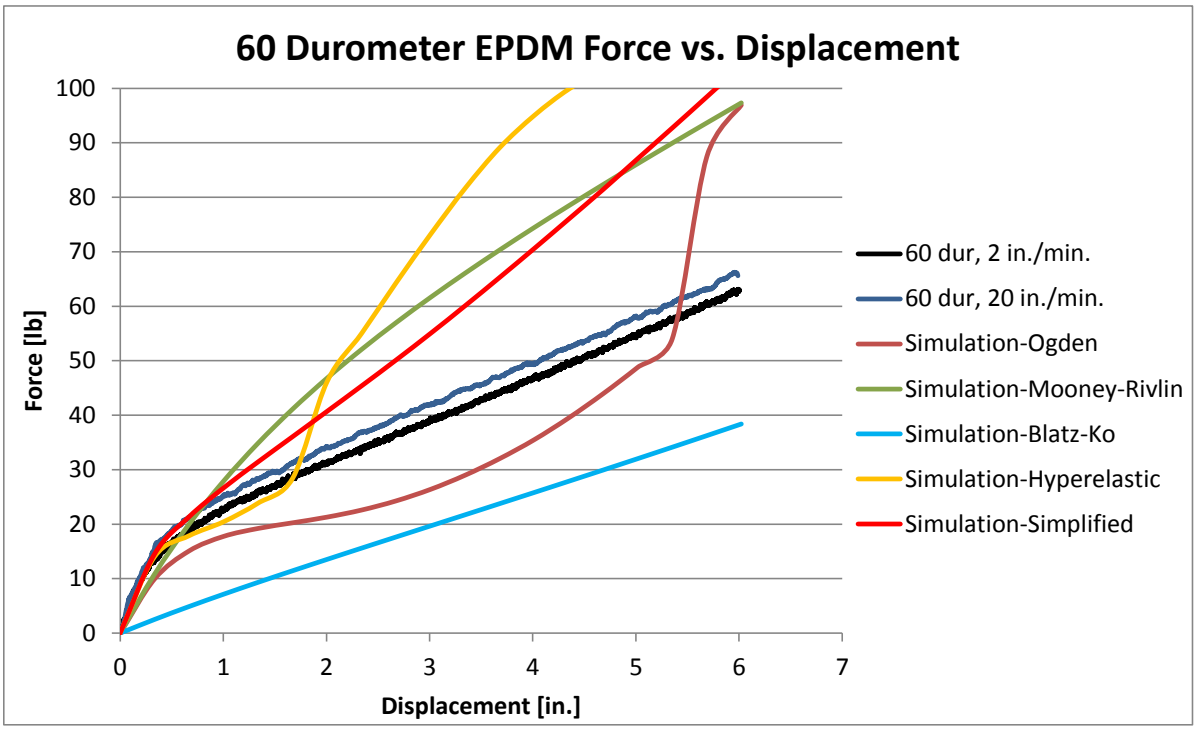

Figure 55. Comparison of Rubber Shell Elements – 60 Durometer – 0.833/sec

Strain Rate - 0.0083/sec

Strain Rate – 0.833/sec

Figure 56. Blatz-Ko Shell Element Deformation

The Mooney-Rivlin model deformed in a uniform manner at both strain rates that was consistent with the tensile test, as shown in Figure 57. There was no hourglass energy, and the internal energy at the final state was 345 k-in. (39 kJ) at both strain rates. The forces were approximately 50 percent larger than the tensile test. At small deflections, this model was fairly accurate at 0.833/sec strain rate.

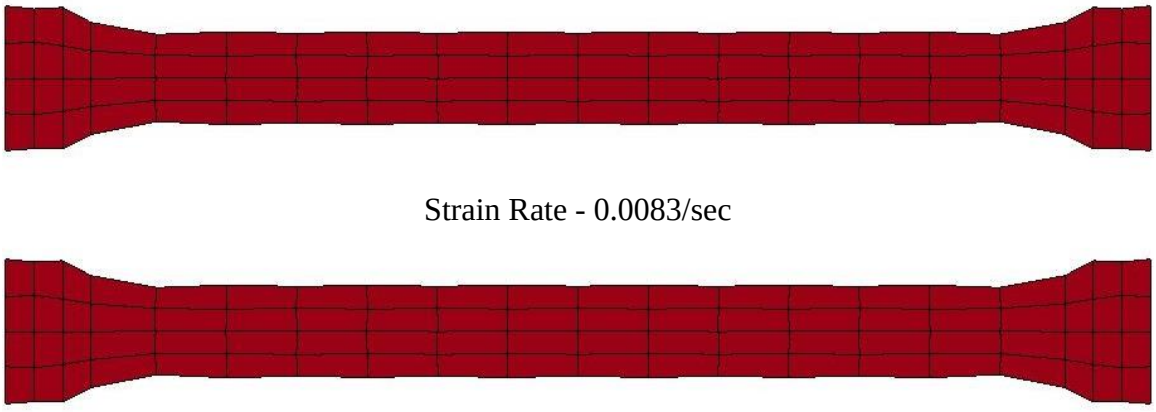

Strain Rate - 0.0083/sec

Strain Rate – 0.833/sec

Figure 57. Mooney-Rivlin Shell Element Deformation

The Hyperelastic model deformed in a non-uniform manner that physically resembled hourglassing at 0.0083/sec, as shown in Figure 58. The model had several nodes with out-of-range velocities at 140,000 ms. The hourglass energy was 664 k-in. (75 kJ), and the internal

energy at the last state was -443 k-in. (-50 kJ). However, at 0.833/sec, the model deformed in a more uniform manner, with minimal physical hourglassing, also shown in Figure 58. The hourglass energy was 35 k-in. (4 kJ), and the internal energy at the final state was 301 k-in. (34 kJ). The force versus deflection curve was almost identical to the tensile test over the first 1 in. (25 mm) of deflection, then the forces rapidly increased higher than observed the tensile test.

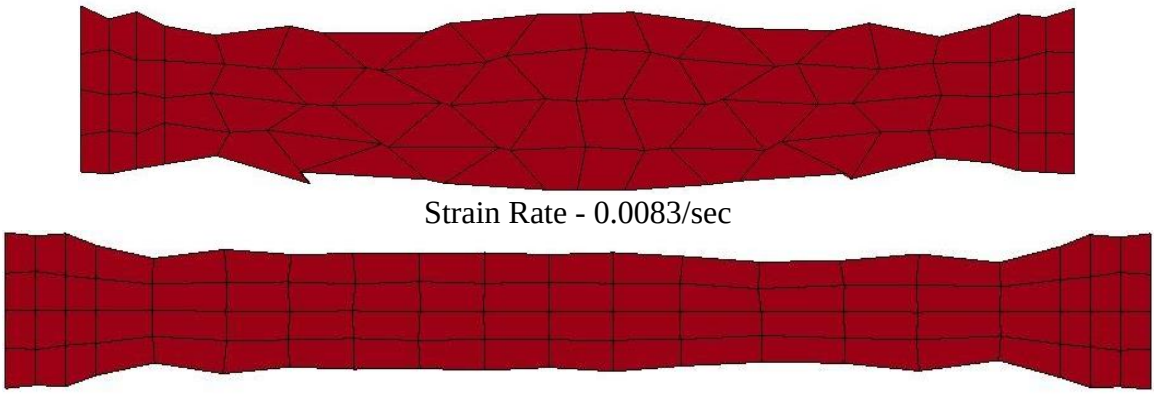

Strain Rate - 0.0083/sec

Strain Rate – 0.833/sec

Figure 58. Hyperelastic Shell Element Deformation

The Ogden model deformed in a non-uniform manner that physically resembled hourglassing at 0.0083/sec, as shown in Figure 59. The hourglass energy was 35 k-in. (4 kJ), and the internal energy was 204 k-in. (23 kJ). At 0.833/sec, the model deformed in a more uniform manner, with minimal physical hourglassing, also shown in Figure 59. The hourglassing energy was 9 k-in. (1 kJ), and the internal energy was 186 k-in. (21 kJ). The force versus deflection curve was identical to the tensile test over the first 2 in. (51 mm) of deflection but then was sporadic. The Ogden model had a noticeable parabolic shape within the expected linear portion of the force versus deflection curve.

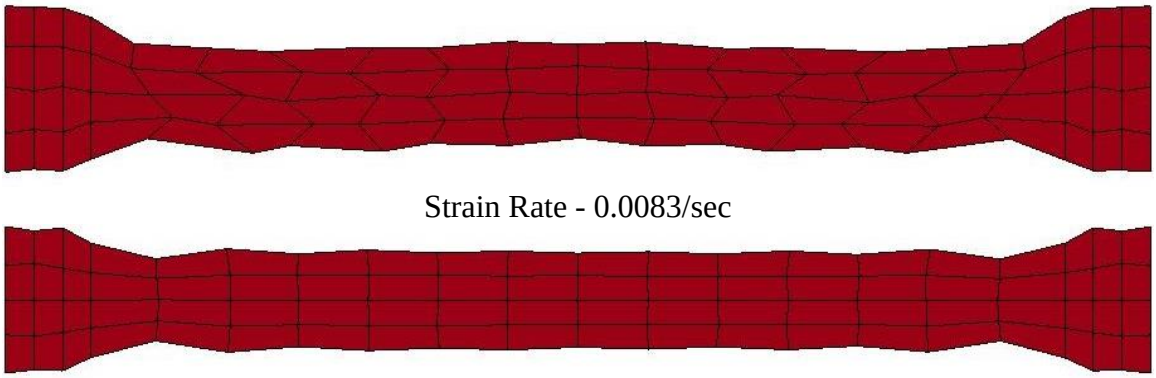

Strain Rate - 0.0083/sec

Strain Rate – 0.833/sec

Figure 59. Ogden Shell Element Deformation

The Simplified Rubber/Foam model deformed in a uniform manner at both strain rates that was consistent with the tensile test, as shown in Figure 60. There was no hourglass energy, and the internal energy at the final state was 327 k-in. (37 kJ) at both strain rates. The force versus deflection curves were almost identical to the tension test over the first 1 in. (25 mm) of deflection, and then became mostly linear only at a steeper slope than the tension test. Changing the bulk modulus had very minor effects on the forces, so the results for K = 15,333 psi (0.105 GPa) are shown. This suggests that the value of the bulk modulus is fairly insignificant for this material model.

Strain Rate - 0.0083/sec

Strain Rate – 0.833/sec

Figure 60. Simplified Shell Element Deformation

5.2.4 Solids Elements

Simulated testing with shell elements reasonably replicated the physical tension tests, but solid elements were preferred for modeling the more complicated part geometries. The Blatz-Ko, Mooney-Rivlin, Frazer-Nash, Hyperelastic, Ogden, Arruda-Boyce, and Simplified rubber material models were evaluated with solid elements. The default constant stress solid elements were used for the initial explicit analysis. The force vs. displacement from the simulations at the two strain rates (0.0083/sec and 0.833/sec) were compared to the 60-durometer EPDM tensile tests, as shown in Figures 61 and 62, respectively. At the lower strain rate, all of the forces (except Blatz-Ko) were very low as compared to the tensile test forces. This result could have been due to the out-of-plane hourglassing and severe deformation that occurred in all of the simulations. Most of the solid elements that were stretched at 0.833/sec had accurate force versus deflection curves up to 1.5 in. (38 mm) of deflection, but moderate deformations and hourglassing still occurred. The Simplified Rubber/Foam material model was almost identical to the 20 in./min. (0.0085 mm/ms) tension test data, as shown in Figure 62.

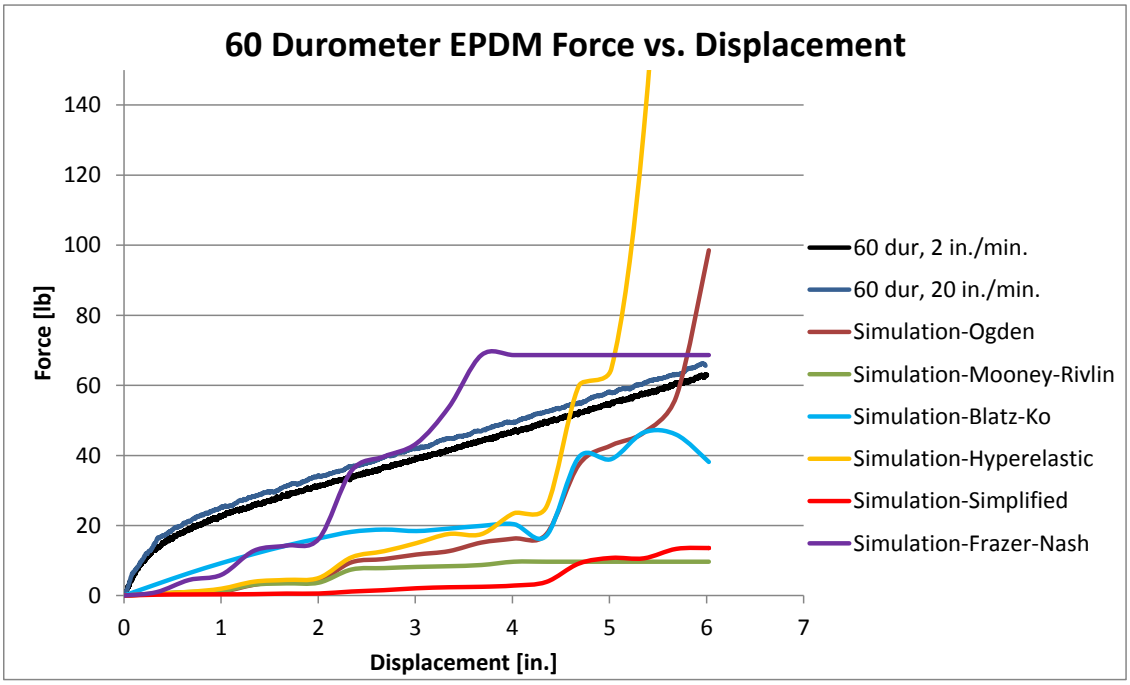

Figure 61. Comparison of Rubber Models with Solid Elements – 60 Durometer – 0.0083/sec

The Blatz-Ko model deformed in a non-uniform manner at both strain rates that resembled hourglassing, as shown in Figure 63. The hourglass energy was zero, and the internal energy at the final state was 84 k-in. (9.5 kJ) at both strain rates. At 0.0083/sec, the forces were about one-half of the tensile test forces, and the forces increased rapidly and inconsistently. At 0.833/sec, the forces were one-third of the tensile test forces. Once again, the shear modulus could be modified to provide more accurate forces at the strains of interest.

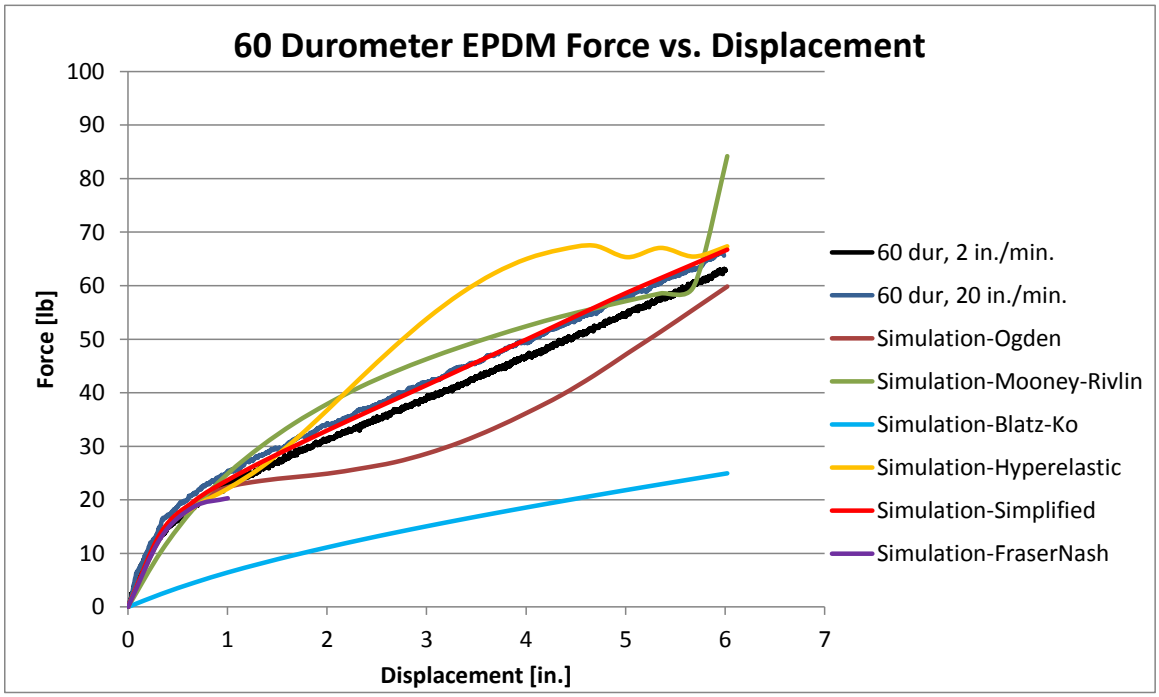

Figure 62. Comparison of Rubber Models with Solid Elements – 60 Durometer – 0.833/sec

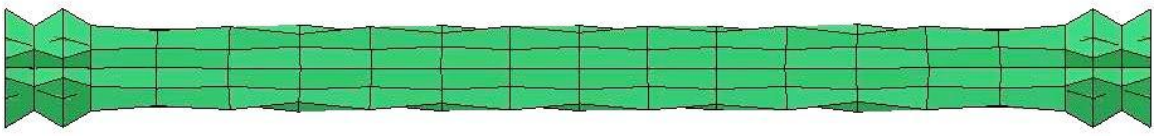

Strain Rate - 0.0083/sec

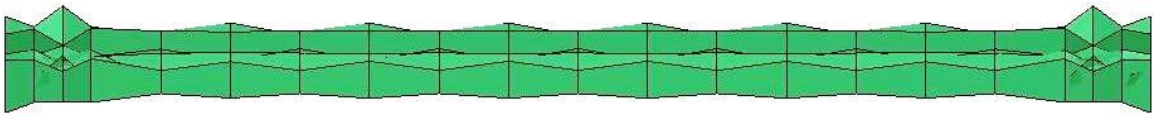

Strain Rate – 0.833/sec

Figure 63. Blatz-Ko Solid Element Deformation

The Mooney-Rivlin model at 0.0083/sec had several nodes with out-of-range velocities at 121,410 ms, as shown in Figure 64. The hourglass energy was 56 k-in. (6.3 kJ), and the internal energy at the last state was 2 k-in. (0.2 kJ). The forces were very low compared to the tensile test forces. The Mooney-Rivlin model at 0.833/sec was stable, but the physical deformation resembled hourglassing, as shown in Figure 64. However, the hourglass energy was zero, and the internal energy at the final state was 248 k-in. (28 kJ). The forces were a good match compared to the tensile test forces, except for the steep upturn in the force versus deflection curve near the end of the simulation.

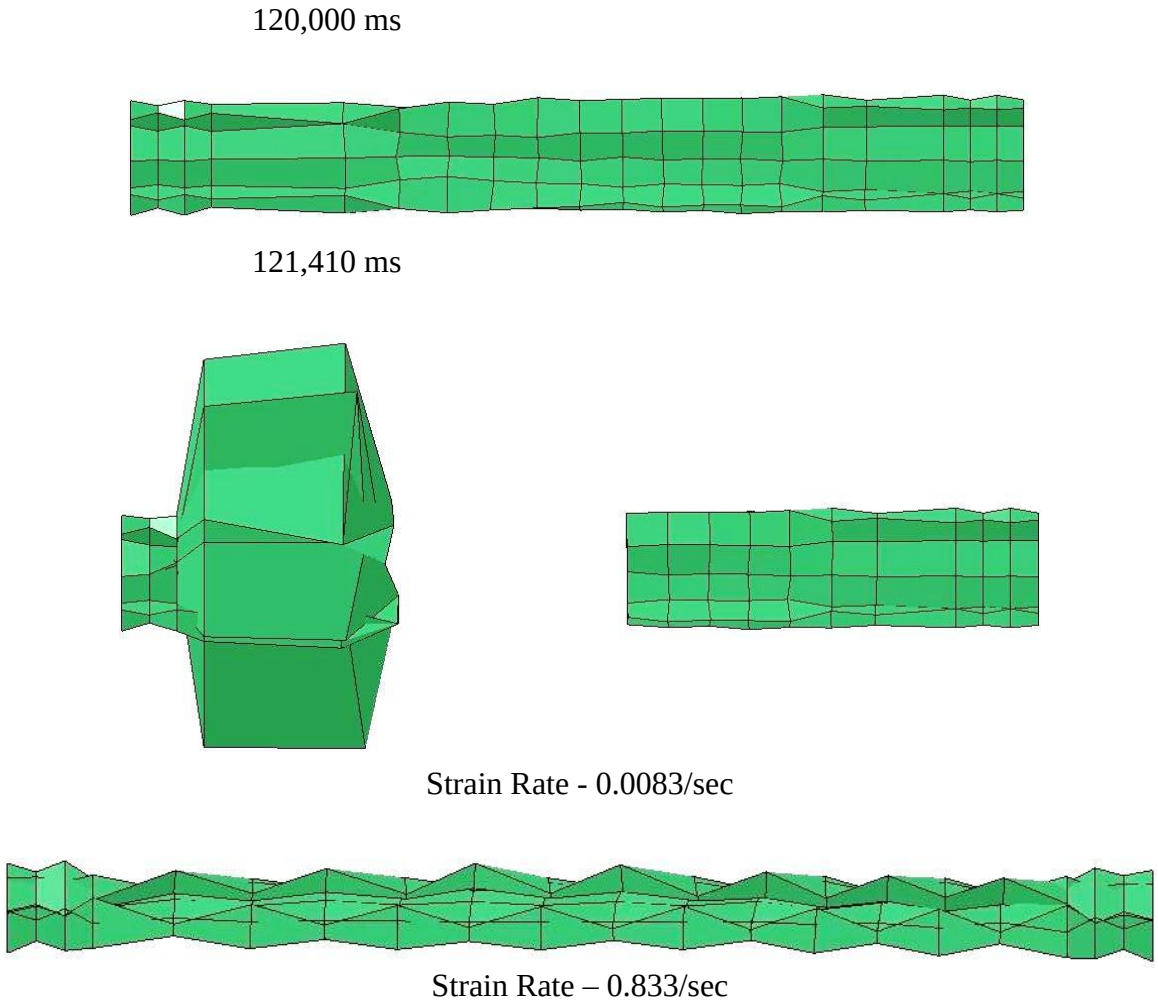

Figure 64. Mooney-Rivlin Solid Element Deformation

The Frazer-Nash model at 0.0083/sec had several nodes with out-of-range velocities at 109,110 ms, as shown in Figure 65. The hourglass energy was 150 k-in. (17 kJ), and the internal energy at the last state was 27 k-in. (3 kJ). The forces were very low compared to the tensile test forces. The model at 0.833/sec stopped running for an unknown reason after 264 ms, and the deformation is shown in Figure 65. The hourglass energy was zero, and the internal energy at the last state was (1.4 kJ). The forces were accurate while the simulation was stable, but the problem was not resolved with this model.

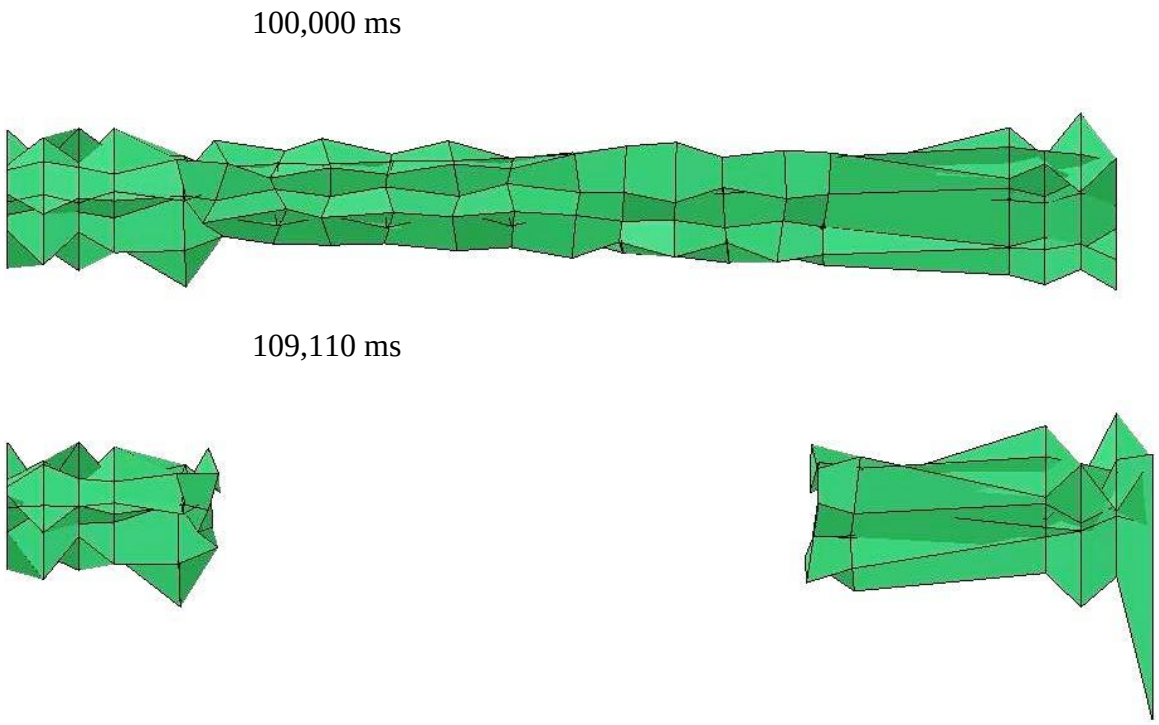

Strain Rate - 0.0083/sec

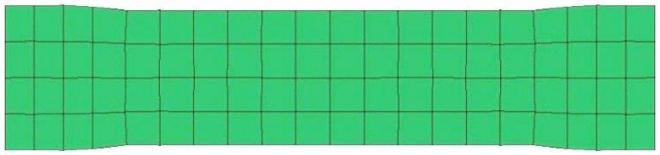

Strain Rate – 0.833/sec

Figure 65. Frazer-Nash Solid Element Deformation

The Hyperelastic model at 0.0083/sec deformed in a non-uniform manner that resembled severe hourglassing, as shown in Figure 66. The hourglass energy was 10 k-in. (1.1 kJ), and the internal energy at the final state was 1 k-in. (0.1 kJ). The forces were very low compared to the tensile test forces, until about two-thirds through the simulation when the forces increased rapidly and inconsistently. The Hyperelastic model at 0.833/sec deformed fairly uniformly, but there was a lot of out-of-plane deformation, as shown in Figure 66. The hourglass energy was 279 k-in. (31.5 kJ), and the internal energy at the final state was 13 k-in. (1.5 kJ). The forces were very accurate compared to the tensile test forces over the first 1½ in. (38 mm) of deformation. The forces were then approximately one-third higher.

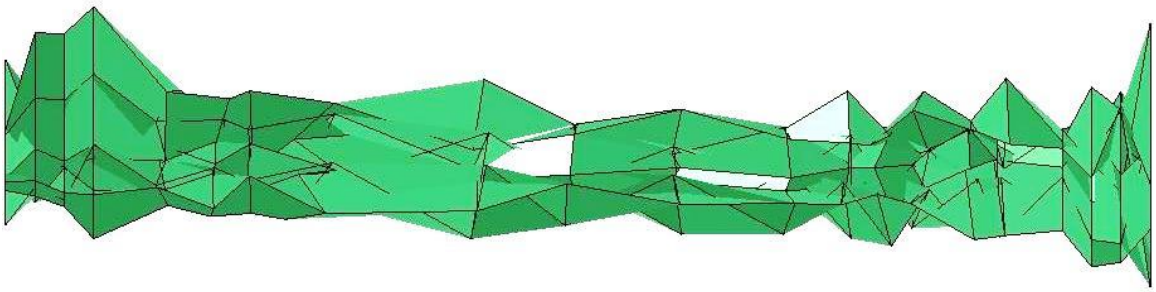

Strain Rate - 0.0083/sec

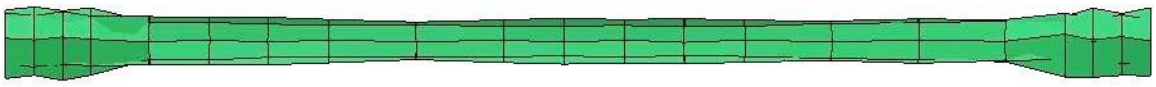

Strain Rate – 0.833/sec

Figure 66. Hyperelastic Solid Element Deformation

The Ogden model at 0.0083/sec deformed in a non-uniform manner that resembled severe hourglassing, as shown in Figure 67. The hourglass energy was greater than 17,000 k-in. (2,000 kJ), and the internal energy at the final state was also greater than 17,000 k-in. (2,000 kJ). The forces were very low compared to the tensile test forces. The Ogden model at 0.833/sec had less severe hourglassing, as shown in Figure 67. The hourglass energy was 9 k-in. (1 kJ), and the

internal energy at the final state was 212 k-in. (24 kJ). The forces were accurate over the first 1 in. (25 mm) of deformation and then were lower than the tensile test forces.

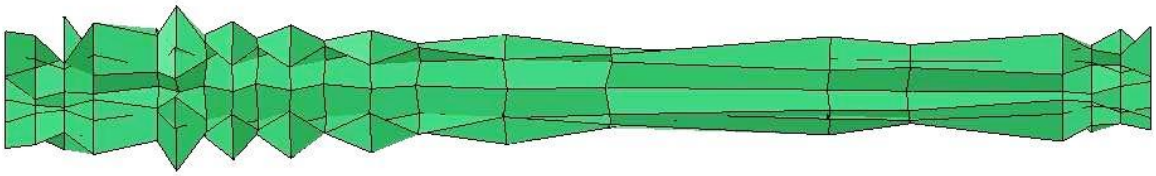

Strain Rate - 0.0083/sec

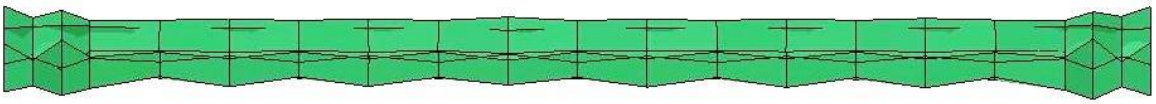

Strain Rate – 0.833/sec

Figure 67. Ogden Solid Element Deformation

This Arruda-Boyce simulation became unstable with all values of *K* before any d3plot states were created due to several nodes with out-of-range velocities. The instabilities in this model were not further investigated since there were more promising stable models.

The Simplified model deformed in a non-uniform manner at both strain rates that resembled hourglassing, as shown in Figure 68. At 0.0083/sec, the hourglass energy was 5 k-in. (0.6 kJ), and the internal energy at the final state was 6 k-in. (0.7 kJ). The forces were very low compared to the tensile test forces. At 0.833/sec, the hourglass energy was 4 k-in. (0.5 kJ), and the internal energy at the final state was 239 k-in. (27 kJ). The forces were identical to the tensile test forces conducted at 20 in./min. (0.0085 mm/ms).

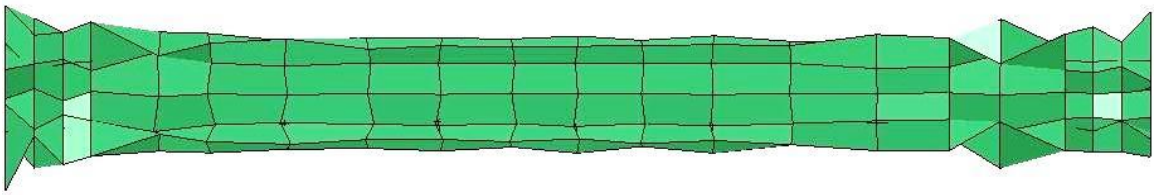

Strain Rate - 0.0083/sec

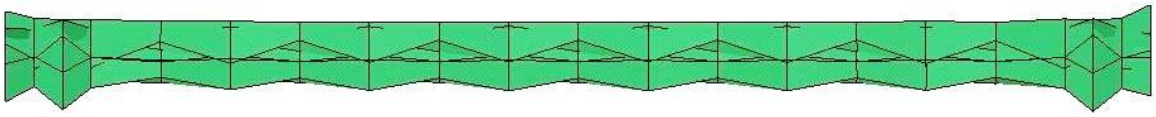

Strain Rate – 0.833/sec

Figure 68. Simplified Solid Element Deformation

5.2.5 Hourglass Problems

Hourglassing and model stability was clearly a problem with all of the rubber material models with the constant stress solid elements. The Simplified Rubber/Foam material model showed some promise and was used to investigate the hourglass and stability problems. In general, the simulations were more stable and accurate at the higher strain rate, so the new simulations had a strain rate of 0.833/sec. First, the mesh was refined, and the deformation is shown in Figure 69. Although the physical deformation of the model appeared to follow hourglass modes, hourglass energy was minimal. The hourglass energy was 4 k-in. (0.5 kJ), and the internal energy at the final state was 239 k-in. (27 kJ).

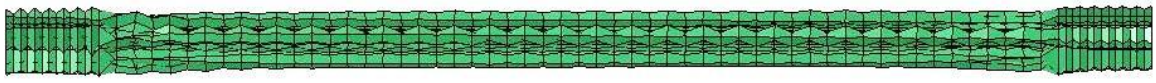

Figure 69. Refined Solid Element Deformation

The *HOURGLASS controls that were available in LS-DYNA for solid elements were explored [13]:

1 – Standard LS-DYNA viscous form

2 – Flanagan-Belytschko viscous form

3 – Flanagan-Belytschko viscous form with exact volume integration for solid elements

4 – Flanagan-Belytschko stiffness form

5 – Flanagan-Belytschko stiffness form with exact volume integration for solid elements

6 – Belytschko-Bindeman assumed strain co-rotational stiffness form

7 – Linear total strain form of type 6 hourglass control

9 – Puso enhanced assumed strain stiffness form

The viscous hourglass control is recommended for problems deforming with high velocities, while the stiffness control is preferable for lower velocities. The type 3 hourglass control was recommended for relatively soft materials, like rubber [93]. The tension test simulations had lower velocity deformations. The resulting deformation of the models with each hourglass control is shown in Figure 70.

(a) Type 1

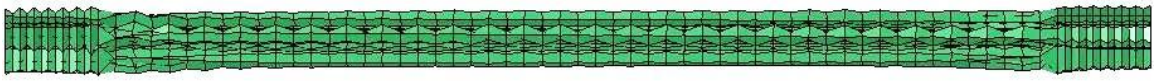

(b) Type 2

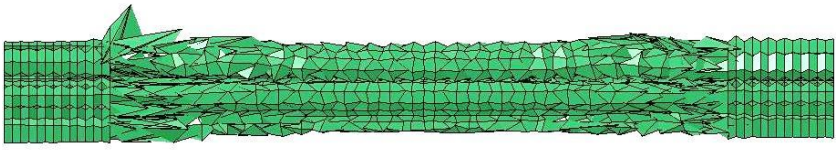

(c) Type 3

(d) Type 4

Figure 70. Hourglass Control Solid Element Deformation

(e) Type 5

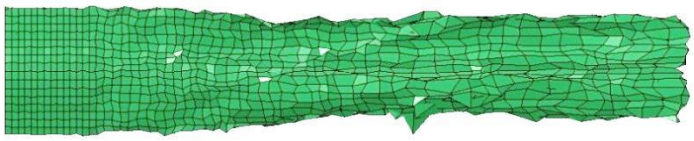

(f) Type 6

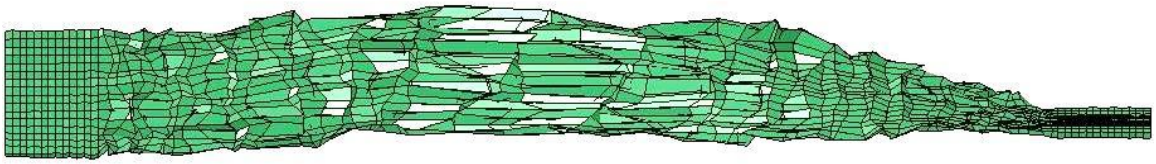

(g) Type 7

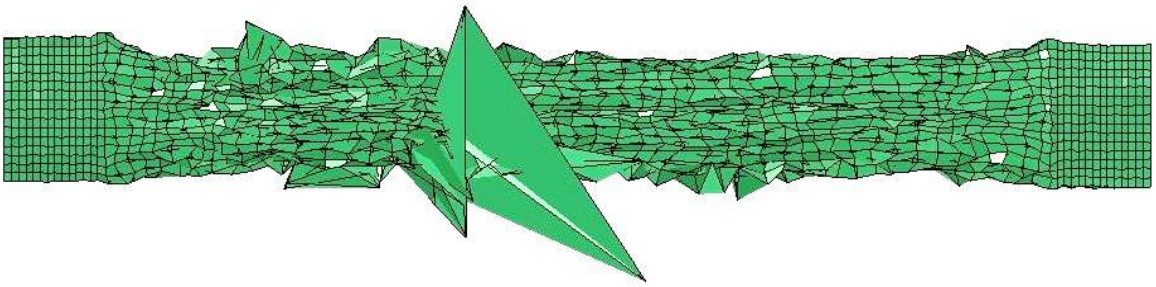

(h) Type 9

Figure 70. Hourglass Control Solid Element Deformation (cont.)

The type 4 and 5 stiffness form did not show any physical hourglassing like the other hourglass controls did. However, both of these models began to curve into the z-direction, as shown in the end-on view in Figure 71. The force vs. deflection curves for types 4 and 5 hourglass controls did not change from the Simplified simulation previously shown in Figure 62.

Figure 71. Type 4 and 5 Hourglass Control Solid Element Deformation, End View

When modeling thin elements with solid elements, it is recommended that two or more elements are through the thickness. Each solid hexahedral element was split in 64 hexahedral elements, so the sample model was four elements thick. However, in addition to significantly increasing the run time, most of the material model simulations had negative volumes in elements at the boundary between the nodes with a prescribed velocity and those without.

Fully-integrated elements eliminate hourglassing problems that occur in under-integrated elements. The fully integrated S/R solid and the type 3 fully integrated quadratic 8 node element formulations with nodal rotations were explored. The fully integrated S/R solid element formulation deformation looked very similar to the solid elements with the type 4 and 5 hourglass control, as shown in Figure 72. While the deformation had no hourglassing, the model curled in the z-direction. The fully-integrated quadratic 8 node element formulation had elements with negative volumes and stopped running very quickly.

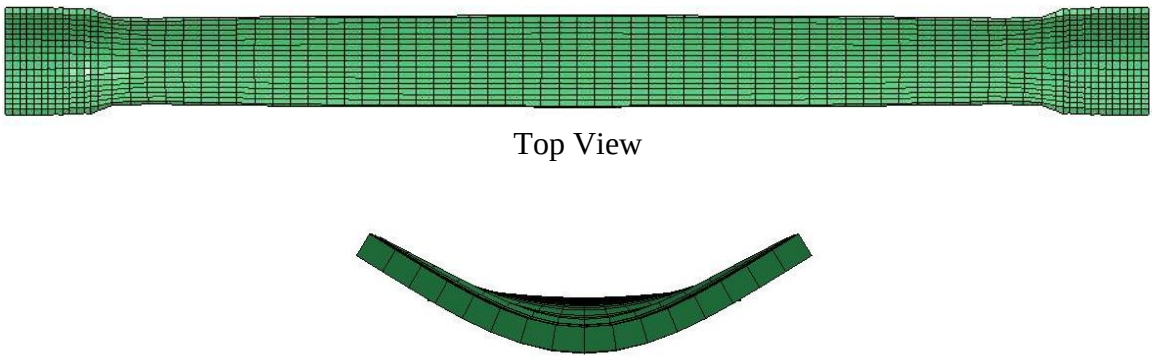

Top View

End View

Figure 72. Fully Integrated S/R Solid Element Formulation Deformation

All types of solid element hourglass control and several element formulations were investigated, but none resulted in solid element deformation that replicated the tensile test. One research presentation suggested using tetrahedral solid element meshes with the 1 point nodal

pressure tetrahedron element formulation for incompressible material behavior [94]. Tetrahedral elements cannot hourglass. Hexahedral elements are under-integrated with a single Gauss point to volumetric locking in large strain applications [95]. Therefore, the 1 point nodal pressure tetrahedron element uses average nodal pressures to reduce volumetric locking which can occur in large deformation, incompressible materials in dynamic explicit applications. Since rectangular and hexahedral elements work very well in most applications, triangular shell elements and tetrahedral solid elements are generally not preferred. Triangular and tetrahedral elements are stiffer than rectangular/hexahedral elements and are more costly due to a reduction in the time step and an increased number of elements. However, when modeling elastomers and other nearly incompressible materials, tetrahedral solid elements perform acceptably and more accurately than hexahedral elements, as shown in Figure 73. The force vs. deflection curve compared very close to the tensile test data, as shown in Figure 74.

5.2.6 80 Durometer Rubber

The same simulations were run at strain rate 0.833/sec with the force versus deflection curve obtained from a tensile test of an 80-durometer EPDM rubber sample. For the default Belytschko-Tsay shell elements, the material models that had force versus deflection curves as inputs were very similar to one another with force levels two-thirds greater than the actual tensile tests, as shown in Figure 75. Most of the material models with the 1 point nodal pressure tetrahedron elements were only slightly higher than the actual tensile tests, as shown in Figure 76.

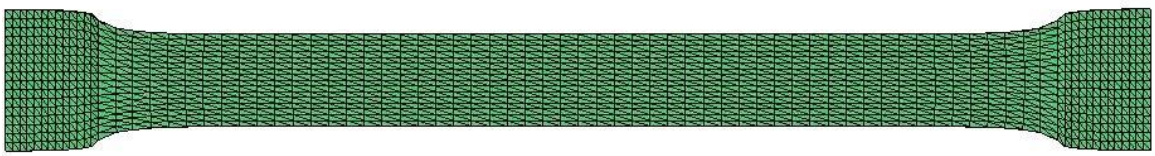

Figure 73. 1 Point Nodal Pressure Tetrahedron Solid Element Formulation Deformation

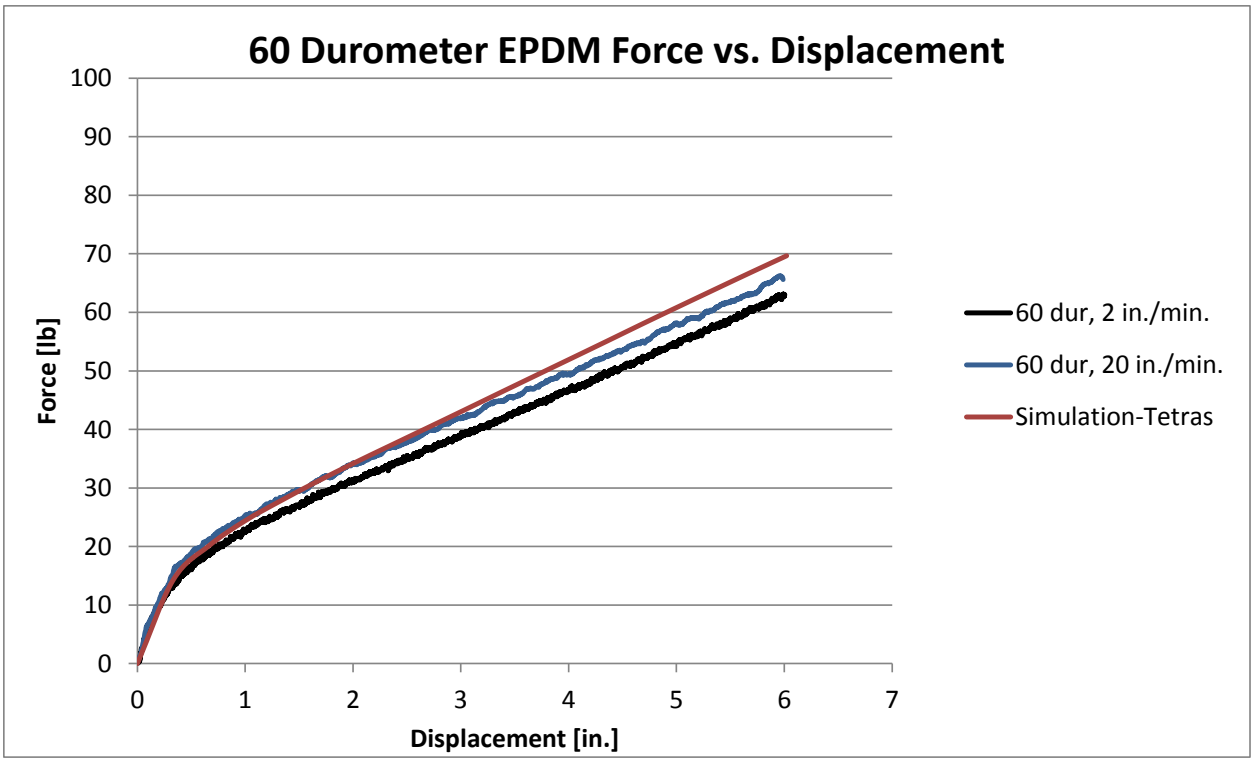

Figure 74. Comparison of Tetrahedral Solid Elements – 60 Durometer – 0.833/sec

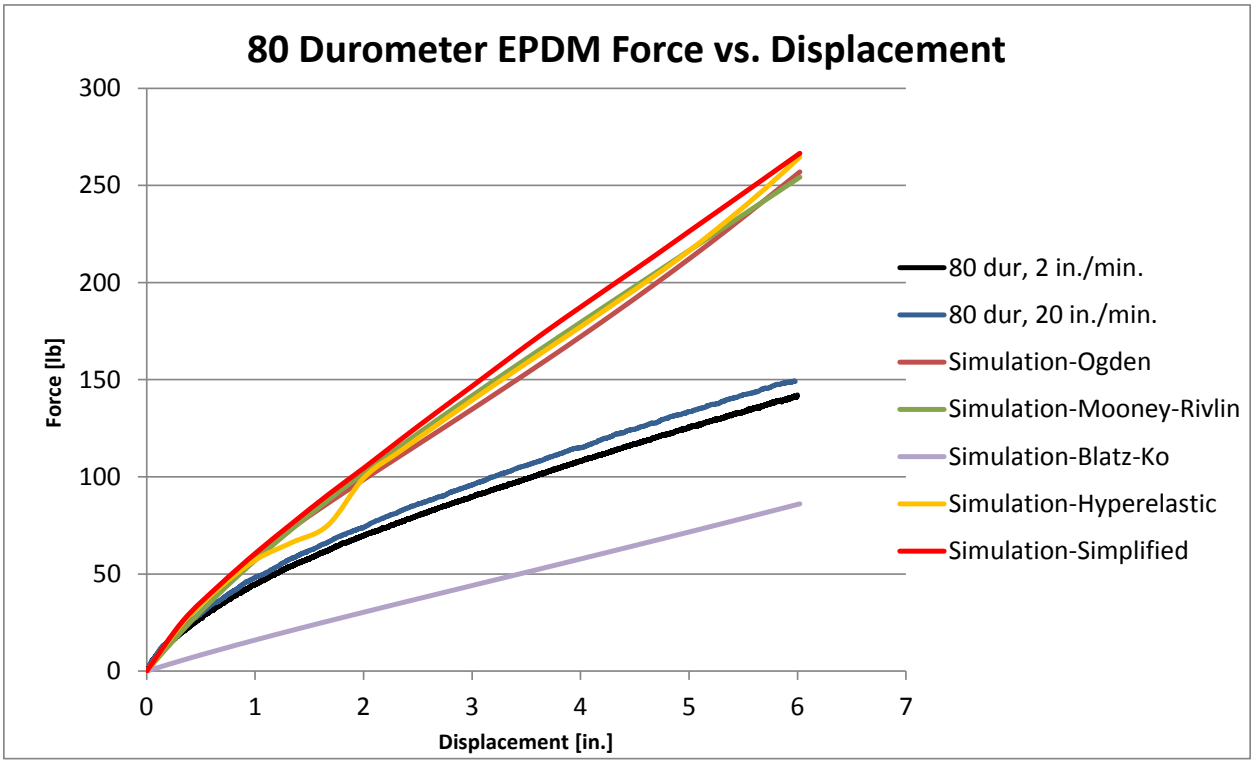

Figure 75. Comparison of Rubber Models with Shell Elements – 80 Durometer – 0.833/sec

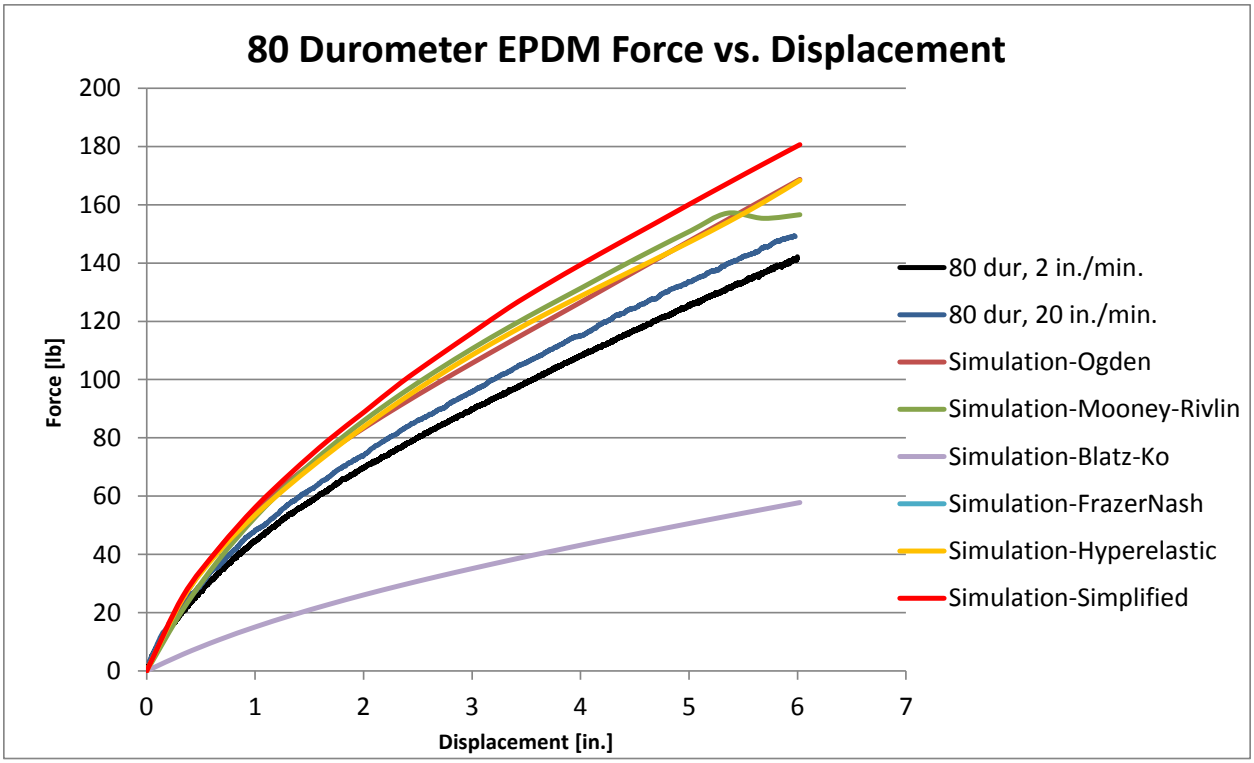

Figure 76. Comparison of Tetrahedral Solid Elements – 80 Durometer – 0.833/sec

5.3 Shear Fender Material Tests

The basic hyperelastic properties of the shear fender rubber, which has a durometer from 50 to 55, were desired for simulations. Samples were sent to and tested at Axel Products, Inc. in Ann Arbor, Michigan. Three tests were performed at room temperature: simple tension, planar tension (pure shear), and biaxial extension (equal biaxial). The simple tension test involved a thin rectangular sample to obtain stress vs. strain when pulled at 4 strains: 25, 50, 100, and 150 percent. The planar tension (pure shear) test is like a tensile test with a very wide sample. Since rubber is nearly incompressible, a state of pure shear exists at a 45 degree angle to the direction of stretching. The planar tension test was conducted at 4 strains: 25, 50, 100, and 150 percent. The biaxial extension (equal biaxial) test radially stretches a circular disc so that a state of pure compression exists for nearly incompressible materials. The biaxial extension test was conducted at 3 strains: 25, 50, and 100 percent. The stress vs. strain curves for these three tests at 100

percent strain are shown in Figure 77. This information can be used to calculate the shear modulus as well as be input in LS-DYNA material models.

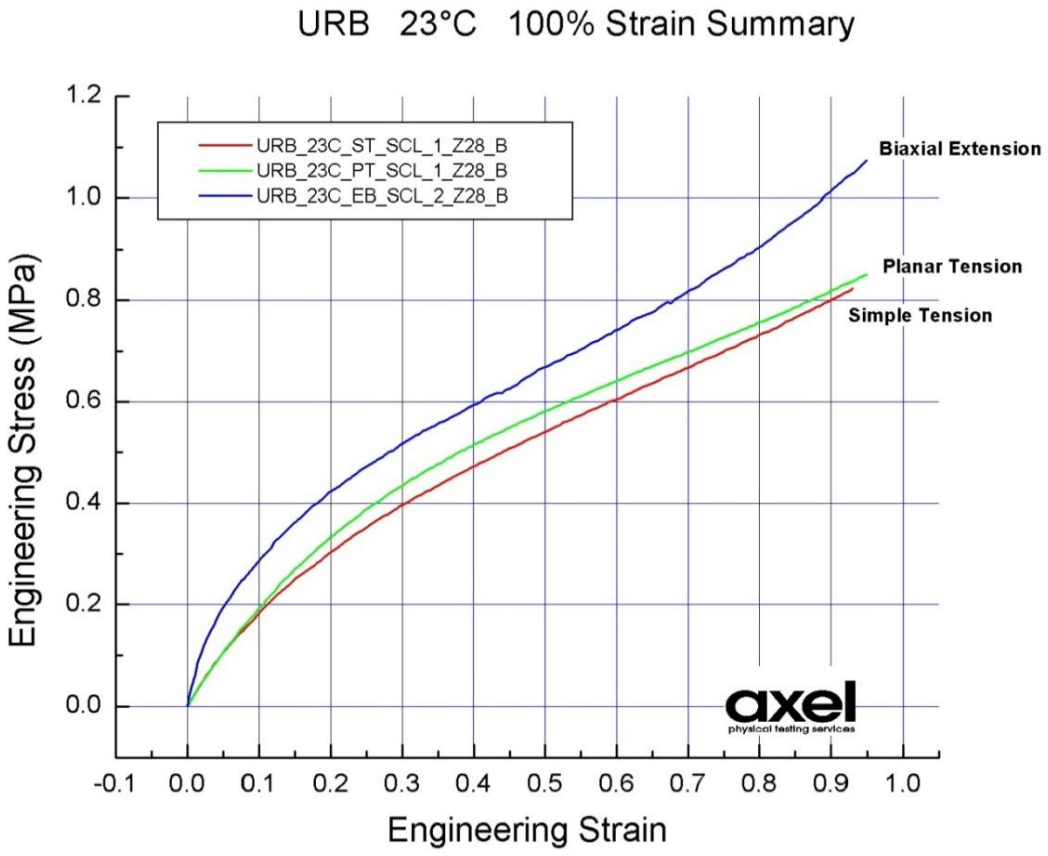

Figure 77. Summary of Material Tests at 100 Percent Strain

5.4 Shear Fender Rubber Tension Test Simulation

The simulation of the tension test only included solid elements, since many of the energy absorber shapes had complicated geometry that would best be modeled with solid elements. Using previously-gained knowledge about modeling rubber, the one point nodal pressure tetrahedron elements and the most promising material models were further investigated. The tensile test model is shown in Figure 78. The same boundary conditions that were applied in the previous tension test simulation were used. The Blatz-Ko, Simplified Rubber/Foam, and Ogden material models were investigated. The Ogden rubber material model is the only material

formulation that allows pure shear and equal biaxial data curves to be input. The shear and compression modes were not important when modeling the tension tests. However, the shear and compression loading were important to consider for energy absorber simulations, so they were investigated at this point.

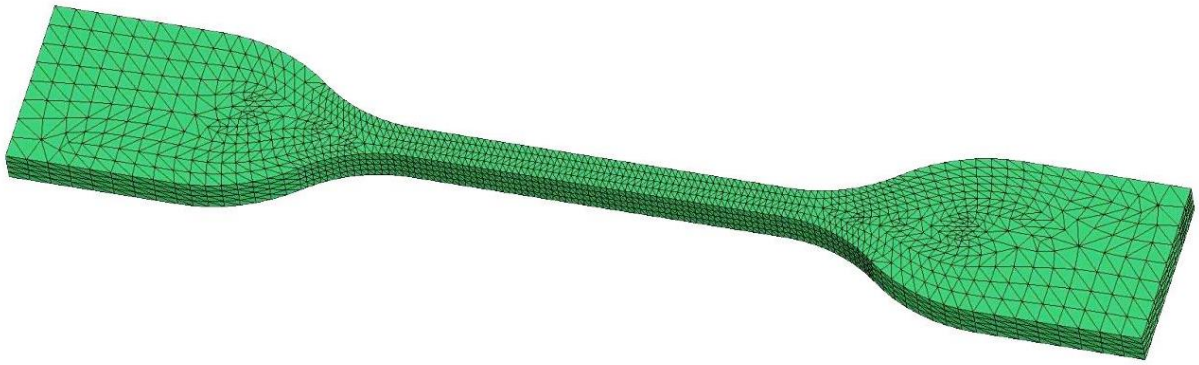

Figure 78. Simulation of Shear Fender Tensile Test – Stress vs. Strain

From the tensile test data, the shear modulus was calculated to be 0.616 MPa (88 psi). Three stress-strain curves were generated for LS-DYNA using the highest strain tested for each of the three tests. The test data was decimated to have less than 100 data points. Stress vs. strain for each of the material models was compared to the tension test, as shown in Figure 79. The Ogden model with tension test data was almost exactly the same. The Simplified Rubber/Foam model also compared very well. The stress vs. strain curves for these two models are more easily seen in Figure 80.

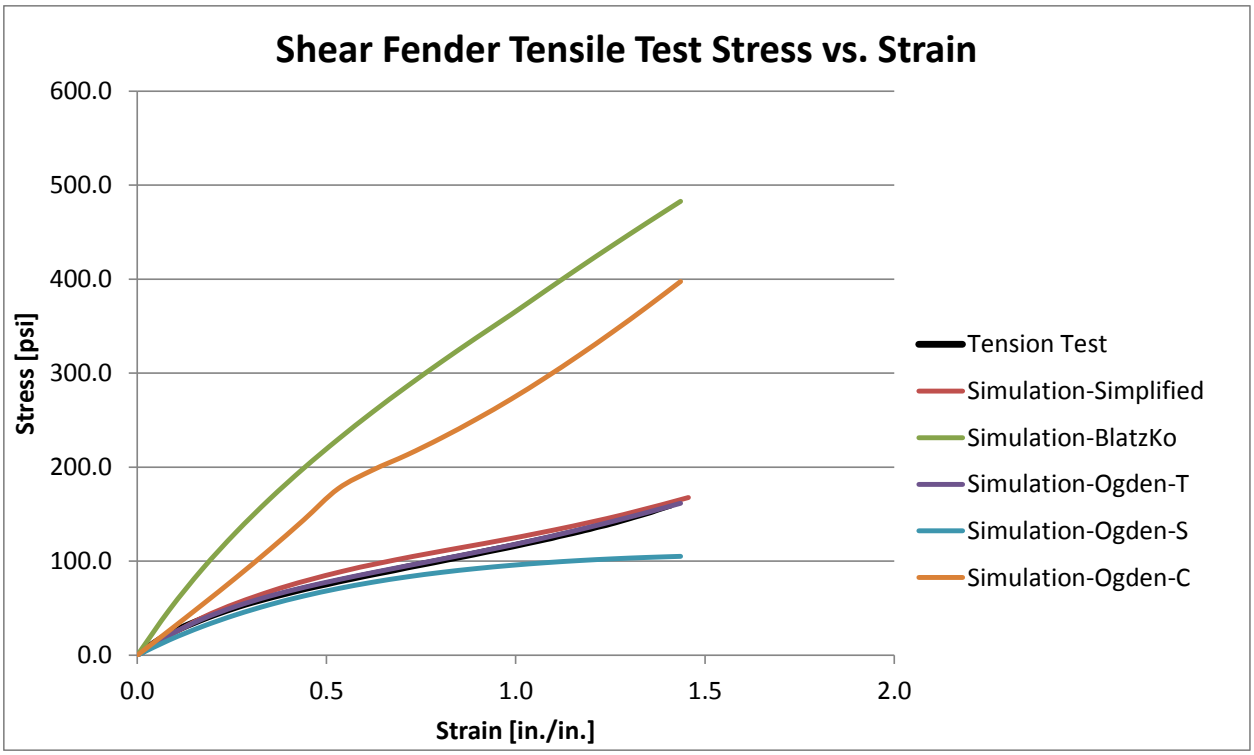

Figure 79. Simulation of Shear Fender Tensile Test – Stress vs. Strain

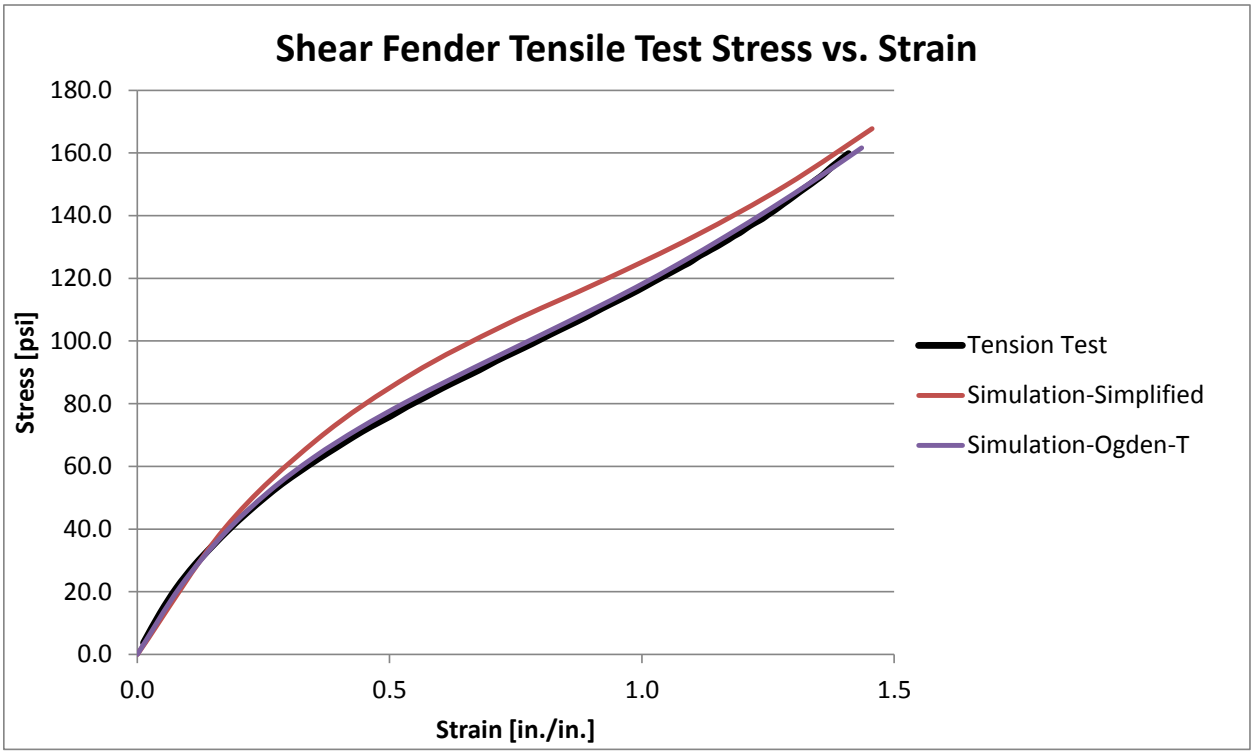

Figure 80. Simulation of Shear Fender Tensile Test – Stress vs. Strain

5.5 Findings from Rubber Modeling

LS-DYNA rubber material models were compared to the tension tests conducted at 2 in./min. (0.00085 mm/ms) and 20 in./min. (0.0085 mm/ms). LS-DYNA does not incorporate strain rate effects in any of the rubber models, unless multiple force vs. deflection curves at different rates are input. The tension tests were conducted at strain rates that were much lower than the expected load rates for the energy absorbers in a barrier system. Therefore, the strain rate effects were not incorporated in the simulations.

Almost all of the rubber material models with shell elements (except Blatz-Ko) could fairly accurately predict the force versus deflection curve up to 25 percent strain, as shown in Figures 54 and 55. For larger strains though, some of the models began to deviate significantly. All of the simulations stretched at 0.0083/sec had unstable forces after halfway through the runtime, likely due to excessive error accumulation in the explicit analysis. Most of these model instabilities were reduced in the simulations performed at 0.833/sec, and the physical deformation of the models looked good. However, the force versus deflection curves did not match that well. The Simplified Rubber/Foam material model most accurately resembled the shape of the tension test force versus deflection curve for both the 60- and 80-durometer EPDM, but the linear region had an increased slope. The Blatz-Ko material model could have been more accurate by adjusting the shear modulus. Since this model is cheaper and requires less material properties, it would be preferred as long as it is accurate.

All of the solid element simulations that were stretched at 0.0083/sec were poor models. The forces were low compared to the tension tests, and the models deformed with severe hourglassing and inconsistencies. All of the solid element simulations that were stretched at 0.833/sec had reasonable forces, but the models deformed with moderate hourglassing and inconsistencies. The Simplified rubber model force vs. deflection was almost identical to the 20

in./min. (0.0085 mm/ms) tensile test data. Ogden and Mooney-Rivlin material models were also reasonable fits.

Since solid elements were desired to simulate the energy absorbers, several ways to improve the physical deformation of the solid elements were explored. Hourglass control type 4 and 5 and the fully integrated S/R element formulation all produced models that did not physically hourglass. However, these models had unrealistic out-of-plane bending.

One point nodal pressure tetrahedron elements physically deformed well and had forces similar to the tension tests. The 60-durometer EPDM test at 20 in./min. (0.0085 mm/ms) and the Simplified tetrahedral model had nearly identical force vs. deflection curves. The material models of the 80-durometer EPDM were reasonable, and the Ogden and Hyperelastic material models provided the closest fits. The Simplified and Ogden material models with the tetrahedron elements were both very accurate at modeling the shear fender rubber.

When modeling rubber in tension at large strains, the one point nodal pressure solid tetrahedron elements are recommended. However, the best rubber material model is dependent on type of rubber. If uniaxial tension test data is available, using a material model with the tension curve input is the most accurate. The Simplified material model was the most accurate. The Ogden model was also decently accurate. If uniaxial test data is unavailable, the Blatz-Ko material model can also be accurate, but the shear modulus parameter can be difficult to determine accurately. The Frazer-Nash rubber material model is not recommended, because the simulations always encountered an error with nodes with out-of-range velocities.

Several of the material models were promising when simulating tension loads. The most promising models were further investigated with other load scenarios through component test simulations.

6 COMPONENT TESTS

In conjunction with the material tests and simulations, FEA was also used to determine the size and shape of the energy absorber that would have the capacity to contain and redirect a TL-4 single-unit truck impact and also reduce the accelerations in the 1100C small car and 2270P pickup truck impacts. Preliminary simulations were conducted with axially-load cone and cylinder energy absorbers.

6.1 Cone-Shaped Energy Absorber

For the axial compression simulation of the rubber cone, two rigid plates were used to sandwich the cone. The rubber cone had constant stress solid hexahedral elements, as shown in Figure 81. Since the cone had an irregular shape and thick walls, solid hexahedral elements were used in lieu of shell elements. The dimensions of the cone were 12 in. (304 mm) high, an 11.6 in. (296 mm) top diameter, a 2 in. (51 mm) wall thickness, and a 10.7 degree slope. Other cone geometries were explored, but the 12-in. high cone provided the most uniform deformation and adequate energy-absorbing capacity. The specific compound of rubber and material properties had yet to be determined, so the *MAT_OGDEN_RUBBER with a generic rubber force-deflection curve was adapted from Reid [96] since it was available.

The rigid plates were Belytschko-Tsay shell elements. The top rigid plate had a *BOUNDARY_PRESCRIBED_MOTION_RIGID displacement of 8½ in. (216 mm) over 18.6 ms, which was equivalent to the lateral velocity of a vehicle traveling at 25 degrees and 62 mph (27.78 mm/ms). The bottom rigid plate was fixed. The *CONTACT_AUTOMATIC_SINGLE_SURFACE was used for the self-contact, but the *CONTACT_NODES_TO_SURFACE was used between the rigid plates and the cone. Since the bottom of the cone would most likely be bolted or fixed in a barrier system, a friction coefficient of 1.0 was assigned to the lower plate.

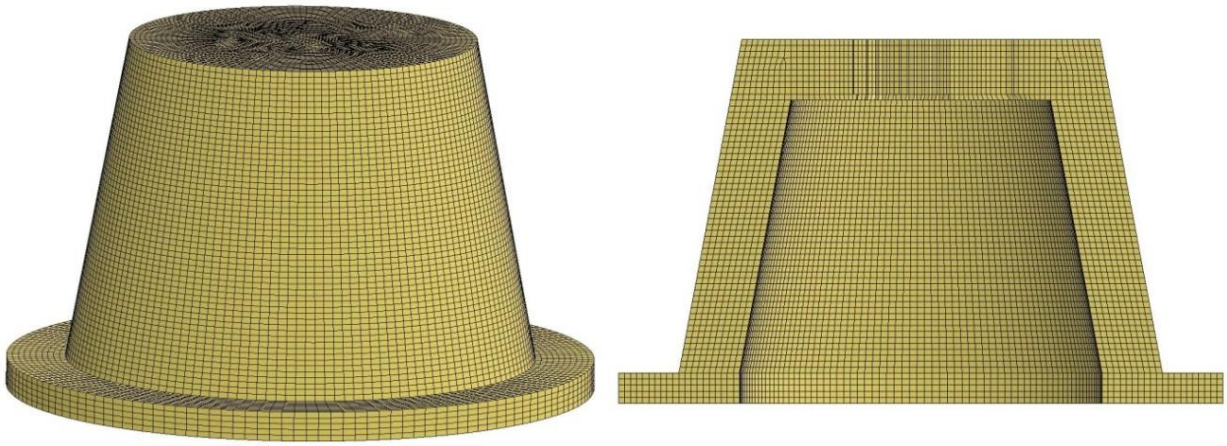

Figure 81. Cone FEA Model

The sequential deformation of the cone is shown in Figure 82 along with an enlarged cross-section view at 16 ms.

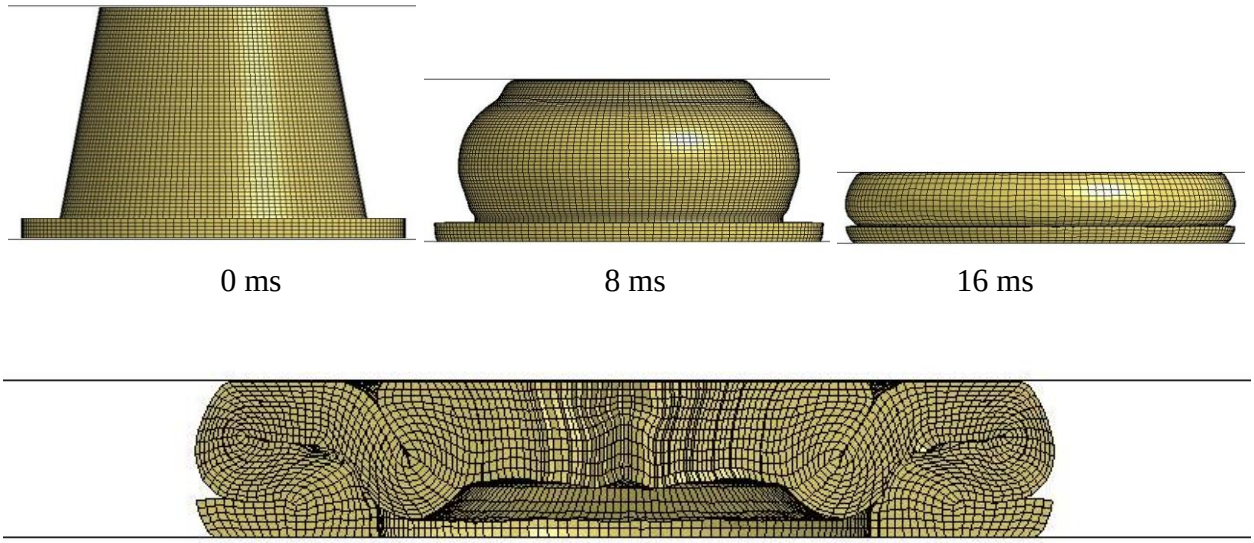

Figure 82. Cone FEA Sequential Deformation

Preliminary simulation indicated that the 12-in. (304-mm) high conical rubber shape would absorb 92 k-in. (10.4 kJ) of energy with 8½ in. (216 mm) of deflection, as shown in Figure 83.

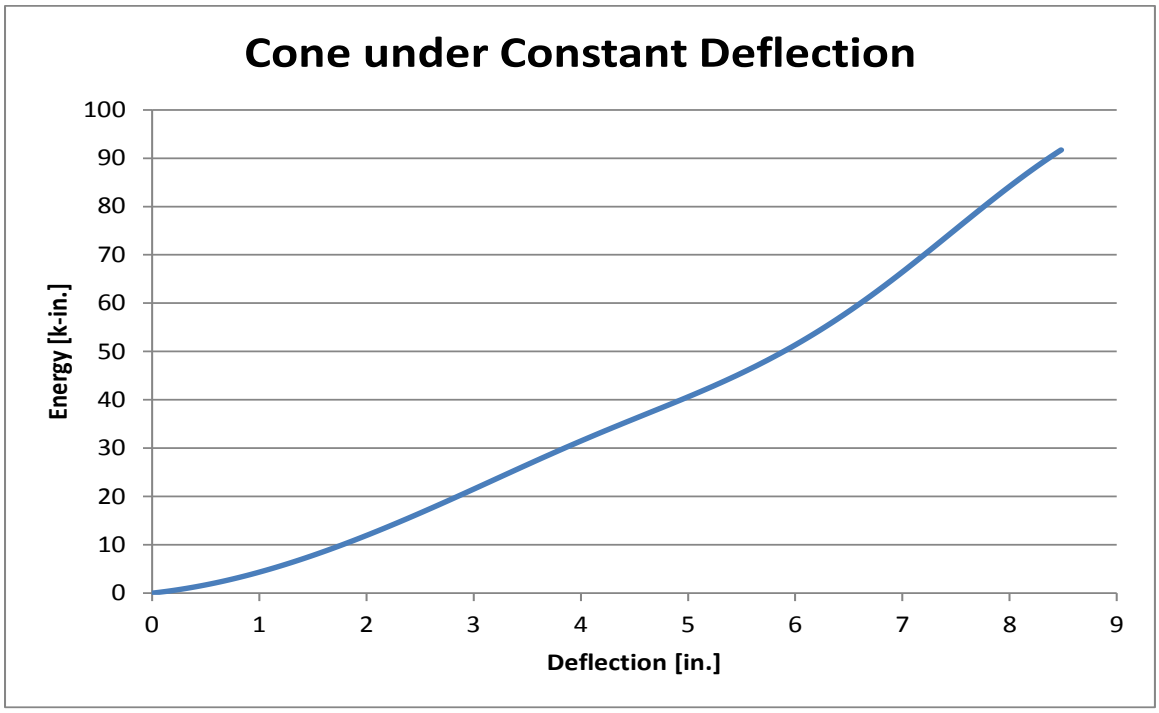

Figure 83. Energy vs. Deflection for Cone Simulation

A physical component test was required to validate the simulation. Due to the limited availability for pre-made conical fender sizes, cylindrical shapes were further explored since the components could be mandrel-wrapped in any size without a custom mold.

6.2 Cylindrical Energy Absorber

6.2.1 Preliminary Simulation

The energy-absorbing capacity of axially-loaded cylinders was evaluated using the generic rubber model previously used in the conical model. Constant stress hexahedral solids elements were used, and the model is shown in Figure 84. The *CONTACT_AUTOMATIC_SINGLE_SURFACE was used for the self-contact that occurred.

The diameter and thickness was varied on 10-in. (254-mm) long cylinders. Two 12-in. (305-mm) inner diameter (ID) cylinders had a wall thickness (t) of 1 in. (25 mm) and 2 in. (51 mm). Two 8-in. (203-mm) inner diameter cylinders had a wall thickness of 1 in. (25 mm) and 2 in. (51 mm).

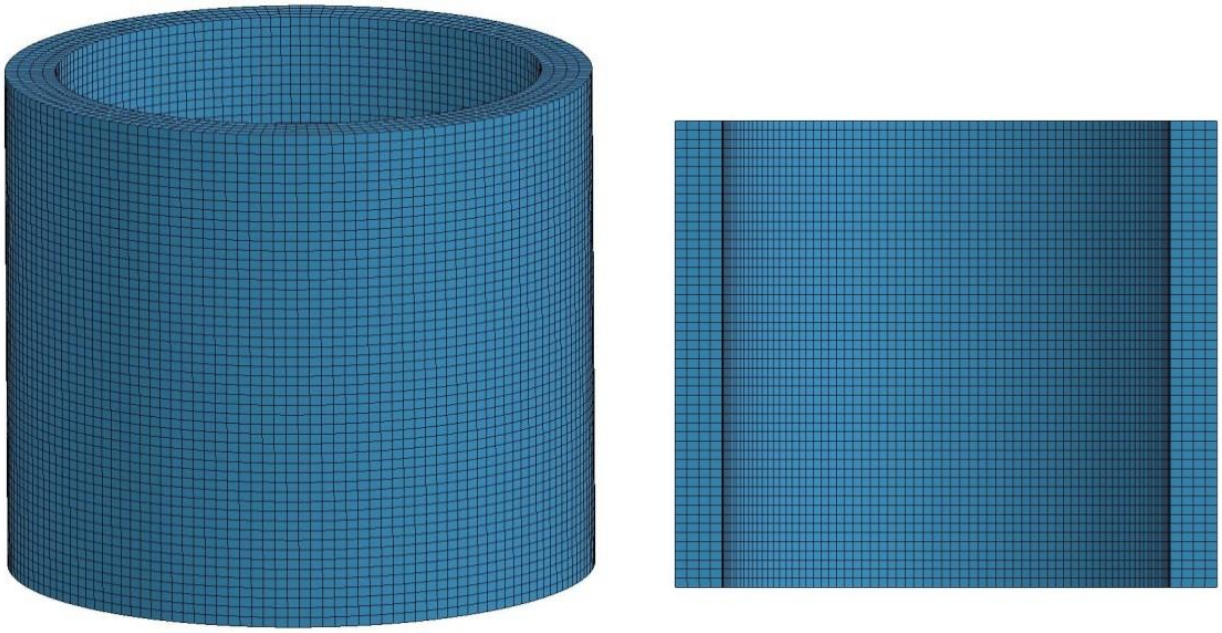

Figure 84. Cylinder FEA Model

The top flat geometric rigidwall applied a constant deflection of 6 in. (152 mm) over 13 ms (the velocity of the lateral component of a TL-4 impact). The bottom rigidwall was fixed. The energy absorption for 10-in. (254-mm) long, axially-loaded cylinders is shown in Figure 85. At least 16.7 kip-ft (22.6 kJ) of kinetic energy needs to be absorbed to reduce the lateral vehicle accelerations by 30 percent for TL-4 impacts with an 1100C small car. At least 34.4 kip-ft (46.6 kJ) of kinetic energy needs to be absorbed to reduce the lateral vehicle accelerations by 30 percent for TL-4 impacts with a 2270P pickup truck. Using the desired energy per foot of barrier length of 0.88 kip-ft/ft and a span length of 40 ft (12.2 m), the 12-in. (305-mm) inner diameter x 2-in. (51-mm) thick cylinders would need to be spaced at 2.5 ft (0.8 m) to absorb the kinetic energy of the TL-4 2270P impact. If the cylinders could be loaded to a greater deflection, they could absorb significantly more energy. Although other cylinder lengths could also work, a 10-in. (254-mm) long cylinder was chosen as a baseline configuration.

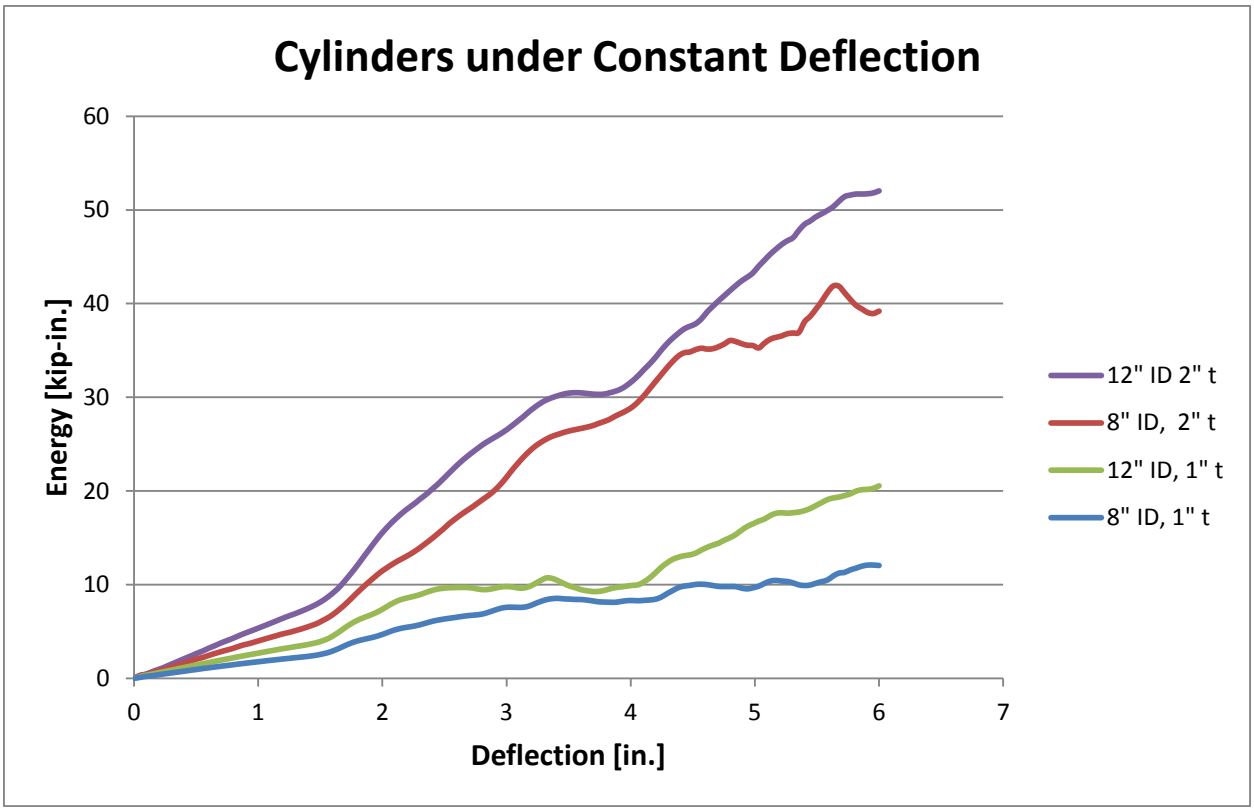

Figure 85. Energy vs. Deflection for Four Cylinders under Constant Deflection

The physical deformation of all the simulations was unrealistic. For example, the deformation of the 8-in. (203-mm) ID by 2-in. (51-mm) thick cylinder is shown in Figure 86. The motion wave was apparent since the wall thickness varied throughout the cross-section when compressed. The rubber should not appear to be so soft, and some shooting nodes appear near the end of the simulation. However, the energy absorption seemed reasonable compared to that of laterally-loaded cylinders from previous literature [36].

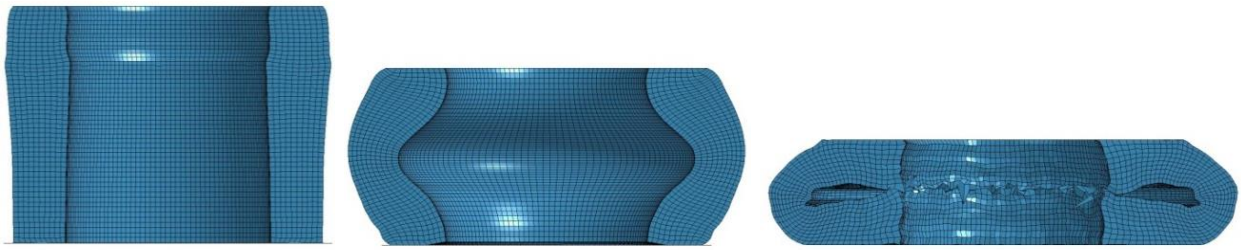

Figure 86. Deformation of the 8-in. (203-mm) ID, 2-in. (50.8-mm) Thick Cylinder

6.2.2 Component Tests

From the preliminary finite element simulations, three different cylinders were selected for further investigation and were manufactured by Eutsler Technical Products, Inc. in Houston, TX. The dimensions and durometer of the three different rubber cylinders are shown in Table 6. One cylinder was 60-durometer EPDM. The other two cylinders were 80-durometer EPDM. Component testing was needed to determine the dynamic properties and behavior of the cylinders as well as to improve the finite element simulations.

Table 6. Dimensions and Durometer of Rubber Cylinders

Test No.	Durometer	Thickness in. (mm)	Inner Diameter in. (mm)	Outer Diameter in. (mm)	Length in. (mm)
EPDM-1	80	2 (51)	8⅛ (206)	12⅛ (308)	10 (254)
EPDM-2	60	2 (51)	8⅛ (206)	12⅛ (308)	10 (254)
EPDM-3 - EPDM-12	80	1 (25)	9⅝ (244)	11⅝ (295)	10 (254)

A total of 12 bogie tests were conducted on axially-loaded EPDM rubber cylinders. The 1,689-lb (766-kg) bogie had a large wood impact face to uniformly compress the cylinders. The component test setup is shown in Figure 87. One bogie test was conducted on an 80-durometer, 2-in. (51-mm) thick cylinder. One bogie test was conducted on a 60-durometer, 2-in. (51-mm) thick cylinder. Ten bogie tests were conducted on an 80-durometer, 1-in. (25-mm) thick cylinder. The target impact conditions included a speed of 5 mph (8 km/h) and an angle of 0 degrees, which axially compressed the cylinders.

The information desired from the bogie tests was the relation between the applied force and deflection of the energy absorber. This data was then used to find total energy (the area under the force versus deflection curve) dissipated during each test. The dimensions of the cylinders were measured before and after each test. All of the cylinders restored to within 1/16

in. (1.6 mm) of the original dimensions after the component tests. The results of the bogie tests are shown in Table 7. Summary sheets for each of the tests are shown in Appendix C. A complete description of the bogie tests can be found in Schmidt, et. al [97].

Figure 87. Cylinder Component Test Setup

Table 7. Cylinder Dynamic Testing Results

Test No.	Durometer	Dimensions (in.)	Temperature (°F)	Impact Velocity (mph)	Max Deflection (in.)	Peak Force (k)	Total Energy (k-in.)
EPDM-1	80	8 ⅛ ID x 2 t x 10 L	97	4.3	1.9	12.3	12.4
EPDM-2	60	8 ⅛ ID x 2 t x 10 L	91	4.9	2.2	13	16.1
EPDM-3	80	9 ⅝ ID x 1 t x 10 L	91	6.8	6.1	6.7	30.9
EPDM-4	80	9 ⅝ ID x 1 t x 10 L	125	7.0	7.2	8.4	33.5
EPDM-5	80	9 ⅝ ID x 1 t x 10 L	159	6.0	6.6	5.8	24.1
EPDM-6	80	9 ⅝ ID x 1 t x 10 L	163	6.4	7.0	6.6	27.4
EPDM-7	80	9 ⅝ ID x 1 t x 10 L	150	6.3	7.1	6.5	26.6
EPDM-8	80	9 ⅝ ID x 1 t x 10 L	144	6.1	6.9	5.4	25.1
EPDM-9	80	9 ⅝ ID x 1 t x 10 L	128	5.7	6.3	5.1	22.3
EPDM-10	80	9 ⅝ ID x 1 t x 10 L	124	6.0	6.5	5.5	24.5
EPDM-11	80	9 ⅝ ID x 1 t x 10 L	122	5.3	5.6	4.5	19.1
EPDM-12	80	9 ⅝ ID x 1 t x 10 L	114	7.1	7.6	10.1	34.4

Force vs. deflection and energy vs. deflection were compared for the three different cylinder types, as shown in Figures 88 and 89, respectively. Only a slight difference was

observed between the 60 and 80 durometer rubber cylinders (test nos. EPDM-1 and EPDM-2). The 1-in. (25-mm) thick cylinder (test no. 3) had one-half of the peak force, 2.5 times the total energy, and deflected 3 times as much as the 2-in. (51-mm) thick cylinder (test no. EPDM-1). The velocity of test no. EPDM-3 was also 1.5 times greater than test no. EPDM-1. At such a low impact velocity, it was difficult to maintain the 5 mph (8 km/h) constant velocity. This inconsistency in velocity made it hard to compare the cylinders.

Force vs. deflection and energy vs. deflection were compared for the repeated impacts of the one-inch (25-mm) thick cylinder (test nos. EPDM-3 through EPDM-12), as shown in Figures 90 and 91. These tests showed that the energy absorber did not degrade with repeated impacts, and any fluctuations in the peak force or energy were primarily due to the velocity inconsistencies. Although the surface temperature of each cylinder was measured prior to impact, there was no correlation between temperature and energy absorption.

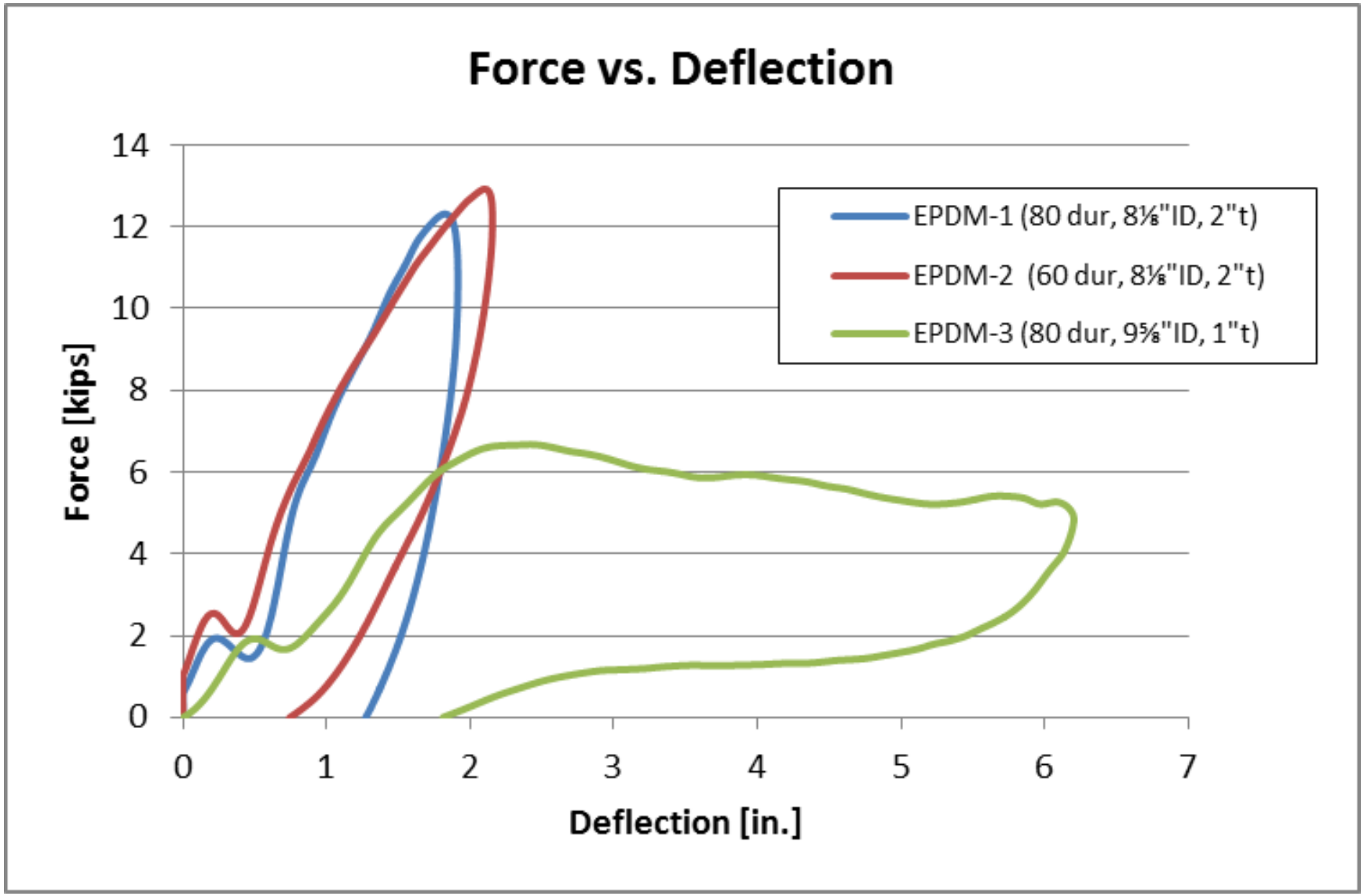

Figure 88. Force vs. Deflection Comparison Plot, Test Nos. EPDM-1 through EPDM-3

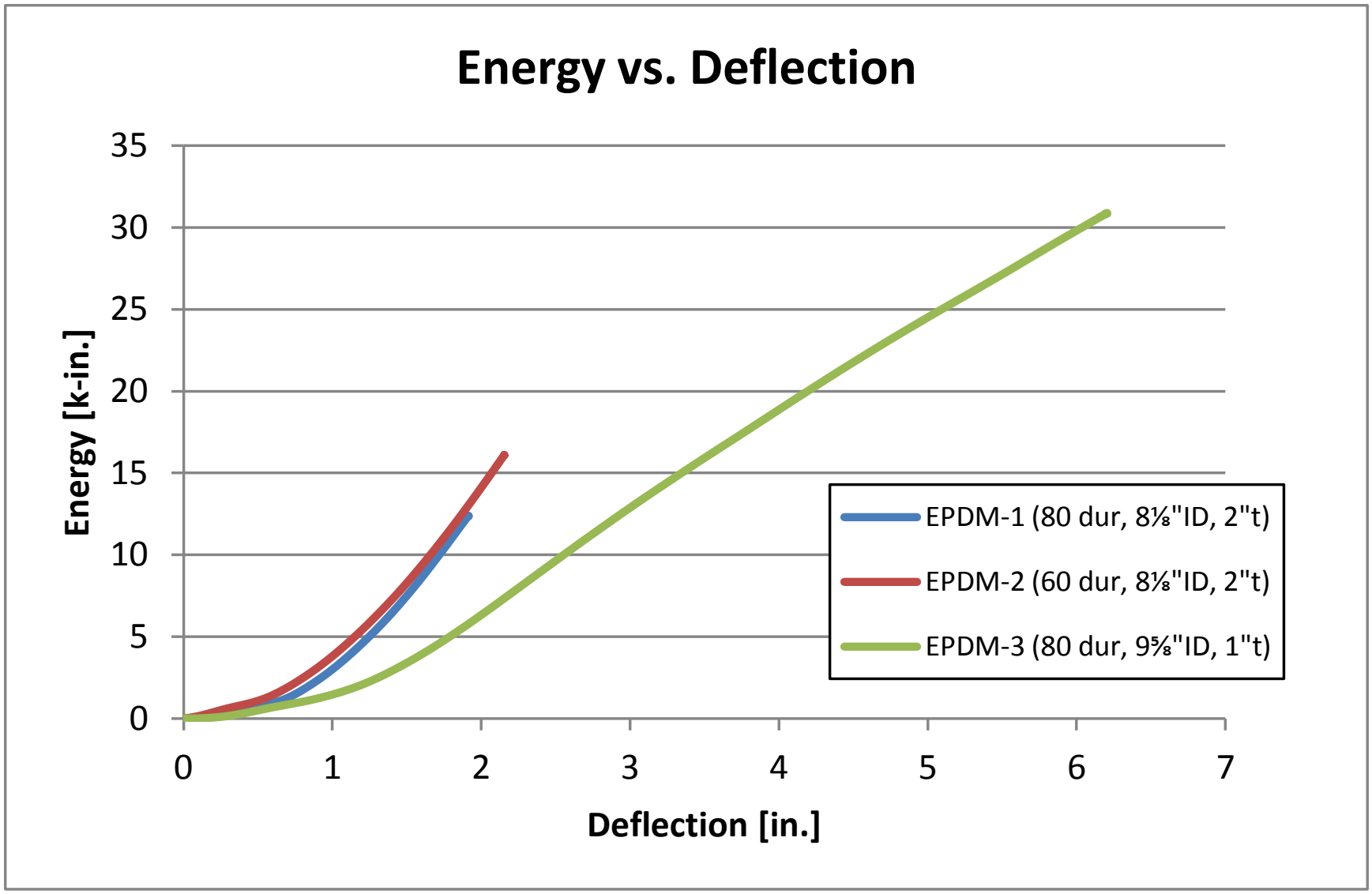

Figure 89. Energy vs. Deflection Comparison Plot, Test Nos. EPDM-1 through EPDM-3

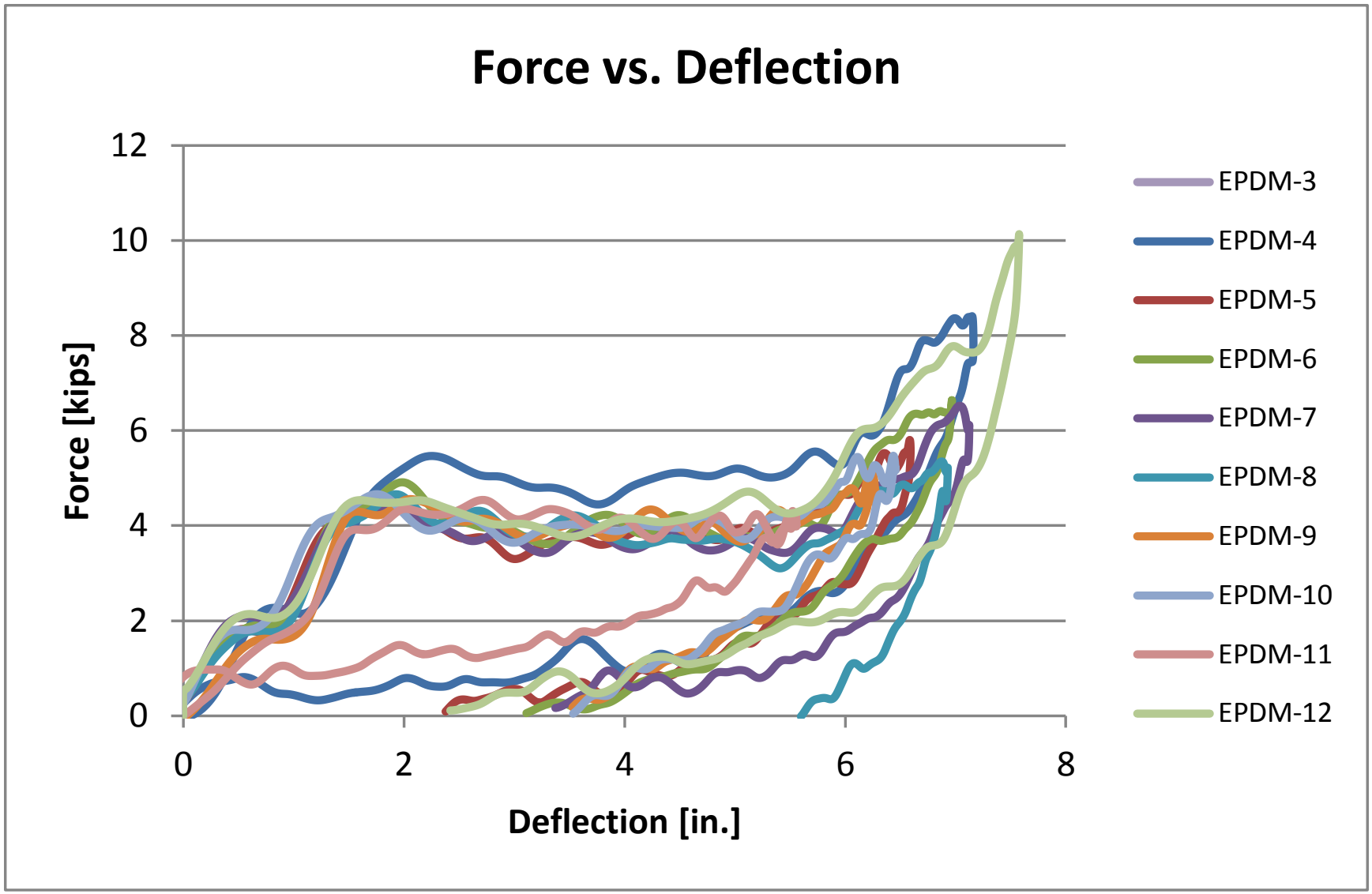

Figure 90. Force vs. Deflection, Test Nos. EPDM-3 through EPDM-12

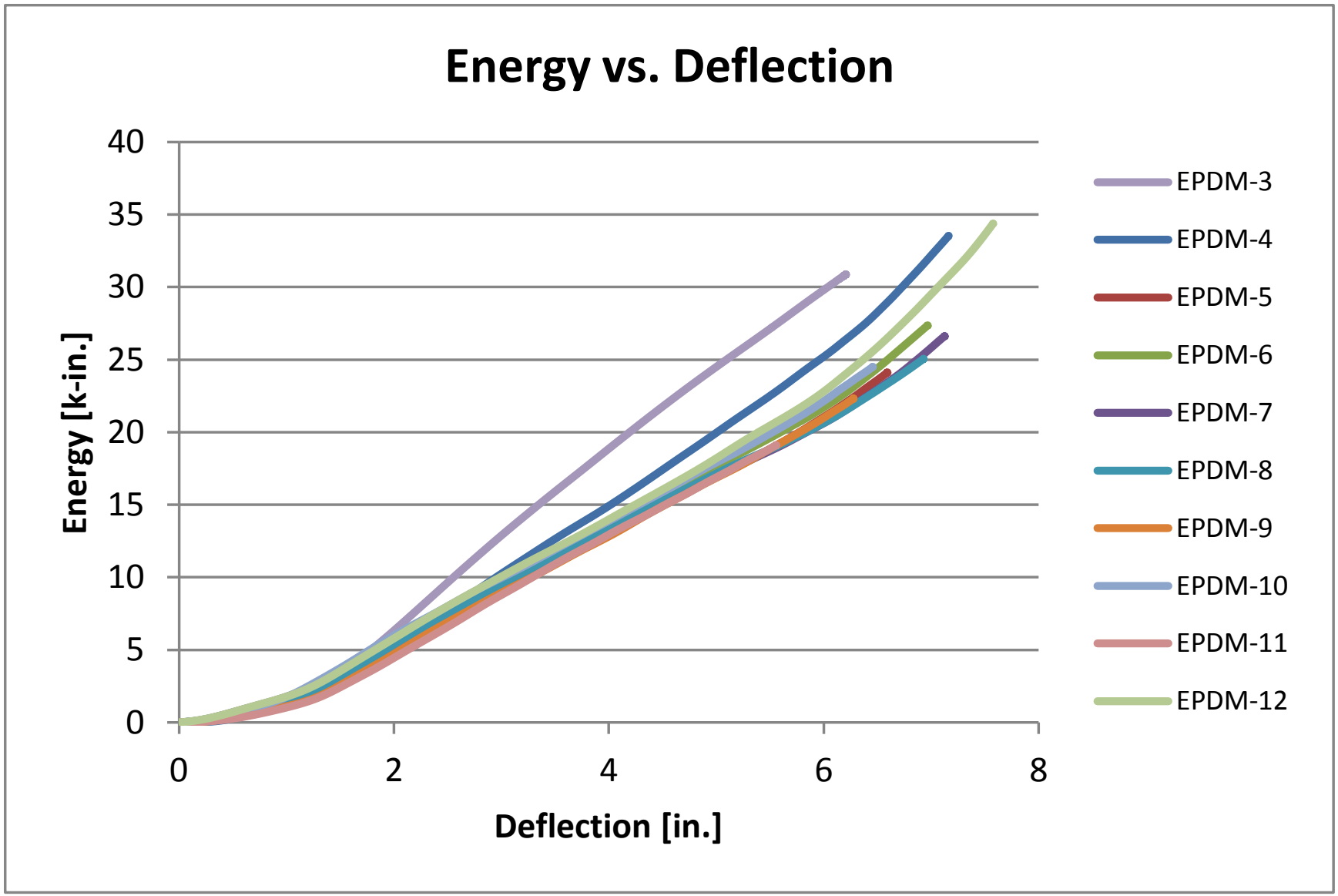

Figure 91. Energy vs. Deflection, Test Nos. EPDM-3 through EPDM-12

6.2.3 Component Test Simulation

The best rubber material models from the tensile test simulations were used to simulate component test no. EPDM-3. Since hexahedral elements are preferred, they were used first to see if they could accurately model deformation in compression. The most promising material models were Simplified and Ogden with hourglass control type 4 or 5. The Blatz-Ko model was also evaluated since it is the simplest and most computationally efficient model. The same parameters as the preliminary simulation were used, and the material model formulation and the hourglass control were varied. The top rigidwall had a mass of 1,689 lb (766 kg) and a velocity of 6.8 mph (3.022 mm/ms).

The Ogden material model with the type 3 hourglass control resulted in hourglassing and elements penetrating through each other where the cylinder wall buckled, as shown in Figure 92. Changing the contact definition did not improve the element penetration problem.

The Ogden material model with type 4 hourglass control resulted in uniform, non-hourglassing deformation, as shown in Figure 93. However, this model was too stiff, and the cylinder did not deflect as much as desired. Since the coefficient of friction was 1.0 on the rigidwalls, this prevented the ends of the cylinder from displacing laterally. In test no. EPDM-3, the ends were not restricted from moving laterally outward, but they also did not appear to move much. Since the backboard and bogie impact head were both faced with rough plywood, the coefficient of friction between the rubber and plywood was high.

So, the Ogden material model with type 4 hourglass control and a coefficient of friction of 0.7 on the rigidwalls was simulated. The cylinder appeared much softer, and the bottom of the cylinder folded inward, as shown in Figure 94.

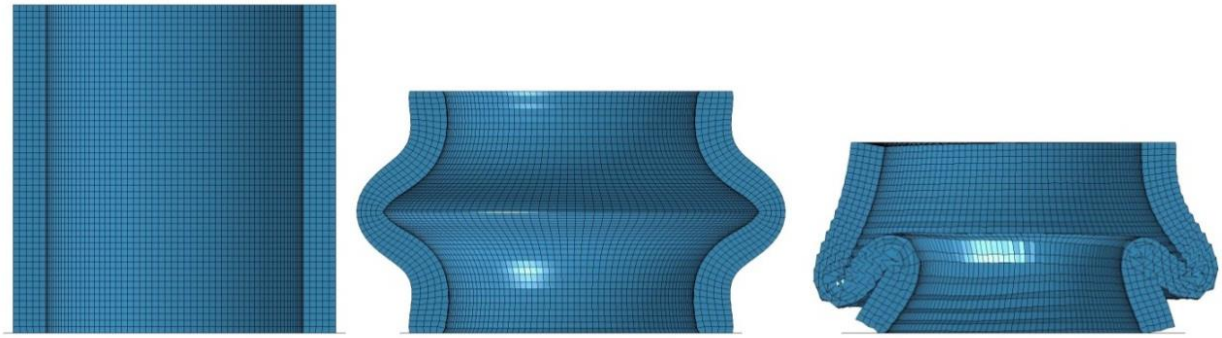

Figure 92. Type 3 Hourglass Control, Test No. EPDM-3 Simulation

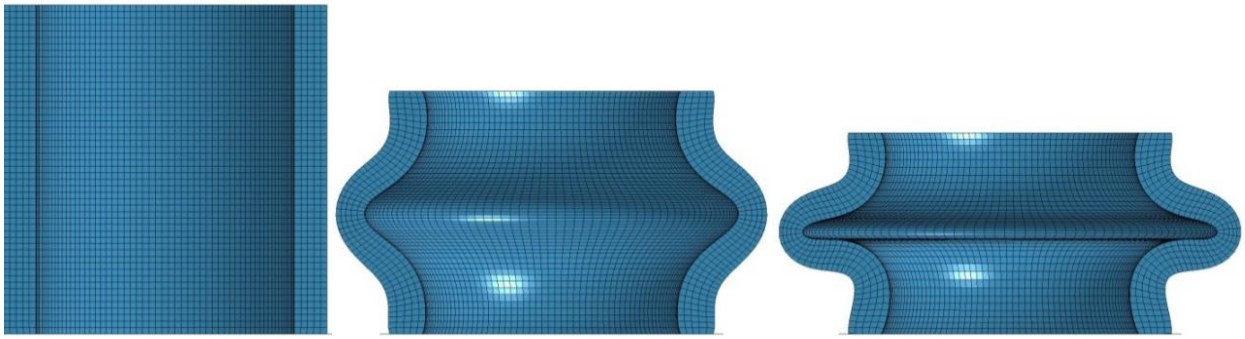

Figure 93. Type 4 Hourglass Control and Friction = 1.0, Test No. EPDM-3 Simulation

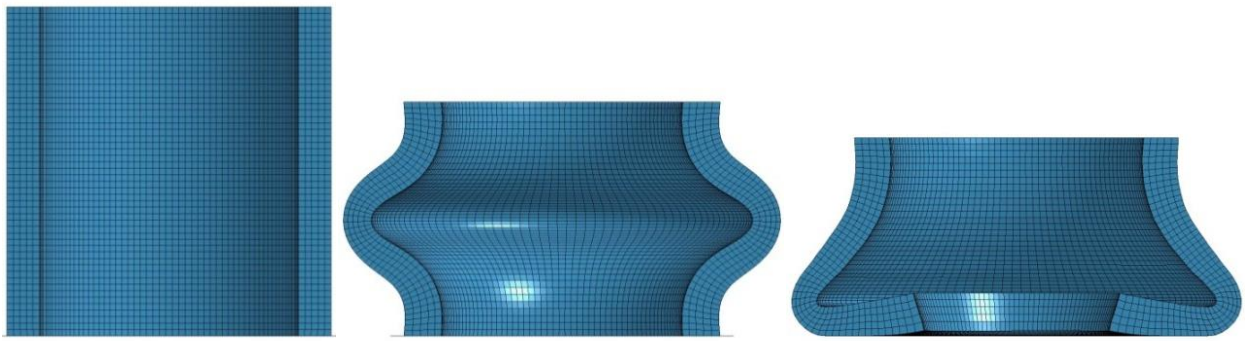

Figure 94. Type 4 Hourglass Control and Friction = 0.7, Test No. EPDM-3 Simulation

Fully-integrated solid elements resulted in nodes with out-of-range velocities when the cylinder walls started to buckle. Therefore, the fully-integrated elements did not model elastomers in tension or compression, except at low strains.

The hexahedral mesh was divided into a tetrahedral mesh, and the element formulation was changed to the 1 point nodal pressure tetrahedron element, as shown in Figure 95.

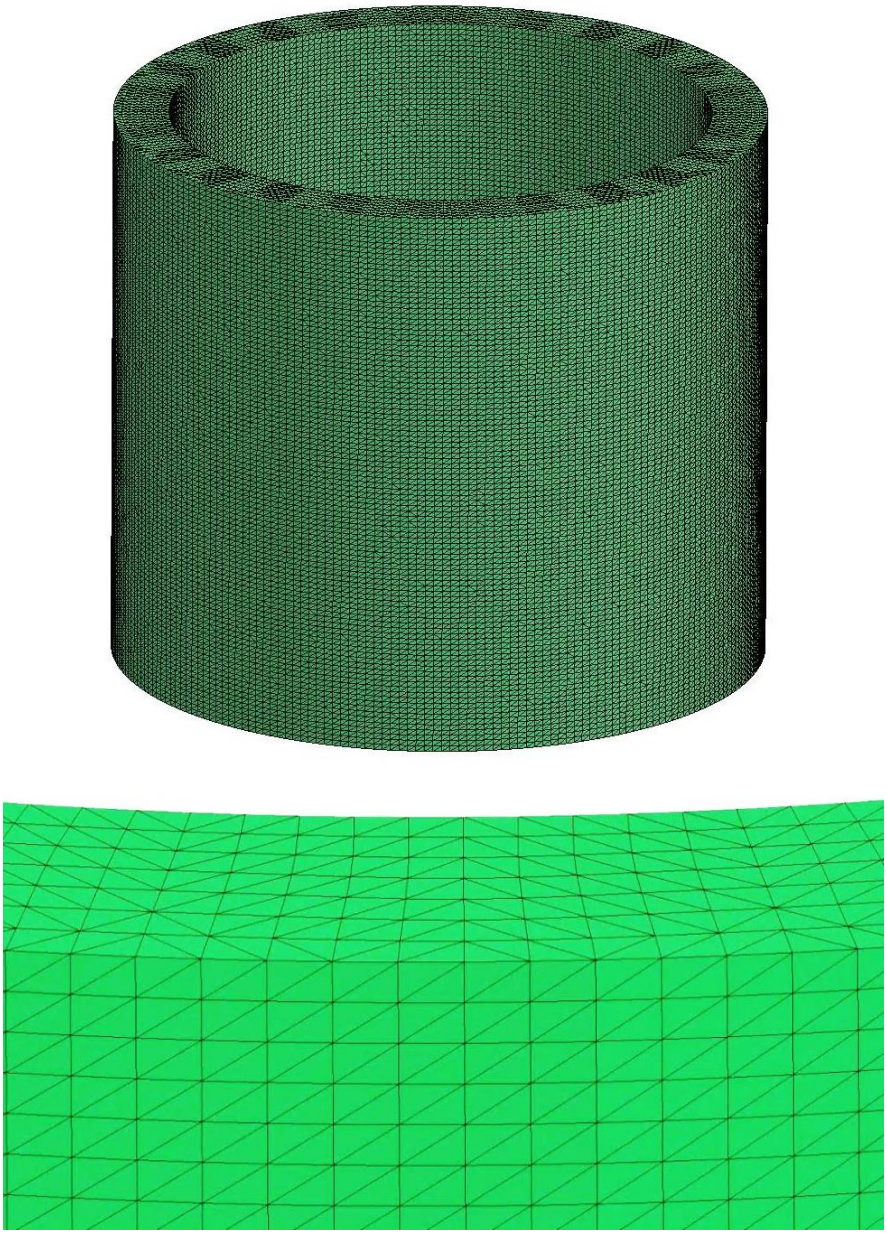

Figure 95. Tetrahedral Mesh, Test No. EPDM-3 Simulation

The Ogden and Simplified models were too stiff. The Blatz-Ko model was too soft. The shear modulus in the Blatz-Ko material formulation was increased to 450 psi (3.1 MPa) until the forces and deflections matched those in test no. EPDM-3. The deflection of the Blatz-Ko

cylinder model is shown in Figure 96. The force vs. deflection and energy vs. deflection curves of the Blatz-Ko model and test no. EPDM-3 are shown in Figure 97. The maximum deformation was 6.8 in. (172 mm). Several coefficients of friction were explored and 0.8 provided the most accurate deformation. However, this allowed the ends of the cylinder to fold in after 5.3 in. (135 mm) of deflection.

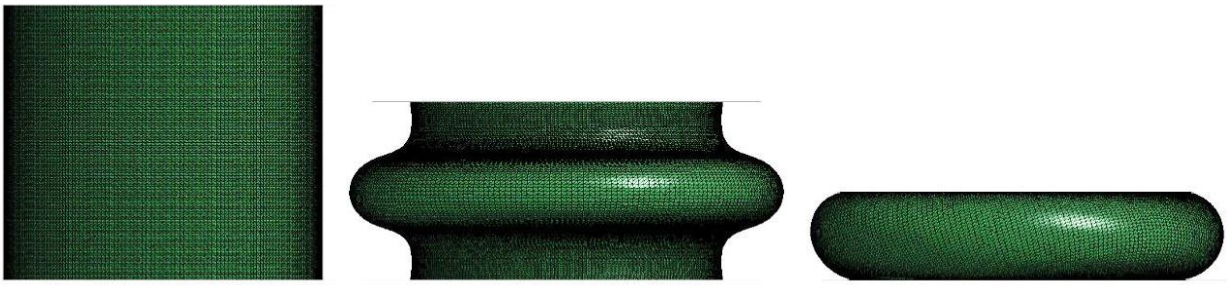

Figure 96. Blatz-Ko Cylinder Deformation, Test No. EPDM-3 Simulation

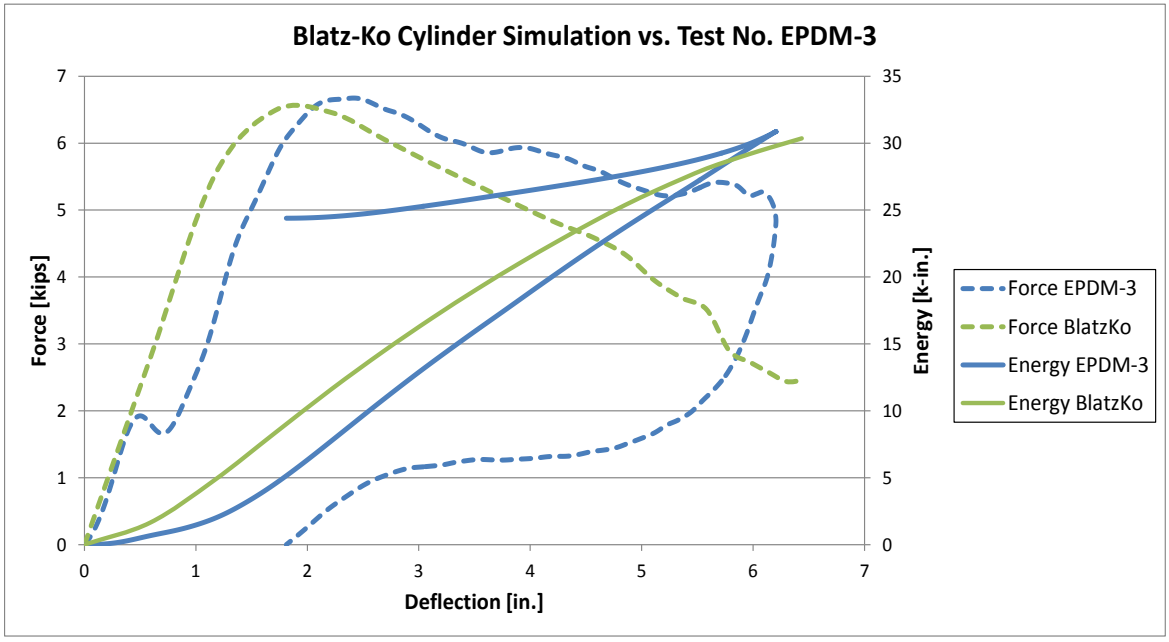

Figure 97. Blatz-Ko Force vs. Deflection, Test No. EPDM-3 Simulation

The Simplified model was accurate when the force vs. deflection input curve was reduced by 40 percent and friction on the rigidwalls was 0.5. The deformation was very similar to the

Blatz-Ko model deformation, and the ends of the cylinder folded in after 5.3 in. (135 mm) of deflection. The force vs. deflection curves for the Simplified model and test no. EPDM-3 are shown in Figure 98. The maximum deformation was 6.3 in. (159 mm).

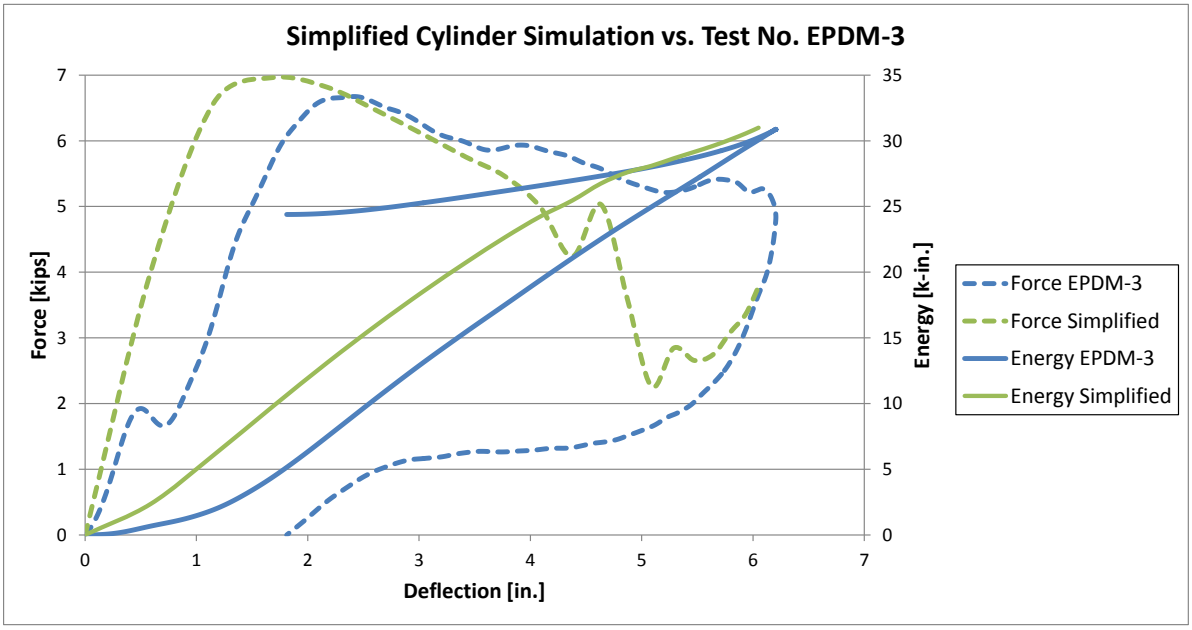

Figure 98. Simplified Force vs. Deflection, Test No. EPDM-3 Simulation

The Blatz-Ko Rubber and Simplified Rubber/Foam material models with tetrahedral solid elements were both accurate at simulating the 80-durometer EPDM cylinders in compression. However, modeling elastomers was not as straightforward as just inputting the shear modulus and/or tensile force vs. deflection parameters. These factors had to be modified to accurately model the component test.

6.3 Shear Fender Energy Absorber

6.3.1 Component Tests

The energy absorbers considered thus far deformed in compression. Maritime International, Inc. from Broussard, LA donated two HSF14 shear fenders so that the dynamic shear properties could be evaluated. The dimensions of each shear fender were 16 in. (406 mm) high x 14 in. (356 mm) wide x 22 in. (559 mm) long. The top and bottom flanges contained ½-in.

(13-mm) thick steel plates. The rubber is 50 to 55 durometer ASTM D2000 5AA425 A_{13} B_{13} C_{20} F_{17} K_{11} L_{14}.

A total of 5 bogie tests were conducted on HSF14 shear fenders provided by Maritime International, Inc. One bogie test was conducted with the shear fender loaded laterally, which is perpendicular to the length of hole. Four bogie tests were conducted with the shear fender loaded longitudinally, which is parallel to the length of the hole. The target impact conditions were at speeds of 5 mph (8 km/h), 5 mph (8 km/h), 10 mph (16 km/h), 15 mph (24 km/h), and 10 mph (16 km/h), respectively for test nos. HSF14-1 through HSF14-5. For test nos. HSF14-1 through HSF14-4, a 1,818 lb (825 kg) bogie was used. For test no. HSF14-5, a 4,946 lb (2,243 kg) bogie was used. The test setup for the bogie tests is shown in Figure 99.

Figure 99. Shear Fender Bogie Test Setup

The information desired from the bogie tests was the relation between the applied force and deflection of the energy absorber. This data was then used to find total energy (the area

under the force versus deflection curve) dissipated during each test. All of the shear fenders returned to their original shape and had no permanent set upon unloading, except after test no. HSF14-5. During test no. HSF14-4, the bogie vehicle became airborne and landed on top of the shear fender. The bogie remained on top of the shear fender for several minutes, which ½-in. (13-mm) vertical deformation that eventually restored. The results of the bogie tests are shown in Table 8. Summary sheets for each of the tests are shown in Appendix C. A complete description of the bogie tests can be found in Schmidt, et. al [97].

Table 8. Shear Fender Dynamic Testing Results

Test No.	Bogie Weight (lb)	Impact Direction	Dimensions (in.)	Surface Temp (°F)	Impact Velocity (mph)	Max Deflection (in.)	Peak Force (k)	Total Energy (k-in.)
HSF14-1	1818	Lateral	16 H x 14 W x 22 L	84	4.9	6.2	12.1	17.8
HSF14-2	1818	Longitudinal	16 H x 14 W x 22 L	73	5.0	5.3	13.0	18.2
HSF14-3	1818	Longitudinal	16 H x 14 W x 22 L	66	9.1	10.5	26.5	60.5
HSF14-4	1818	Longitudinal	16 H x 14 W x 22 L	75	14.3	37.3	42.9	149.7
HSF14-5	4946	Longitudinal	16 H x 14 W x 22 L	138	11.9	28.5	41.2	268.4

Force vs. deflection and energy vs. deflection were compared for test nos. HSF14-1 and HSF14-2, as shown in Figures 100 and 101, respectively. The tests were conducted at the same speed but had different impact orientations. The shear fender absorbed the same total energy in both orientations, but in the longitudinal direction, the deflection was 2 in. (51 mm) less than in the lateral direction.

Force vs. deflection and energy vs. deflection were compared for test nos. HSF14-2 through HSF14-5, as shown in Figures 102 and 103, respectively. These tests were all conducted at the same orientation with varying speeds. During test no. HSF14-4, the impact plate on top of the shear fender rotated upward and snagged on the top of the bogie impact head, thus resulting in a zero longitudinal force for a few inches of deflection. The bottom of the bogie impact head then contacted the shear fender rubber after traveling for 28 in. (711 mm).

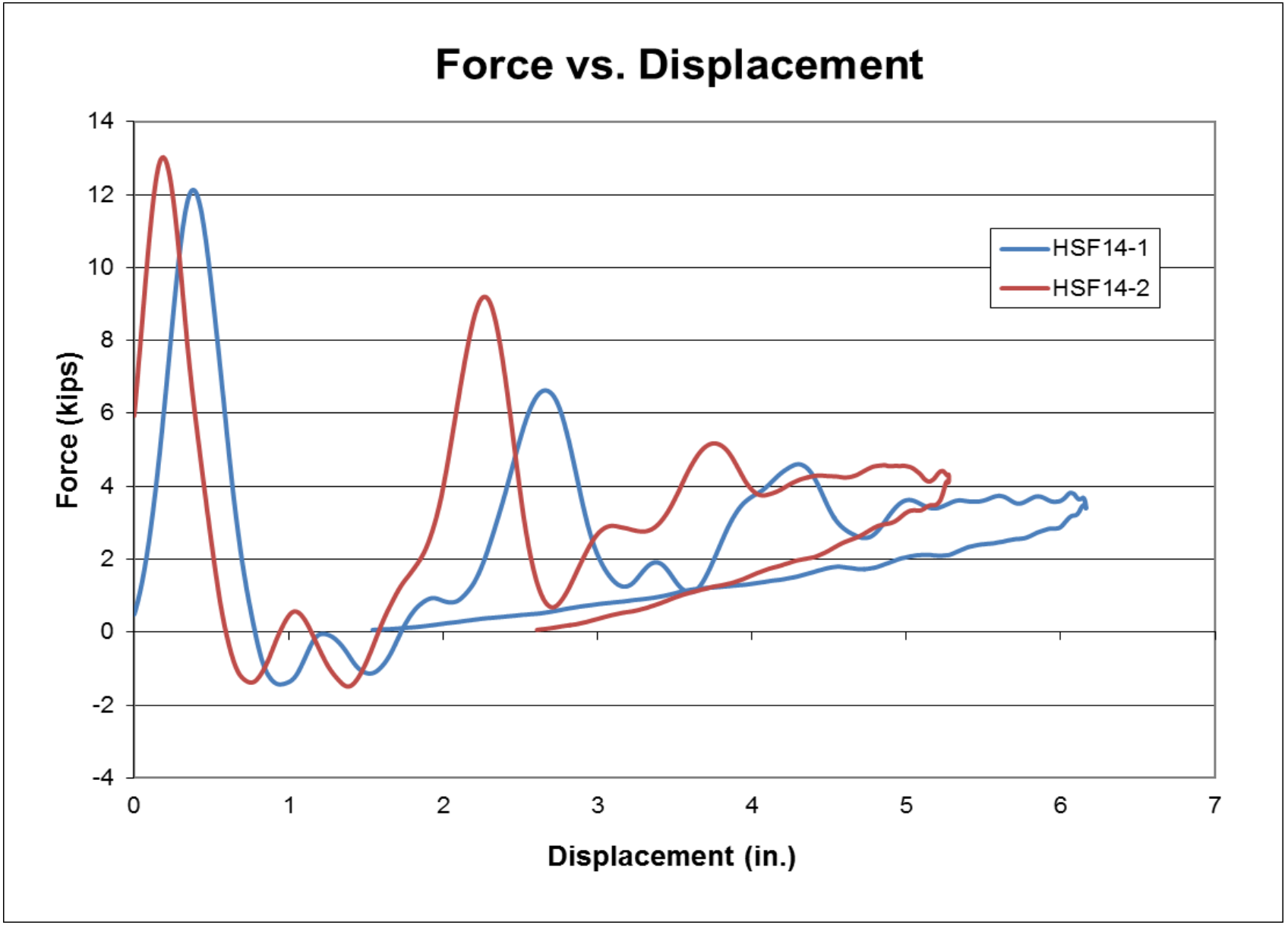

Figure 100. Force vs. Deflection Comparison Plot, Test nos. HSF14-1 and HSF14-2

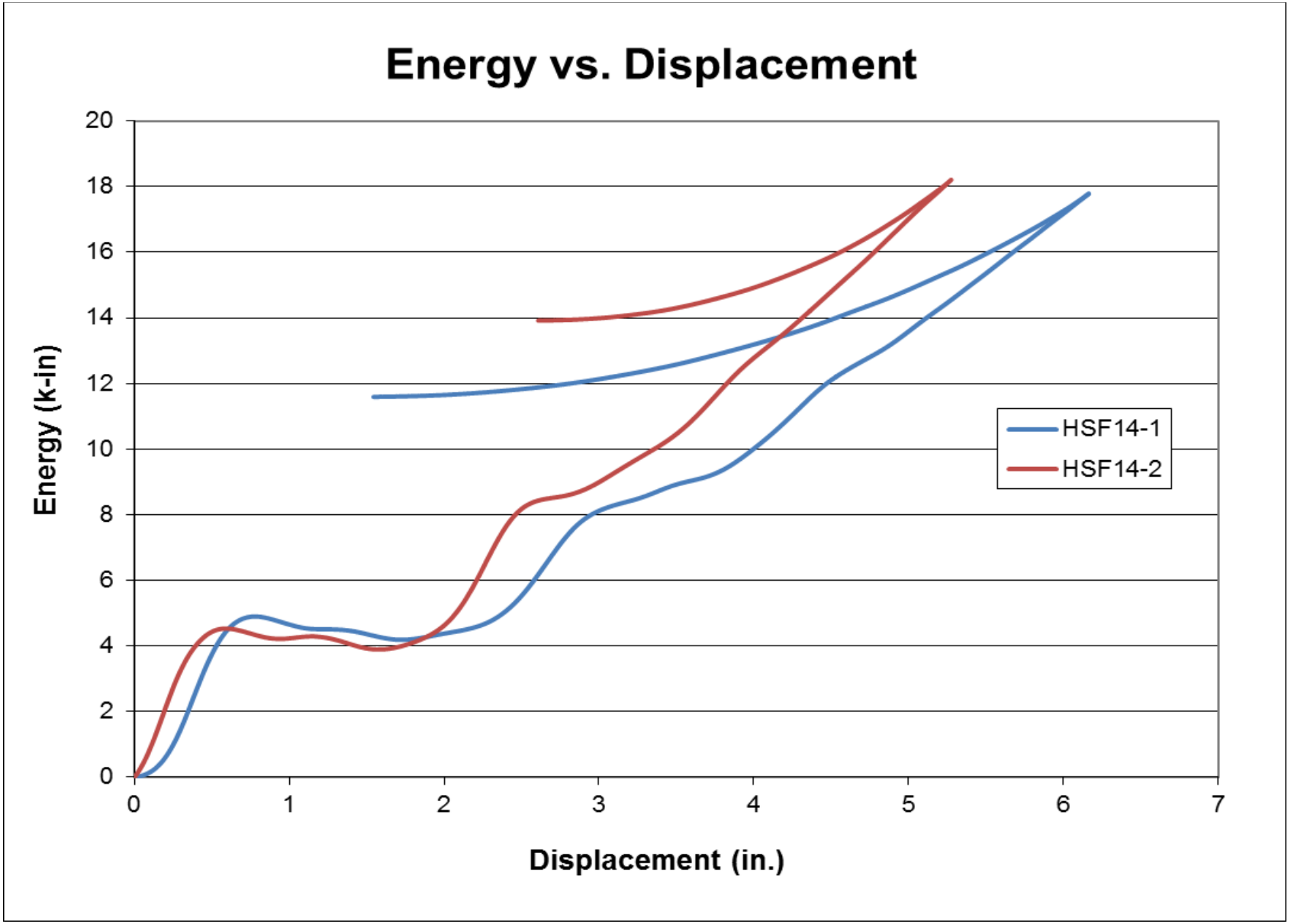

Figure 101. Energy vs. Deflection Comparison Plot, Test Nos. HSF14-1 and HSF14-2

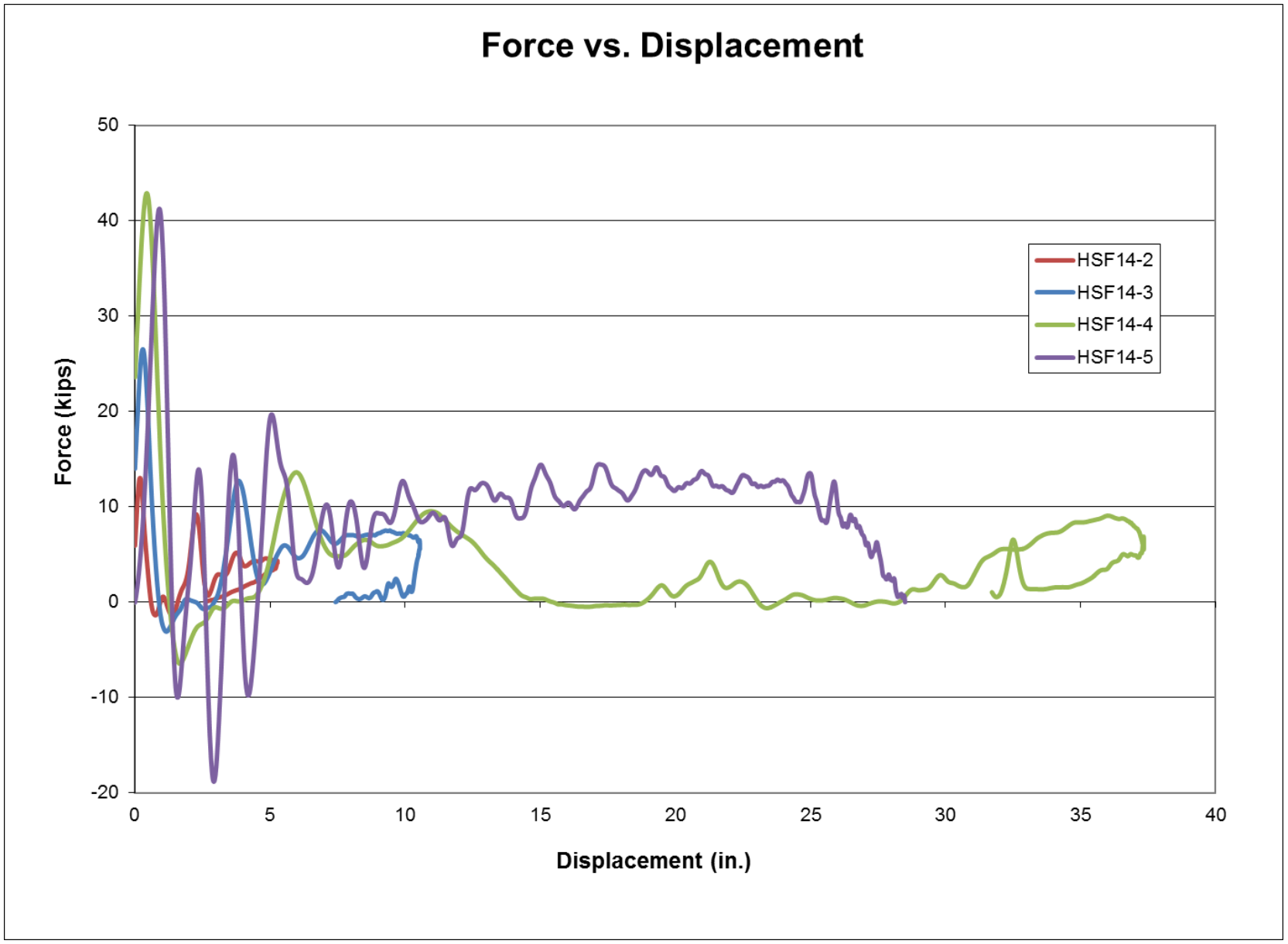

Figure 102. Force vs. Deflection Comparison Plot, Test nos. HSF14-2 through HSF14-5

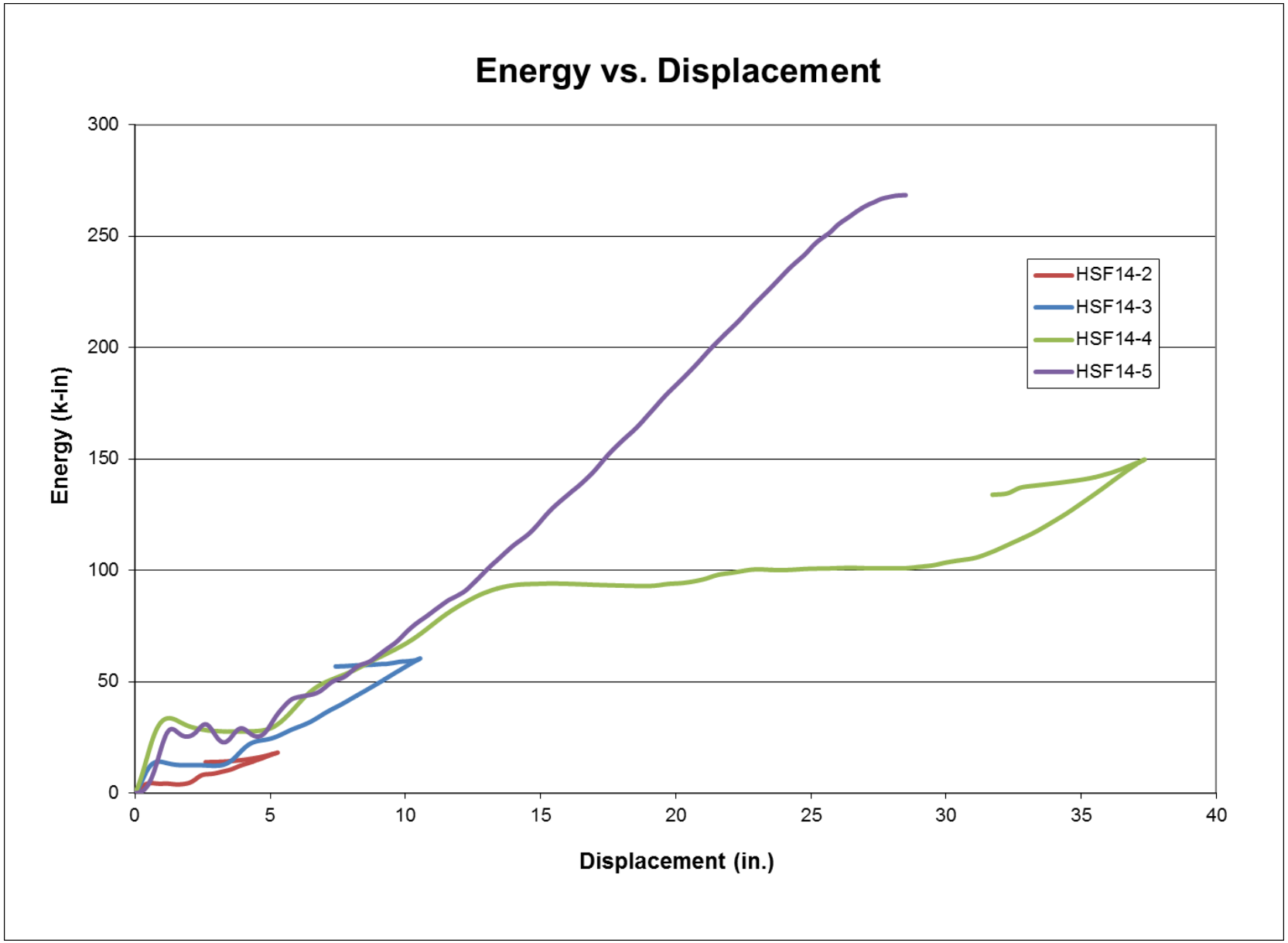

Figure 103. Energy vs. Deflection Comparison Plot, Test nos. HSF14-2 through HSF14-5

6.3.2 Component Test Simulation

Simulations of test no. HSF14-4 were used to validate the shear fender rubber material model. An existing bogie model was adjusted so that the mass was 1,818 lb (825 kg). The bogie and shear fender simulation is shown in Figure 104. The wood bogie impact head was modeled with a *MAT_PIECEWISE_LINEAR_PLASTICITY material with a mass density of 39.1 lb/ft^3 (6.2740E-7 kg/mm^3) and a modulus of elasticity of 1,595 ksi (11 GPa). The impact structure attached to the top of the shear fender was rigid steel material. The bolts were rigid steel, and the bottom anchorage bolts were fixed to the ground. The rubber was meshed with 1 point nodal pressure tetrahedron solid elements. An automatic single surface contact was the main contact between the bogie impact head and the parts of the shear fender and impact structure. The automatic nodes to surface contact was used between the bogie impact head and the shear fender rubber. The tied nodes to surface contact was used between the ½-in. (13-mm) steel plates and the shear fender rubber. The two parameters that needed to be adjusted were the material model properties and the friction between the wood impact head and the steel impact structure.

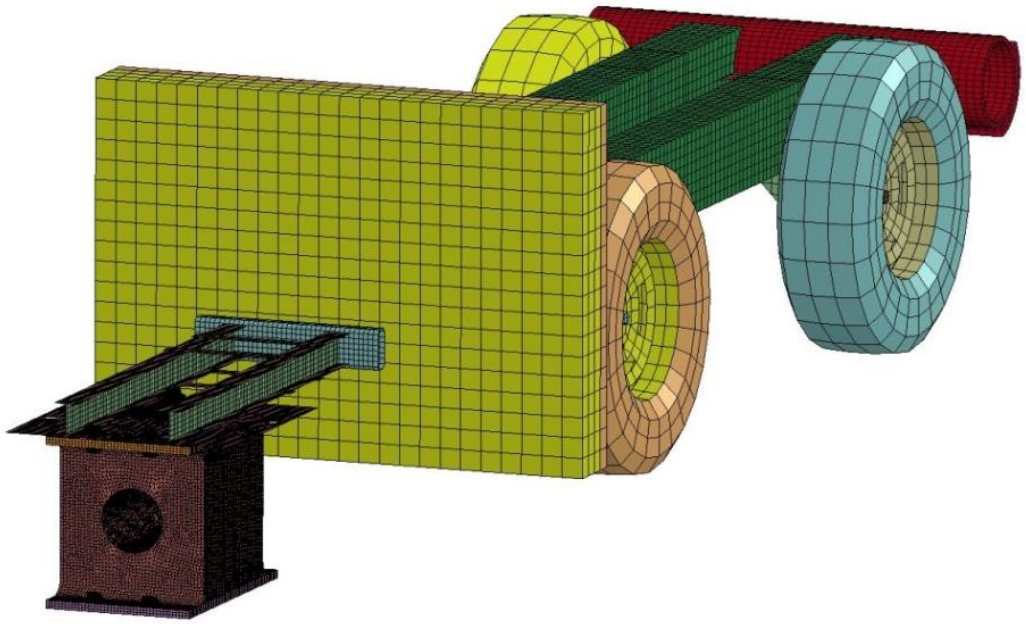

Figure 104. Shear Fender Simulation

Friction between two parts can be defined in many ways: within a contact definition between parts, *DEFINE_FRICTION, and *PART_CONTACT. Various coefficients of friction were applied to the main automatic single surface contact that was between most of the parts. This effort resulted in accurate sliding on the bogie impact head, but it also created friction between all the other parts in the contact, which resulted in significant sliding energy. A separate contact was defined between the bogie impact head and the steel impact structure with various coefficients of friction. However, the impact head appeared to have little or no friction between the parts, even with a high coefficient of friction. *DEFINE_FRICTION between the two parts also appeared to have little or no friction between the parts. Using *PART_CONTACT to assign a static coefficient of friction of 0.5 and a dynamic coefficient of friction of 0.15 to the steel impact structure, the contact and friction between the bogie impact head and the impact structure appeared the most accurate.

The accelerations in the simulation were calculated at the center of gravity of the bogie; since, the accelerations in test no. HSF14-4 were also measured at the center of gravity of the bogie. The simulation accelerations were filtered with the same methodology and customized spreadsheets that were used to filter test no. HSF14-4 test data. The Ogden model with tensile test data had forces higher than those in test no. HSF14-4. The Ogden model with the shear data quit running after 110 ms due to an element in the rubber with a negative volume. The Ogden model with equal biaxial data produced forces identical to the Ogden model with tensile data. The deformation of the Ogden models appeared to be too elastic.

The deformation of the Simplified model appeared to be accurate when compared to test no. HSF14-4, as shown in Figure 105. The Simplified material model was the most accurate when comparing forces and deflections to test no. HSF14-4, as shown in Figure 106. The energy versus deflection was accurate at the beginning and end of the event but inaccurate in the middle

of the event, as shown in Figure 107. The steel impact structure did not stay in contact with the bogie impact head for as long as in test no. HSF14-4, so less energy was absorbed at the beginning of the event. No force occurred in the simulation from 5 to 10 in. (127 to 254 mm) since the steel impact structure was not in contact with the bogie vehicle as it rotated upward. Increasing the stiffness of the rubber and changing the coefficient of friction between the bogie impact head and the steel impact structure, did not remedy this discrepancy.

The Blatz-Ko material model deformed similar to the Simplified model, as shown in Figure 108. The Blatz-Ko force vs. deflection curve compared to test no. HSF14-4 is shown in Figure 109. The energy vs. deflection was accurate at the beginning and end of the event, as shown in Figure 110. The same as the Simplified model, the steel impact structure did not stay in contact with the bogie impact head for as long as in test no. HSF14-4, so less energy was absorbed through the middle of the event.

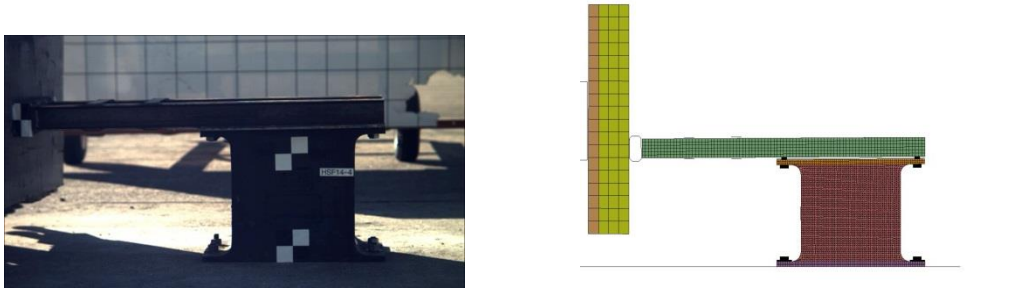
Time = 0 ms

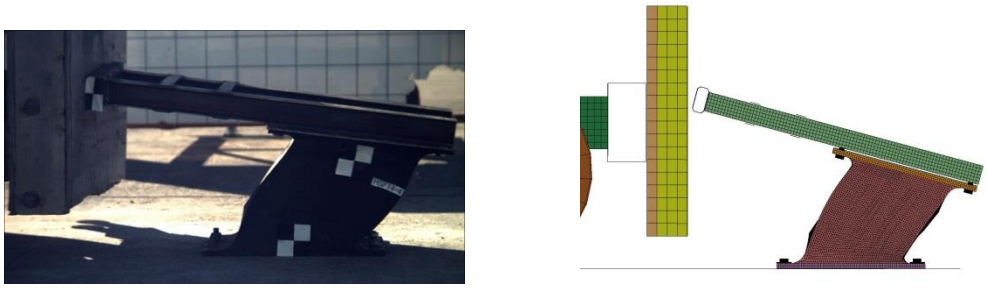
Time = 40 ms


Time = 130 ms

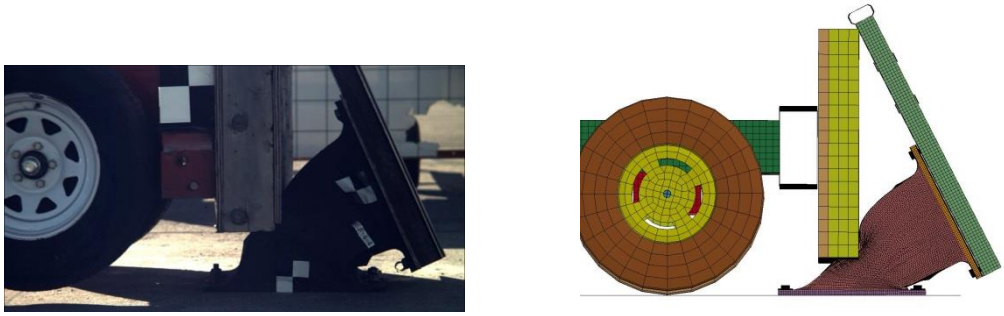
Time = 190 ms

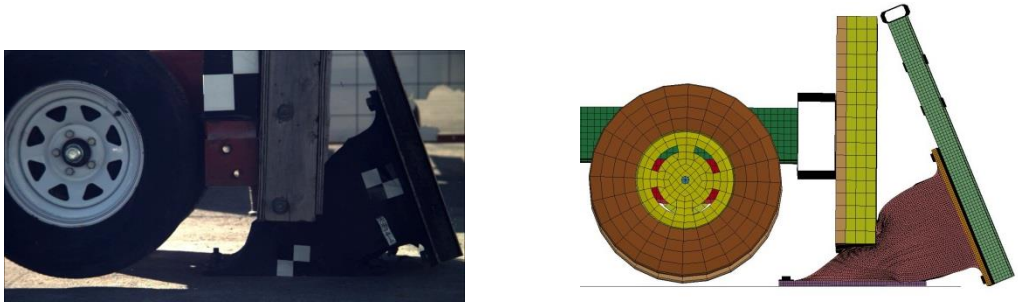
Time = 240 ms

Figure 105. Simplified Shear Fender Simulation Deformation, Test No. HSF14-4

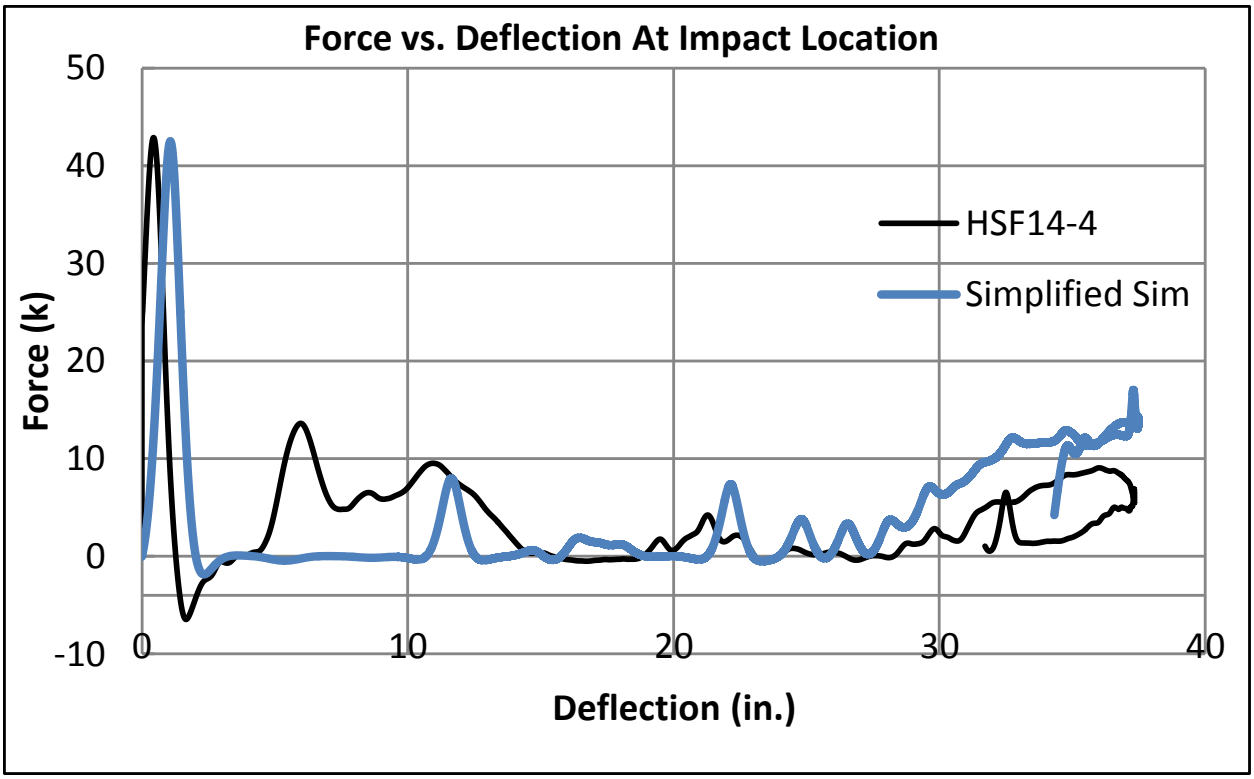

Figure 106. Simplified Force vs. Deflection, Test No. HSF14-4

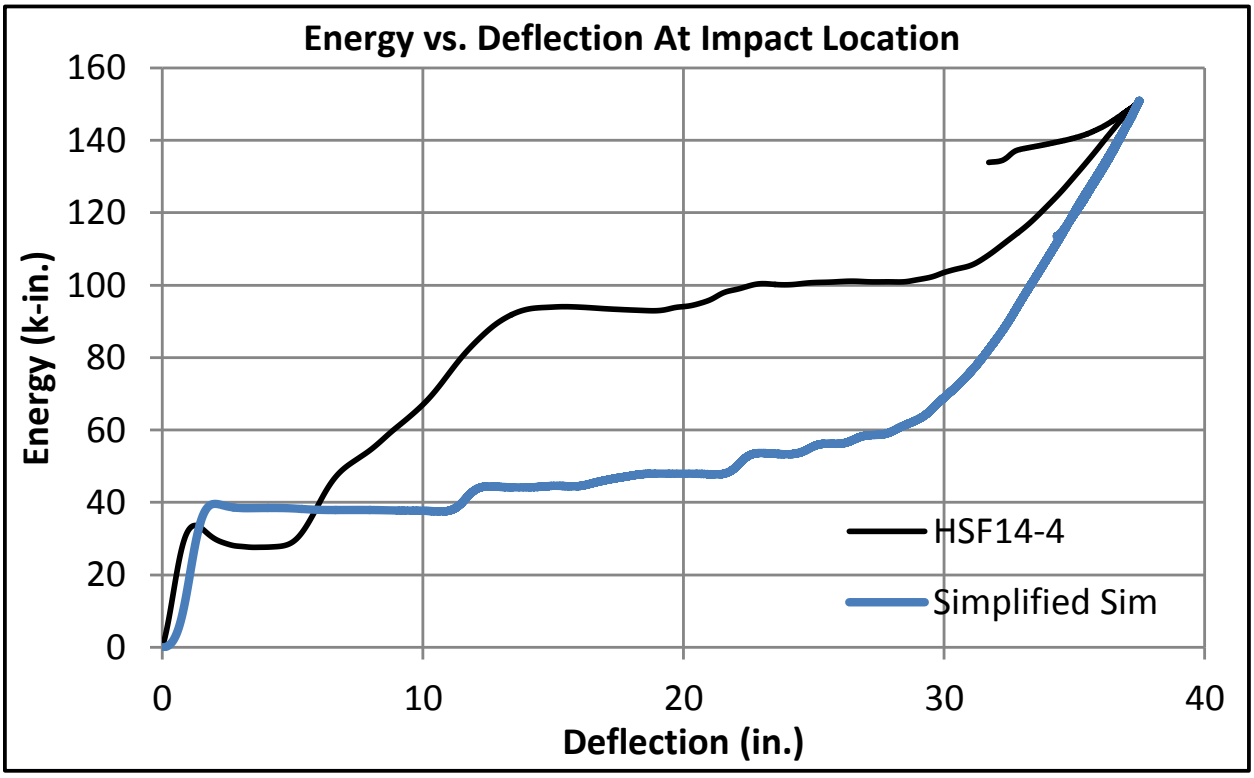

Figure 107. Simplified Energy vs. Deflection, Test No. HSF14-4

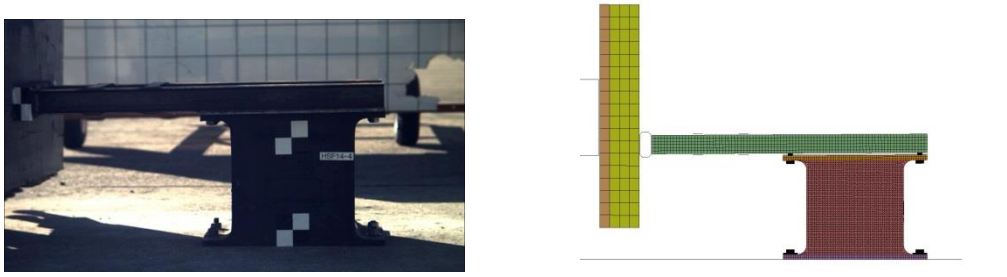
Time = 0 ms

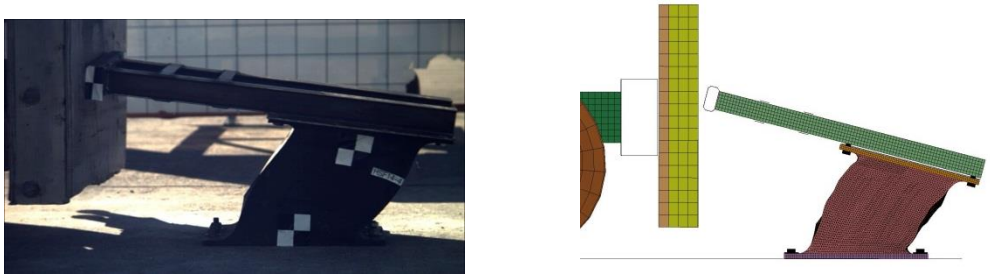
Time = 40 ms


Time = 130 ms

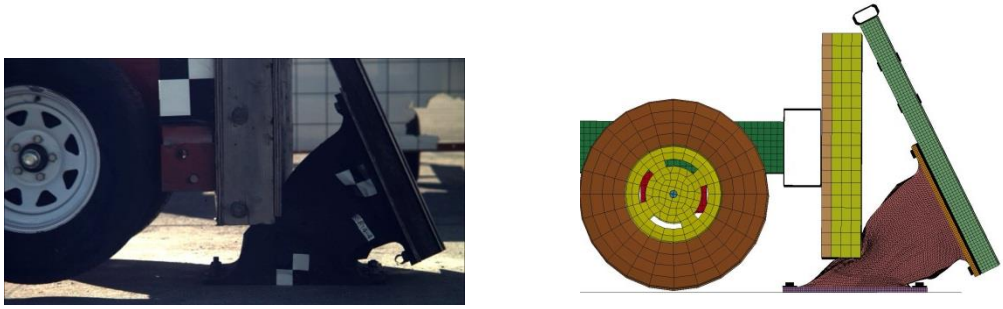
Time = 190 ms

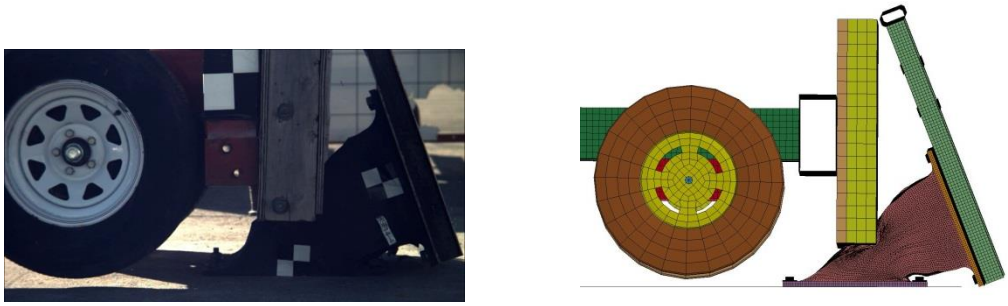
Time = 240 ms

Figure 108. Blatz-Ko Shear Fender Simulation Deformation, Test No. HSF14-4

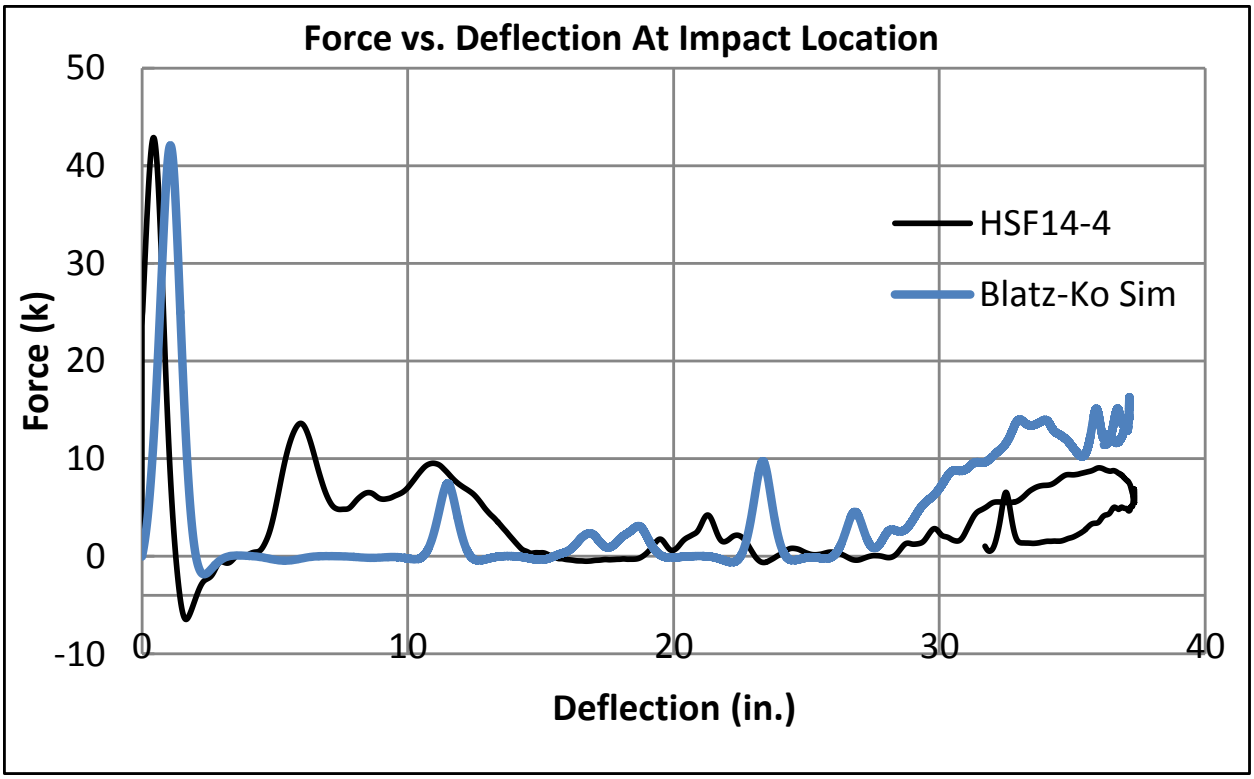

Figure 109. Blatz-Ko Force vs. Deflection, Test No. HSF14-4

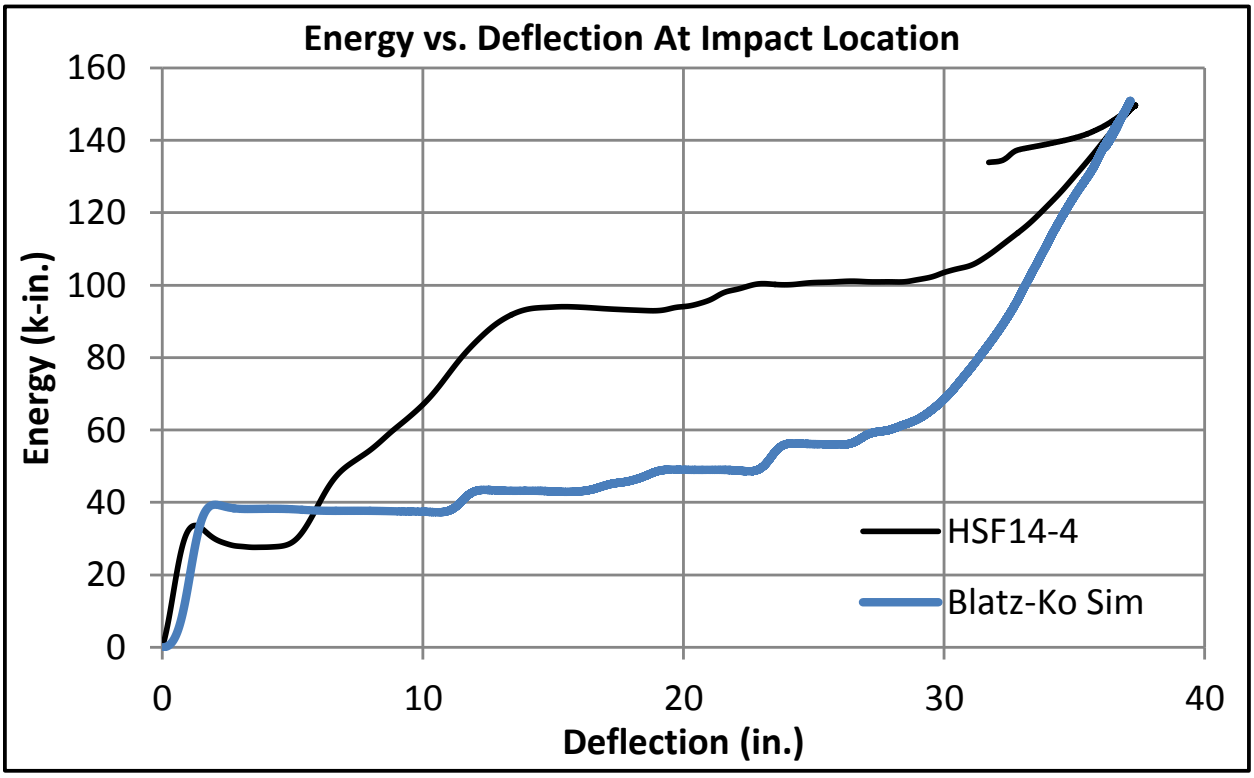

Figure 110. Blatz-Ko Energy vs. Deflection, Test No. HSF14-4

The Simplified rubber model required mass density and a force versus deflection (or stress versus strain) curve to be input. The Blatz-Ko rubber model only required shear modulus and mass density for material inputs. Since the tensile test data was obtained for this project, the Simplified model is recommended as the best fit.

6.4 Conclusions

Accurate elastomeric models in high-speed impact applications can be achieved in LS-DYNA with limited material properties, such as shear modulus and simple tension force vs. deflection curves. Rubber material properties for LS-DYNA finite element analysis software have limited public availability. The LS-DYNA input decks for the best material models found are shown in Appendix D.

One point nodal pressure tetrahedron elements can accurately model the deformation of elastomers under many load cases. Constant stress hexahedral solid elements with hourglassing control type 4 or 5 may also provide fairly accurate results and are less expensive than tetrahedral elements. Constant stress hexahedral solid elements are only accurate for small deformations in elastomers. Elastomer material models that use tension test data as inputs may accurately model tensile loads. However, tension test data needs to be modified to model compression or shear loads. While the Ogden material model allows shear or compression data inputs, the shear model encountered errors, and the compression model produced the same results as the tension data. The tensile test forces may need to be scaled down by 20 to 40 percent to model compression or shear deformation in elastomers.

In test no. HSF14-4, the shear fender demonstrated that it could be loaded in shear and torsion for up to 35 in. laterally and still restore to its original shape upon unloading. After 15 in. (381 mm) of deflection, the average force and the peak force were nearly the same. However, the deflections of this magnitude are not expected in a barrier system. At 10 in. (254 mm) of

deflection, approximately 6 kip-ft (8.1 kJ) of energy was absorbed by a single energy absorber, which lies in the minimum required range of 4.4 to 17.6 kip-ft (6.0 to 23.9 kJ). Therefore, the energy absorbers could be spaced at a minimum of 7 ft (2.1 m) apart based on the previous assumption that energy absorbers will deflect to 60 percent of the maximum deflection over a 40 ft span (12.2 m). However, if the rail is designed to be continuous, energy absorbers over a longer span could be activated, and the spacing between energy absorbers could be increased.

7 VALIDATION OF VEHICLE MODELS

Baseline simulations were needed to compare the performance of the new barrier with that obtained for a rigid, concrete barrier. Several vehicle models were used, including the 1100C Dodge Neon model developed by the National Crash Analysis Center (NCAC) [98] and modified by MwRSF, the 2270P Chevrolet Silverado model developed by NCAC [99-100] and modified by MwRSF, and the 10000S single-unit truck model originally developed by NCAC and modified by TTI. The 10000S simulation matched vehicle roll and pitch characteristics of the single-unit truck test no. RF476260-1 [21,101]. The static and dynamic coefficients of friction between the vehicles' bodies and the barrier as well as the tires and the barrier were adjusted to produce similar results to those observed for the full-scale crash tests into rigid barriers. Since the vehicle models have been used in previous simulations, a full verification and validation effort was not conducted.

7.1 1100C Dodge Neon

In MwRSF test no. 2214NJ-1 [16], an 1100C Kia Rio sedan impacted a 32-in. (813-mm) tall New Jersey barrier at a speed of 60.8 mph (27.2 m/s) and an angle of 26.1 degrees. The 1100C Dodge Neon model impacted a 32-in. (813-mm) tall New Jersey barrier in a LS-DYNA simulation at a speed of 62 mph (27.8 m/s) and at an angle of 25 degrees. A static and dynamic coefficient of friction of 0.10 was applied between the Neon body and the barrier through *CONTACT_AUTOMATIC_SINGLE_SURFACE. A static and dynamic coefficient of friction of 0.30 was applied between the Neon tires and the barrier through *CONTACT_AUTOMATIC_SURFACE_TO_SURFACE.

Accelerations, velocities, and displacements were found at the center of gravity of the 1100C model at every 0.01 ms and filtered using a customized Excel spreadsheet that is used for filtering full-scale crash test data. A comparison of the occupant risk data is shown in Table 9.

Comparisons of the SAE CFC180 lateral and longitudinal change in velocity are shown in Figures 111 and 112.

The vehicle kinematics at various points in time for test no. 2214NJ-1 and the simulated test are shown in Figure 113. The simulated vehicle's yaw and roll motions are slightly different than those observed in test no. 2214NJ-1 as it exited the barrier.

Table 9. 1100C Comparison of Occupant Risk Data

	Test No. 2214NJ-1	1100C Baseline Simulation
Lateral OIV ft/s (m/s)	35.1 (10.7)	33.1 (10.1)
Longitudinal OIV ft/s (m/s)	16.1 (4.9)	20.7 (6.3)
Lateral ORD g's	8.1	8.2
Longitudinal ORD g's	5.4	4.2

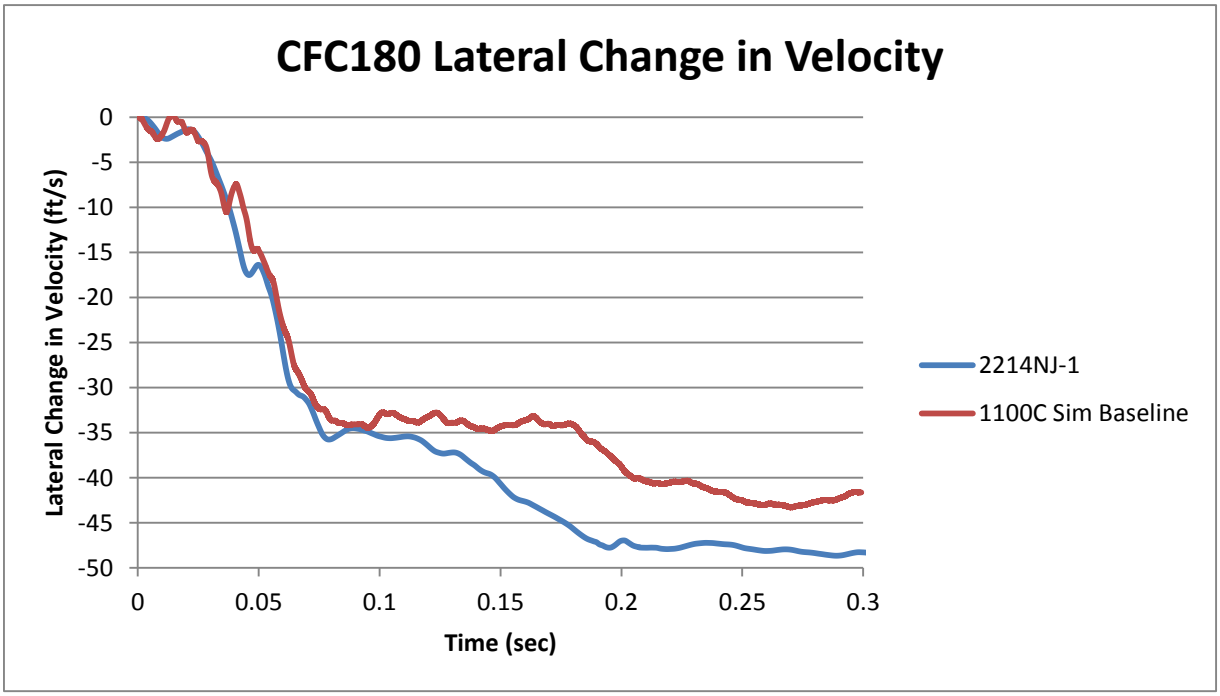

Figure 111. Comparison of 1100C Actual and Simulated Lateral Change in Velocity

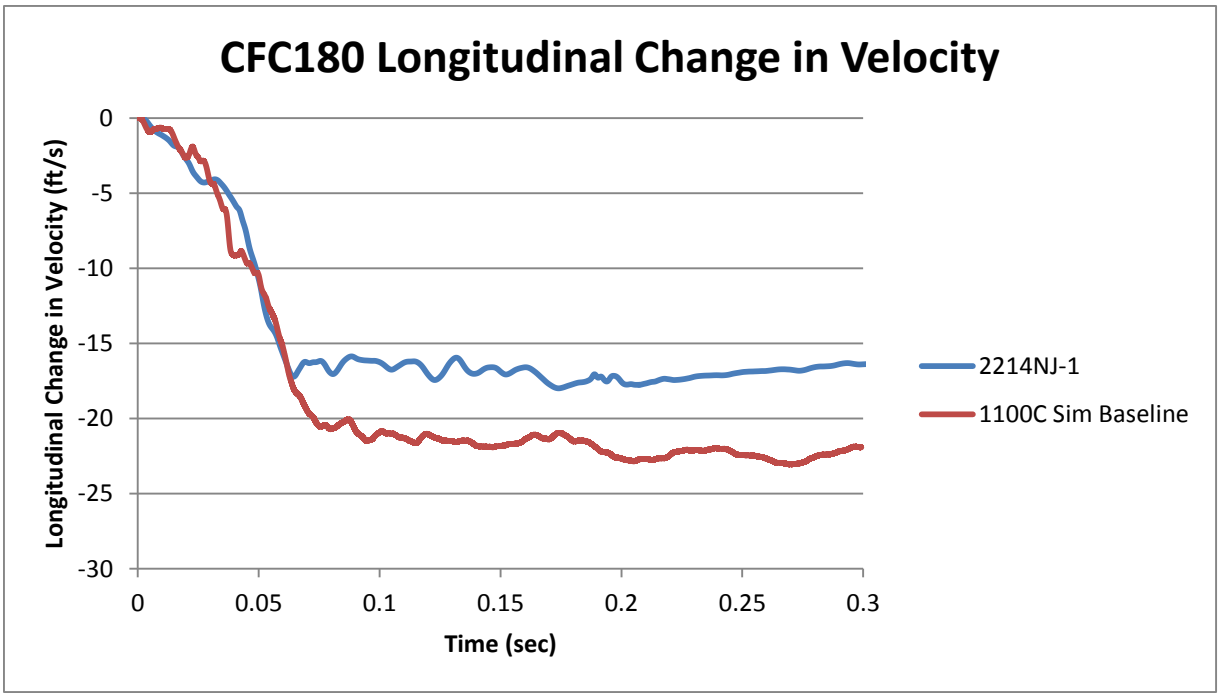

Figure 112. Comparison of 1100C Actual and Simulated Longitudinal Change in Velocity

7.2 2270P Silverado Truck

In TTI test no. 420020-3 [17], a 2270P Dodge Ram 1500 Quad Cab pickup truck impacted a 36-in. (914-mm) tall single-slope barrier at a speed of 63.8 mph (28.5 m/s) and an angle of 24.8 degrees. The 2270P Chevrolet Silverado pickup truck model impacted a 36-in. (914-mm) tall single-slope barrier at a speed of 62 mph (27.8 m/s) and an angle of 25 degrees in a LS-DYNA simulation. A static and dynamic coefficient of friction of 0.25 was applied between the pickup body and the barrier through *CONTACT_AUTOMATIC_SURFACE_TO_SURFACE. A static and dynamic coefficient of friction of 0.15 was applied between the pickup tires and the barrier through *CONTACT_AUTOMATIC_SURFACE_TO_SURFACE. Increasing the body and barrier contact friction value any higher than 0.25 resulted in nodes with out-of-range velocities. The vehicle kinematics at various points in time for test no. 420020-3 and the simulated test are shown in Figure 114.

0.000 sec

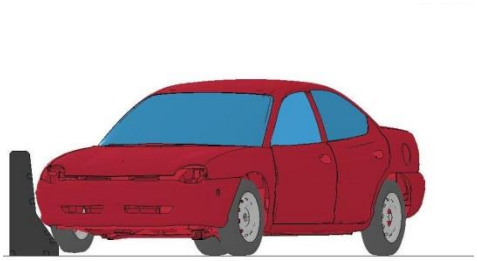

0.000 sec

0.060 sec

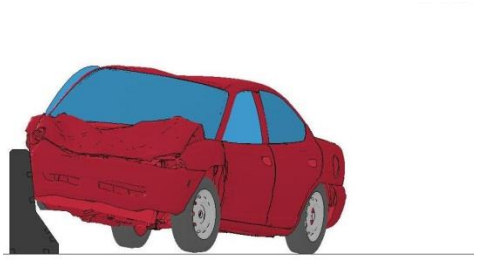

0.060 sec

0.138 sec

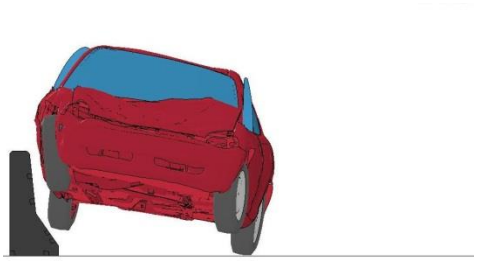

0.140 sec

0.266 sec

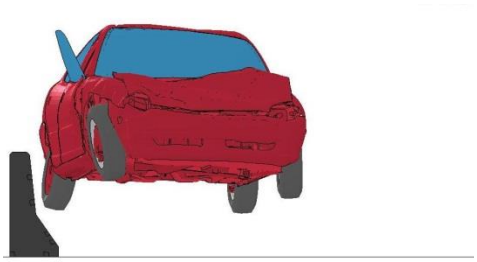

0.270 sec

Figure 113. Comparison between MwRSF Test No. 2214NJ-1 and Simulation

0.322 sec

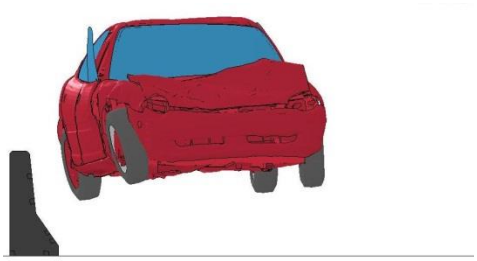

0.320 sec

0.452 sec

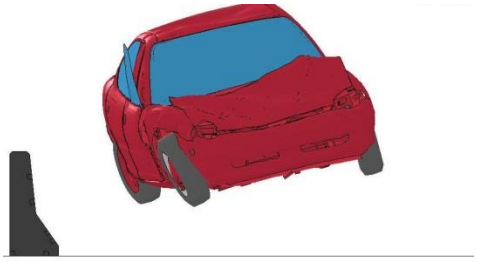

0.450 sec

0.608 sec

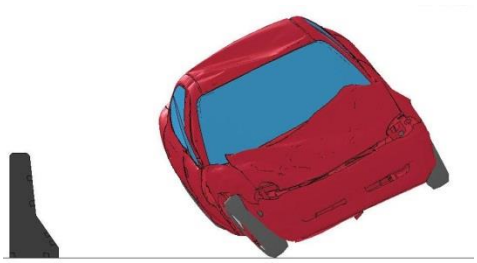

0.610 sec

0.728 sec

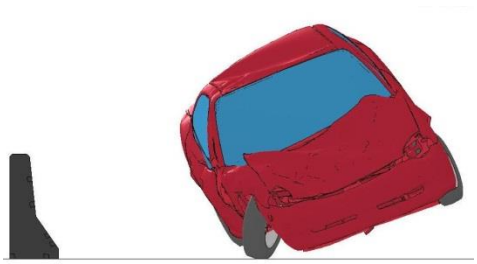

0.660 sec

Figure 113. Comparison between MwRSF Test No. 2214NJ-1 and Simulation (cont.)

The vehicle trajectory and roll, pitch, and yaw motions match closely between the actual test and the simulation. However, in test no. 420020-3, the right-rear tire disengaged, and this failure was not enabled to happen in the simulation, so the pitch of the truck differed slightly toward the end of the simulation. Since the vehicle's trajectory after leaving the barrier was not a concern for the validation of the vehicle model, simulations of the rear tire disengaging were not conducted. The right-front tire disengaged in both the crash test and simulation.

Accelerations, velocities, and displacements were found at the center of gravity of the 2270P model at every 0.01 ms and filtered using a customized Excel spreadsheet that is used for filtering full-scale crash test data. Comparisons of the SAE CFC180 lateral and longitudinal change in velocity are shown in Figures 115 and 116. The change in velocity was found at the c.g of the pickup truck model in local coordinates, but the lateral and longitudinal change in velocity both started increasing 60 ms after impact, which is not consistent with the results of the full-scale crash test. This discrepancy was explored and believed to be attributed to the default integration option (INTOPT) of nodal output accelerations in LS-DYNA. The default INTOPT integrates velocities from global accelerations and transforms them into the local coordinate system of the accelerometer. However, INTOPT = 1 integrates velocities directly from the local accelerations of the accelerometer, which is also how velocities are calculated in full-scale crash tests. A comparison of the lateral and longitudinal changes in velocity for the actual and simulated crash test is shown in Figures 117 and 118, respectively. The velocity curves were more consistent with full-scale crash test velocities, so INTOPT=1 was used for the simulations with the 2270P model. However, the lateral and longitudinal changes were not as high in the simulation as they were in the full-scale crash test. A comparison of the occupant risk data is shown in Table 10. The OIV values were also lower in the simulation than the full-scale crash test. The peak lateral and longitudinal accelerations that occurred in test no. 420020-3 were some

of the highest values found compared to other NCHRP Report No. 350 and MASH pickup truck crash tests. With modifying the Silverado components, these high accelerations could not be achieved. Therefore, the discrepancies between the baseline simulation and the full-scale crash test were considered in later comparisons between simulations.

Table 10. 2270P Comparison of Occupant Risk Data

	Test No. 420020-3	2270P Baseline Simulation
Lateral OIV ft/s (m/s)	29.9 (9.1)	25.6 (7.8)
Longitudinal OIV ft/s (m/s)	22.0 (6.7)	14.8 (4.5)
Lateral ORD g's	11.7	20.8
Longitudinal ORD g's	5.3	6.3

0.000 sec

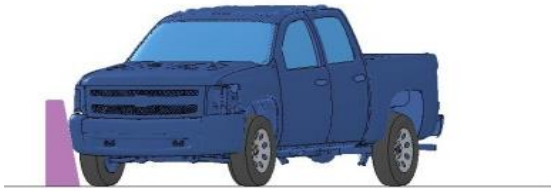

0.000 sec

0.089 sec

0.090 sec

0.175 sec

0.170 sec

0.263 sec

0.260 sec

Figure 114. Comparison between TTI Test No. 420020-3 and Simulation

0.352 sec

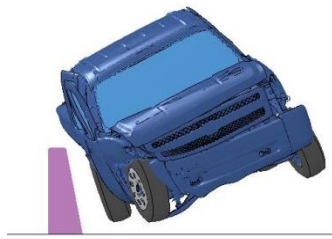

0.350 sec

0.440 sec

0.440 sec

0.526 sec

0.530 sec

0.615 sec

0.580 sec

Figure 114. Comparison between TTI Test No. 420020-3 and Simulation (cont.)

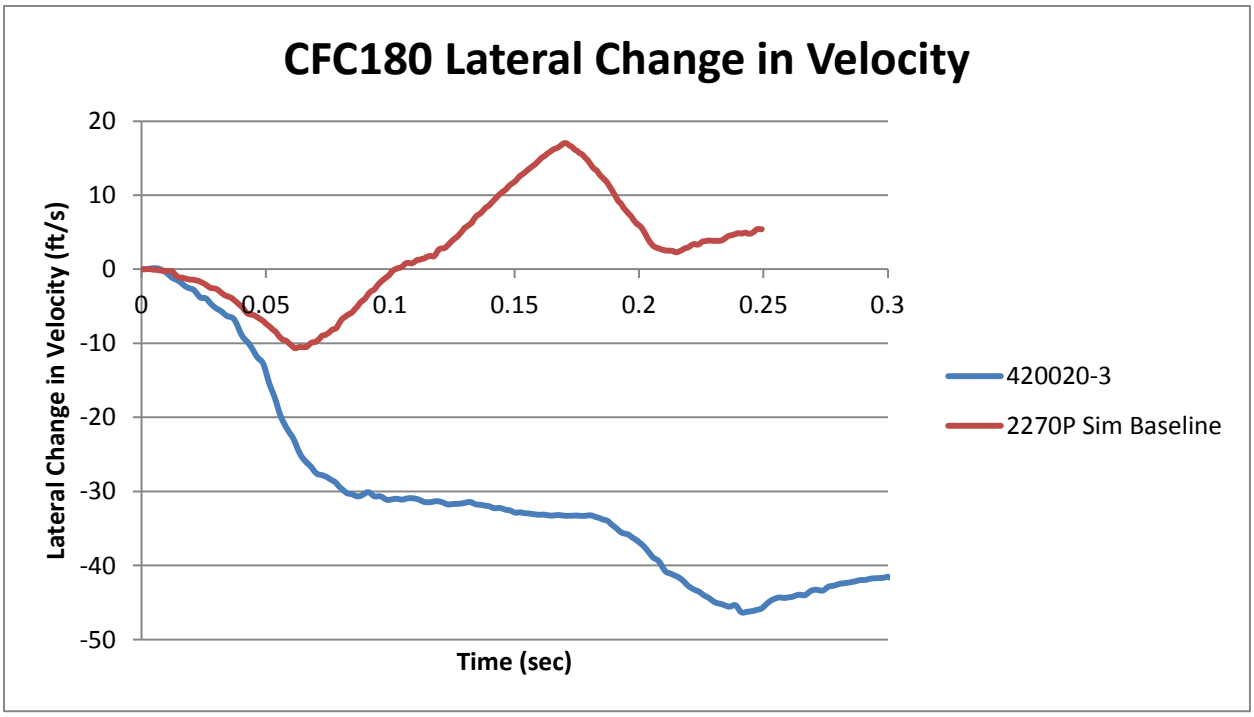

Figure 115. Comparison of 2270P Actual and Simulated Lateral Change in Velocity – INTOPT=0

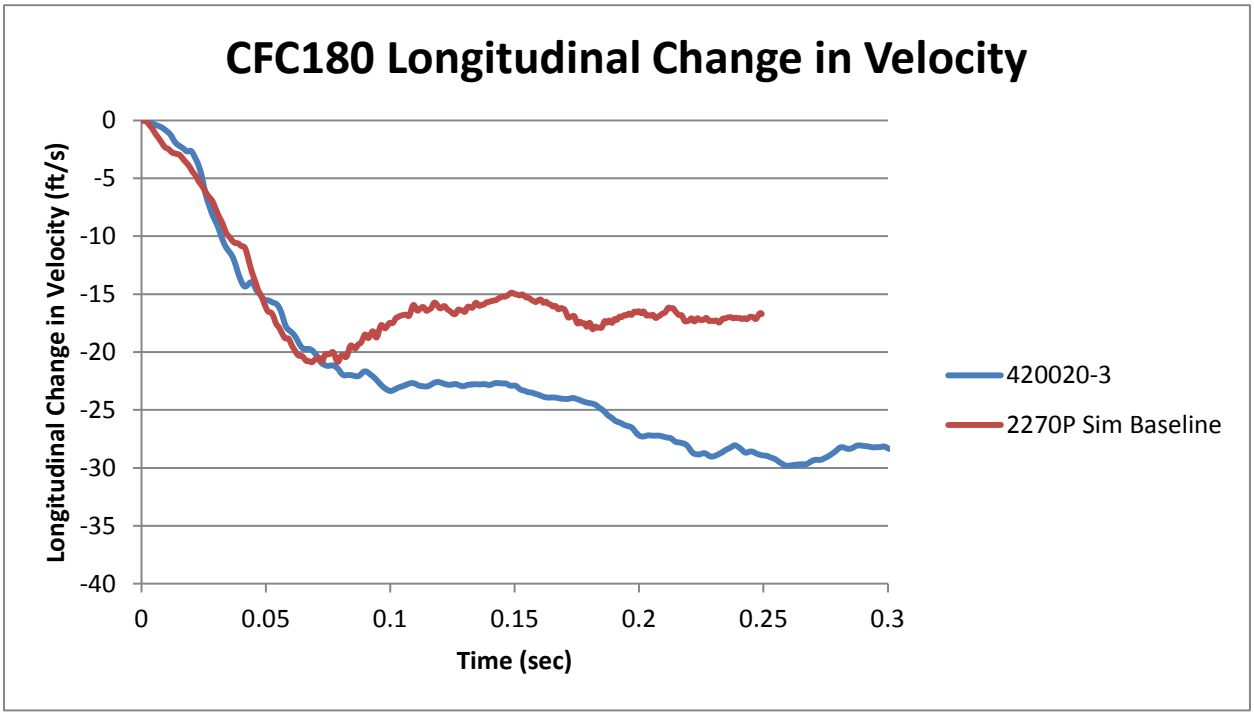

Figure 116. Comparison of 2270P Actual and Simulated Longitudinal Change in Velocity – INTOPT=0

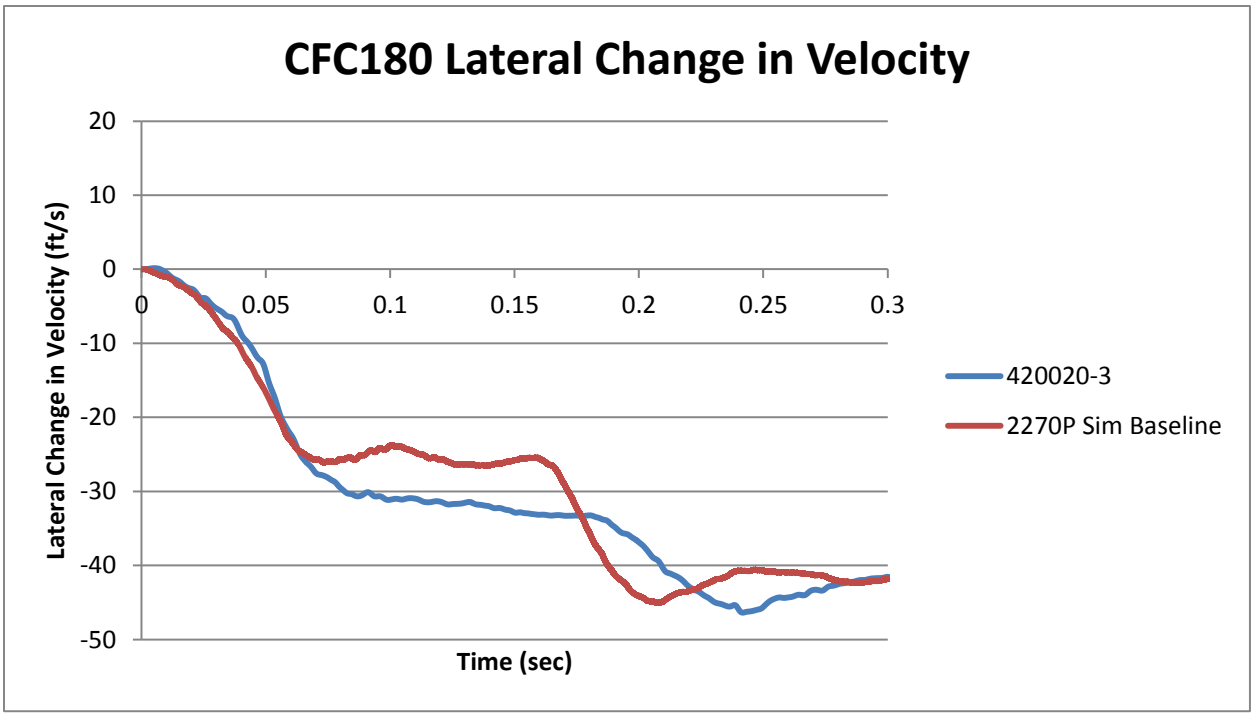

Figure 117. Comparison of 2270P Actual and Simulated Lateral Change in Velocity – INTOPT=1

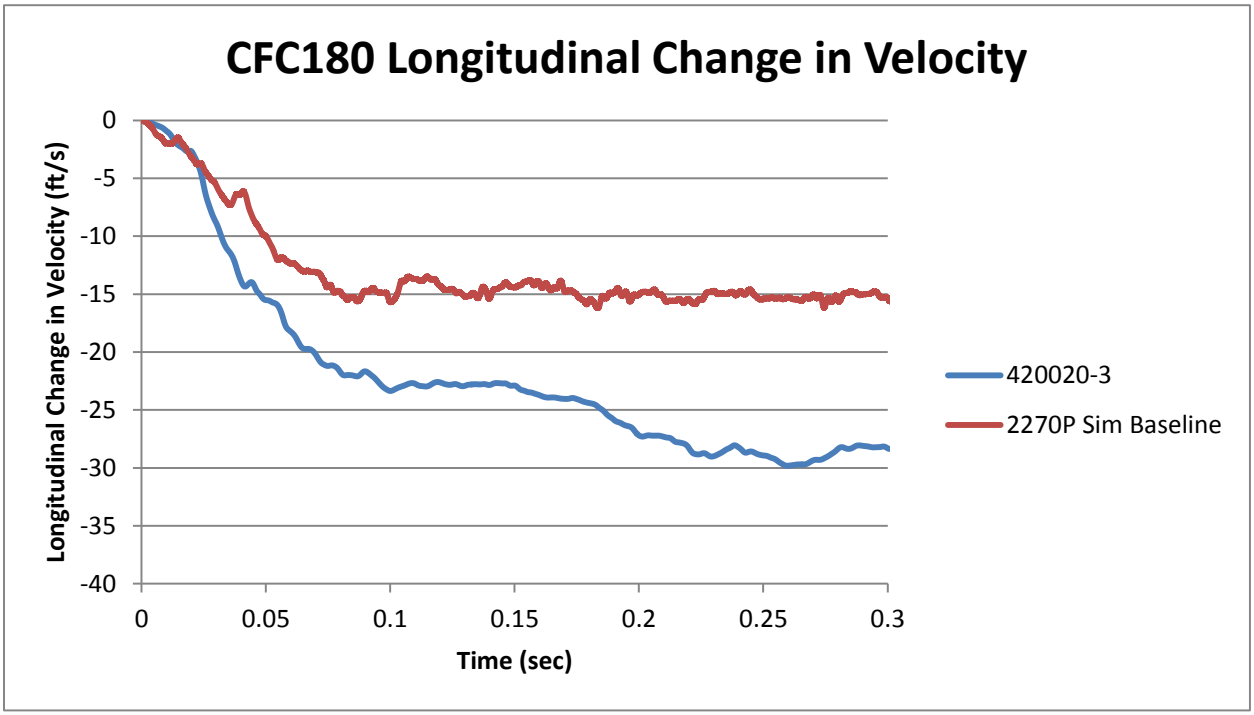

Figure 118. Comparison of 2270P Actual and Simulated Longitudinal Change in Velocity – INTOPT=1

7.3 Single-Unit Truck

In TTI test no. 420020-9b [21], a single-unit truck impacted a 36-in. (914-mm) tall single-slope barrier at a speed of 57.2 mph (25.6 m/s) and an angle of 16.1 degrees. The 10000S single-unit truck model impacted a 36-in. (914-mm) tall single-slope barrier in a LS-DYNA simulation at 57.2 mph (25.6 m/s) and an angle of 15 degrees. A static and dynamic coefficient of friction of 0.10 was applied between the single-unit truck body/tires and the barrier through *CONTACT_AUTOMATIC_SINGLE_SURFACE.

Occupant impact velocity and occupant ridedown acceleration are not required evaluation criteria in MASH for the single-unit truck. Thus, only vehicle trajectory, motion of the single-unit truck model, and the barrier forces were compared to those obtained from the full-scale crash test.

The vehicle's yaw data was not available for test no. 420020-9b, so the 50-ms average lateral acceleration was multiplied by the total weight of the single-unit truck to find the force on the barrier. It was expected that the initial peak in the barrier force would be low. However, the highest peak barrier force, which is of concern for design purposes, was expected to be approximately the same in global and local coordinates; since, the vehicle is parallel (or near parallel) to the barrier. As discussed previously, the cargo box of the vehicle acts somewhat independently of the cab of the vehicle, so it may not be appropriate to use the entire weight of the vehicle when calculating barrier forces. However, additional data was not available to improve the accuracy of the barrier forces for the actual test. The barrier force was found in the simulation using a *CONTACT_FORCE_TRANSDUCER. The initial peak barrier force that occurred at 0.130 sec was 30 percent less in the simulation than observed in test no. 420020-9b, as shown in Figure 119. The second peak barrier force was 7 percent less and occurred 0.050 sec

sooner in the simulation than in test no. 420020-9b. Based on the prior discussion, these differences were expected, so the model was accurate enough for the barrier evaluation.

The vehicle kinematics at various points in time for test no. 420020-9b and the simulated test are shown in Figure 120.

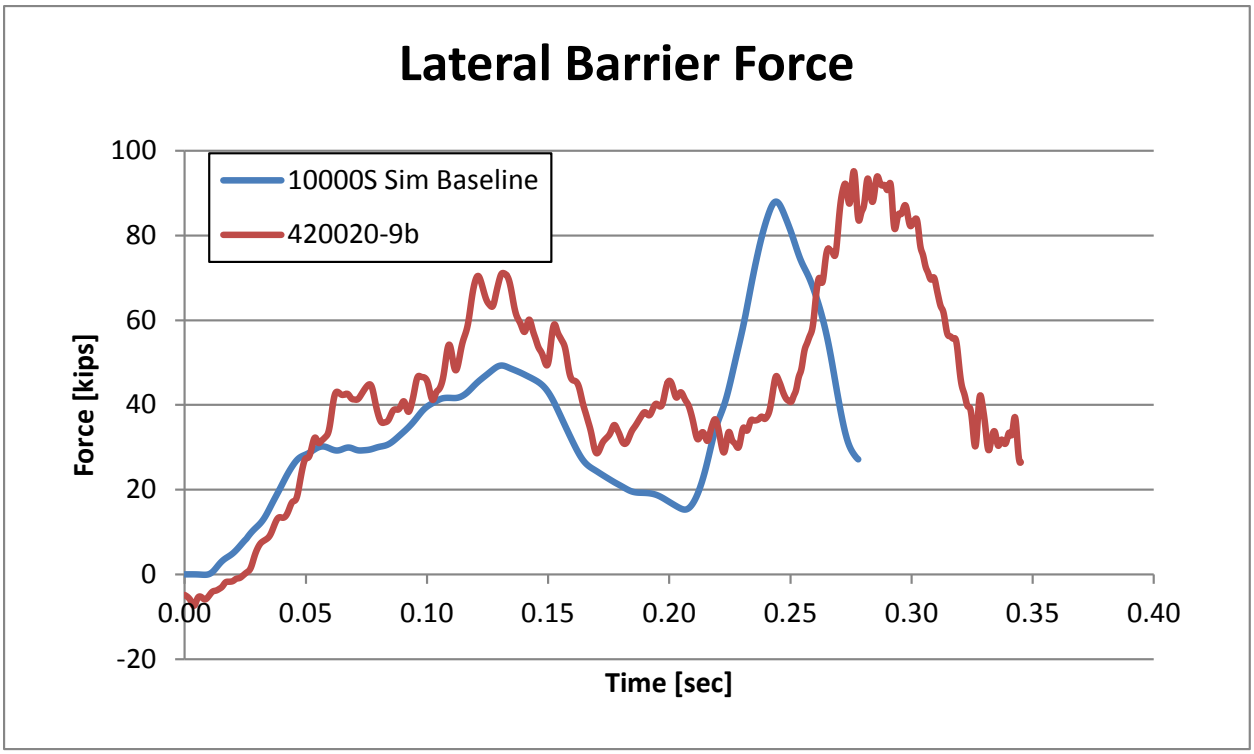

Figure 119. Comparison between TTI Test No. 420020-9b and Simulation

0.000 sec

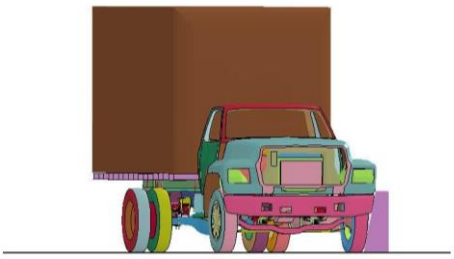

0.0 sec

0.085 sec

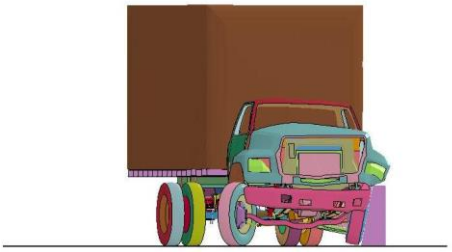

0.080 sec

0.170 sec

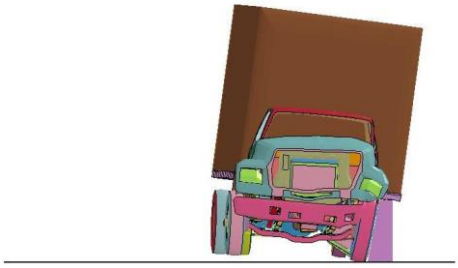

0.180 sec

0.255 sec

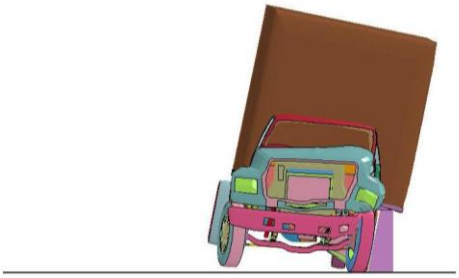

0.250 sec

Figure 120. Comparison between TTI Test No. 420020-9b and Simulation

0.340 sec

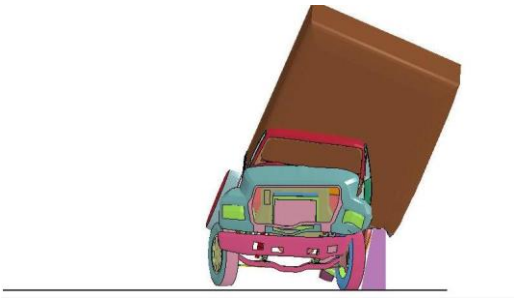

0.340 sec

0.425 sec

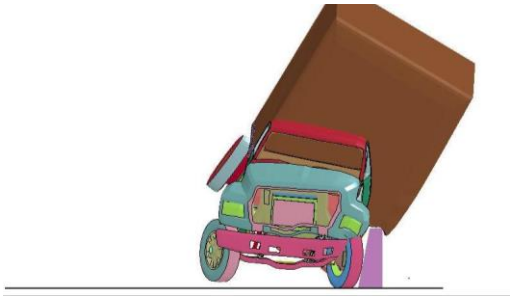

0.420 sec

0.510 sec

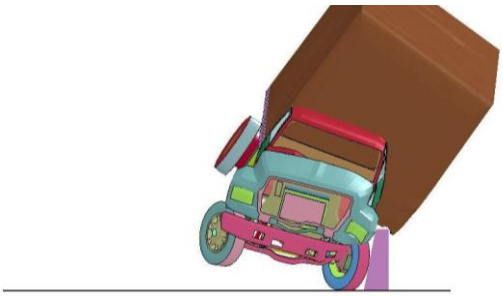

0.520 sec

0.595 sec

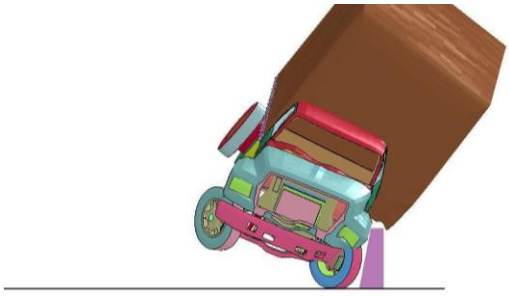

0.600 sec

Figure 120. Comparison between TTI Test No. 420020-9b and Simulation (cont.)

8 DESIGN, ANALYSIS, AND SIMULATION OF NEW BARRIER

The cylinder and shear fender models were both validated and compared to actual component testing. The design, simulation, and evaluation of the open concrete rail with shear fender rubber post concept were further pursued. For TL-4 applications, the barrier system should be tall and stiff enough in the vertical direction to allow the cargo box of the single-unit truck to roll onto and engage the top of the barrier but not override the barrier. The barrier system also needs to provide sufficient flexibility in the lateral direction to reduce the accelerations on the 1100C and 2270P vehicles but also be strong enough to resist the lateral impact loads imparted from the single-unit truck.

8.1 Barrier Model

The shear fenders were oriented so that the hole through the shear fender was parallel to the lateral impact force, which is the configuration that absorbs the most energy. Several simulations were conducted using the *MAT_SIMPLIFIED_RUBBER material model that was determined to be the most accurate for the shear fenders in Chapter 6. Initially, the *MAT_ELASTIC material model with properties of generic reinforced concrete was used to model a 120-ft (36.6-m) long continuous beam. The height and width of the beam was varied as well as the size and spacing of rubber posts to find a combination that satisfactorily reduced the lateral accelerations.

The initial objective was to reduce lateral passenger vehicle accelerations by 30 percent. Since it impossible to reduce the entire acceleration trace by at least 30 percent, it was desired to reduce at least the peak lateral acceleration by 30 percent and reduce lateral OIV and ORD. A reduction in the initial peak acceleration also reduces the OIV, and it was desired for the lateral OIV to be below the MASH evaluation criteria preferred limit of 30 ft/s (9.1 m/s). The best combination of energy absorber size and spacing as well as beam size for the 1100C impact

event consisted of the previously-tested HSF14 shear fender spaced at 10 ft (3 m) on center with a 16-in. (406-mm) wide by 20-in. (254-mm) tall concrete beam.

A segmented precast concrete beam was desired for ease of construction, so the modeled beam in the model was divided into 19 ft-10½ in. (6.1-m) long segments with a 1½-in. (38.1-mm) gap between the beam ends. Since the exact beam dimensions and reinforcement had yet to be designed, the beam was modeled as one continuous *MAT_ELASTIC material with a modulus of elasticity of 7,250 ksi (50 GPa). Initially, the beams were spliced with a pin-and-loop connection at the midspan between the posts, as shown in Figure 121. However, this connection allowed too much deflection at the impacted splice, up to 24 in. (610 mm) with an 1100C impact event, as shown in Figure 122. The splice also created pockets and possible snag points at the discontinuities in the rail.

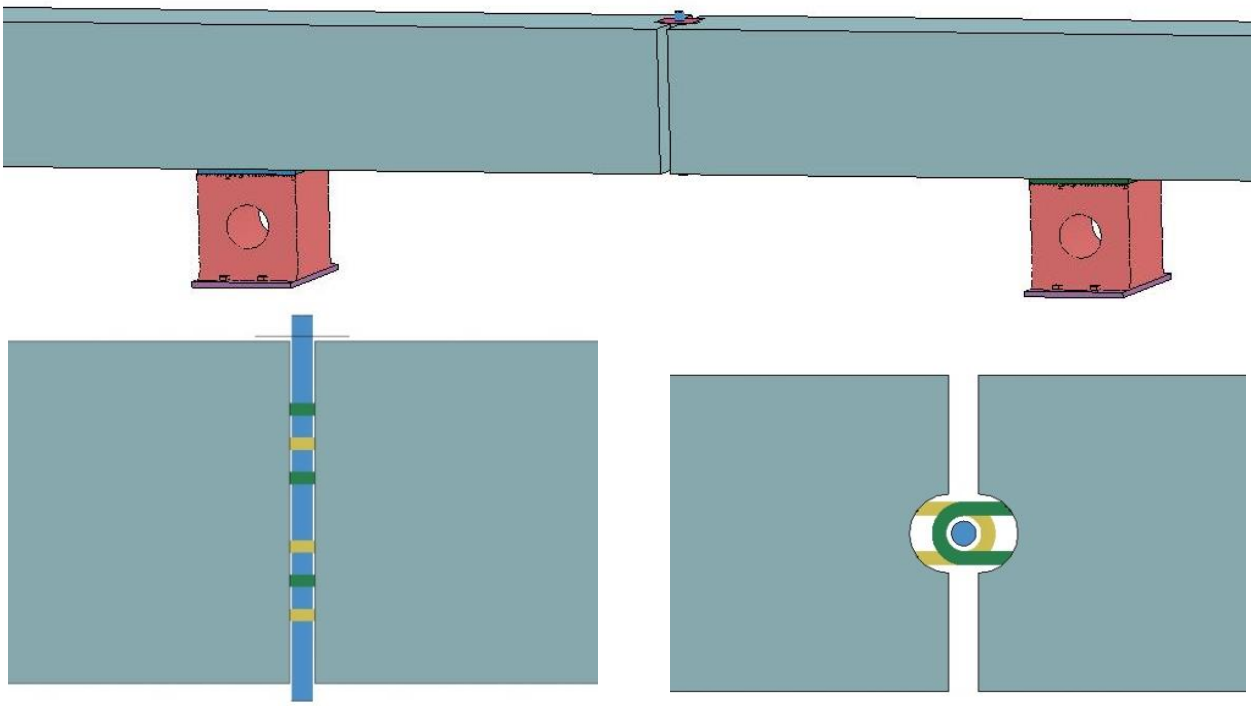

Side View Top View

Figure 121. New Barrier Design Spliced at Post Midspan

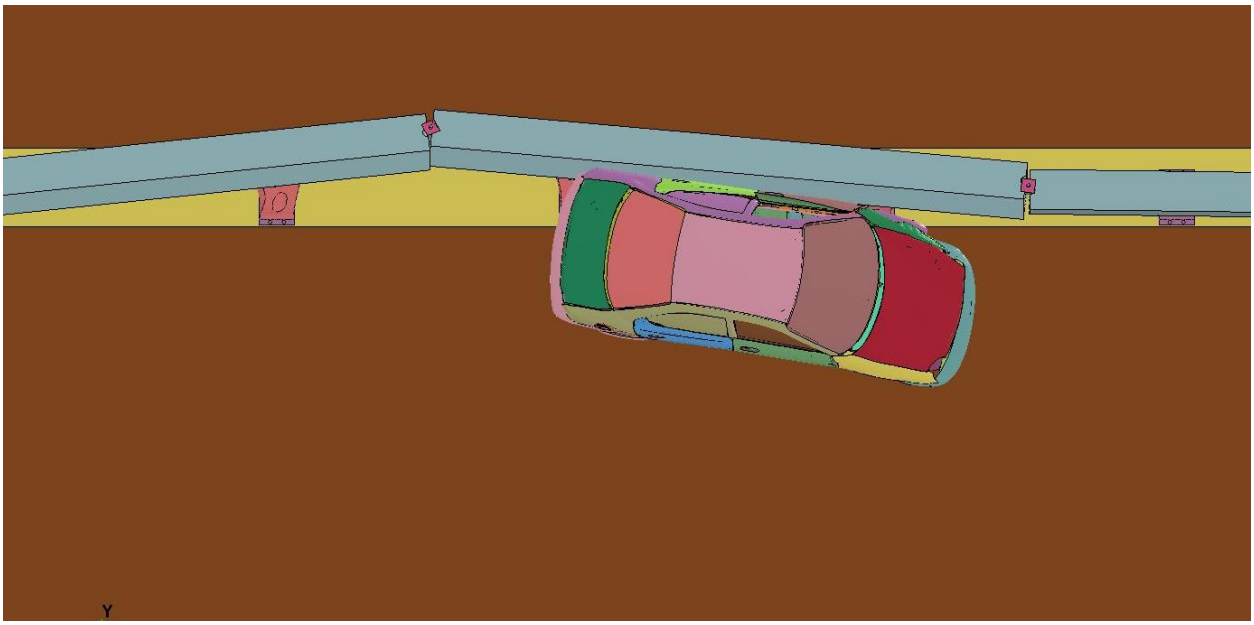

Figure 122. Deflection of New Barrier Design Spliced at Post Midspan

The segments were then spliced at the shear fender posts to create a more continuous rail. Since each shear fender has a ½-in. (13-mm) thick steel plate in the top and bottom flanges with four bolt holes, the end of each segment could be bolted at the shear fenders which would increase rail continuity; since, the shear fender's steel plate is essentially rigid. The pin-and-loop splice is not necessary to connect the beams as long as the shear fender's steel plate does not undergo plastic deformation or twisting. Thus, the splice loops and vertical pin were incorporated in the model for the rest of the simulations.

Simulations with the 16-in. (406-mm) wide concrete beam showed the potential for all the vehicles to snag on the exposed shear fender posts. The small car's front bumper and front impact-side tire contacted the post, as shown in Figure 123a. The pickup truck's impact-side tire snagged on the post, as shown in Figure 123b. Therefore, the rail width was increased to 22 in. (559 mm), while the beam height remained at 20 in. (254 mm) to achieve an overall barrier height of 36 in. (914 mm). The final barrier design, as shown in Figure 124, was then simulated with the 1100C, 2270P, and 10000S vehicle models. The final simulation had eight barrier

segments for a total system length of 160 ft (48.8 m). It was also decided that in real-world situations, this barrier would terminate into a permanent rigid concrete barrier or bridge pier. Thus, a small transition was included using posts spaced at 5 ft (1.5 m) on center at the end of the system, as shown in Figure 125. The end rail segment has several rebar loops extending out of the end that would incorporate a rigid steel drop pin to make the connection to a permanent concrete barrier. The permanent concrete barrier was not modeled; since, the transition and barrier termination were outside the scope of this project. However, the steel drop pin was modeled as a rigid, fixed object, so that the propensity for backward rotations of the barrier could be realistically modeled and evaluated.

(a) Small Car (b) Pickup Truck

Figure 123. Vehicle Snag on Posts

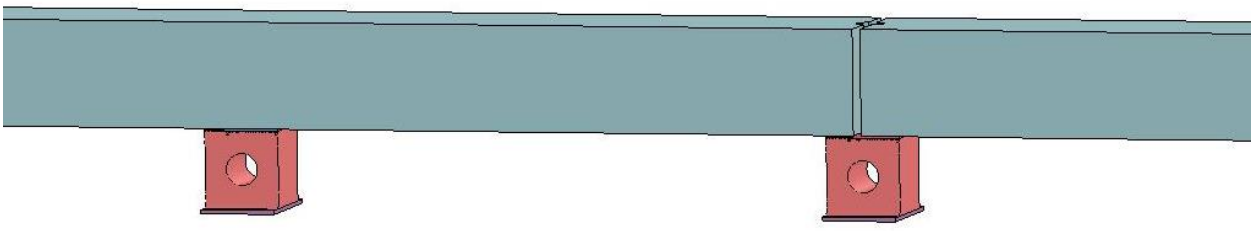

Figure 124. New Barrier Design Spliced at Posts

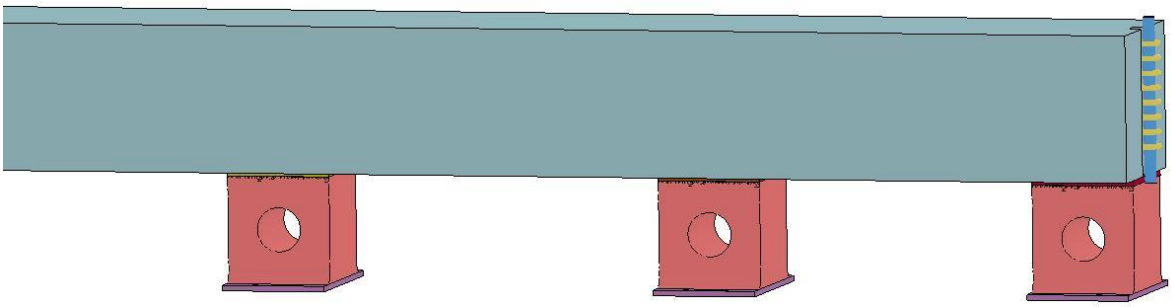

Figure 125. New Barrier Design - Transition and Termination

The final shear fender barrier model has the parts, element types, and material models shown in Table 11. The same contacts and static and dynamic coefficients of friction between the vehicles' bodies/tires and the barrier from the baseline simulation were used for the simulations of the new barrier, except for the single-unit truck contact which was changed to *CONTACT_AUTOMATIC_SURFACE_TO_SURFACE. Tied contacts were used between the shear fender rubber posts and embedded steel plates as well as between the concrete beam and the top shear fender steel plates. The bottom shear fender steel plates were constrained from all motion.

Table 11. Shear Fender Barrier Model Parts, Elements, and Materials

Part	Part No.	Element Type	Material
Shear Fender Steel - Top Post 1	1003	Type 1 Solid	*MAT_PIECEWISE_LINEAR_PLASTICITY
Shear Fender Rubber	1004	Type 13 Solid	*MAT_SIMPLIFIED_RUBBER/FOAM
Stear Fender Steel - Bottom	1008	Type 1 Solid	*MAT_RIGID
Shear Fender Steel - Top Posts 2-19	1009-1026	Type 1 Solid	*MAT_PIECEWISE_LINEAR_PLASTICITY
Pin	2028	Type 1 Solid	*MAT_RIGID
Loops - Right	2125	Type 1 Solid	*MAT_PIECEWISE_LINEAR_PLASTICITY
Loops - Left	2126	Type 1 Solid	*MAT_PIECEWISE_LINEAR_PLASTICITY
Concrete Beam	5000	Type 1 Solid	*MAT_ELASTIC

8.1.1 1100C Dodge Neon

The 1100C Neon model impacted the shear fender barrier at a speed of 62 mph (27.8 m/s) and an angle of 25 degrees at the splice at the center of the barrier system. The barrier laterally deflected a maximum of 5.1 in. (129 mm) at the splice location near impact. In addition, the barrier vertically deflected a maximum of 2.7 in. (68 mm) at the splice location near impact. Other impact points were simulated, but this investigation did not demonstrate an increased potential for vehicle snag or significantly change the results.

Accelerations, velocities, and displacements were found at the center of gravity of the 1100C model at every 0.01 ms and filtered using a customized Excel spreadsheet that is used for filtering full-scale crash test data. The CFC 180 10-ms average lateral acceleration trace is shown in Figure 126. The initial peak acceleration was reduced by 30 percent in the shear fender barrier simulation as compared to the baseline simulation into a rigid New Jersey-shaped concrete barrier at the same impact conditions. The lateral OIV was reduced by 18 percent in the shear fender barrier simulation as compared to the baseline simulation and was 27.0 ft/s (8.2 m/s) versus the MASH threshold of 40 ft/s (12.2 m/s). The lateral ORD was 8.0 g's, which was only a reduction of 3 percent, but it is still well below the MASH threshold limit of 20 g's. The longitudinal OIV and ORD were greater than those observed for the baseline simulation, but they were still below the MASH threshold limits. The vehicle trajectory is shown in Figure 127.

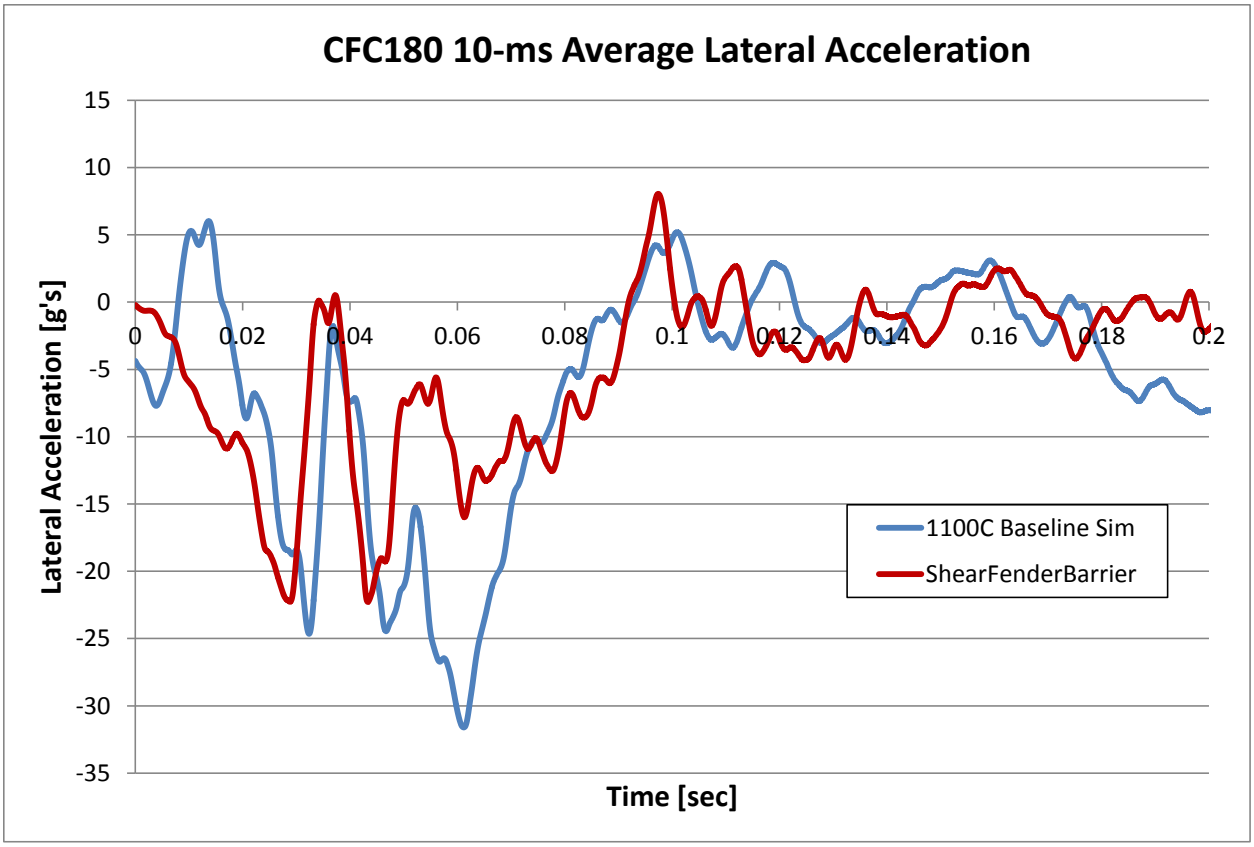

Figure 126. Comparison of 1100C Simulations – Lateral Acceleration

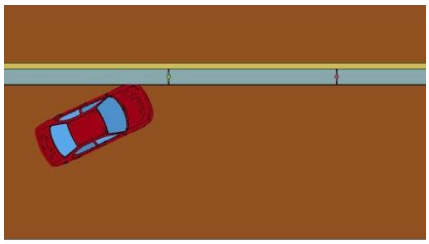

0.000 sec

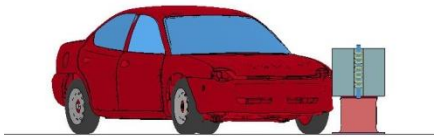

0.000 sec

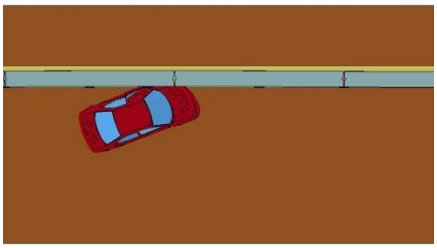

0.060 sec

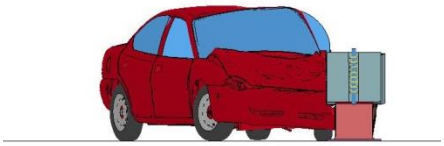

0.060 sec

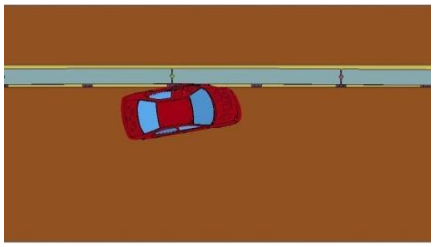

0.140 sec

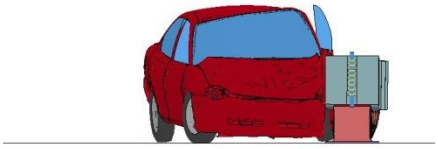

0.140 sec

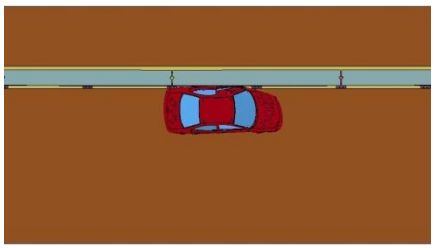

0.220 sec

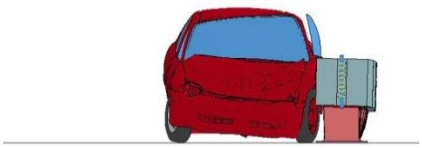

0.220 sec

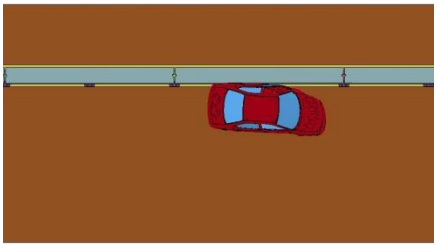

0.300 sec

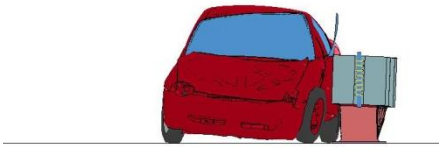

0.300 sec

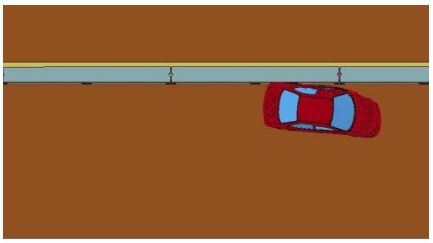

0.420 sec

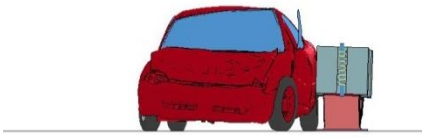

0.420 sec

Figure 127. New Barrier with TL-4 1100C Impact Simulation

8.1.2 2270P Chevrolet Silverado

The 2270P Silverado model impacted the shear fender barrier at a speed of 62 mph (27.8 m/s) and at an angle of 25 degrees at the splice at the center of the barrier system. The barrier laterally deflected a maximum of 8.3 in. (212 mm) at the splice location near impact. In addition, the barrier vertically deflected a maximum of 3.7 in. (94 mm) at the splice location near impact. Other impact points were simulated, but this investigation did not demonstrate an increase in the potential for vehicle snag or significantly change the results.

Accelerations, velocities, and displacements were found at the center of gravity of the 2270P model at every 0.01 ms and filtered using a customized Excel spreadsheet that is used for filtering full-scale crash test data. The CFC 180 10-ms average lateral acceleration trace is shown in Figure 128. The initial peak acceleration was the same magnitude in the shear fender barrier simulation as compared to the baseline simulation into a rigid single-slope concrete barrier at the same impact conditions. This peak was not reduced like in the small car simulations, since the c.g. of the pickup truck is much higher than the small car, so the vehicle's force is applied much higher on the barrier. An impact height of 16 in. (406 mm) will provide the optimal energy absorption initially; since, the force is applied directly at the top of the shear fender. The impact location in the simulation was also at a joint in the beam, which may have caused the pickup truck bumper to snag some on the joint, so the initial acceleration peak was not reduced by the levels seen in the small car simulation. However, the lateral OIV was reduced by 14 percent in the shear fender barrier simulation as compared to the baseline simulation, and was 22.0 ft/s (6.7 m/s) versus the MASH threshold of 40 ft/s (12.2 m/s). The lateral ORD was 16.0 g's, which was a reduction of 23 percent, and it is below the MASH threshold limit of 20 g's. The longitudinal OIV and ORD were greater than those observed for the baseline simulation, but they were still below the MASH threshold limits. The vehicle trajectory is shown in Figure 129.

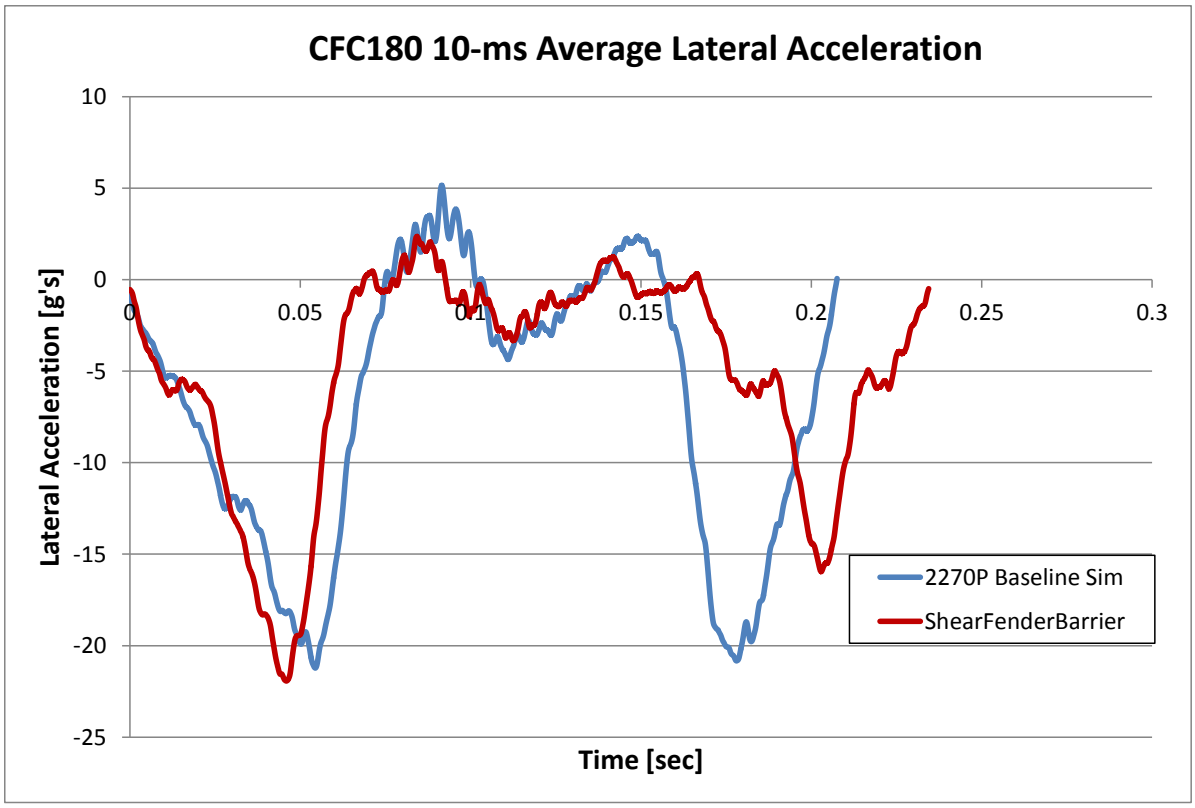

Figure 128. Comparison of 2270P Simulations – Lateral Acceleration

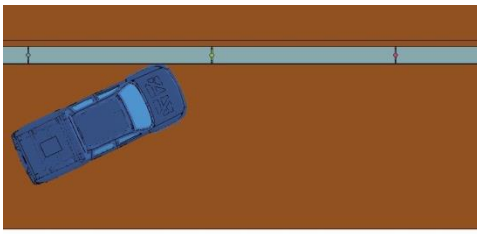

0.000 sec

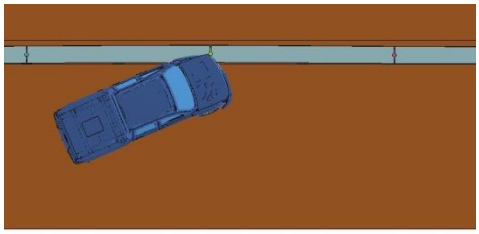
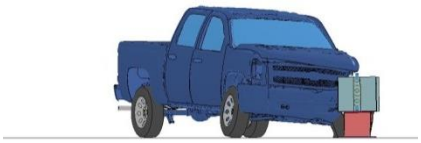
0.060 sec

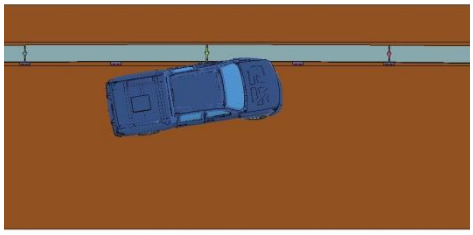
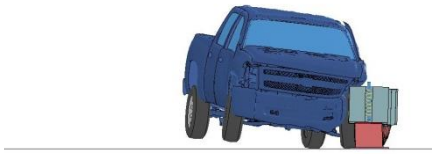
0.140 sec

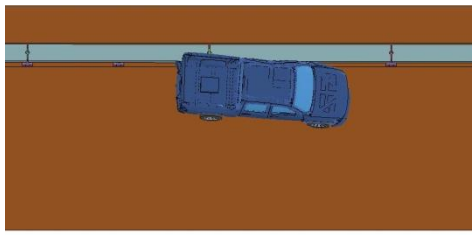

0.240 sec

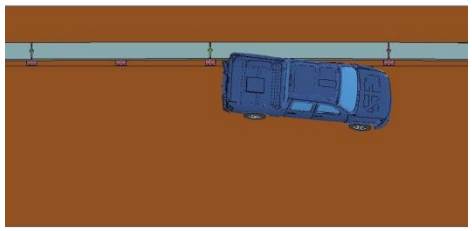

0.310 sec

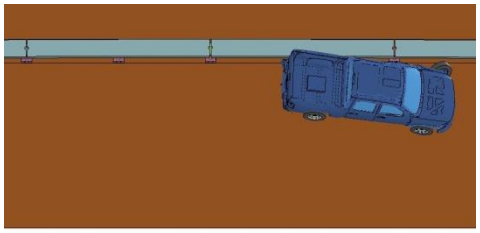

0.400 sec

Figure 129. New Barrier with TL-4 2270P Impact Simulation

8.1.3 10000S Single-Unit Truck

The 10000S single-unit truck model impacted the shear fender barrier at a speed of 56 mph (25 m/s) and at an angle of 15 degrees at the splice at the center of the barrier system. The barrier laterally deflected a maximum of 13.5 in. (342 mm) at the splice location near impact. The barrier vertically deflected a maximum of 7.4 in. (188 mm) in the region where the cargo box traveled along and leaned on top of the concrete beam. The vehicle trajectory is shown in Figure 130.

The lateral barrier forces decreased by more than 50 percent in the shear fender barrier as compared to the baseline simulation into a rigid single-slope concrete barrier at the same impact conditions, as shown in Figure 131. Since the lateral barrier force in the 10000S baseline simulation did not have as high of forces that were found in the full-scale crash test, the barrier forces in the shear fender simulation were also expected to be somewhat low. The vertical forces on the barrier are also shown in Figure 132.

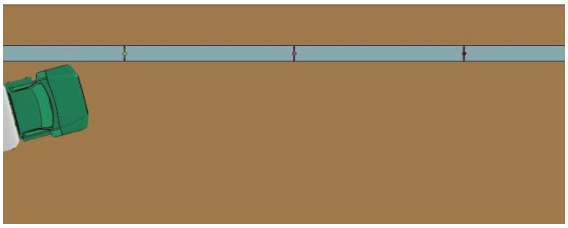
0.000 sec

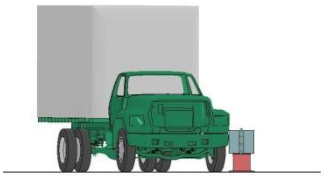
0.000 sec

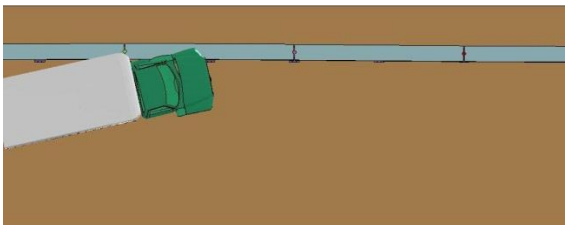
0.160 sec


0.160 sec

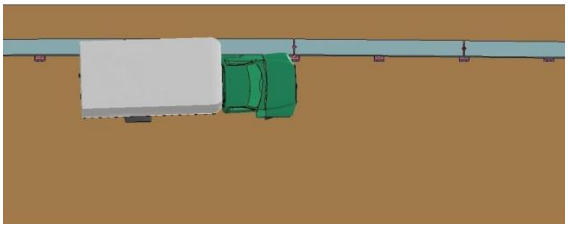
0.290 sec

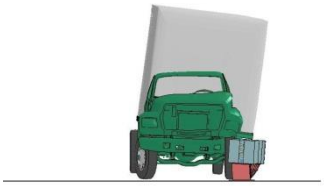
0.290 sec

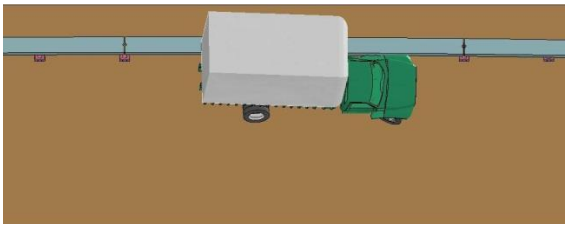
0.480 sec


0.480 sec

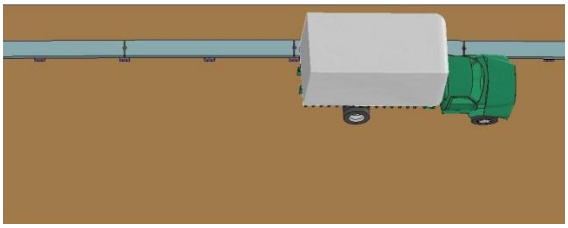
0.640 sec

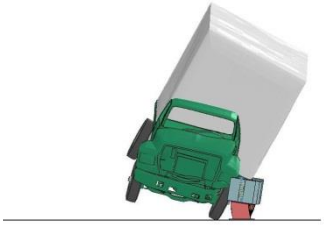
0.640 sec

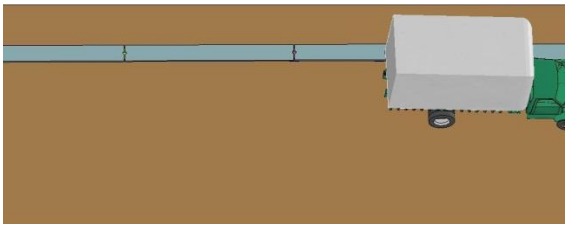
0.780 sec

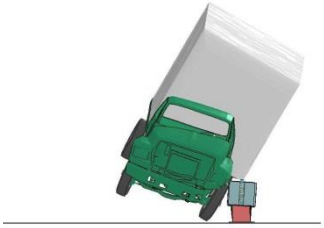
0.780 sec

Figure 130. New Barrier with TL-4 10000S Impact Simulation

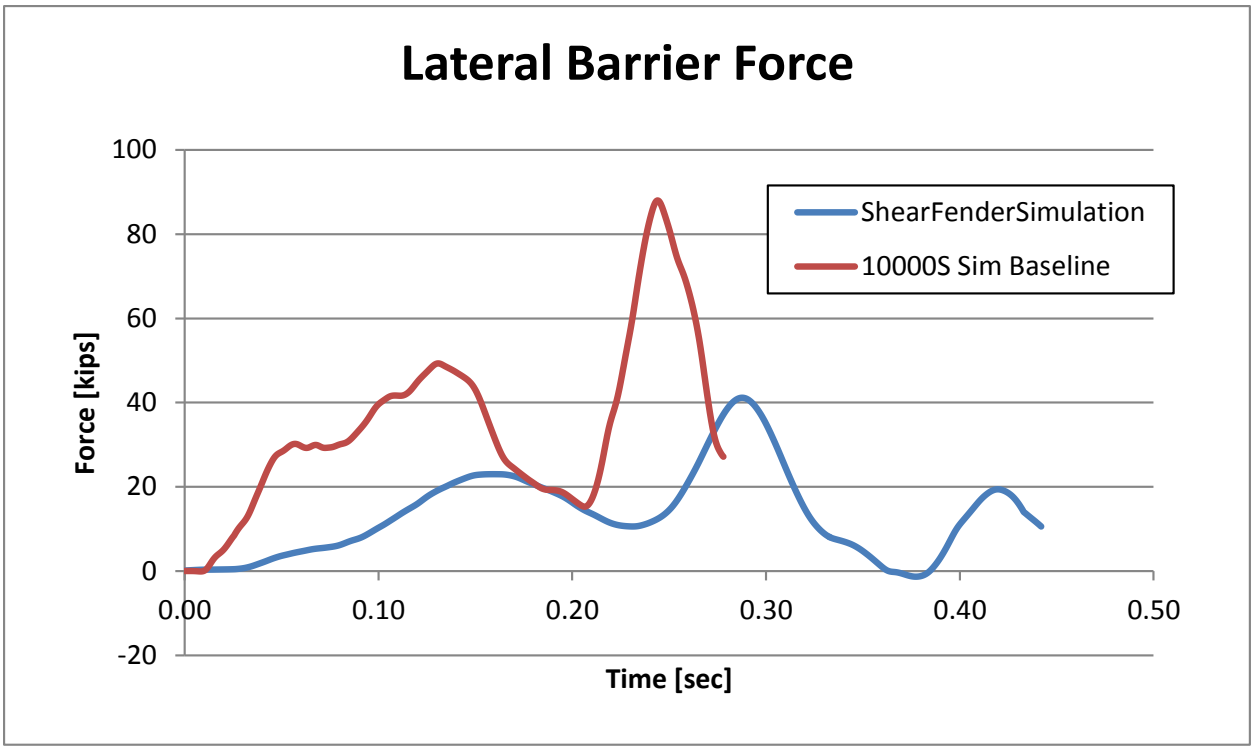

Figure 131. Lateral Barrier Forces 10000S Impact Baseline and Shear Fender Simulations

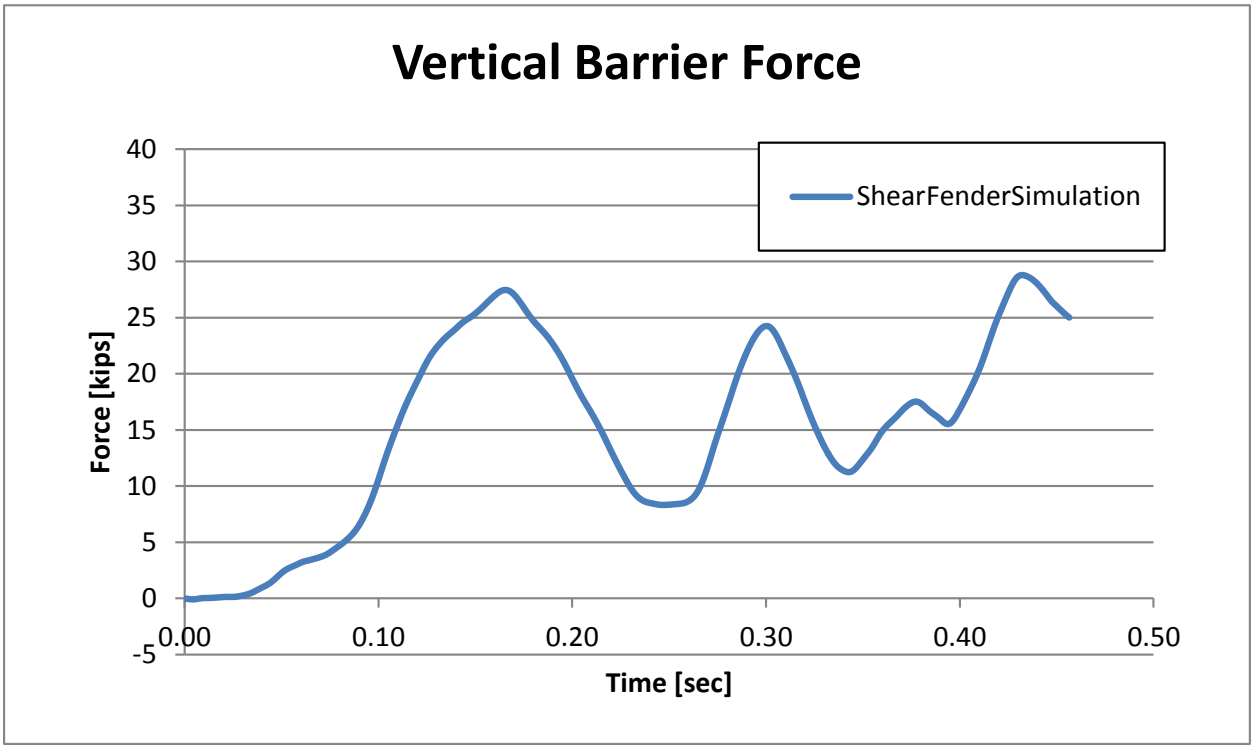

Figure 132. Vertical Barrier Forces on Shear Fender Barrier

8.2 Barrier Design

The recommended design concept consists of an open concrete rail with shear fender rubber posts anchored to a concrete slab, as shown in Figure 133. The design was configured to be quick and easy to assemble. The precast concrete beams were 22 in. (560 mm) wide x 20 in. (254 mm) tall x 20 ft (7 m) long and spliced at the rubber post locations. The shear fender posts were spaced on 10 ft (3.5 m) centers. The steel plate at the bottom of the shear fender would be slotted in the longitudinal direction of the rail to allow for construction tolerances.

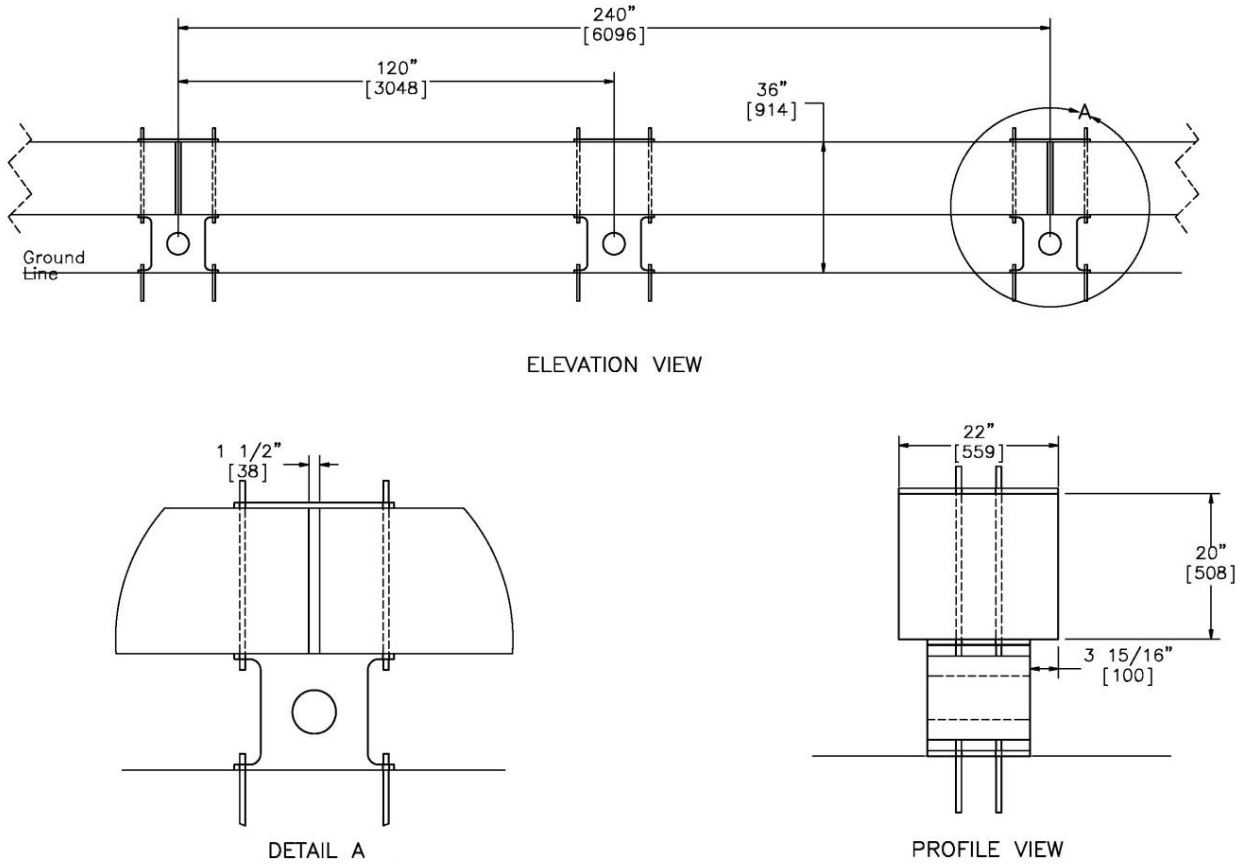

Figure 133. Proposed Design Concept for Shear Fender Barrier

The deformable barrier was designed to resist a lateral impact load of 75 kips (334 kN) for the single-unit truck; since, the simulation forces were believed to be low. The beam acts similar to a continuous beam, since the ends of the precast segments are fixed to the steel in the

rubber so that they cannot rotate or deflect with respect to each other. However, the degree of fixity at the splices was not known; since, it is not a perfectly continuous beam. The reinforcement was designed for a 20-ft (6.1-m) span continuous beam with a 75-kip (334-kN) point load, which produced a maximum moment of 2,250 k-in. (255 kN-m) in the beam. The reinforcement required for this design moment is larger than any current TL-4 and TL-5 concrete median barriers, so the design should still be conservative. The torsional resistance of the beam with a 780 k-in. moment similar to that of a pickup truck (65 kips (289 kN) at a height of 28 in. (711 mm) above the ground or 12 in. (305 mm) above the bottom of the beam) was also checked.

The concrete beam reinforcement is shown in Figure 134. The compression strength of the concrete was 4 ksi (27.6 MPa). The longitudinal reinforcement is six no. 6 bars on the vertical faces, and an additional no. 6 bar on the top and bottom faces. The stirrups are double leg no. 4 bars spaced as shown in Figure 134. The concrete beam weighs approximately 460 lb per linear foot (685 kg/m).

Four and two ¾-in. (19-mm) ASTM A193 Gr. B7 threaded thru-bolts are located at the midspan and each end, respectively, to attach the beam to the rubber posts. The thru-bolts are bolted through a 22-in. (559-mm) x 22-in. (559-mm) x ½-in. (13-mm) ASTM A529 Gr. 50 steel plate on top of the beam at each post location. The simulation showed the potential for some snagging on the beam splices. However, the splice was not modeled with an upper steel plate, so it is expected that there will be more continuity at the beam splices with the additional plate.

The rubber posts are a modified version of the Maritime International, Inc. HSF14 shear fenders, as shown in Figure 135. The rubber is type ASTM D2000 5AA425 A_{13} B_{13} C_{20} F_{17} K_{11} L_{14}. The bottom bolt holes are slotted longitudinally with the barrier to allow for construction tolerances. The ¾-in. (19-mm) x 15-in. (381-mm) ASTM A193 Gr. B7 threaded rod post anchorage should be embedded 12 in. (305 mm) in the concrete slab.

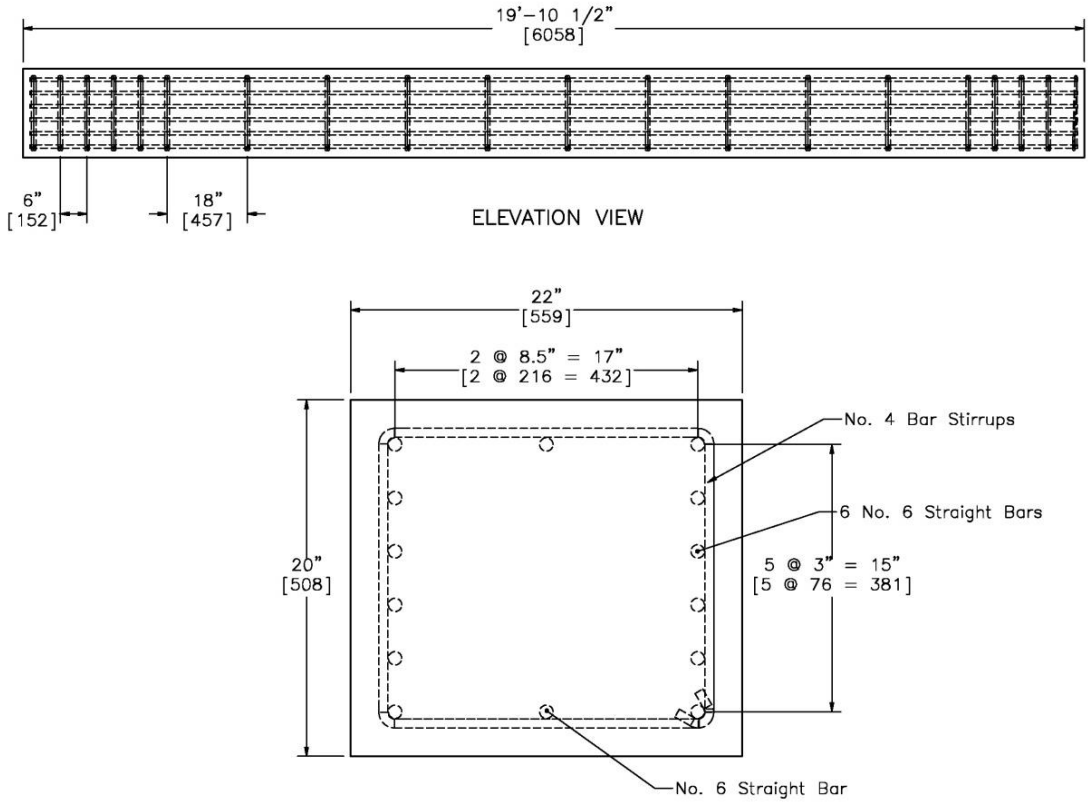

Figure 134. Concrete Beam Reinforcement

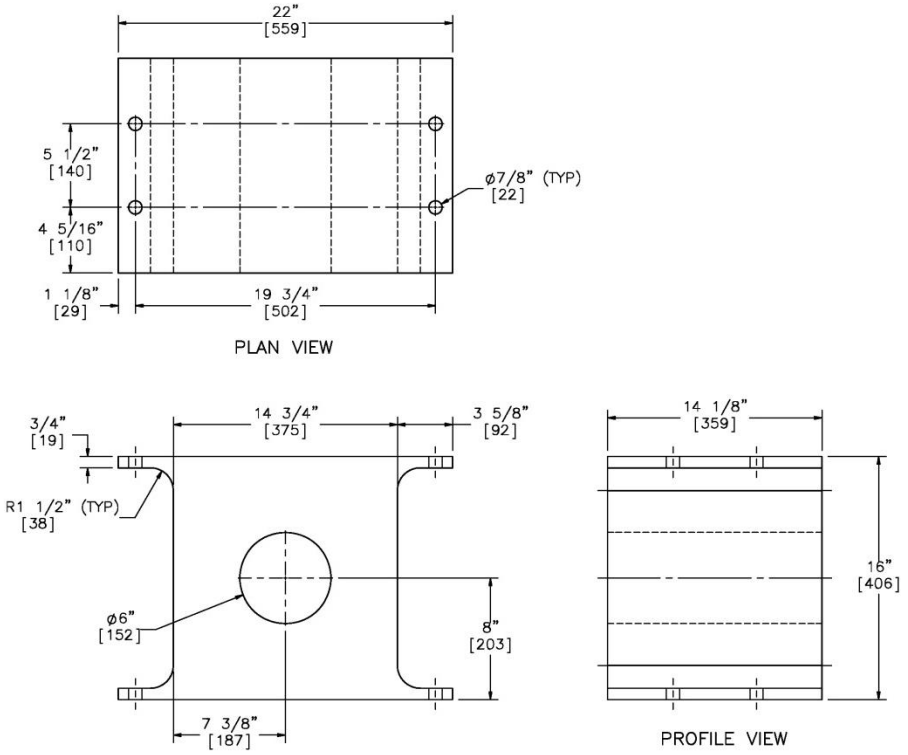

Figure 135. Shear Fender Posts

8.3 Barrier Cost

The cost of the 22-in. (560-mm) wide x 20-in. (254-mm) tall x 19-ft 10½-in. (6.1-m) reinforced concrete beam is approximately $40/ft ($131/m). The splice and anchorage hardware is approximately $15/ft ($29/m). A custom mold would need to be made for the rubber posts, which could incur a large initial cost. Thus, it is estimated that each post would cost up to $1000, or $100/ft ($328/m) after the initial mold cost. The cost of the foundation was not included; since, it is generally not included in the barrier price tabulated by State Departments of Transportation. The installation and labor cost should be much lower than typical slipformed concrete median barriers; since, all the components only need to be set and bolted into place. The installation cost was estimated to be $20/ft ($66/m), but, as mentioned previously, this cost can vary significantly depending on the installation length and mobilization costs. The total cost of the barrier is estimated to be $175/ft ($574/m). However, this barrier could pay for itself on a stretch of highway if one fatality was eliminated considering an average motor vehicle fatality can cost up to $6 million [102].

8.4 Further Considerations

Each shear fender post supports approximately 4,600 lb (2,087 kg) of weight from the beam. From Figure 32, the weight of the beam will compress the shear fender posts approximately 2 in. (51 mm). This initial compression of the shear fenders was not modeled in the shear fender simulations. This could be a concern with the 10,000S impact, since the minimum height of TL-4 barriers was previously determined to be 36 in. (914 mm). More simulations need to be done in the future with the initial compression of the shear fender posts. If the 10,000S single-unit truck shows the propensity to override the barrier, the height of the rail may need to be increased or the weight of the rail may need to be reduced. The weight of the rail

could be reduced with a hollow pipe or core in the center of the 22-in. (559-mm) by 20-in. (508-in.) cross-section.

The height of the shear fender barrier was compromised when the cargo box pushed the rail down over 7 in. (178 mm). Additional supports may be considered to prevent vertical rail deflections, which may increase the single-unit truck stability by reducing roll and pitch motions.

The boundary conditions at the end of the barrier system need further evaluation. The rigid fixed drop pin allowed the rail to rotate less than 4 degrees backward in the simulation. However, a longer barrier length should be simulated to determine if the barrier system will allow vehicle override when the boundary conditions are further from the impact. A real-world installation length could be longer than 1 mile (1.6 km) without termination into a fixed permanent barrier. The transition and upstream and downstream termination needs to be designed and evaluated to MASH TL-4 standards.

The barrier performance needs to be evaluated over a large range of temperatures. The barrier may be stiffer at cold temperatures, which should not compromise the ability of the barrier to contain and redirect vehicles, but the lateral accelerations will not be reduced as much as designed. The barrier may be more flexible at hot temperatures. Therefore, the barrier needs to be analyzed to make sure it can still contain and redirect vehicles with hot temperatures.

9 SUMMARY, CONCLUSIONS, AND RECOMMENDATIONS

Concrete median barriers are largely considered to be maintenance free and can provide the structural capacity to contain high-energy truck impacts. However, accident data has shown that impacts with these barriers cause more fatalities and can increase the rate of rollovers compared to flexible guardrails. A reusable, restorable, energy-absorbing roadside/median barrier was designed to replace concrete median barriers that produce high vehicle accelerations when impacted.

Several design objectives were established to guide the development of a completely new barrier. Crash testing standards and previously crash tested rigid barriers were examined to help determine design objectives. The target test level was MASH TL-4. The system height was determined to be a minimum of 36 in. (914 mm) to contain and redirect a single-unit truck. The system width was restricted to 36 in. (914 mm) to accommodate current median widths. The construction cost was targeted to be under $200/ft ($656/m) to be cost-effective compared to concrete median barriers. The barrier needed to be restorable and reusable, so that maintenance costs are low. The SAFER barrier reduced lateral accelerations up to 30 percent, so this reduction in lateral acceleration was also desired for a new barrier. Based on static analysis and review of barriers that withstand extreme impact events and/or absorb impact energy during displacement, the barrier deflection required to obtain the desired reduction in occupant ridedown acceleration was estimated to be 7 to 10 in. (178 to 254 mm).

The steel impact face and the foam cartridges from the current SAFER barrier design were both to be modified and/or replaced for the new barrier. Many different concepts were analyzed for both retrofit applications (to be mounted on a rigid concrete parapet) and a completely new design.

Several crash cushions, existing roadside barriers, and other energy-absorbing applications were reviewed. Energy-absorbing materials were reviewed and analyzed for properties such as superior restorability, reusability, compressibility, and resistance to environmental effects. Subsequently, elastomers were determined to be the best material for this application. Several pre-existing elastomer shapes were evaluated based on four measures of efficiency and overall energy-absorbing capacity. The axially-loaded cone and cylinder had high measures of efficiency and were selected for further evaluation. The shear fender was also selected for further evaluation.

9.1 Finite Element Material Model Evaluation

Material tests were conducted on 60-durometer EPDM rubber, 80-durometer EPDM rubber, and the shear fender rubber. Seven LS-DYNA rubber material models were evaluated using the properties obtained from the material tests. Simulations of the tension tests were conducted at 2 in./min. (0.00085 mm/ms) and 200 in./min. (0.085 mm/ms) using shell and solid elements.

Almost all of the rubber material models with shell elements (except Blatz-Ko) could reasonably predict the force versus deflection curve up to 25 percent strain, as shown in Figures 54 and 55. For larger strains though, some of the models began to deviate significantly. All of the simulations that were stretched at 2 in./min. (0.00085 mm/ms) had unstable forces develop, likely due to excessive error accumulation in the explicit analysis. Most of these model instabilities were reduced in the simulations performed at 200 in./min. (0.085 mm/ms), and the physical deformation characteristics resembled those of the actual component tests. However, the force versus deflection curves did not match that well. The Simplified Rubber/Foam material model most accurately resembled the shape of the tension test force versus deflection curve for both the 60- and 80-durometer EPDM, but the linear region had an increased slope.

All of the solid element simulations that were stretched at 2 in./min. (0.00085 mm/ms) had poor results. The forces were low compared to the tension tests, and the models deformed with severe hourglassing and inconsistencies. All of the solid element simulations that were stretched at 200 in./min. (0.085 mm/ms) had reasonable forces, but all of the models deformed with moderate hourglassing and inconsistencies. The Simplified rubber model force vs. deflection was almost identical to the 20 in./min. (0.0085 mm/ms) tensile test data. Ogden and Mooney-Rivlin material models also provided reasonable fits to the tensile test data.

Since solid elements were desired to simulate the energy absorbers, several ways to improve the physical deformation of the solid elements were explored. Hourglass control type 4 and 5 and the fully integrated S/R element formulation all produced models that did not physically hourglass. However, these models had unrealistic out-of-plane bending.

One point nodal pressure tetrahedron elements were explored because they eliminate hourglassing and were developed for incompressible materials, like rubber. The tetrahedron elements physically deformed well and had forces similar to the tension tests. The 60-durometer EPDM test at 20 in./min. (0.0085 mm/ms) and the Simplified tetrahedral model had nearly identical force vs. deflection curves. The material models of the 80-durometer EPDM were reasonable, and the Ogden and Hyperelastic material models provided the closest fits. The Simplified and Ogden material models with the tetrahedron elements were very accurate at modeling the shear fender rubber.

When modeling rubber in tension at large strains, the one point nodal pressure solid tetrahedron elements are recommended. However, the best rubber material model is dependent on type of rubber. The Simplified and Ogden material model were the most accurate when simulating tension tests. The Hyperelastic model was also decently accurate. The Blatz-Ko material model is recommended if tension test data is unavailable and/or a very simple and

computationally cheap material model is desired. The Frazer-Nash and Arruda-Boyce rubber material models are not recommended, because the simulations always encountered an error with nodes with out-of-range velocities.

The compression of rubber cylinders and the shear deformation of the shear fenders were evaluated through component tests. Simulations of two of these component tests were used to evaluate the most promising rubber material models with other load scenarios. Hexahedral elements had excessive hourglassing and contact problems. Hexahedral elements with hourglass control 4 deflected much less than what occurred during a bogie test with the same impact conditions. The Blatz-Ko Rubber and Simplified Rubber/Foam material models with tetrahedral solid elements were both accurate at simulating the 80-durometer EPDM cylinders in compression.

The Simplified and Blatz-Ko material models appeared to accurately represent the shear fender rubber when compared to a bogie test with the same impact conditions. The Simplified material model was the most accurate when comparing forces, energy, and deflections to the bogie test. The forces and energy during the middle of the event did not compare that well, and this was believed to be due to not accurately modeling the friction on the bogie impact head.

The shear fender rubber energy absorber met the energy requirements desired from an energy absorber, and the design concept with shear fender posts was pursued. Simulations of MASH TL-4 test conditions showed that the barrier reduced lateral accelerations up to 33 percent. The forces and moments in the barrier due the vehicle impacts were used to design the concrete rail.

9.2 Barrier Performance

The proposed barrier design is for an open concrete rail with shear fender rubber posts that are anchored to a concrete foundation. The design was made to be quick and easy to

assemble. The concrete beams are 22-in. (560-mm) wide x 20-in. (254-mm) tall x 19-ft 10½-in. (6.1-m) long precast concrete segments and are spliced at shear fender posts which are spaced at 10 ft (3.5 m) on center. The deformable barrier was designed to resist a lateral impact load of 75 kips (334 kN) for the single-unit truck. The barrier was estimated to cost $175/ft ($574/m).

From FEA, the peak lateral accelerations of the 1100C car were reduced up to 30 percent compared to a rigid, Jersey-shaped concrete barrier simulation. Lateral OIV was reduced 18 percent and lateral ORD was reduced 3 percent. For the 2270P impact, the lateral OIV was reduced 14 percent and lateral ORD was reduced 23 percent in the shear fender barrier simulation as compared to a rigid, single-slope concrete barrier simulation. The performance criterion for test no. 4-12 was that the barrier needs to contain and redirect the single-unit truck. The simulation of the 10000S truck met all of the criteria and reduced the lateral barrier forces over 50 percent. The lateral accelerations of the passenger vehicles were adequately reduced and the TL-4 vehicle was contained, redirected, and appeared stable. However, further splice design evaluation, optimization of the barrier, and future needs should be addressed before the new barrier is recommended further evaluation and testing.

9.3 Future Needs

The performance of the new barrier in the simulations was not validated using full-scale crash tests. Further bogie testing of the shear fenders could be used to improve the accuracy of the rubber material models used in the simulations.

More full-scale test simulations need to be conducted to evaluate several details: 1) the reduced height of the barrier due to the beam weight, 2) the effect of the end constraints on the barrier system, 3) the transition and upstream and downstream termination, and 4) the effect of temperature on the rubber posts. After further evaluation, the barrier is recommended for a MASH TL-4 crash testing program.

10 REFERENCES

1. Mak, K.K., Sicking, D.L., Coon, B.A., Albuquerque, F.D.B., and Stolle, C.S., *Identification of Vehicular Impact Conditions Associated with Serious Ran-Off-Road Crashes*, Final Report to the National Cooperative Highway Research Program, MwRSF Research Report No. TRP-03-219-09, Midwest Roadside Safety Facility, University of Nebraska-Lincoln, Lincoln, Nebraska, May 7, 2009.

2. Albuquerque, F.D.B. and Sicking, D.L., *Evaluation of the In-Service Safety Performance of Safety-Shape and Vertical Concrete Barriers*, Final Report to the Midwest States Regional Pooled Fund Program, MwRSF Research Report No. TRP-03-259-11, Project No. SPR-3(017)-Year 16, University of Nebraska-Lincoln, Lincoln, Nebraska, December 16, 2011.

3. Reid, J.D., Faller, R.K., and Sicking, D.L., *High-Speed Crash Barrier Investigation Using Simulation*, Crashworthiness, Occupant Protection, and Biomechanics in Transportation Systems – 2000, Applied Mechanics Division (AMD) – Vol. 246, BED – Vol. 49, 2000 ASME International Mechanical Engineering Congress and Exposition, Orlando, Florida, November 5-10, 2000.

4. Reid, J.D., Faller, R.K., Holloway, J.C., Rohde, J.R., and Sicking, D.L., *A New Energy-Absorbing High-Speed Safety Barrier*, Paper No. 03-2218, Transportation Research Record No. 1851, Journal of the Transportation Research Board, Transportation Research Board, Washington, D.C., January 2003.

5. Bielenberg, R.W. and Reid, J.D., *Modeling of Crushable Foam for the SAFER Racetrack Barrier*, 8th International LS-DYNA Users Conference, Simulation 2004, Dearborn, Michigan, May 2-4, 2004.

6. Bielenberg, R.W., Faller, R.K., Sicking, D.L., Rohde, J.R, Reid, J.D., Polivka, K.A., and Holloway, J.C., *Initial In-Service Performance Evaluation of the SAFER Racetrack Barrier*, Paper No. 2004-01-3526, Publication No. P-392, Proceedings of the 2004 SAE Motorsports Engineering Conference and Exhibition, Dearborn, Michigan, November 30 through December 2, 2004.

7. Bielenberg, R.W., Rohde, J.R., and Reid, J.D., *Design of the Safer Emergency Gate Using LS-DYNA*, IMECE2005-81078, Crashworthiness, Occupant Protection, and Biomechanics in Transportation Systems – 2005, Proceedings of IMECE'05, 2005 ASME International Mechanical Engineering Congress and Exposition, Orlando, Florida, November 5-11, 2005.

8. Melvin, J.W., Begeman, P.C., Faller, R.K., Sicking, D.L., McClellan, S.B., Maynard, E., Donegan, M.W., Mallott, A.M., and Gideon, T.W., *Crash Protection of Stock Car Racing Drivers – Application of Biomedical Analysis of Indy Car Crash Research*, Stapp Car Crash Journal No. 50, 415-428, Paper No. 2006-22-0016, The Stapp Association, 50th Stapp Car Crash Conference, Dearborn, Michigan, November 6-8, 2006.

9. Faller, R.K., Bielenberg, R.W., Sicking, D.L., Rohde, J.R., and Reid, J.D., *Development and Testing of the SAFER Barrier – Version 2, SAFER Barrier Gate, and Alternative Backup Structure*, Paper No. 2006-01-3612, Publication No. P-399, Proceedings of the 2006 SAE Motorsports Engineering Conference and Exhibition, Dearborn, Michigan, December 5-7, 2006.

10. Reid, J.D. and Bielenberg, R.W., *Modeling Rebound of Foam Backed Racetrack Barrier*, 10th International LS-DYNA Users Conference, pp. 6-43 to 6-50, Dearborn, Michigan, June 2008.

11. Faller, R.K., Sicking, D.L, Rohde, J.R., Reid, J.D., Keller, E.A., Bielenberg, R.W., Holloway, J.C., Addink, K.H., and Polivka, K.A., *High-Impact, Energy-Absorbing Vehicle Barrier System*, U.S. Patent No. 6,926,461 B1, August 9, 2005.

12. Faller, R.K., Rohde, J.R., Sicking, D.L., Bielenberg, R.W., Reid, J.D., Holloway, J.C., and Polivka, K.A., *High-Impact, Energy-Absorbing Vehicle Barrier System,* U.S. Patent No. 7,410,320 B2, August 12, 2008.

13. Livermore Software Technology Corporation (LSTC), LS-DYNA Keyword User's Manual Volume I, Version 971, Livermore, California, May 2007.

14. *Manual for Assessing Safety Hardware (MASH)*, American Association of State Highway and Transportation Officials (AASHTO), Washington, D.C., 2009.

15. Ross, H.E., Sicking, D.L., Zimmer, R.A., and Michie, J.D., *Recommended Procedures for the Safety Performance Evaluation of Highway Features*, National Cooperative Highway Research Program (NCHRP) Report No. 350, Transportation Research Board, Washington, D.C., 1993.

16. Polivka, K.A, Faller, R.K., Sicking, D.L., Rohde, J.R., Bielenberg, B.W., Reid, J.D., and Coon, B.A., *Performance Evaluation of the Permanent New Jersey Safety Shape Barrier – Update to NCHRP 350 Test No. 3-10 (2214NJ-1)*, Final Report to the National Cooperative Highway Research Program, NCHRP Project No. 22-14, MwRSF Research Report No. TRP-03-177-06, Midwest Roadside Safety Facility, University of Nebraska-Lincoln, Lincoln, Nebraska, October 13, 2006.

17. Williams, W.F., Bligh, R.P., and Menges, W.L., *MASH Test 3-11 of the TxDOT Single Slope Bridge Rail (Type SSTR) on Pan-Formed Bridge Deck (9-1002-3)*, Research Report No. 9-1002-3, Texas Transportation Institute, Texas A&M University, College Station, Texas, March 2011.

18. Rosenbaugh, S.K., Sicking, D.L., and Faller, R.K., *Development of a TL-5 Vertical Faced Concrete Median Barrier Incorporating Head Ejection Criteria*, Final Report to the Midwest States' Regional Pooled Fund Program, MwRSF Research Report No. TRP-03-194-07, Project No. SPR-3(017)-Year 15, Midwest Roadside Safety Facility, University of Nebraska-Lincoln, Lincoln, Nebraska, December 10, 2007.

19. American Association of State Highway and Transportation Officials, *AASHTO LRFD Bridge Design Specifications*, Third Edition, Washington D.C., 2004.

20. Polivka, K.A, Faller, R.K., Sicking, D.L., Rohde, J.R., Bielenberg, B.W., Reid, J.D., and Coon, B.A., *Performance Evaluation of the Permanent New Jersey Safety Shape Barrier – Update to NCHRP 350 Test No. 4-12 (2214NJ-2)*, Final Report to the National Cooperative Highway Research Program, NCHRP Project No. 22-14, MwRSF Research Report No. TRP-03-178-06, Midwest Roadside Safety Facility, University of Nebraska-Lincoln, Lincoln, Nebraska, October 13, 2006.

21. Sheikh, N.M., Bligh, R.P., and Menges, W.L., *Determination of Minimum Height and Lateral Design Load for MASH Test Level 4 Bridge Rails*, Cooperative Research Program Test Report No. 9-1002-5, Texas Transportation Institute, Texas A&M University, College Station, Texas, October 2011.

22. Stolle, C.J., Lechtenberg, K.A., Reid, J.D., Faller, R.K., Bielenberg, R.W., Rosenbaugh, S.K., Sicking, D.L., and Johnson, E.A., *Determination of the Maximum MGS Mounting Height – Phase I Crash Testing*, Final Report to the Midwest States Regional Pooled Fund Program, MwRSF Research Report No. TRP-03-255-12, Project No. TPF-5(193)-Year 20, Midwest Roadside Safety Facility, University of Nebraska-Lincoln, Lincoln, Nebraska, March 9, 2012.

23. Rosenbaugh, S.K., Faller, R.K., Bielenberg, R.W., Sicking, D.L., and Reid, J.D., *Phase I Development of an Aesthetic, Precast Concrete Bridge Rail*, Final Report to the Nebraska Department of Roads, MwRSF Research Report No. TRP-03-239-12, NDOR Project No. SPR-P1(07) P596, Midwest Roadside Safety Facility, University of Nebraska-Lincoln, Lincoln, Nebraska, February 13, 2012.

24. Olson, R.M. and Post, E.R., *Tentative Service Requirements for Bridge Rail Systems*, National Cooperative Highway Research Program (NCHRP) Report No. 86, Washington, D.C., 1970.

25. Mak, K.K., Beason, W.L., Hirsch, T.J., and Campise, W.L., *Oblique Angle Crash Tests of Loaded Heavy Trucks into an Instrumented Wall*, Texas Transportation Institute, Texas A&M University, College Station, TX, February 1988.

26. Beason, W.L. and Hirsch, T.J., *Measurement of Heavy Vehicle Impact Forces and Inertia Properties: Final Report*, Texas Transportation Institute, Texas A&M University, College Station, TX, January 1989.

27. Beason, W.L., Cain, J.C., and Hirsch, T.J., *A Low Maintenance, Energy-Absorbing Bridge Rail*, Report No. FHWA/TX-86/14-417-1F, Texas Transportation Institute, Texas A&M University, College Station, Texas, October 1986.

28. Kimball, C.E., Bronstad, M.E., Michie, J.D., Wentworth, J.A., and Viner, J.G., *Development of a Collapsing Ring Bridge Railing System*, Report No. FHWA-RD-76-39, Southwest Research Institute, San Antonio, Texas, January 1976.

29. Nordlin, E.F., Stoker, J.R., and Doty, R.N., *Dynamic Tests of an Energy-Absorbing Barrier Employing Sand-Filled Frangible Plastic Barrel*, Research Report No. M&R HRB 636405-4, State of California, Department of Public Works, January 1972.

30. Marquis, E.L. and Hirsch, T.J., *Test and Evaluation of a Tire-Sand Inertia Barrier*, TRR566, Texas Transportation Institute, Texas A&M University, College Station, Texas, 1976.

31. The Energite III Inertial Barrier System, Energy Absorption Systems, Incorporated, January 1983.

32. Horne, D.A., Federal Highway Administration, NCHRP350 *Approval Letter No. CC-52 for the TrafFix Devices Sand Barrel System.* To Dave Gertz, TrafFix Devices, Inc., San Clemente, California, July 10, 1998.

33. Michie, J.D., *Recommended Procedures for the Safety Performance Evaluation of Highway Appurtenances*, National Cooperative Highway Research Program (NCHRP) Report No. 230, Transportation Research Board, Washington, D.C., March 1981.

34. Lawrence, L.R. and Halton, J.H., *Crash Cushions Selection Criteria and Design*, United States Department of Transportation, Federal Highway Administration, September 1975.

35. Carney, J.F., *Performance and Operational Experience of Crash Cushions: A Synthesis of Highway Practice*, NCHRP Synthesis 205, Transportation Research Board, Washington, D.C., 1994.

36. Sicking, D.L., Thompson, M.F., and Ross, H.E., *Energy Dissipation Characteristics of Clustered Rubber Cylinders*, Report No. FHWA/TX-89/453-1F, Texas Transportation Institute, Texas A&M University, College Station, Texas, February 1989.

37. Dougan, C.E. and Carney, J.F., *Summary of the Results of Crash Tests Performed on the Narrow Connecticut Impact Attenuation System* (NCIAS), Report No. FHWA-CT-RD-89-3, Connecticut Department of Transportation, March 1989.

38. Carney, J.F., *A Generalized Design for the Connecticut Impact Attenuation System: Final Report, Report*, No. 1222-F-88-15, Connecticut Department of Transportation, December 1988.

39. Wright, F.G., Federal Highway Administration, NCHRP350 *Approval Letter No. CC-71 for EASI-Cell TL-1 Crash Cushion*. To Barry Stephens, Energy Absorption Systems, Inc., Rocklin, California, December 6, 2000.

40. Alberson, D.C., *Crash Testing a Reusable Polyethylene Narrow Impact Attenuation System*, Project No. 472380, Texas Transportation Institute, Texas A&M University, College Station, Texas, March 1994.

41. Carney, J.F., Chatterjee, S., and Albin, R.B., *Development of a 100-km/h Reuseable High-Molecular – Weight/High - Density Polyethylene Truck-Mounted Attenuator*, Paper No. 98-0164, Transportation Research Record No. 1647, Journal of the Transportation Research Board, Transportation Research Board, Washington, D.C., 1998.

42. Carney, J.F., Alberson, D.C., Bullard, D.L., Chatterjee, S. and Menges, W., *Reuseable High-Molecular Weight, High-Density Polyethylene Crash Cushions for Wide Hazards*, Paper No. 99-0329, Transportation Research Record No. 1690, Journal of the Transportation Research Board, Washington, D.C., 1999.

43. Carney, J.F., Faramawi, M.I., and Chatterjee, S., *Development of a Reuseable High-Molecular-Weight-High-Density Polyethylene Crash Cushions*, Transportation Research Record No. 1528, Journal of the Transportation Research Board, Transportation Research Board, Washington, D.C., pp. 11-27, 1996.

44. Ostensen, A.G., Federal Highway Administration, NCHRP350 *Approval Letter No. CC-73a for the REACT350 Crash Cushion*. To Barry Stephens, Energy Absorption Systems, Inc., Rocklin, California, April 30, 2002.

45. Laturner, J.F., *NCHRP 350 Crash Test Results for the QuadGuard System*, Project No. 01-7620, E-Tech Testing Services Incorporated, Rocklin, California, May 1996.

46. Horne, D.A., Federal Highway Administration, NCHRP350 *Approval Letter No. CC-43 for the QuadGuard – Low Maintenance Cartridge (LMC) system*. To J.M. Essex, Energy Absorption Systems, Inc., Chicago, Illinois, December 1, 1997.

47. Horne, D.A., Federal Highway Administration, NCHRP350 *Approval Letter No. CC-45 for QuadGuard Low Maintenance Crash Cushion*. To J.M. Essex, Energy Absorption Systems, Inc., Chicago, Illinois, March 19, 1998.

48. Horne, D.A., Federal Highway Administration, NCHRP350 *Approval Letter No. CC-49 for the QuadTrend-350 End Treatment*. To J.M. Essex, Energy Absorption Systems, Inc., Chicago, Illinois, June 1998.

49. Wright, F.G., Federal Highway Administration, NCHRP350 *Approval Letter No. CC-75 for the TAU-II Crash Cushion*. To James Keaton, Barrier Systems, Inc., Rio Vista, California, September 14, 2001.

50. Bligh, R.P., Sheikh, N.M., Menges, W.L., and Haug, R.R., *Portable Concrete Traffic Barrier for Maintenance Operations*, Report No. FHWA/TX-05/0-4692-1, Texas Transportation Institute, Texas A&M University, College Station, Texas, May 2005.

51. Baxter, J.R., Federal Highway Administration, NCHRP350 *Approval Letter No. CC-87 for the QUEST Crash Cushion*. To Barry Stephens, Energy Absorption Systems, Inc., Rocklin, California, February 2005.

52. Baxter, J.R., Federal Highway Administration, NCHRP350 *Approval Letter No. CC-85 for the Smart Cushion Innovations SCI-100GM Crash Cushion*. To Randy Warner, Stabler Companies, Inc., Harrisburg, Pennsylvania, September 12, 2003.

53. Baxter, J.R., Federal Highway Administration, NCHRP350 *Approval Letter No. CC-89 for the Hybrid Energy Absorbing Reusable Terminal (HEART)*, To Dean Alberson, Texas Transportation Institute, Texas A&M University, College Station, Texas, March 17, 2005.

54. Sheikh, N.M., Alberson, D.C., and Bullard, D.L., *Development of a Hybrid Energy Absorbing Reusable Terminal (HEART) for Roadside Safety Applications*, submitted to the 84th Annual Meeting of the Transportation Research Board, Paper No. 05-2571, Texas Transportation Institute, Texas A&M University, College Station, Texas, November 17, 2004.

55. Baxter, J.R., Federal Highway Administration, NCHRP350 *Approval Letter No. CC-95 for the Compressor Crash Cushion*. To Felipe Alexander and Jan Miller, TrafFix Devices, Inc., San Clemente, California, February 26, 2007.

56. Wright, F.G., Federal Highway Administration, NCHRP350 *Approval Letter No. CC-66 for the Absorb350 Crash Cushion*. To Edwin Wood, Barrier Systems, Inc., Carson City, Nevada, May 11, 2001.

57. Griffeth, M.S., Federal Highway Administration, NCHRP350 *Approval Letter No. CC-114 for the SLED – Sentry Longitudinal Energy Dissipator*. To Geoff Maus, TrafFix Devices, Inc., San Clemente, California, February 9, 2011.

58. Griffeth, M.S., Federal Highway Administration, NCHRP350 *Approval Letter No. CC-117 for the SLED – Sentry Longitudinal Energy Dissipator*. To Felipe Almanza, TrafFix Devices, Inc., San Clemente, California, June 21, 2011.

59. Nicol, D.A., Federal Highway Administration, NCHRP350 *Approval Letter No. CC-37D Mod. TRITON Concrete End Treatment ACZ-350 System*. To Barry Stephens, Energy Absorption Systems, Inc., Rocklin, California, February 13, 2009.

60. Griffeth, M.S., Federal Highway Administration, NCHRP350 *Approval Letter No. CC-110 for the TL-2 ACZ-350 System*. To Barry Stephens, Energy Absorption Systems, Inc., Rocklin, California, November 16, 2011.

61. Ivey, D.L. and Marek, M.A., *Development of a Low Cost High Performance Terminal for Concrete Median Barriers and Portable Concrete Barriers*, Project No. 9901-E, Texas Transportation Institute, August 1991.

62. Energy Absorption Systems, Inc. "N-E-A-T Crash Cushion System", www.energyabsorption.com/products/products_neat_crash.asp, Accessed October 2, 2012.

63. Nabors, D.T. and Hossain, M., *Development of a Low-Cost Crash Cushion Using Recycled Automobile Tires*, Final Report to the Kansas Department of Transportation, Report No. KSU-96-8, Kansas State University, September 1998.

64. Airfence Safety Systems, "Airfence IIs – The Engineered Solution", www.airfence.com/airfenceIIs.html, Accessed October 2, 2012.

65. Mayer, J.B. and Bronstad, M.E., *Experimental Evaluation of the Combination-Attenuator-Terminal (C-A-T)*, SWRI Project Report No. 06-1618, Southwest Research Institute, San Antonio, Texas, February 1998.

66. Lattin, D.J., *SENTRE and TREND Attenuator Field Installations*, FHWA-AZ-8802 & FHWA-AZ-8803, Arizona Transportation Research Center, February 1990.

67. Horne, D.A., Federal Highway Administration, NCHRP350 *Approval Letter no. CC-41 for the Brakemaster System TL-3 Terminal*. To J.M. Essex, Energy Absorption Systems, Inc., Chicago, Illinois, June 19, 1997.

68. Pfeiffer, B.G., Rohde, J.R., and Sicking, D.L., *Improved Guardrail Terminal Development of a BEST Terminal to Comply with NCHRP350 Requirements*, MATC Project No. MATC UNL96-7, Midwest Roadside Safety Facility, Lincoln, Nebraska, December 1998.

69. Horne, D.A., Federal Highway Administration, NCHRP350 *Approval Letter no. CC-40 for the Sequential Kinking Terminal (SKT-350)*. To Kaddo Kothmann, Road Systems, Inc., Big Springs, Texas, April 2, 1997.

70. Horne, D.A., Federal Highway Administration, NCHRP350 *Approval Letter No. CC-46 for the Flared Energy Absorbing Terminal (FLEAT)*. To Kaddo Kothmann, Road Systems, Inc., Big Springs, Texas, April 2, 1998.

71. Polivka, K.A., Rohde, J.R., Reid, J.D., Sicking, D.L., Faller, R.K., and Holloway, J.C., *Evaluation of the Box-Beam Burster Energy Absorbing Terminal-Median Barrier Terminal* (BEAT-MT), Final Report to the Safety By Design Co., Inc., MwRSF Research Report No. TRP-03-110-01, Midwest Roadside Safety Facility, Lincoln, Nebraska, December 14, 2001.

72. Bielenberg, B.W., Faller, R.K., Holloway, J.C., Reid, J.D., Rohde, J.R., and Sicking, D.L., *Performance Evaluation of the Redesigned BEAT Bridge Pier Protection System*, Final Report to Safety By Design Company, MwRSF Research Report No. TRP-03-140-03, Midwest Roadside Safety Facility, Lincoln, Nebraska, August 12, 2003.

73. Hirsh, T.J., Stocker, A.J., and Ivey, D.L., *Energy-Absorbing Bridge Rail (Fragmenting Tube)*, Contract No. CPR-11-5851, Texas Transportation Institute, Texas A&M University, College Station, Texas, February 1970.

74. Jehu, V.J. and Laker, I.B., *Vehicle Impact Tests on Reinforced Concrete Bridge Parapets*, TRPL Report LR 485, Transport and Road Research Laboratory, Crowthorne, Berkshire, England, 1972.

75. Bronstad, M.E., *Recommended Procedures for Vehicle Crash Testing of Highway Appurtenances*, National Cooperative Highway Research Program Report 153, 1978.

76. Kimball, C.E., Wiles, E.O., and Michie, J.D., *Test Evaluation of Tubular Thrie Beam for Upgrading Concrete Bridge Railing*, Southwest Research Institute, San Antonio, Texas, 1976.

77. Kimball Jr., C.E., Bronstad, M.E., and Michie, J.D., *Heavy Vehicle Tests of Tubular Thrie Beam Retrofit Bridge Railing*, Report No. FHWA/RD-82/007, Southwest Research Institute, San Antonio, Texas, March 1985.

78. Bronstad, M.E. and McDevitt, C.F., *Self-Restoring Median Barriers and Bridge Railings – Research Report*, Report No. FHWA/RD-87/002, Southwest Research Institute, San Antonio, Texas, January 1987.

79. Bligh, R.P., Sheikh, N.M., Obu-Odeh, A.Y., and Menges, W.L., *Evaluation of Barriers for Very High Speed Roadways*, Report No. FHWA/TX-10/0-6071-2, Texas Transportation Institute, Texas A&M University, College Station, Texas, March 2010.

80. Sharma, H., Hurlbaus, S., and Gardoni, P., *Development of a Bridge Bumper to Protect Bridge Girders from Overheight Vehicle Impacts*, Computer-Aided Civil and Infrastructure Engineering, Volume 23, pp. 415-426, 2008.

81. Loading Dock Supply LLC, dockbumpersupply.com, Accessed September 12, 2012.

82. Trelleborg Marine Systems, *Section 1: High Performance Fenders*, 2008.

83. N.S. Marine and Leisure Inc., http://www.anchoring.com/four-supafend-boat-fenders.html, Accessed September 12, 2012.

84. Leitman, M.J. and Villaggio, P., *The Dynamics of a Membrane Shock-Absorber*, Mechanics Based Design of Structures and Machines, Volume 34, pp. 277-292, 2006.

85. Urethane Technologies, Inc., "Buoys, Fenders, Buoyant Equipment, Floats, and Navigational Aids", www.utibuoys.com, Accessed September 12, 2012.

86. Enertrols, "Elastomeric Bumpers for Energy Control", www.enertrols.com/pdfs/Enertrols_ElastomerBumpers.pdf, Accessed October 2, 2012.

87. Sorbothane, http://www.sorbothane.com/material-properties.php, Accessed September 12, 2012.

88. Shigley, J.E. and Mischke, C.R., *Mechanical Engineering Design*, Fifth Edition, McGraw-Hill, Inc., New York, pp. 413-449, 1989.

89. CLA-VAL, *Selection Guide for Chemical Resistance of Elastomer*, www.cla-val.com/pdfs/N-Elastomer_Selection_Guide.pdf, 2003.

90. Roschke, P.N., Thompson, M.F., and Sicking, D.L., *Selection of Rubber Materials and Shapes for Energy-Absorbing Elements*, Paper No. 25223, Journal of Materials in Civil Engineering, Volume 2, No. 4, November 1990.

91. MSC Software, *Whitepaper - Nonlinear Finite Element Analysis of Elastomers*, www.axelproducts.com/downloads/WP_Nonlinear_FEA-Elastomers.pdf

92. Gent, A.N., *Engineering with Rubber: How to Design Rubber Components 2nd Edition*, Hanser Publishers, Munich, 2001.

93. *Modeling Guidelines Document Version 11-1*, LS-DYNA Aerospace Working Group, July 28, 2011.

94. Erhart, T., LS-DYNA Forum 2011 – Entwicklerforum, Stuttgart, Germany, Oktober 12, 2011.

95. Bonet, J. and Burton, A.J., *A Simple Average Nodal Pressure Tetrahedral Element for Incompressible and Nearly Incompressible Dynamic Explicit Applications*, Communications in Numerical Methods in Engineering, Volume 14, No. 5, pp. 437-449, May 1998.

96. Reid, J.D., MECH950 Impact Engineering Course Notes, October 2008.

97. Schmidt, J.D., Faller, R.K., Sicking, D.L., Reid, J.D., Lechtenberg, K.A., Bielenberg, R.W., Rosenbaugh, S.K., and Holloway, J.C., *Evaluation of Energy Absorbers for Use in a Roadside/Median Barrier*, Draft Report to the Nebraska Department of Roads, MwRSF Research Report No. TRP-03-280-13, Midwest Roadside Safety Facility, University of Nebraska-Lincoln, Lincoln, Nebraska, In Progress.

98. FHWA/NHTSA National Crash Analysis Center, *Finite Element Model of Dodge Neon*, Model Year 1996, Version 7, Posted July 3, 2006.

99. FHWA/NHTSA National Crash Analysis Center, *Finite Element Model of Chevy Silverado*, Model Year 2007, Version 2, Posted February 27, 2009.

100. Mohan, P., Marzougui, D., Arispe, E., and Story, C., *Component and Full-Scale Tests of the 2007 Chevrolet Silverado Suspension System*, National Crash Analysis Center, Contract No. DTFH61-02-X-00076, July 2009.

101. Bullard, D.L., Bligh, R.P., and Menges, W.L., *Appendix A: MASH-08 TL-4 Testing and Evaluation of the New Jersey Safety Shape Bridge Rail*, NCHRP Project 22-14, Texas Transportation Institute, College Station, Texas, 2008.

102. USA Today, "AAA: Fatal Motor Vehicle Crash Costs $6 Million", http://usatoday30.usatoday.com/news/nation/story/2011-11-02/fatal-vehicle-crashes-cost-millions/51051030/1, November 4, 2011.

11 APPENDICES

Appendix A. Elastomer Constitutive Equations

Hyperelastic materials are characterized by strain energy density (*W*) functions. Stress, which is of interest in non-linear finite element analysis, is the derivative of *W* with respect to strain. Strain energy density functions are usually expressed in terms of stretch ratios (λ) or strain invariants (I).

$$\lambda = L/L_0 = 1 + e$$

$$L = \text{deformed gauge length}$$

$$L_0 = \text{deformed gauge length}$$

$$e = \text{engineering strain}$$

Principal stretch ratios ($\lambda_1, \lambda_2, \lambda_3$) are found in the principal directions. The three strain invariants (I_1, I_2, I_3) are found as follows:

$$I_1 = {\lambda_1}^2 + {\lambda_2}^2 + {\lambda_3}^2$$

$$I_2 = {\lambda_1}^2{\lambda_2}^2 + {\lambda_2}^2{\lambda_3}^2 + {\lambda_3}^2{\lambda_1}^2$$

$$I_3 = {\lambda_1}^2{\lambda_2}^2{\lambda_3}^2$$

If the material is incompressible, $I_3 = 1$, because volume is constant. For a uniaxial stretch $\lambda_1 = \lambda$. If the material is incompressible, then $\lambda_2 = \lambda_3 = 1/\sqrt{\lambda}$. For an equibiaxial stretch, $\lambda_1 = \lambda_2 = \lambda$, and for an incompressible material $\lambda_3 = \lambda^{-2}$. The following constitutive equations for the rubber materials are found in the LS-DYNA Keyword User's Manual [13].

MAT_BLATZ-KO_RUBBER (MAT_007)

Blatz-Ko rubber is slightly compressible and does not have a strain energy density function. The second Piola-Kirchhoff stress is given by:

$$S_{ij} = G\left[V^{-1}C_{ij} - V^{\left(\frac{1}{1-2v}\right)}\delta_{ij}\right]$$

$$V = \text{relative volume}$$

$$C_{ij} = \text{Cauchy} - \text{Green strain tensor}$$

$$\upsilon = \text{Poisson's ratio}$$

The Cauchy stress is:

$$\sigma_{ij} = V^{-1} F_{ik} F_{jl} S_{kl}$$

$$F_{ij} = \text{deformation gradient tensor}$$

MAT_MOONEY-RIVLIN_RUBBER (MAT_027)

Mooney-Rivlin is an incompressible material model with the strain energy density function:

$$W = A(I_1 - 3) + B(I_2 - 3) + C\left(\frac{1}{{I_3}^2} - 1\right) + D(I_3 - 1)^2$$

A and *B* are user defined constants

$$2(A + B) = G$$

$$C = \frac{1}{2}A + B$$

$$D = \frac{A(5\upsilon - 2) + B(11\upsilon - 5)}{2(1 - 2\upsilon)}$$

$$I_1 = C_{ii}$$

$$I_2 = \frac{1}{2}{C_{ii}}^2 - \frac{1}{2}C_{ij}C_{ij}$$

$$I_3 = \det(C_{ij})$$

The second Piola-Kirchhoff stress tensor is:

$$S_{ij} = 2A\delta_{ij} + 2B\left(I_1\delta_{ij} - C_{ij}\right) - 4C\frac{1}{{I_3}^2}{C_{ij}}^{-1} + 4D(I_3 - 1)I_3{C_{ij}}^{-1}$$

The Cauchy stress tensor is:

$$\sigma_{ij} = \frac{1}{J}F_{ik}S_{kl}F_{jl}$$

$$J = \det(F_{ij})$$

MAT_FRAZER_NASH_RUBBER_MODEL (MAT_031)

The Frazer-Nash model is slightly compressible and implements a modified form of the hyperelastic constitutive law. The strain energy functional, U, is defined in terms of input constants:

$$U = C_{100}I_1 + C_{200}{I_1}^2 + C_{300}{I_1}^3 + C_{400}{I_1}^4 + C_{110}I_1I_{2+}C_{210}{I_1}^2I_2 + C_{010}I_2 + C_{020}{I_2}^2 + f(J)$$

Constants can defined directly or by a least squares fit

$$J = |F_{ij}|$$

$$I_1 = E_{ii}$$

$$I_2 = \frac{1}{2!}\delta^{ij}_{pq}E_{pi}E_{qj}$$

The second Piola-Kirchhoff stress tensor is:

$$S_{ij} = \frac{\partial U}{\partial E_{ij}}$$

The Cauchy stress tensors is:

$$\sigma_{ij} = V^{-1}F_{ik}F_{jl}S_{kl}$$

MAT_HYPERELASTIC_RUBBER (MAT_077_H)

This is a general hyperelastic rubber model with optional linear viscoelasticity. This model is effectively a Maxwell fluid with springs and dampers in series. A hydrostatic work term, $W_H(J)$, is included in the strain energy density function to model the rubber as an unconstrained material:

$$W = \sum_{p,q=0}^{n} C_{pq}{W_1}^p{W_2}^q + W_H(J)$$

Where $W_H(J) = \frac{K}{2}(J-1)^2$

C_{pq} is composed of a series of user defined constants $C_{01}, C_{10}, C_{11}, C_{20}, C_{02}, C_{30}$

$$K = \text{bulk modulus}$$

$$W_1 = I_1 {I_3}^{-1/3} - 3$$

$$W_2 = I_2 {I_3}^{-2/3} - 3$$

$$I_1 = {\lambda_1}^2 + {\lambda_2}^2 + {\lambda_3}^2$$

$$I_2 = {\lambda_1}^2{\lambda_2}^2 + {\lambda_2}^2{\lambda_3}^2 + {\lambda_3}^2{\lambda_1}^2$$

$$I_3 = {\lambda_1}^2{\lambda_2}^2{\lambda_3}^2$$

The constitutive tensor is first calculated in the principal basis.

The principal Kirchhoff stress components are:

$$\tau_{ii}^E = \lambda_i \frac{\partial W}{\partial \lambda_i}$$

Kirchhoff stresses transformed to the standard basis:

$$\tau_{ij} = q_{ik} q_{jl} \tau_{kl}^E$$

The Cauchy stress is:

$$\sigma_{ij} = J^{-1} \tau_{ij}$$

$q_{ij} =$ orthogonal tensor components containing eigenvectors of the principal basis

MAT_OGDEN_RUBBER (MAT_077_O)

This is a general hyperelastic rubber model with optional linear viscoelasticity. This model is effectively a Maxwell fluid with springs and dampers in series. A hydrostatic work term, $W_H(J)$, is included in the strain energy density function to model the rubber as an unconstrained material:

$$W = \sum_{m=1}^{n} \frac{\mu_m}{\alpha_m} \left({\tilde{\lambda}_1}^{\alpha_m} + {\tilde{\lambda}_2}^{\alpha_m} + {\tilde{\lambda}_3}^{\alpha_m} - 3 \right) + W_H(J)$$

μ_m and α_m are material parameters

$$\tilde{\lambda}_i = \frac{\lambda_i}{J^{1/3}}$$

The principal Kirchhoff stress components are:

$$\tau_{ii}^E = \lambda_i \frac{\partial W}{\partial \lambda_i}$$

The Kirchhoff stresses are transformed to the standard basis:

$$\tau_{ij} = q_{ik} q_{jl} \tau_{kl}^E$$

$$\sigma_{ij} = J^{-1} \tau_{ij}$$

MAT_CELLULAR_RUBBER (MAT_087)

This model is essentially the same as the Mooney-Rivlin model with the addition of air pressure and viscosity. A hydrostatic work term, $W_H(J)$, is included in the strain energy density function to model rubber as an unconstrained material:

$$W(J_1, J_2, J) = \sum_{p,q=0}^{n} C_{pq}(J_1 - 3)^p (J_2 - 3)^q + W_H(J)$$

The second invariants are modified to prevent volumetric work from contributing to the hydrostatic work:

$$J_1 = I_1 {I_3}^{-1/3}$$

$$J_2 = I_2 {I_3}^{-2/3}$$

Since the cellular rubber includes air voids, the stress is modified by the air pressure:

$$\sigma_{ij} = \sigma_{ij}^{sk} - \delta_{ij} \sigma^{air}$$

Where $\sigma_{ij}^{sk} =$ the bulk skeletal stress

and $\sigma^{air} =$ air pressure, which is based on the initial foam pressure, relative volume of voids, and initial volumetric strain

The rubber skeletal material is assumed to be incompressible. Rate effects are taken into account through linear viscoelasticity through

$$\sigma_{ij} = \int_0^t g_{ijkl}(1-\tau)\frac{\partial \varepsilon_{kl}}{\partial \tau}\,d\tau$$

The second Piola-Kirchhoff stress is

$$S_{ij} = \int_0^t G_{ijkl}(1-\tau)\frac{\partial E_{kl}}{\partial \tau}\,d\tau$$

Where $g_{ijkl}(1-\tau)$ and $G_{ijkl}(1-\tau)$ are the relaxation functions.

MAT_ARRUDA_BOYCE_RUBBER (MAT_127)

The Arruda-Boyce model also includes the hydrostatic work term in the strain energy density function:

$$W(J_1,J_2,J) = nk\theta\left[\frac{1}{2}(J_1-3)+\frac{1}{20N}(J_1^2-9)+\frac{11}{1050N^2}(J_1^3-27)\right]$$
$$+ nk\theta\left[\frac{19}{7000N^3}\left(J_1{}^4-81\right)+\frac{519}{673750N^4}(J_1^5-9)\right]+W_H(J)$$

Where $W_H(J) = \frac{K}{2}(J-1)^2$

Rate effects are taken into account through linear viscoelasticity through:

$$\sigma_{ij} = \int_0^t g_{ijkl}(1-\tau)\frac{\partial \varepsilon_{kl}}{\partial \tau}\,d\tau$$

The second Piola-Kirchhoff stress is

$$S_{ij} = \int_0^t G_{ijkl}(1-\tau)\frac{\partial E_{kl}}{\partial \tau}\,d\tau$$

MAT_SIMPLIFIED_RUBBER/FOAM (MAT_181)

The Simplified material model is a quasi-hyperelastic rubber, because there is no strain energy density function for determining stresses, which is “simplified” over other models. The hyperelastic constitutive law is determined by:

$$W = W(\lambda_1, \lambda_2, \lambda_3)$$

The principal Kirchhoff stress components are determined by:

$$\tau_{ii}^{E} = \lambda_i \frac{\partial W}{\partial \lambda_i}$$

$$\tau_{ij} = q_{ik} q_{jl} \tau_{kl}^{E}$$

Where q_{ij} are the components of the orthogonal tensor containing the eigenvectors of the principal basis. The Cauchy stress is:

$$\sigma_{ij} = J^{-1} \tau_{ij}$$

Where $J = \lambda_1 \lambda_2 \lambda_3$

The components are transformed to the standard basis. The principal Kirchhoff stress is:

$$\tau_{ii}^{E} = f(\lambda_i) + K(J-1) - \frac{1}{3} \sum_{k=1}^{3} f(\lambda_k)$$

Where *f* is a load curve from uniaxial data

An elastic-plastic stress σ_d can also be added to model the frequency independent damping properties of rubber.

MAT_SIMPLIFIED_RUBBER_WITH_DAMAGE (MAT_183)

This model is similar to the Simplified Rubber model, only with an additional uniaxial curve for unloading.

Appendix B. Single-Element Finite Element Rubber Models

Each rubber material model is listed at the top of the page. The rubber type is from the actual tension test specimens. The input parameters for the material model are listed. The mass density was 1.15×10^{-6} kg/mm^3 (71.8 lb/ft^3). Where tension test data was required, the curves were either:

```
$ 60 durometer EPDM Tension Test
*DEFINE_CURVE
$
$     lcid      sidr      scla      sclo      offa      offo
         3                25.4 .00444822
$
$........>.........1.........>.........2
$               [in]                [lb]
                 0.0                 0.0
           0.0270655           1.3132730
           0.0739562           4.6949513
           0.1542911           8.3721170
           0.3327171          13.5595470
           0.4283950          15.7264490
           0.6692268          18.8126419
           1.0855543          23.4419296
           5.9944248          63.0042880

$ 80 durometer EPDM Tension Test
*DEFINE_CURVE
$
$     lcid      sidr      scla      sclo      offa      offo
         3                25.4 .00444822
$
$........>.........1.........>.........2
$               [in]                [lb]
                 0.0                 0.0
            0.026717            2.702093
            0.132738           10.696643
            0.370295           22.210766
            0.458215           25.789437
            0.728526           35.931189
            1.037798           45.711797
            1.459642           56.927149
            2.340566           76.649232
            3.343372           96.374594
            5.996835          140.142707
```

The element type was either Belytschko-Tsay Shell or Constant Stress Solid. The rate at which the element was stretched in the simulation was either 0.00085 mm/ms (2 in./min.) or 0.085 mm/ms (200 in./min.). The total simulation run time was using 1 dual core processor, MPP processing. Additional comments and errors that occurred are listed. Sequential photos and the force vs. deflection curve are also shown.

The single elements were 38 mm (1.5 in.) wide and 101.6 mm (4 in.) long. The 60-durometer elements had a thickness of 1.96-mm, and the 80-durometer elements had a thickness of 2.34-mm. The specimens were stretched for 152.4 mm (6 in.). The geometry, rate of stretching, element type, and material properties were the only parameters varied between simulations. The top nodes were stretched using *BOUNDARY_PRESCRIBED_MOTION with a velocity vs. time curve. The bottom nodes were fixed in the direction of stretching using *BOUNDARY_SPC.

*MAT_BLATZ-KO_RUBBER (*MAT_007)

Sequentials:

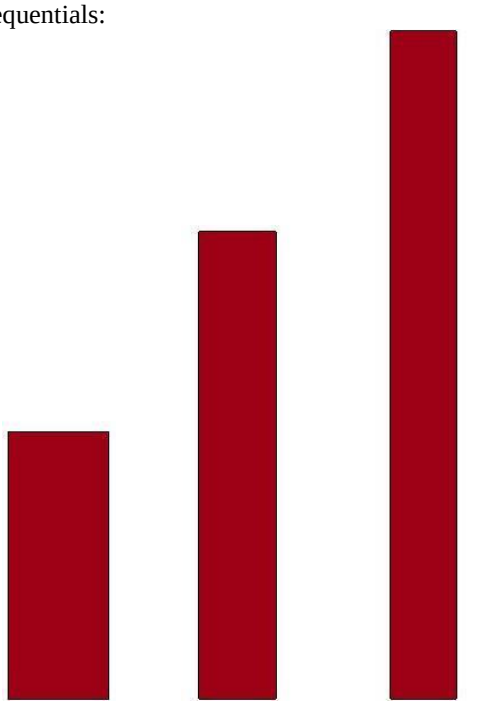

Rubber Type: 60 durometer EPDM
Input Parameters -
Shear Modulus: 6.65×10^{-4} GPa (92 psi)
Element Type: Belytschko-Tsay Shell
Rate: 0.00085 mm/ms (2 in./min.)
Comments:
Force vs. Deflection:

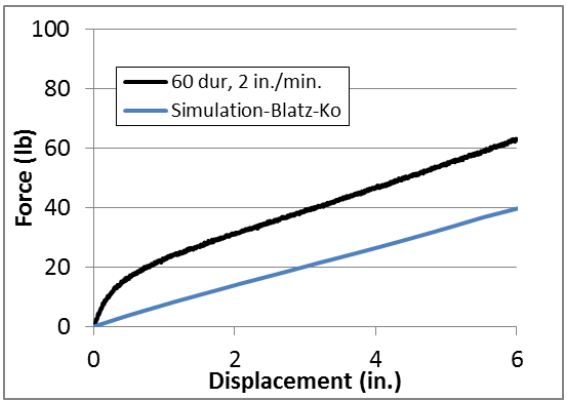

*MAT_BLATZ-KO_RUBBER (*MAT_007)

Sequentials:

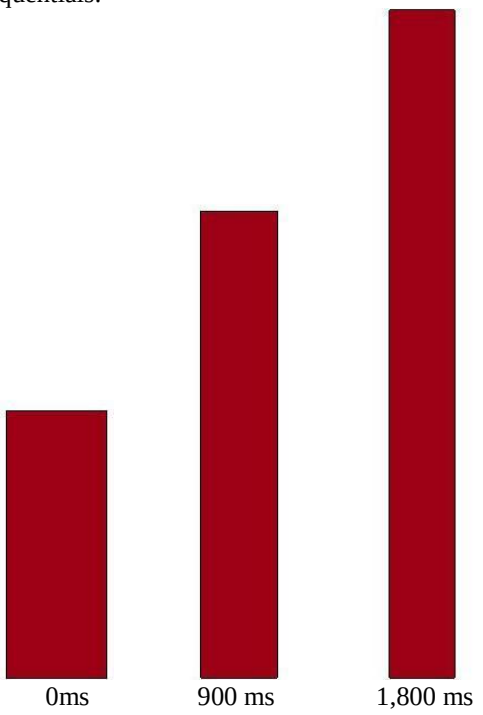

Rubber Type: 60 durometer EPDM
Input Parameters -
Shear Modulus: 6.65×10^{-4} GPa (92 psi)
Element Type: Belytschko-Tsay Shell
Rate: 0.085 mm/ms (200 in./min.)
Comments:
Force vs. Deflection:

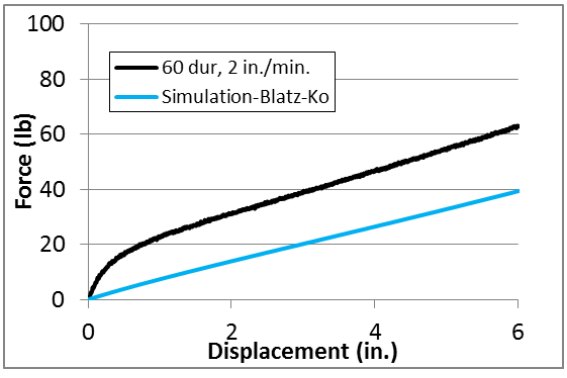

*MAT_MOONEY-RIVLIN_RUBBER (*MAT_027)

Sequentials:

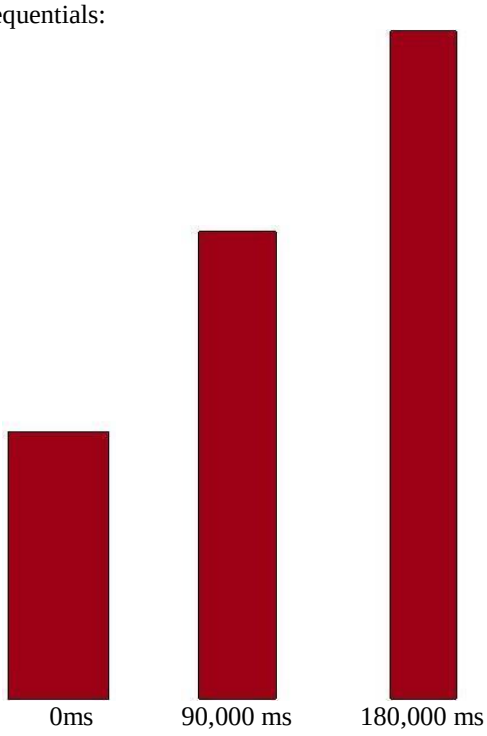

Rubber Type: 60 durometer EPDM
Input Parameters -
60 Durometer EPDM Tension Test
Poisson's Ratio: 0.495
Element Type: Belytschko-Tsay Shell
Rate: 0.00085 mm/ms (2 in./min.)
Comments:
Force vs. Deflection:

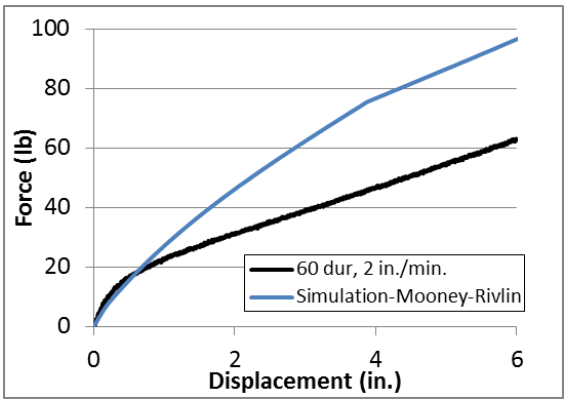

*MAT_MOONEY-RIVLIN_RUBBER (*MAT_027)

Sequentials:

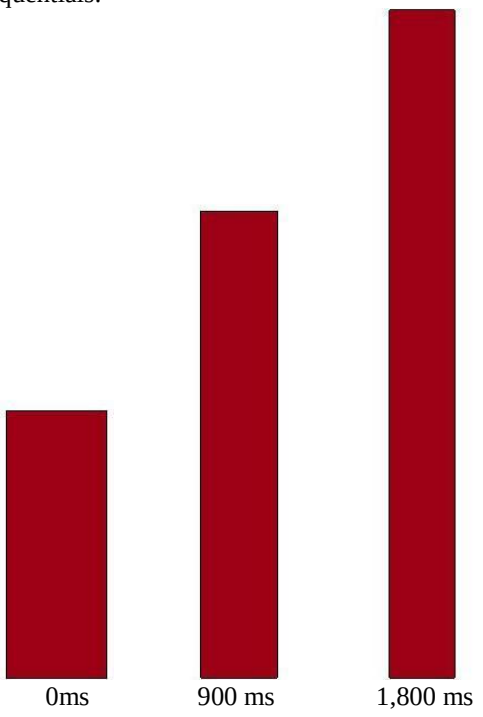

Rubber Type: 60 durometer EPDM
Input Parameters -
60 Durometer EPDM Tension Test
Poisson's Ratio: 0.495
Element Type: Belytschko-Tsay Shell
Rate: 0.085 mm/ms (200 in./min.)
Comments:
Force vs. Deflection:

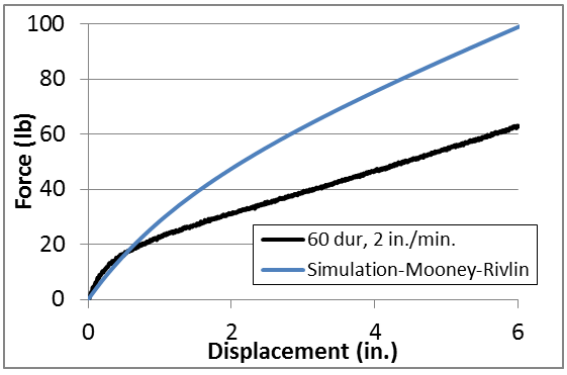

*MAT_HYPERELASTIC_RUBBER (*MAT_077_H)

Sequentials:

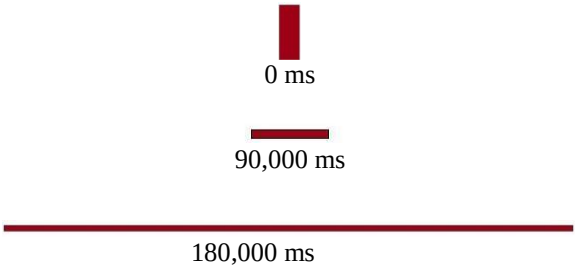

Rubber Type: 60 durometer EPDM
Input Parameters -
60 Durometer EPDM Tension Test
Poisson's Ratio: 0.495
N: 2
Element Type: Belytschko-Tsay Shell
Rate: 0.00085 mm/ms (2 in./min.)
Comments: element is shown small to see full deformation - deformation occurs in wrong direction, forces very high
Force vs. Deflection:

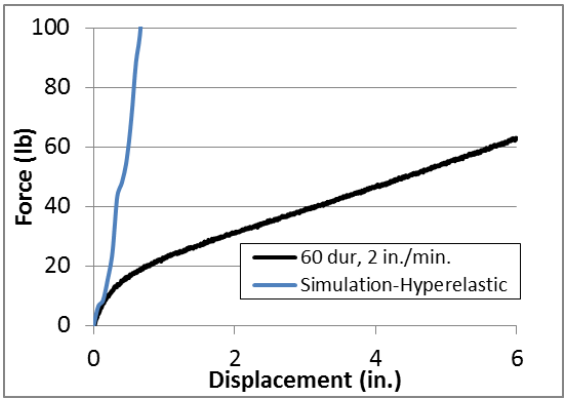

*MAT_HYPERELASTIC_RUBBER (*MAT_077_H)

Sequentials:

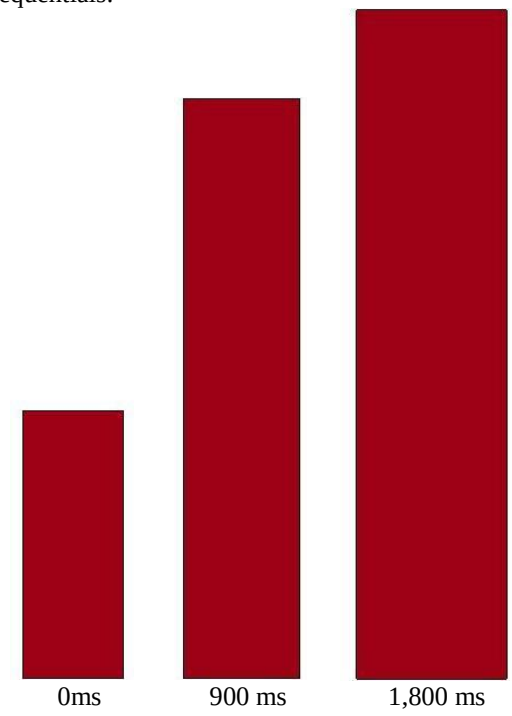

Rubber Type: 60 durometer EPDM
Input Parameters -
60 Durometer EPDM Tension Test
Poisson's Ratio: 0.495
N: 2
Element Type: Belytschko-Tsay Shell
Rate: 0.085 mm/ms (200 in./min.)
Comments: width starts decreasing, then starts increasing after 720 ms
Force vs. Deflection:

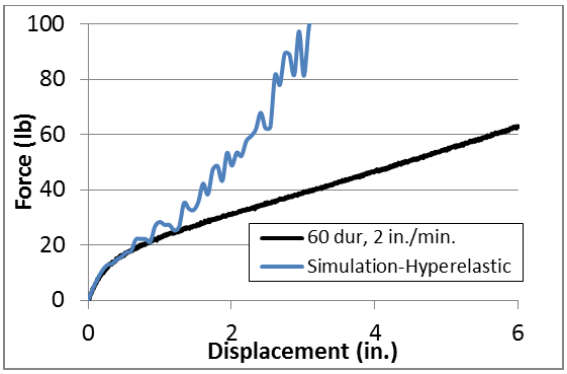

*MAT_OGDEN_RUBBER (*MAT_077_O)

Sequentials:

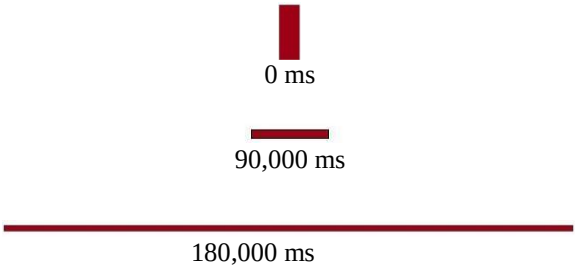

Rubber Type: 60 durometer EPDM
Input Parameters -
60 Durometer EPDM Tension Test
Poisson's Ratio: 0.495
N: 2
Element Type: Belytschko-Tsay Shell
Rate: 0.00085 mm/ms (2 in./min.)
Comments: element is shown small to see full deformation - deformation occurs in wrong direction, forces very high
Force vs. Deflection:

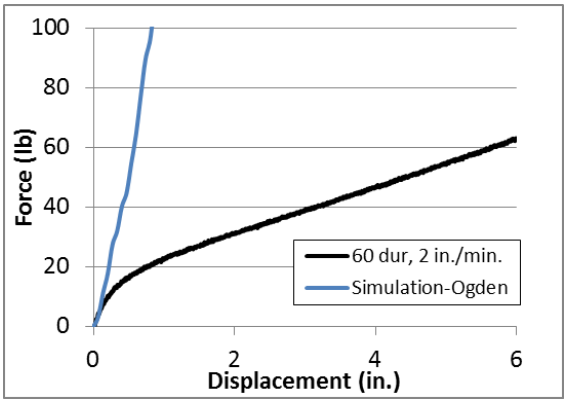

*MAT_OGDEN_RUBBER (*MAT_077_O)

Sequentials:

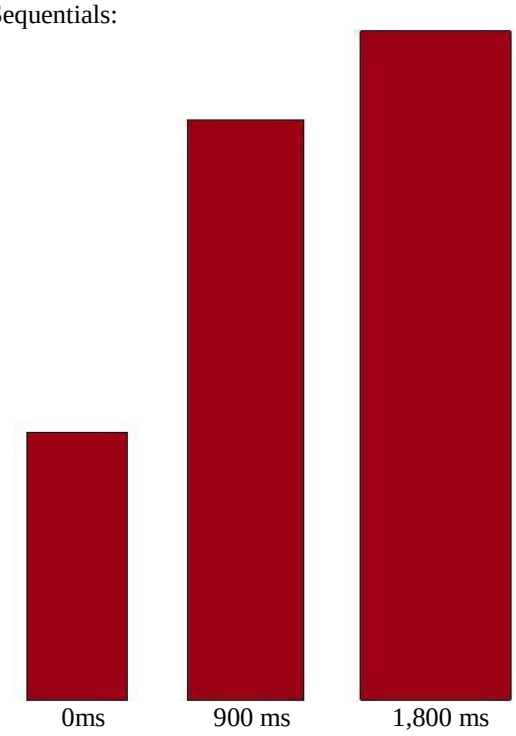

Rubber Type: 60 durometer EPDM
Input Parameters -
60 Durometer EPDM Tension Test
Poisson's Ratio: 0.495
N: 2
Element Type: Belytschko-Tsay Shell
Rate: 0.085 mm/ms (200 in./min.)
Comments: width starts decreasing, then starts increasing after 1140 ms
Force vs. Deflection:

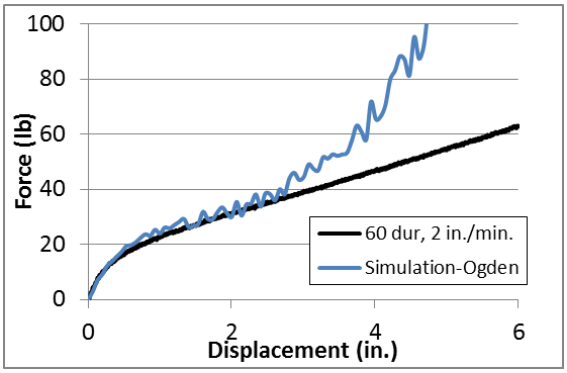

*MAT_SIMPLIFIED_RUBBER/FOAM (*MAT_181)

Sequentials:

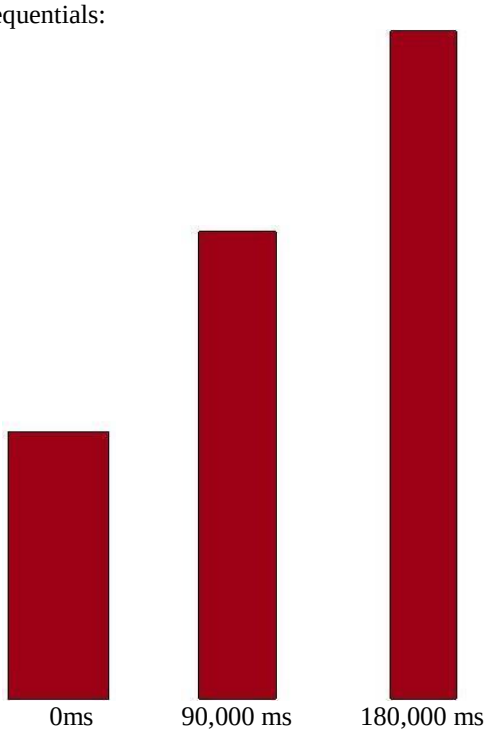

Rubber Type: 60 durometer EPDM
Input Parameters -
60 Durometer EPDM Tension Test
Bulk modulus: 0.103 GPa, 0.517 GPa, 1.4 GPa
Element Type: Belytschko-Tsay Shell
Rate: 0.00085 mm/ms (2 in./min.)
Comments:
Force vs. Deflection:

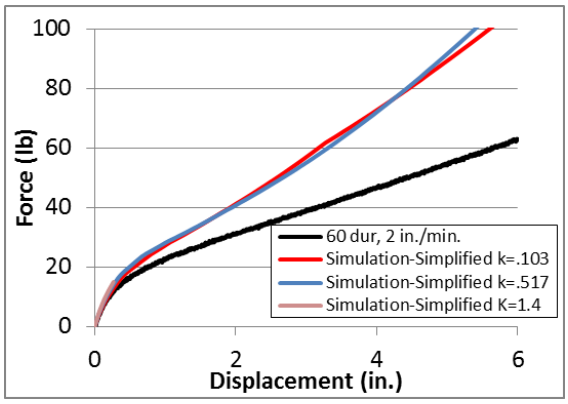

*MAT_SIMPLIFIED_RUBBER/FOAM (*MAT_181)

Sequentials:

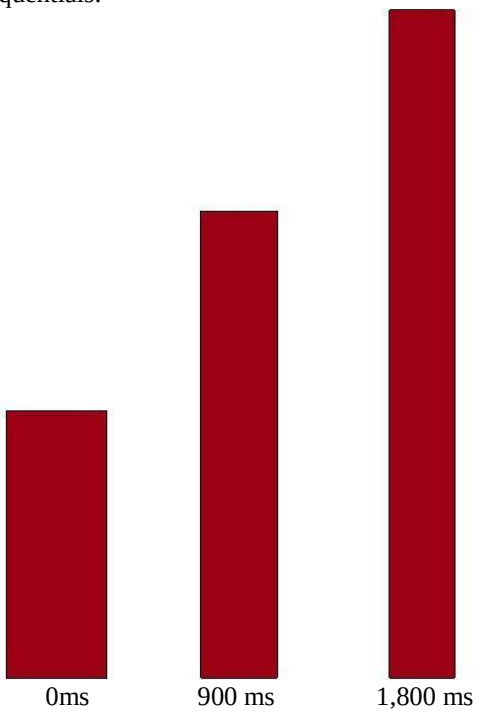

Rubber Type: 60 durometer EPDM
Input Parameters -
60 Durometer EPDM Tension Test
Bulk modulus: 0.103 GPa, 0.517 GPa, 1.4 GPa
Element Type: Belytschko-Tsay Shell
Rate: 0.085 mm/ms (200 in./min.)
Comments:
Force vs. Deflection:

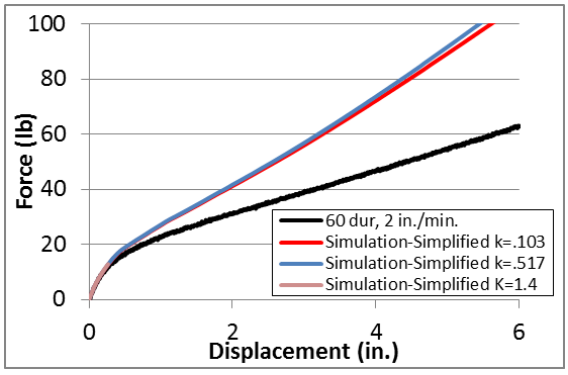

*MAT_BLATZ-KO_RUBBER (*MAT_007)

Sequentials:

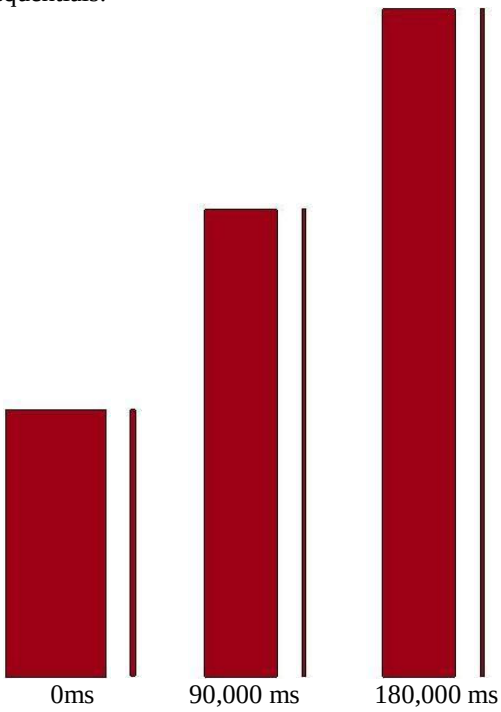

Rubber Type: 60 durometer EPDM
Input Parameters -
Shear Modulus: 6.65x10^{-4} GPa (92 psi)
Element Type: Constant Stress Solid
Rate: 0.00085 mm/ms (2 in./min.)
Comments:
Force vs. Deflection:

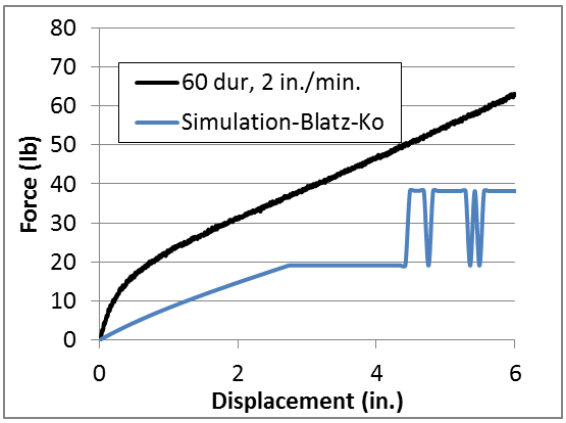

*MAT_BLATZ-KO_RUBBER (*MAT_007)

Sequentials:

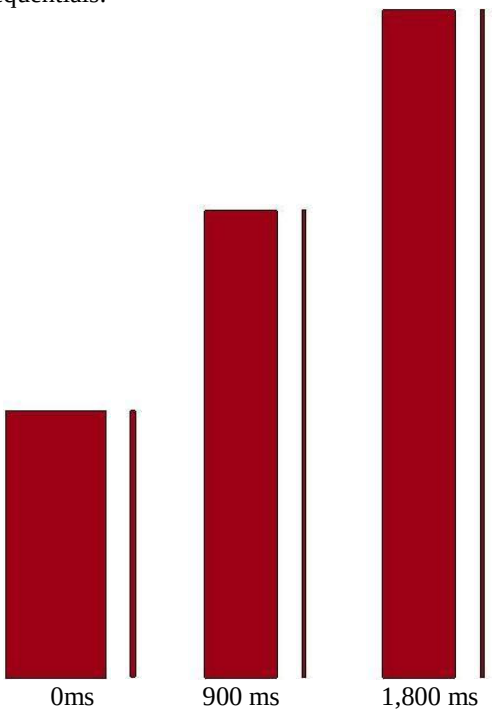

Rubber Type: 60 durometer EPDM
Input Parameters -
Shear Modulus: 6.65x10^{-4} GPa (92 psi)
Element Type: Constant Stress Solid
Rate: 0.085 mm/ms (200 in./min.)
Comments:
Force vs. Deflection:

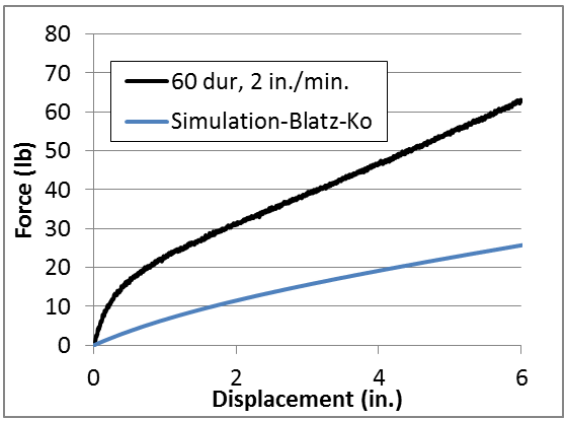

*MAT_MOONEY-RIVLIN_RUBBER (*MAT_027)

Sequentials:

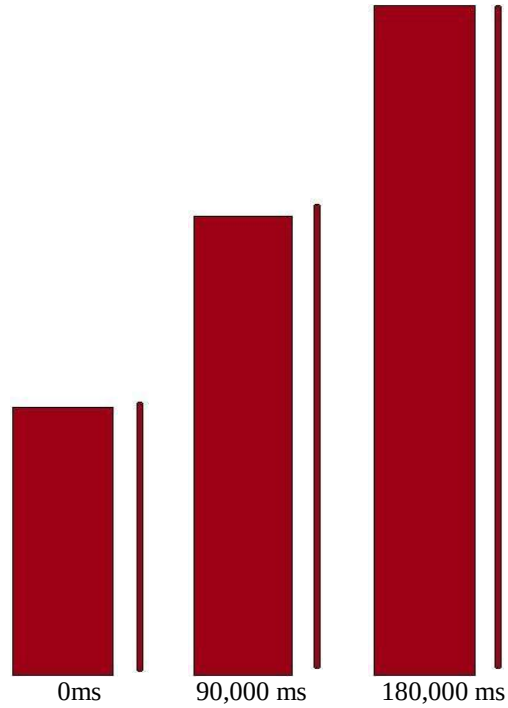

Rubber Type: 60 durometer EPDM
Input Parameters –
60 Durometer EPDM Tension Test
Poisson's Ratio: 0.495
Element Type: Constant Stress Solid
Rate: 0.00085 mm/ms (2 in./min.)
Comments: volume is not constant, forces near zero
Force vs. Deflection:

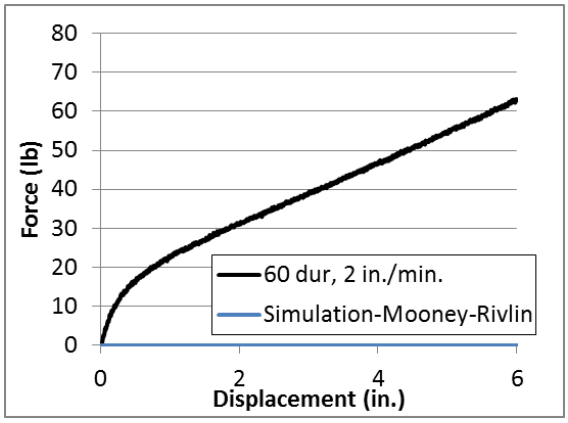

*MAT_MOONEY-RIVLIN_RUBBER (*MAT_027)

Sequentials:

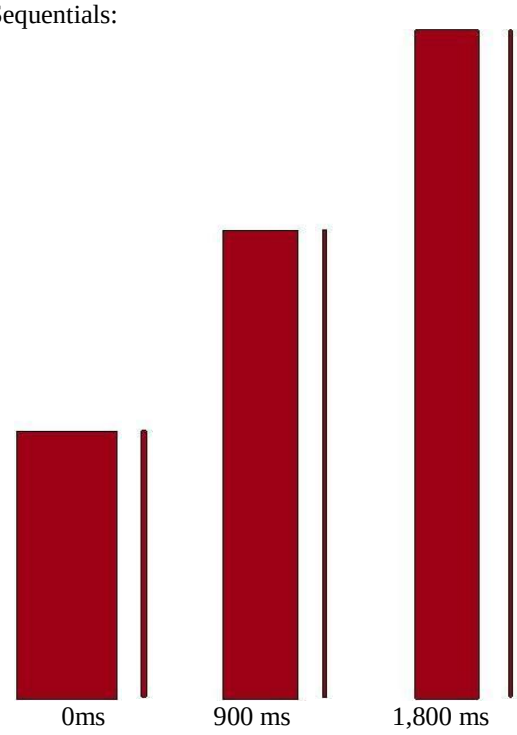

Rubber Type: 60 durometer EPDM
Input Parameters –
60 Durometer EPDM Tension Test
Poisson's Ratio: 0.495
Element Type: Constant Stress Solid
Rate: 0.085 mm/ms (200 in./min.)
Comments:
Force vs. Deflection:

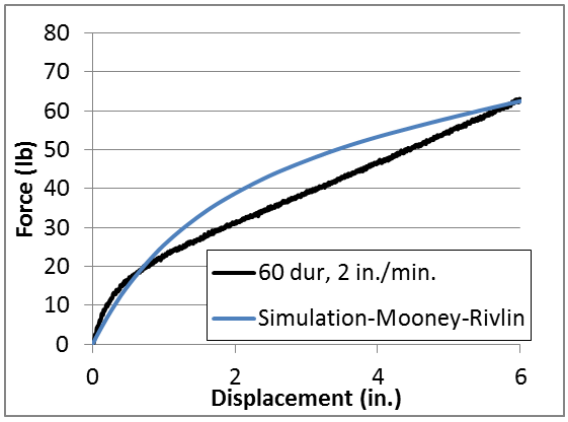

*MAT_FRAZER_NASH_RUBBER_MODEL (*MAT_031)

Sequentials:

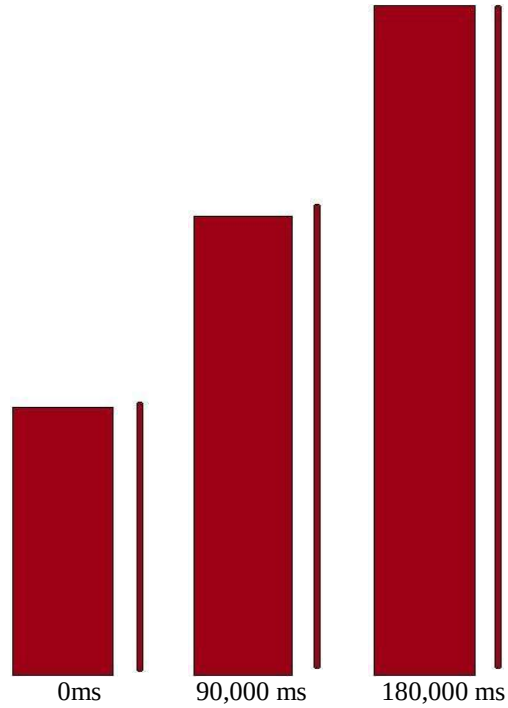

Rubber Type: 60 durometer EPDM
Input Parameters –
60 Durometer EPDM Tension Test
Poisson's Ratio: 0.495
Element Type: Constant Stress Solid
Rate: 0.00085 mm/ms (2 in./min.)
Comments: volume is not constant, forces near zero
Force vs. Deflection:

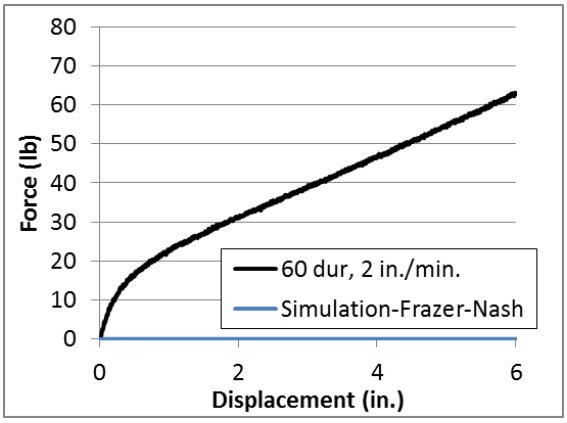

*MAT_FRAZER_NASH_RUBBER_MODEL (*MAT_031)

Sequentials:

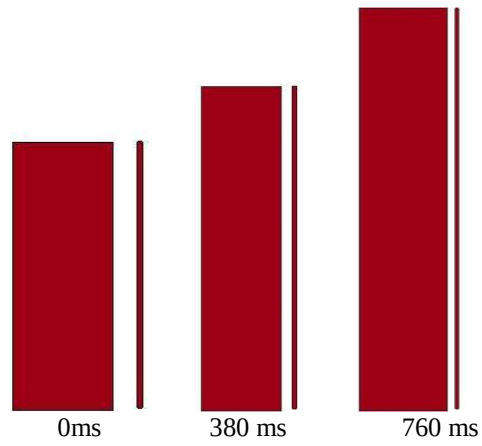

Rubber Type: 60 durometer EPDM
Input Parameters –
60 Durometer EPDM Tension Test
Poisson's Ratio: 0.495
Element Type: Constant Stress Solid
Rate: 0.085 mm/ms (200 in./min.)
Comments: forces near zero, element widens and
negative volume in element at 760 ms
Force vs. Deflection:

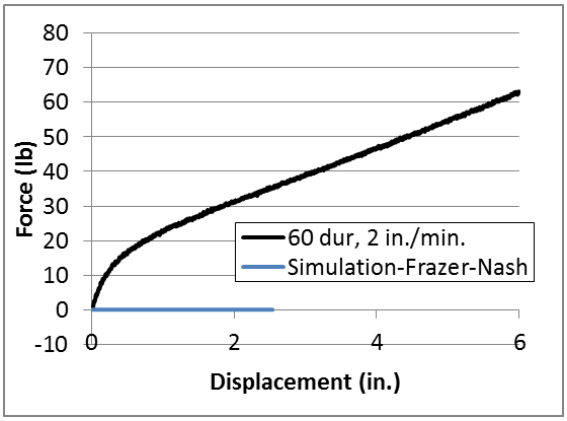

*MAT_HYPERELASTIC_RUBBER (*MAT_077_H)

Sequentials:

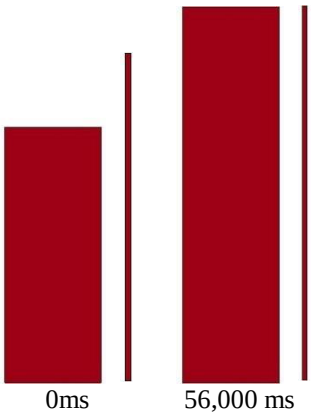

Rubber Type: 60 durometer EPDM
Input Parameters –
60 Durometer EPDM Tension Test
Poisson's Ratio: 0.495
N: 2
Element Type: Constant Stress Solid
Rate: 0.00085 mm/ms (2 in./min.)
Comments: volume is not constant, forces near zero, out of range velocities after 56,000 ms
Force vs. Deflection:

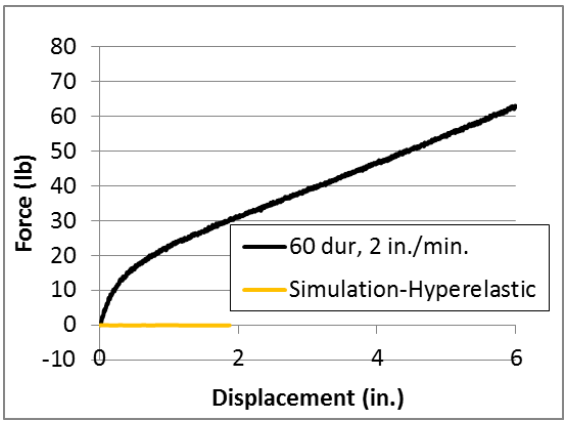

*MAT_HYPERELASTIC_RUBBER (*MAT_077_H)

Sequentials:

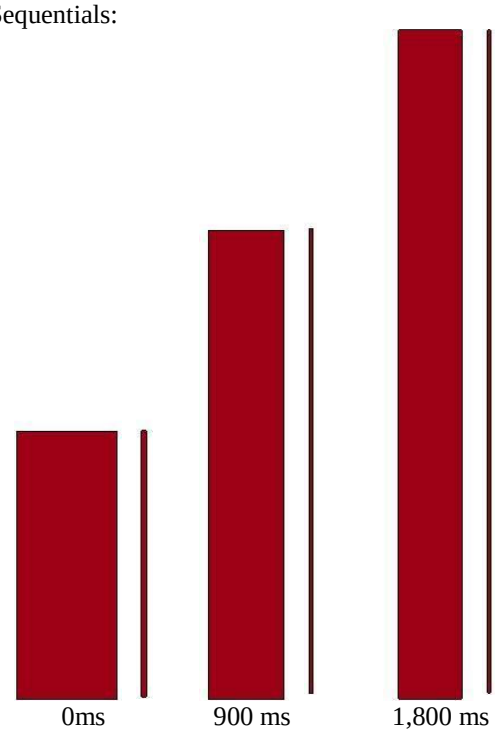

Rubber Type: 60 durometer EPDM
Input Parameters –
60 Durometer EPDM Tension Test
Poisson's Ratio: 0.495
N: 2
Element Type: Constant Stress Solid
Rate: 0.085 mm/ms (200 in./min.)
Comments:
Force vs. Deflection:

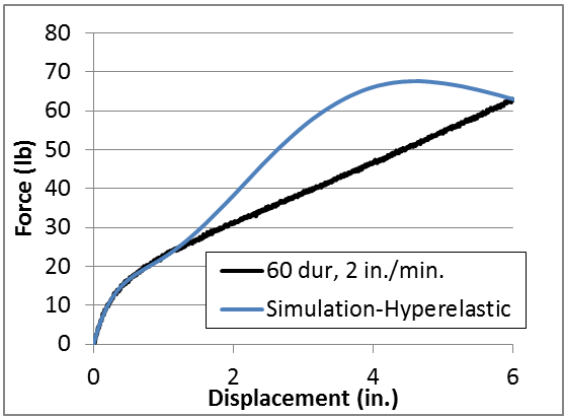

*MAT_OGDEN_RUBBER (*MAT_077_O)

Sequentials:

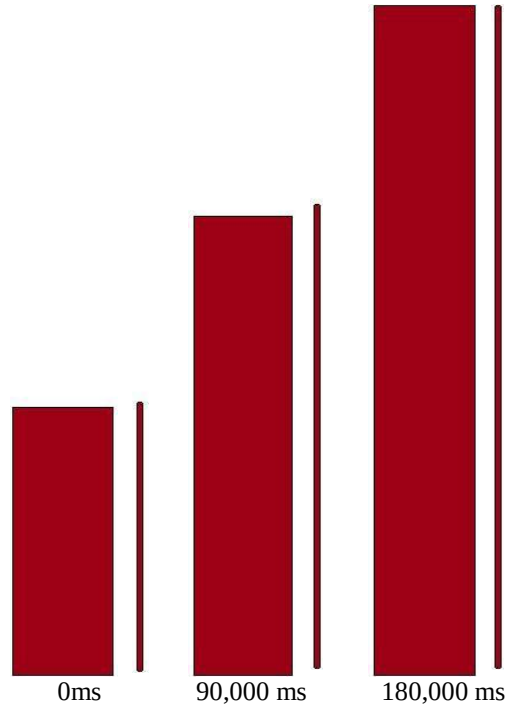

Rubber Type: 60 durometer EPDM
Input Parameters –
60 Durometer EPDM Tension Test
Poisson's Ratio: 0.495
N: 2
Element Type: Constant Stress Solid
Rate: 0.00085 mm/ms (2 in./min.)
Comments: volume is not constant
Force vs. Deflection:

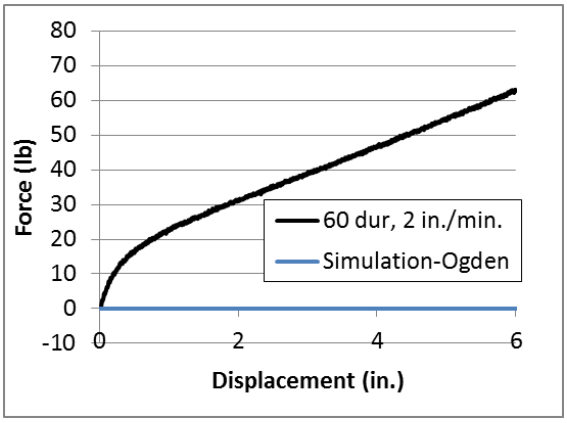

*MAT_OGDEN_RUBBER (*MAT_077_O)

Sequentials:

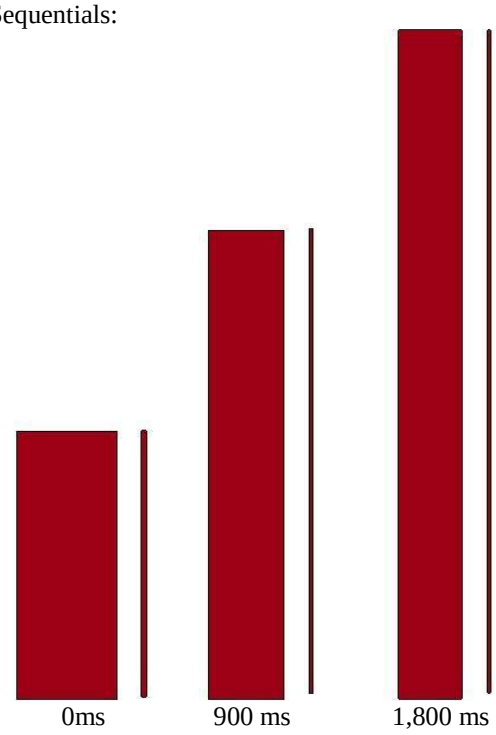

Rubber Type: 60 durometer EPDM
Input Parameters –
60 Durometer EPDM Tension Test
Poisson's Ratio: 0.495
N: 2
Element Type: Constant Stress Solid
Rate: 0.085 mm/ms (200 in./min.)
Comments:
Force vs. Deflection:

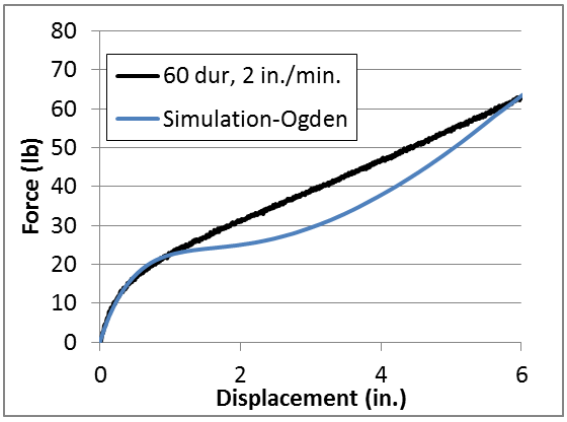

*MAT_ARRUDA_BOYCE_RUBBER (*MAT_127)

Sequentials: not available

Rubber Type: 60 durometer EPDM
Input Parameters –
Bulk modulus: 0.103 GPa, 0.517 GPa, 1.4 GPa
Shear modulus: 6.65×10^{-4} GPa (92 psi)
Element Type: Constant Stress Solid
Rate: 0.00085 mm/ms (2 in./min.)
Comments: nodes with out of range velocities immediately with all shear moduli
Force vs. Deflection: not available

*MAT_ARRUDA_BOYCE_RUBBER (*MAT_127)

Sequentials: not available

Rubber Type: 60 durometer EPDM
Input Parameters –
Bulk modulus: 0.103 GPa, 0.517 GPa, 1.4 GPa
Shear modulus: 6.65×10^{-4} GPa (92 psi)
Element Type: Constant Stress Solid
Rate: 0.085 mm/ms (200 in./min.)
Comments: nodes with out of range velocities immediately with all shear moduli not available

*MAT_SIMPLIFIED_RUBBER/FOAM (*MAT_181)

Sequentials:

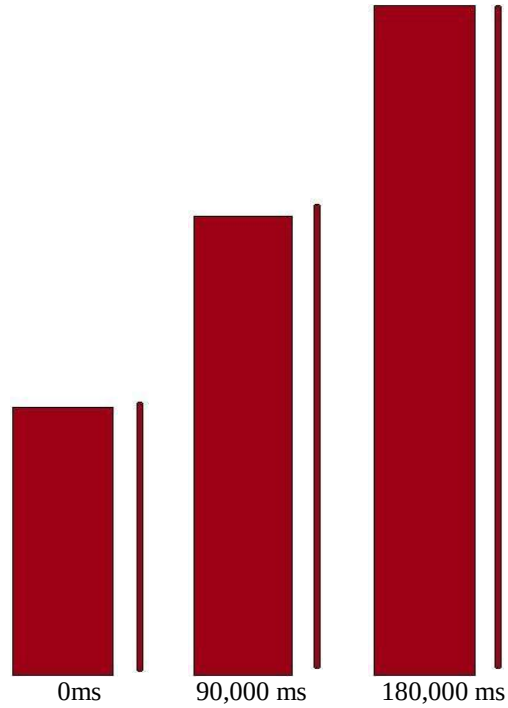

Rubber Type: 60 durometer EPDM
Input Parameters –
60 Durometer EPDM Tension Test
Bulk modulus: 0.103 GPa, 0.517 GPa, 1.4 GPa
Element Type: Constant Stress Solid
Rate: 0.00085 mm/ms (2 in./min.)
Comments: volume is not constant
Force vs. Deflection:

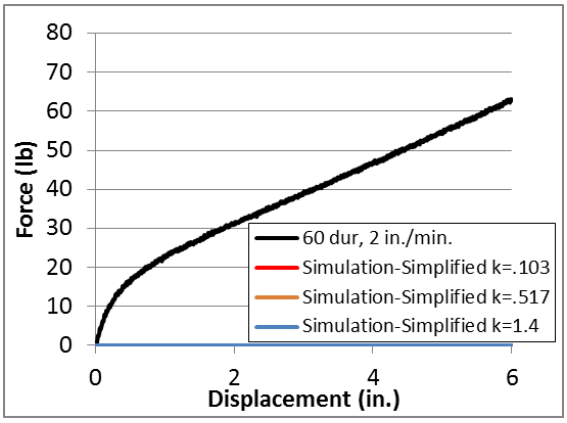

*MAT_SIMPLIFIED_RUBBER/FOAM (*MAT_181)

Sequentials:

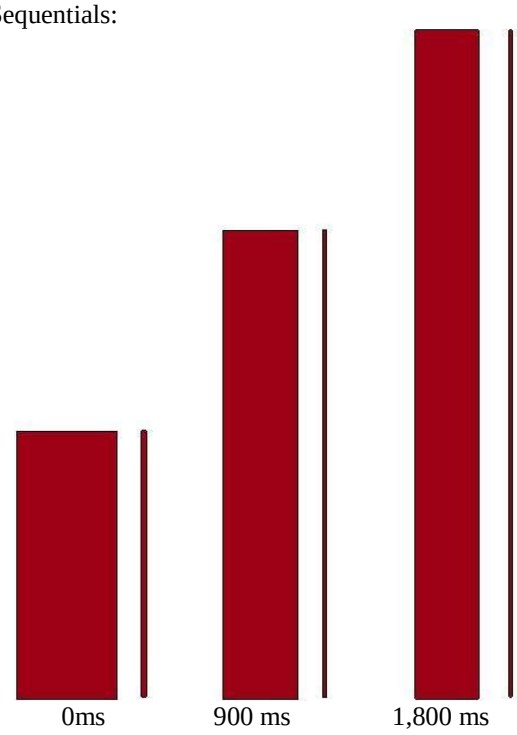

Rubber Type: 60 durometer EPDM
Input Parameters –
60 Durometer EPDM Tension Test
Bulk modulus: 0.103 GPa, 0.517 GPa, 1.4 GPa
Element Type: Constant Stress Solid
Rate: 0.085 mm/ms (200 in./min.)
Comments:
Force vs. Deflection:

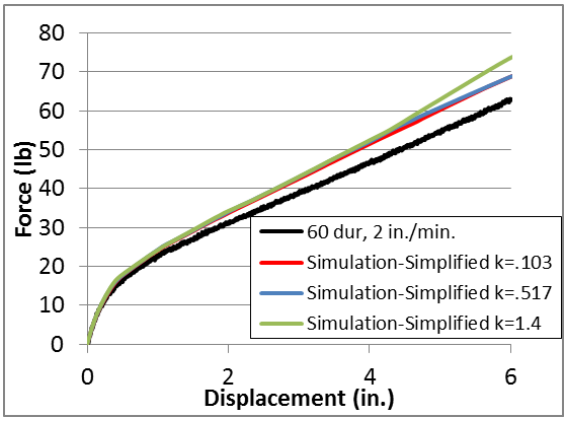

*MAT_BLATZ-KO_RUBBER (*MAT_007)

Sequentials:

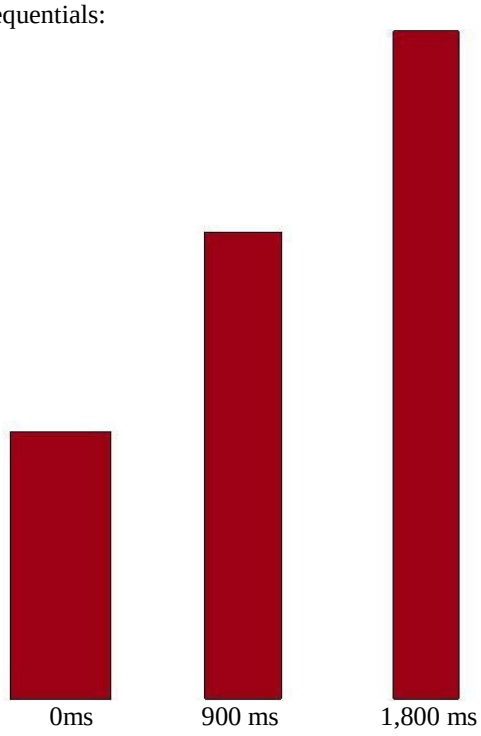

Rubber Type: 80 durometer EPDM
Input Parameters -
Shear Modulus: 1.24 MPa (180 psi)
Element Type: Belytschko-Tsay Shell
Rate: 0.085 mm/ms (200 in./min.)
Comments:
Force vs. Deflection:

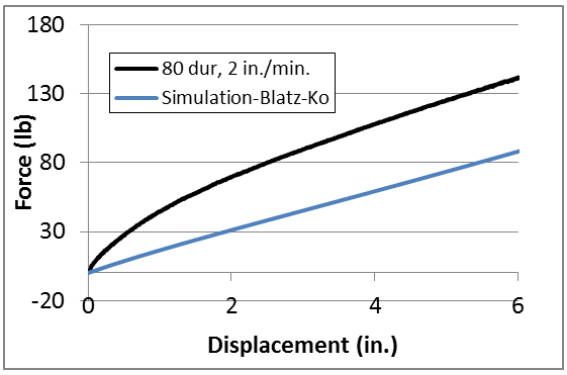

*MAT_MOONEY-RIVLIN_RUBBER (*MAT_027)

Sequentials:

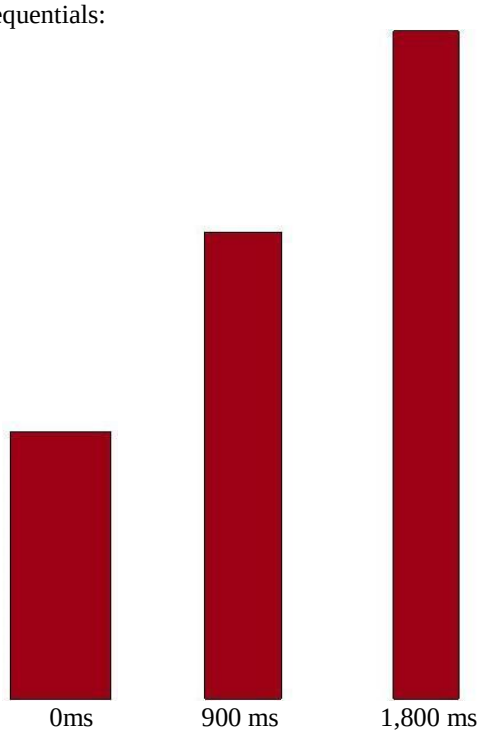

Rubber Type: 80 durometer EPDM
Input Parameters -
80 Durometer EPDM Tension Test
Poisson's Ratio: 0.495
Element Type: Belytschko-Tsay Shell
Rate: 0.085 mm/ms (200 in./min.)
Comments:
Force vs. Deflection:

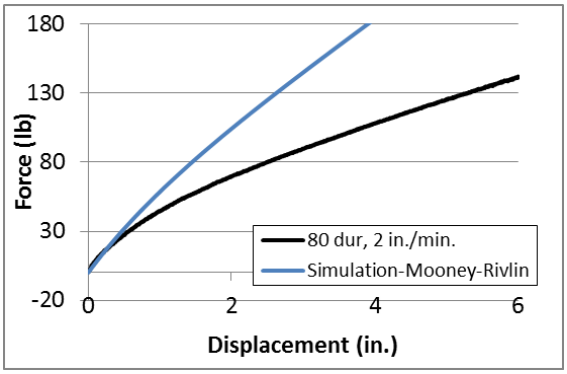

*MAT_HYPERELASTIC_RUBBER (*MAT_077_H)

Sequentials:

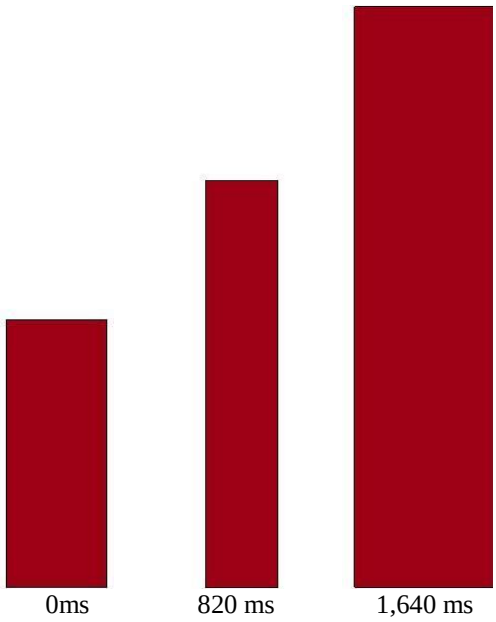

Rubber Type: 80 durometer EPDM
Input Parameters -
80 Durometer EPDM Tension Test
Poisson's Ratio: 0.495
N: 2
Element Type: Belytschko-Tsay Shell
Rate: 0.085 mm/ms (200 in./min.)
Comments: element gets wider after 1,180 ms, nodes with out of range velocities at 1,640 ms
Force vs. Deflection:

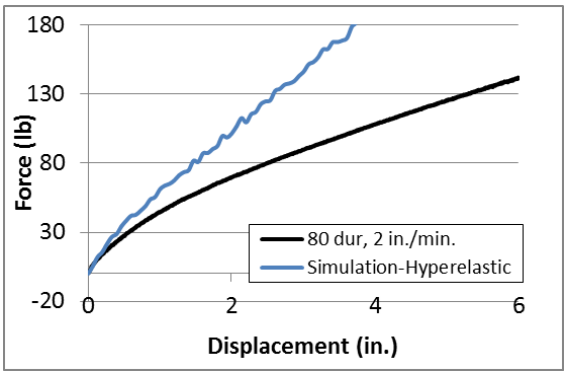

*MAT_OGDEN_RUBBER (*MAT_077_O)

Sequentials:

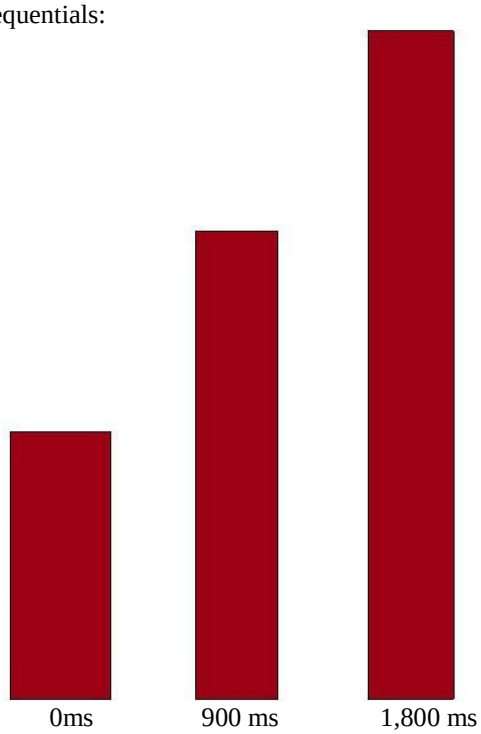

Rubber Type: 80 durometer EPDM
Input Parameters -
80 Durometer EPDM Tension Test
Poisson's Ratio: 0.495
N: 2
Element Type: Belytschko-Tsay Shell
Rate: 0.085 mm/ms (200 in./min.)
Comments: element gets wider after 1,540 ms
Force vs. Deflection:

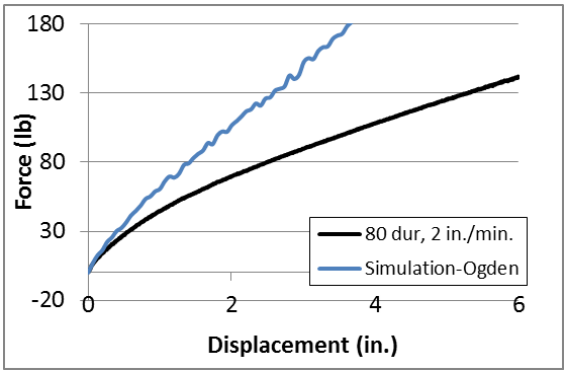

*MAT_SIMPLIFIED_RUBBER/FOAM (*MAT_181)

Sequentials:

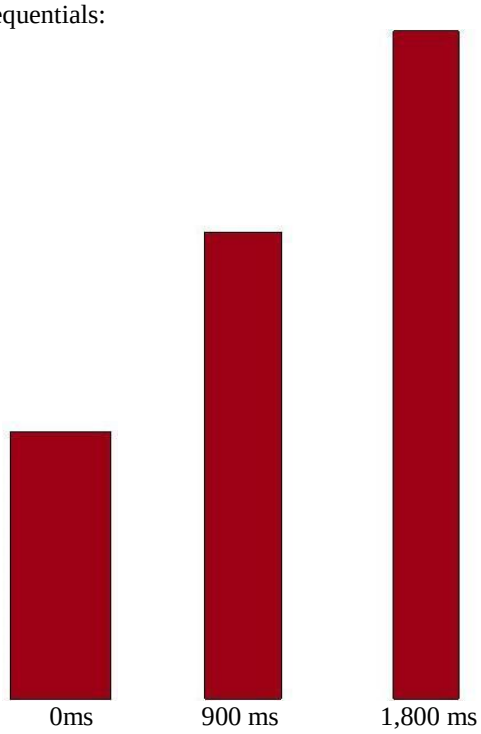

Rubber Type: 80 durometer EPDM
Input Parameters -
80 Durometer EPDM Tension Test
Bulk modulus: 0.103 GPa, 0.517 GPa, 1.4 GPa
Element Type: Belytschko-Tsay Shell
Rate: 0.085 mm/ms (200 in./min.)
Comments:
Force vs. Deflection:

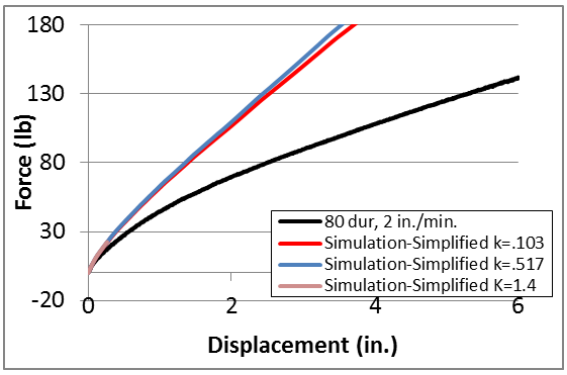

*MAT_BLATZ-KO_RUBBER (*MAT_007)

Sequentials:

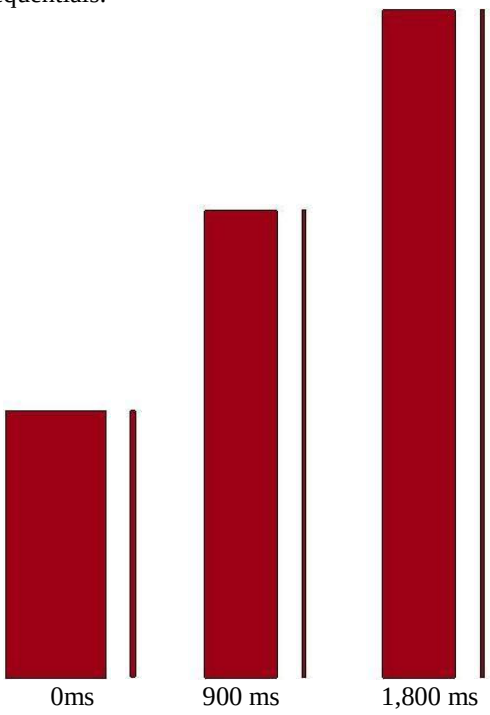

Rubber Type: 80 durometer EPDM
Input Parameters -
Shear Modulus: 1.24 MPa (180 psi)
Element Type: Constant Stress Solid
Rate: 0.085 mm/ms (200 in./min.)
Comments:
Force vs. Deflection:

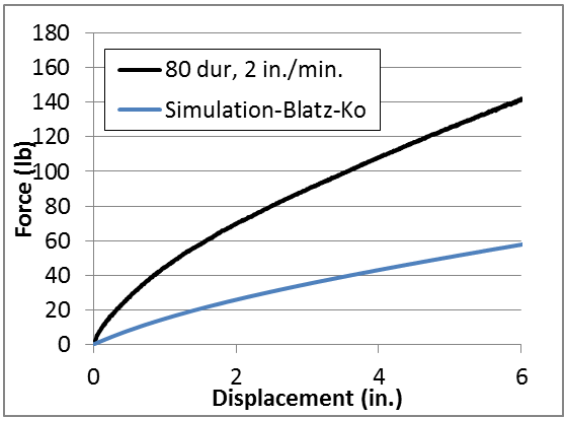

*MAT_MOONEY-RIVLIN_RUBBER (*MAT_027)

Sequentials:

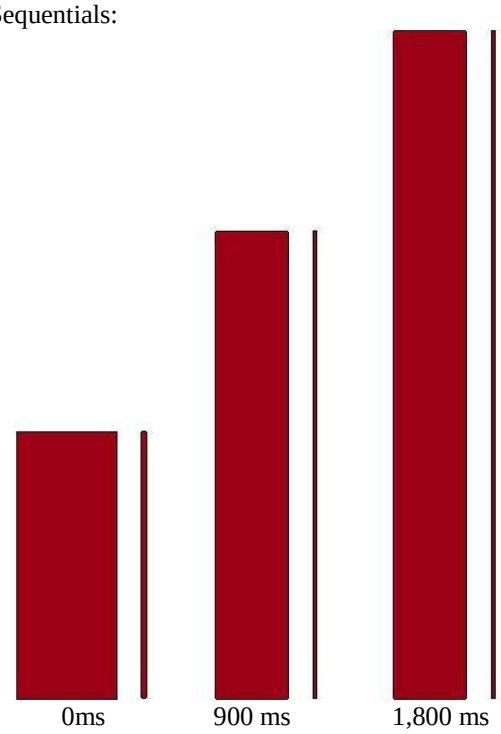

Rubber Type: 80 durometer EPDM
Input Parameters -
80 Durometer EPDM Tension Test
Poisson's Ratio: 0.495
Element Type: Constant Stress Solid
Rate: 0.085 mm/ms (200 in./min.)
Comments:
Force vs. Deflection:

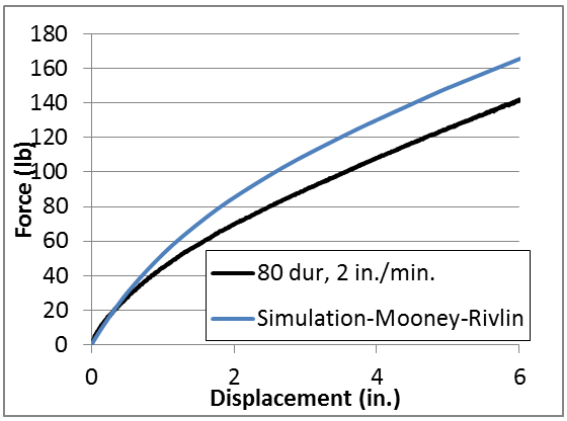

*MAT_FRAZER_NASH_RUBBER_MODEL (*MAT_031)

Sequentials: not available

Rubber Type: 80 durometer EPDM
Input Parameters -
80 Durometer EPDM Tension Test
Poisson's Ratio: 0.495
Element Type: Constant Stress Solid
Rate: 0.085 mm/ms (200 in./min.)
Comments: nodes with out of range velocities immediately
Force vs. Deflection: not available

*MAT_HYPERELASTIC_RUBBER (*MAT_077_H)

Sequentials:

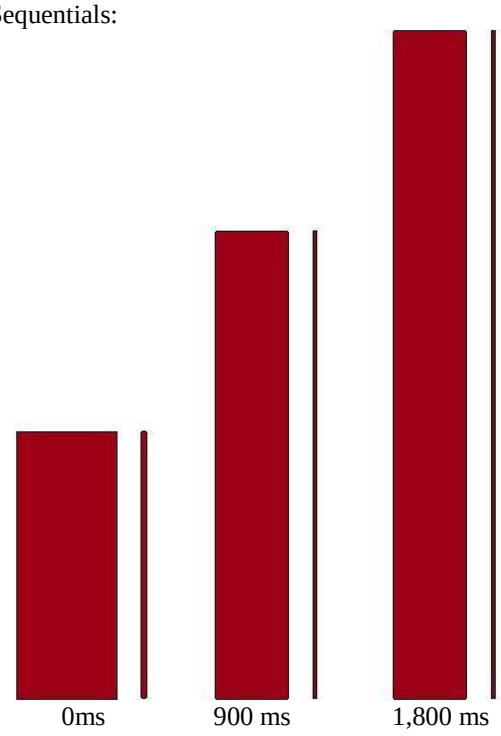

Rubber Type: 80 durometer EPDM
Input Parameters -
80 Durometer EPDM Tension Test
Poisson's Ratio: 0.495
N: 2
Element Type: Constant Stress Solid
Rate: 0.085 mm/ms (200 in./min.)
Comments:
Force vs. Deflection:

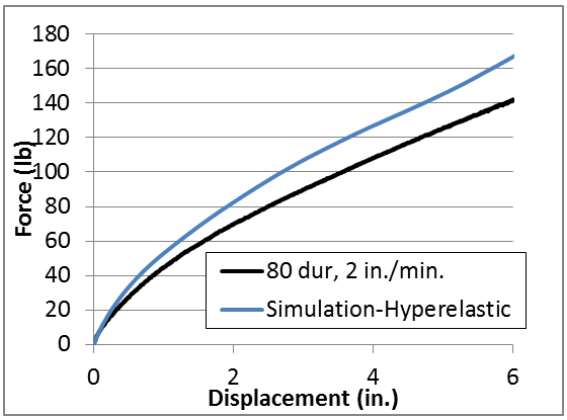

*MAT_OGDEN_RUBBER (*MAT_077_O)

Sequentials:

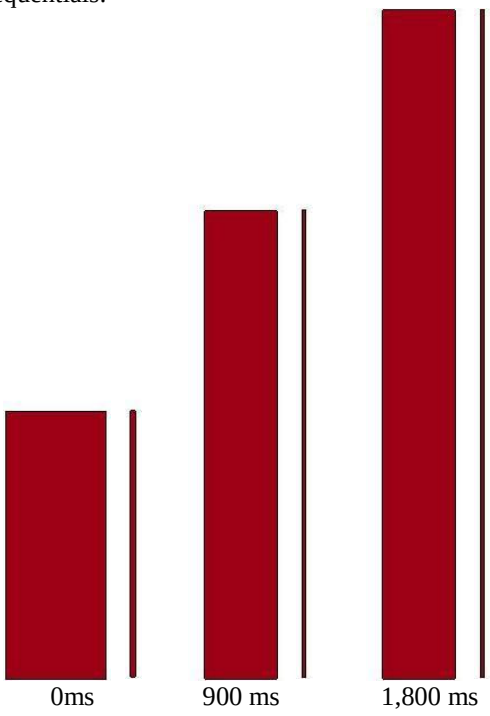

Rubber Type: 80 durometer EPDM
Input Parameters -
80 Durometer EPDM Tension Test
Poisson's Ratio: 0.495
N: 2
Element Type: Constant Stress Solid
Rate: 0.085 mm/ms (200 in./min.)
Comments:
Force vs. Deflection:

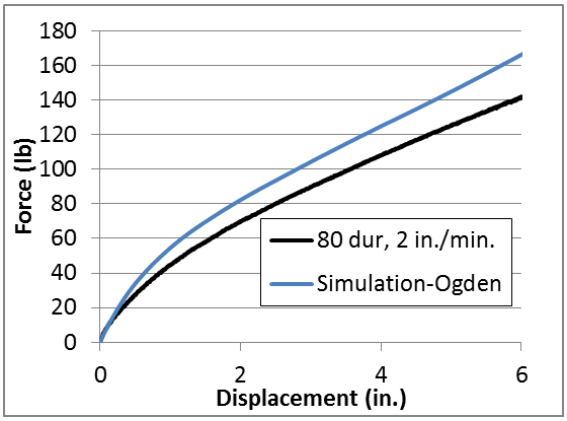

*MAT_ARRUDA_BOYCE_RUBBER (*MAT_127)

Sequentials:

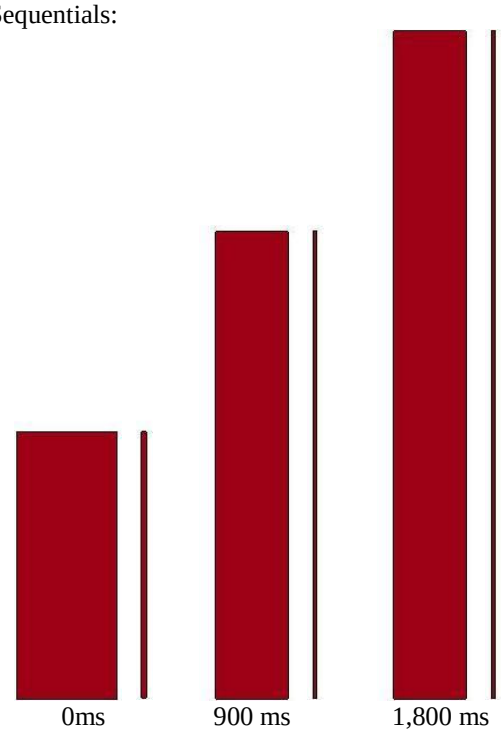

Rubber Type: 80 durometer EPDM
Input Parameters -
Bulk modulus: 0.103 GPa, 0.517 GPa, 1.4 GPa
Shear Modulus: 1.24 MPa (180 psi)
Element Type: Constant Stress Solid
Rate: 0.085 mm/ms (200 in./min.)
Comments: K=0.517 and 1.4 GPa had nodes with out of range velocities immediately
Force vs. Deflection:

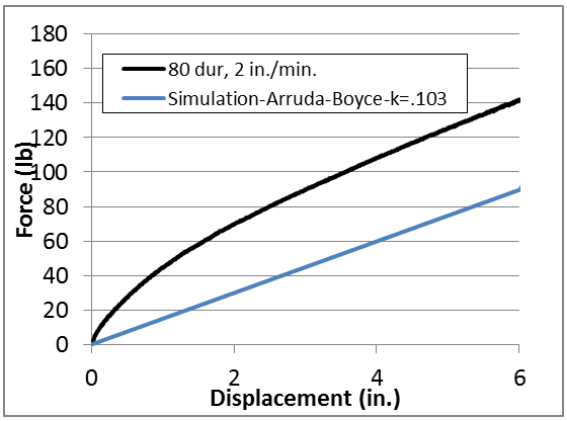

*MAT_SIMPLIFIED_RUBBER/FOAM (*MAT_181)

Sequentials:

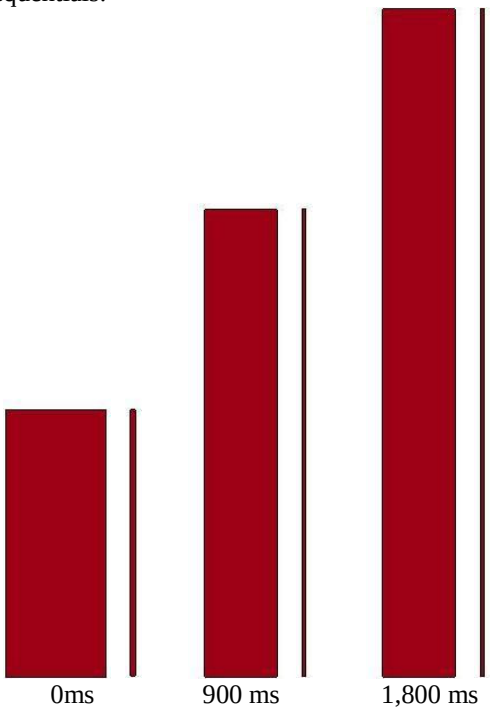

Rubber Type: 80 durometer EPDM
Input Parameters -
80 Durometer EPDM Tension Test
Bulk modulus: 0.103 GPa, 0.517 GPa, 1.4 GPa
Element Type: Constant Stress Solid
Rate: 0.085 mm/ms (200 in./min.)
Comments:
Force vs. Deflection:

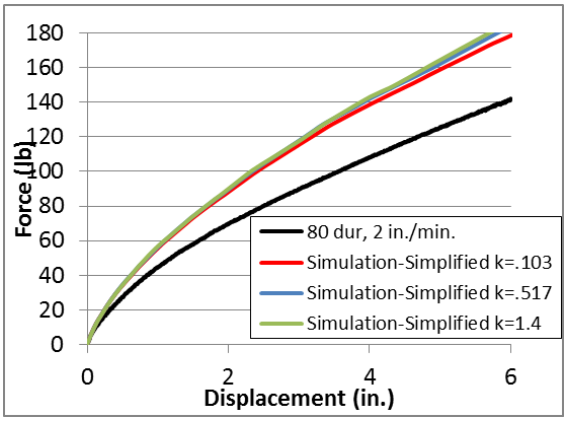

Appendix C. Bogie Test Results

The results of the recorded data from each accelerometer on every dynamic bogie test are provided in the summary sheets found in this appendix. Summary sheets include acceleration, velocity, and displacement versus time plots as well as force and energy versus displacement plots.

MIDWEST ROADSIDE SAFETY FACILITY

Bogie Test Summary

Test Information	SAFER for highways Energy Absorber	
Test Number:	EPDM-1	
Test Date:	22-Jun-2011	
Failure Type:	NA	
Energy Absorber Properties		
Type:	EPDM Rubber Cylinder 1A	
Dimensions:	8⅛" ID x 12⅛" OD	206mmID x 308mmOD
Length:	10 in.	25.4 cm
Durometer:	80 dur	
Orientation:	Axial	
Soil Properties		
Gradation:	NA	
Moisture Content:	NA	
Compaction Method:	NA	
Soil Density, γd:	NA	
Bogie Properties		
Impact Velocity:	4.27 mph (6.3 fps)	1.91 m/s
Impact Height:	22 in.	55.9 cm
Bogie Mass:	1689 lbs	766.1 kg
Data Acquired		
Acceleration Data:	DTS	
Camera Data:	AOS-5 Perpendicular -196 1/2"	

Test Results Summary		
Max. Deflection:	1.9	in.
Peak Force:	12.3	k
Initial Linear Stiffness	6.8	k/in.
Total Energy:	12.4	k-in.

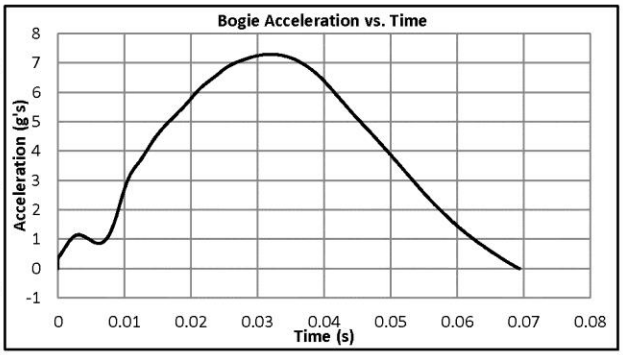

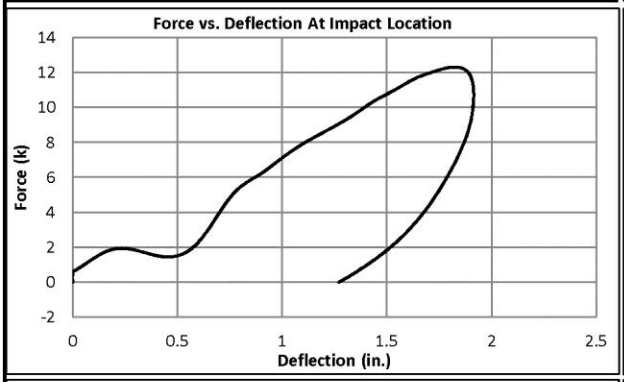

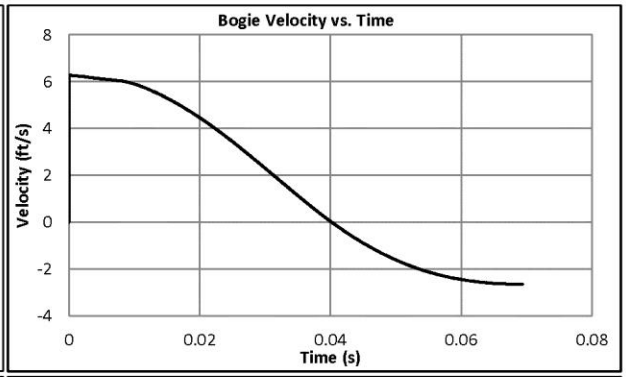

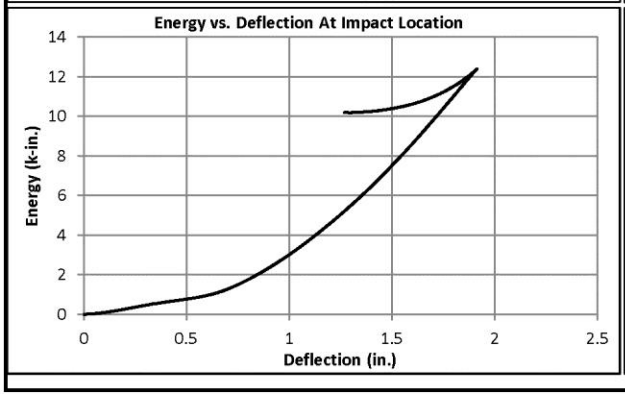

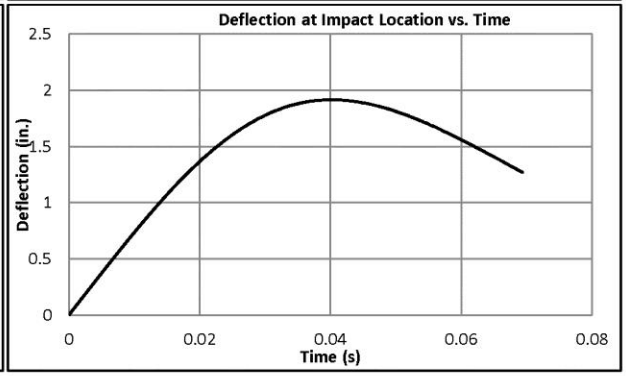

Figure C-1. Results of Test No. EPDM-1

MIDWEST ROADSIDE SAFETY FACILITY

Bogie Test Summary

Test Information	SAFER for highways Energy Absorber	
Test Number:	EPDM-2	
Test Date:	22-Jun-2011	
Failure Type:	NA	
Energy Absorber Properties		
Type:	EPDM Rubber Cylinder 2A	
Dimensions:	8⅛" ID x 12⅛" OD	206mmID x 308mmOD
Length:	10 in.	25.4 cm
Durometer:	60 dur	
Orientation:	Axial	
Soil Properties		
Gradation:	NA	
Moisture Content:	NA	
Compaction Method:	NA	
Soil Density, γd:	NA	
Bogie Properties		
Impact Velocity:	4.88 mph (7.2 fps)	2.18 m/s
Impact Height:	22 in.	55.9 cm
Bogie Mass:	1689 lbs	766.1 kg
Data Acquired		
Acceleration Data:	DTS	
Camera Data:	AOS-5 Perpendicular - 196 1/2"	

Test Results Summary

Max. Deflection:	2.2	in.
Peak Force:	12.9	k
Initial Linear Stiffness	6.1	k/in.
Total Energy:	16.1	k-in.

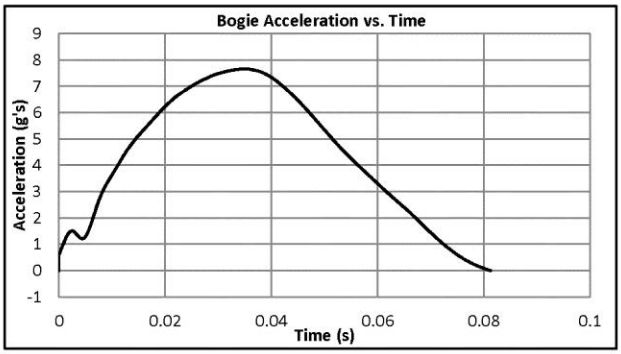

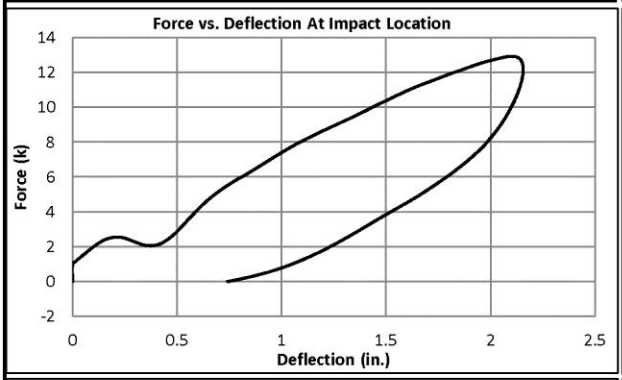

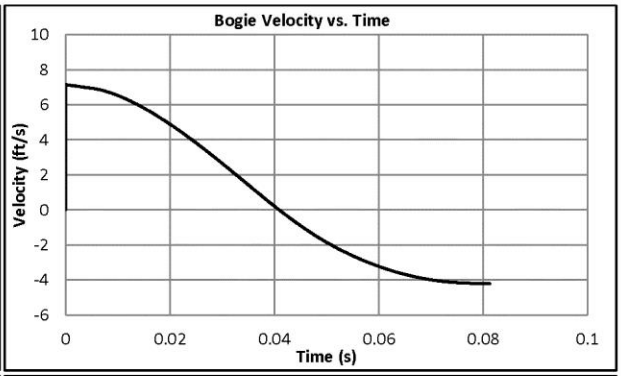

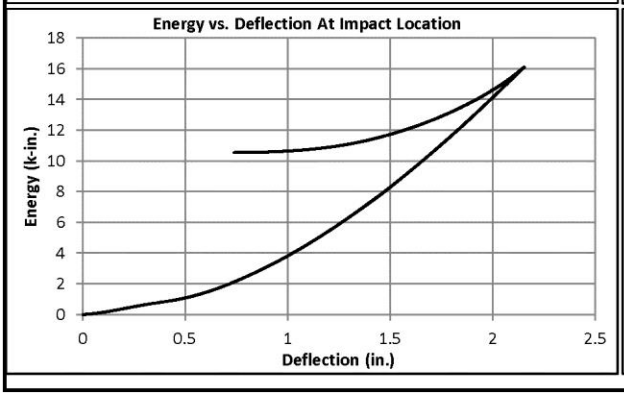

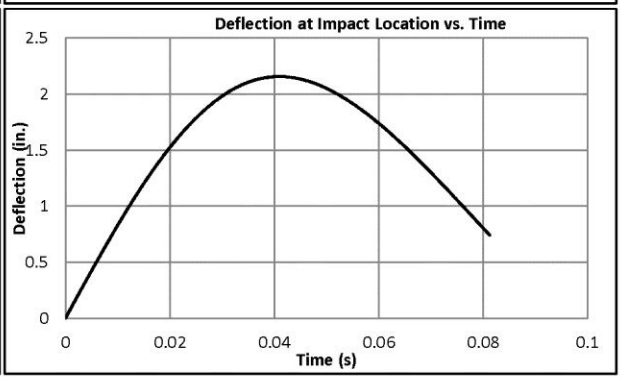

Figure C-2. Results of Test No. EPDM-2

MIDWEST ROADSIDE SAFETY FACILITY

Bogie Test Summary

Test Information	SAFER for highways Energy Absorber	
Test Number:	EPDM-3	
Test Date:	22-Jun-2011	
Failure Type:	NA	
Energy Absorber Properties		
Type:	EPDM Rubber Cylinder 3A	
Dimensions:	9⅝" ID x 11⅝" OD	244mmID x 295mmOD
Length:	10 in.	25.4 cm
Durometer:	80 dur	
Orientation:	Axial	
Soil Properties		
Gradation:	NA	
Moisture Content:	NA	
Compaction Method:	NA	
Soil Density, γd:	NA	
Bogie Properties		
Impact Velocity:	6.76 mph (9.9 fps)	3.02 m/s
Impact Height:	22 in.	55.9 cm
Bogie Mass:	1689 lbs	766.1 kg
Data Acquired		
Acceleration Data:	DTS	
Camera Data:	AOS-5 Perpendicular - 196 1/2"	

Test Results Summary		
Max. Deflection:	6.2	in.
Peak Force:	6.7	k
Initial Linear Stiffness	2.8	k/in.
Total Energy:	30.9	k-in.

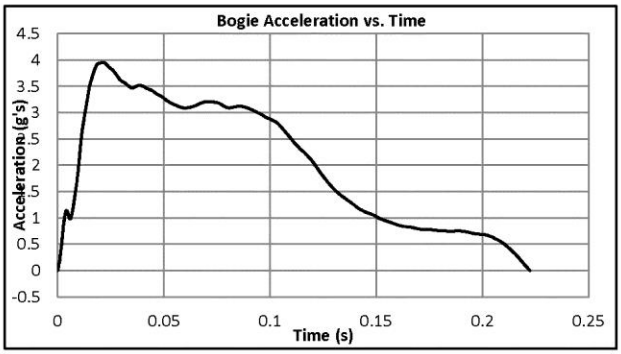

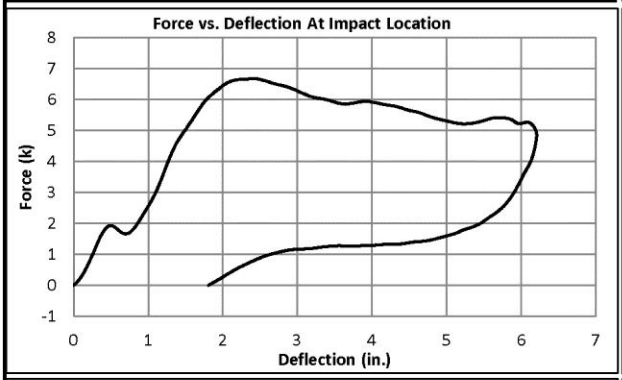

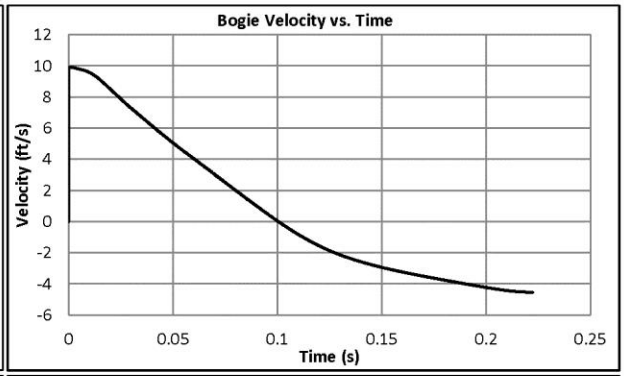

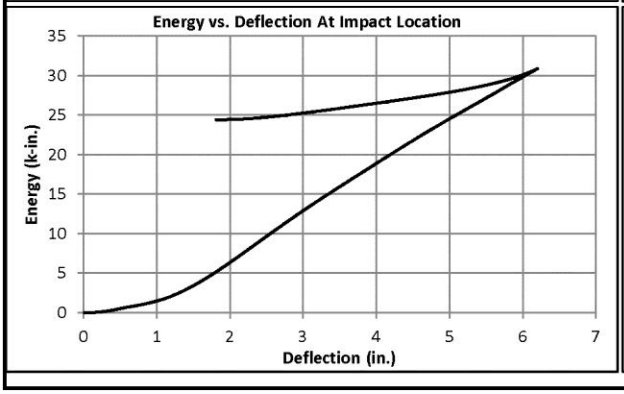

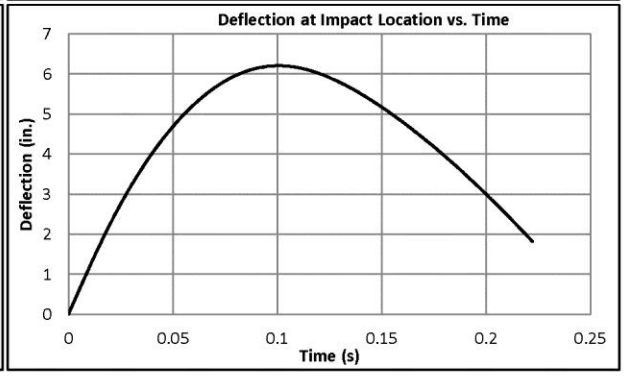

Figure C-3. Results of Test No. EPDM-3

MIDWEST ROADSIDE SAFETY FACILITY

Bogie Test Summary

Test Information	Dynamic Crush Test	
Test Number:	EPDM-4	
Test Date:	2-Sep-2011	
Failure Type:	Rubber Deformation	
Cylinder Properties		
Material:	80 Dur. Rubber	
Outer Diameter:	11.625 in.	29.5 cm
Thickness:	1.0625 in.	2.7 cm
Length:	9.875 in.	25.1 cm
Orientation:	top surface normal to impact	
Soil Properties		
Gradation:	NA	
Moisture Content:	NA	
Compaction Method:	NA	
Soil Density, γd:	NA	
Bogie Properties		
Impact Velocity:	7.02 mph (10.3 fps)	3.14 m/s
Impact Height:	24.875 in.	63.2 cm
Bogie Mass:	1686 lbs	764.8 kg
Data Acquired		
Acceleration Data:	EDR-3	
Camera Data:	AOS-6 Perpendicular - 196"	

Test Results Summary		
Max. Deflection:	7.2	in.
Peak Force:	8.4	k
Initial Linear Stiffness	2.4	k/in.
Total Energy:	33.5	k-in.

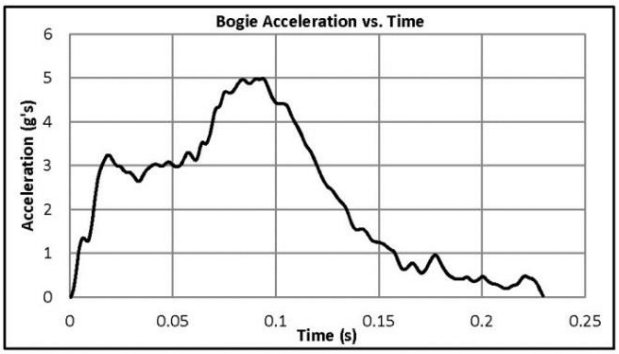

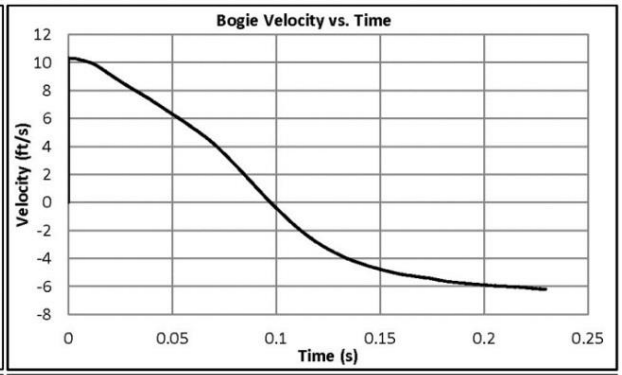

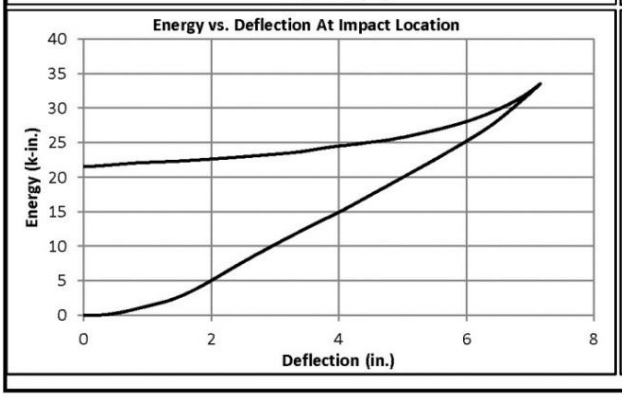

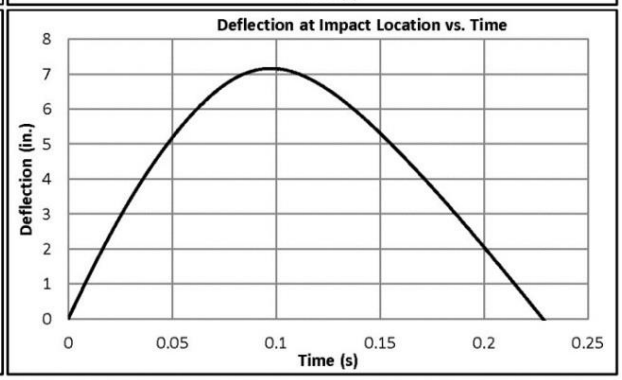

Figure C-4. Results of Test No. EPDM-4

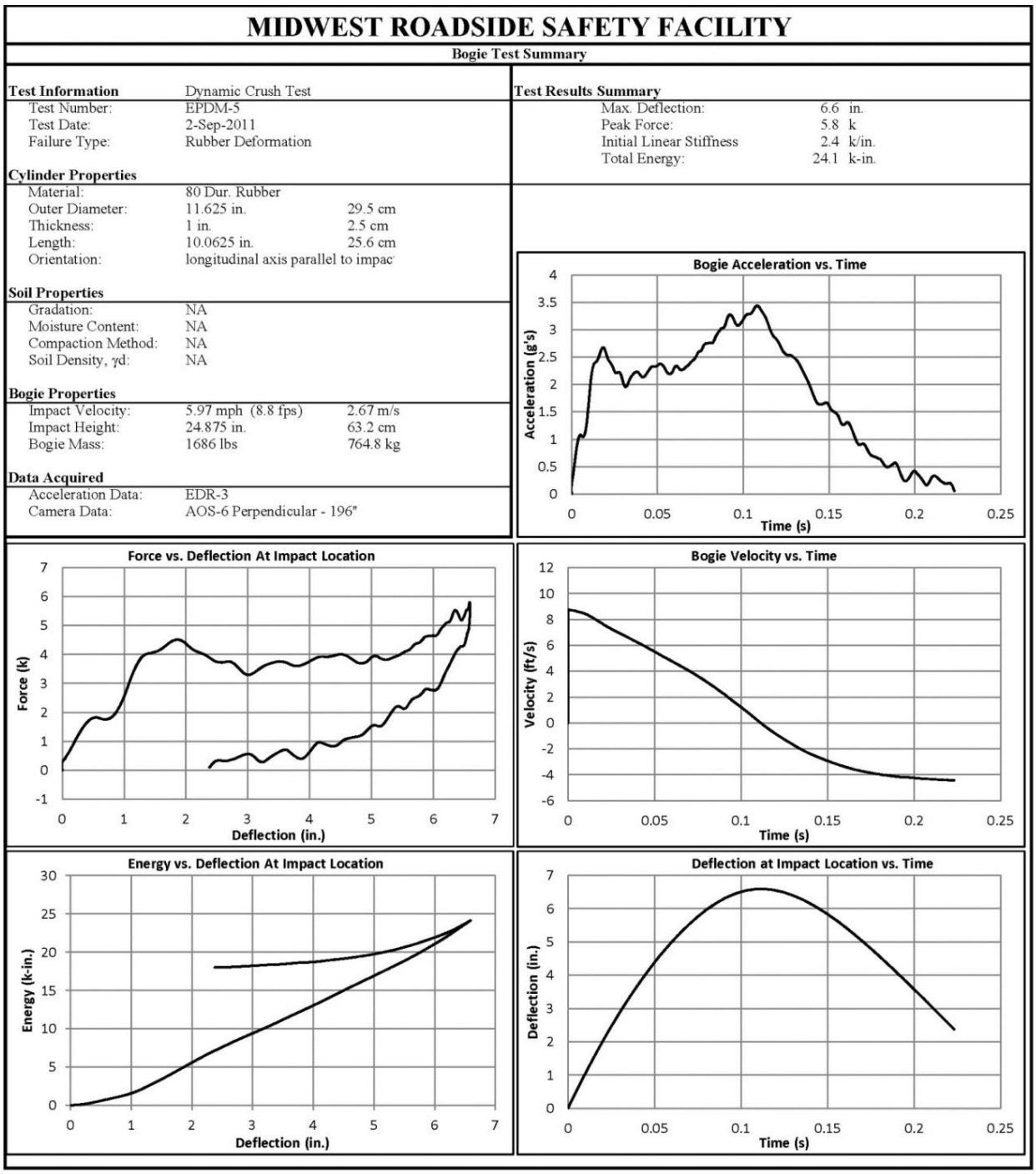

Figure C-5. Results of Test No. EPDM-5

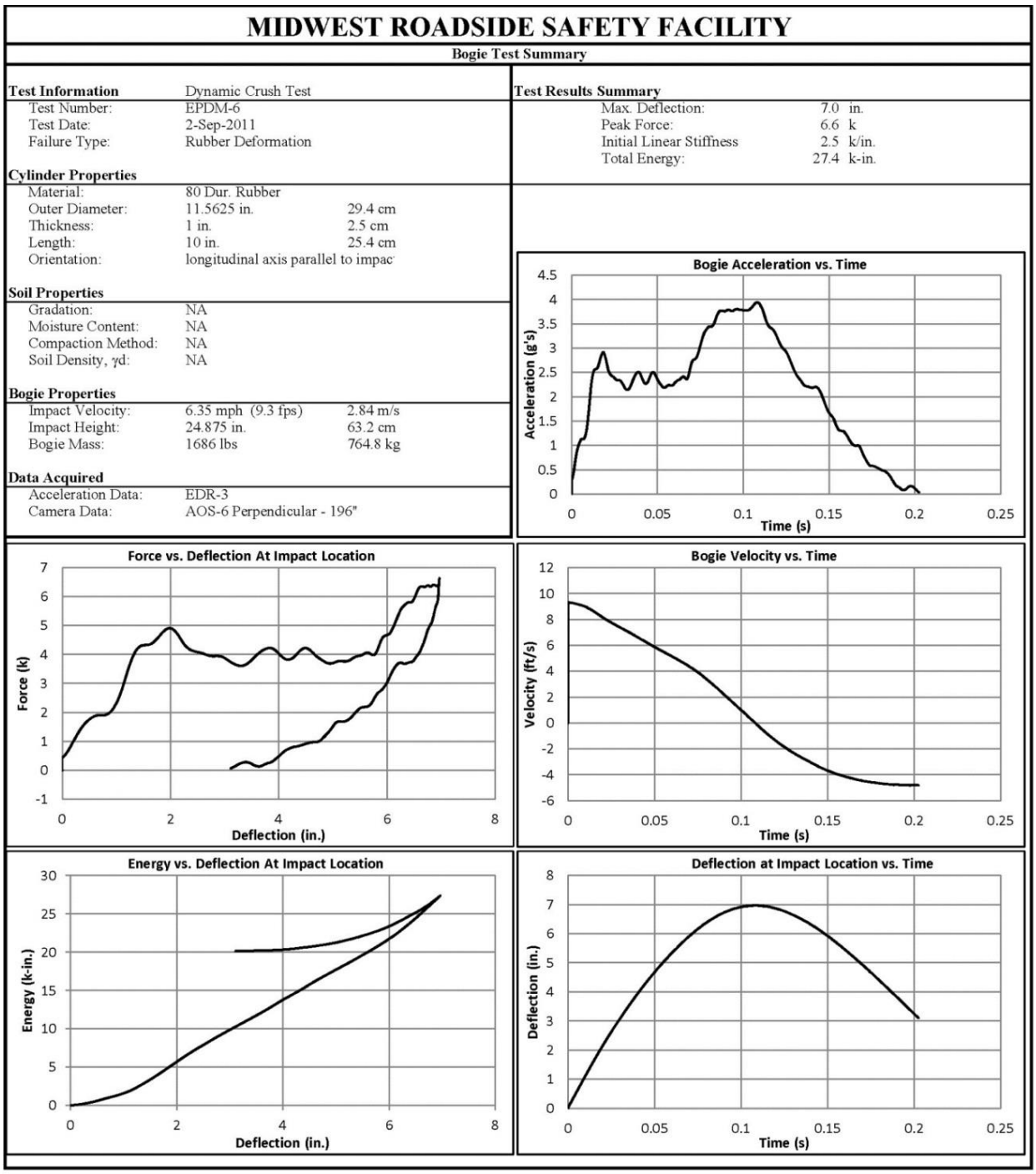

Figure C-6. Results of Test No. EPDM-6

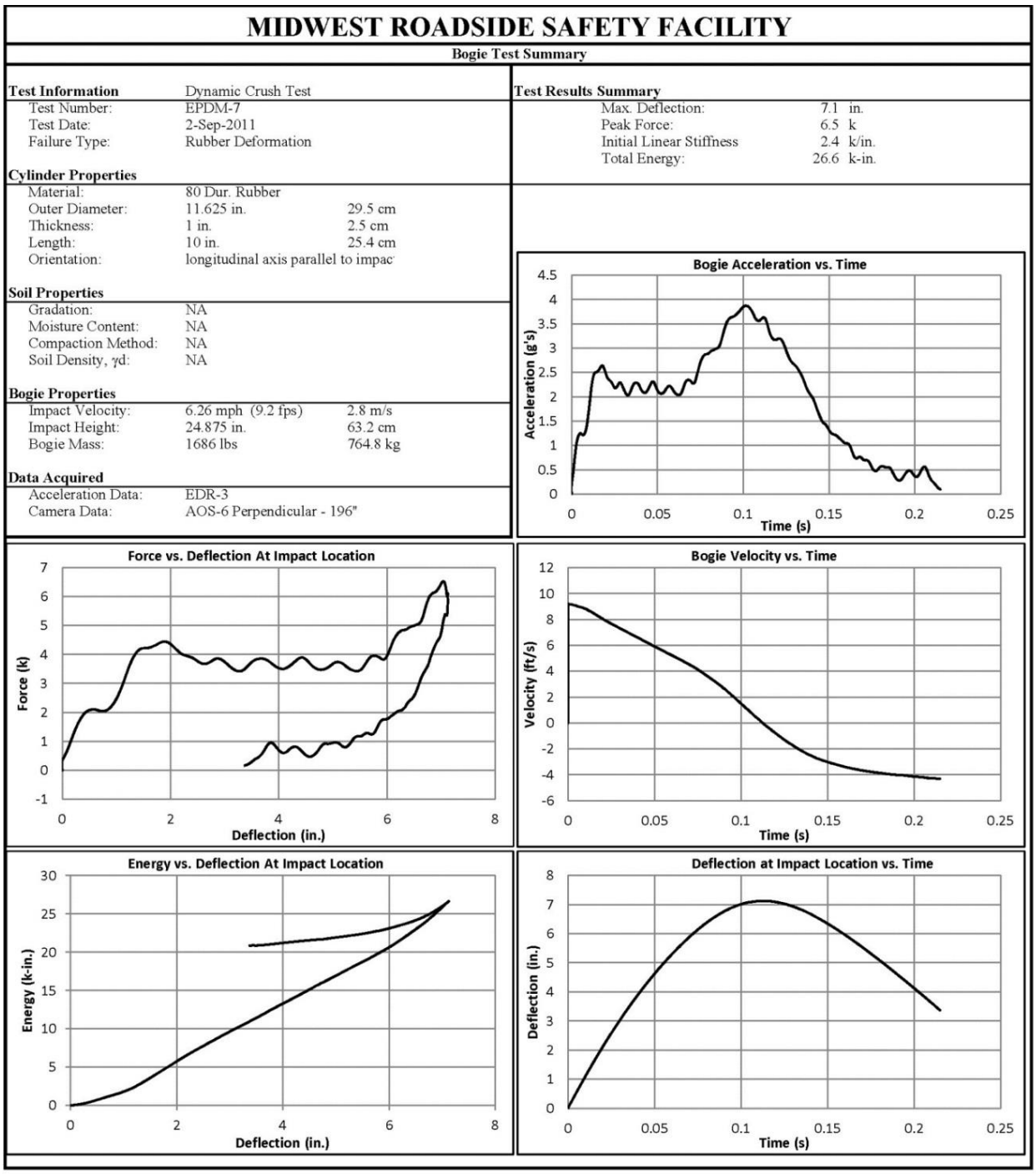

Figure C-7. Results of Test No. EPDM-7

MIDWEST ROADSIDE SAFETY FACILITY

Bogie Test Summary

Test Information	Dynamic Crush Test	
Test Number:	EPDM-8	
Test Date:	2-Sep-2011	
Failure Type:	Rubber Deformation	
Cylinder Properties		
Material:	80 Dur. Rubber	
Outer Diameter:	11.6875 in.	29.7 cm
Thickness:	1 in.	2.5 cm
Length:	10 in.	25.4 cm
Orientation:	longitudinal axis parallel to impac	
Soil Properties		
Gradation:	NA	
Moisture Content:	NA	
Compaction Method:	NA	
Soil Density, γd:	NA	
Bogie Properties		
Impact Velocity:	6.08 mph (8.9 fps)	2.72 m/s
Impact Height:	24.875 in.	63.2 cm
Bogie Mass:	1686 lbs	764.8 kg
Data Acquired		
Acceleration Data:	EDR-3	
Camera Data:	AOS-6 Perpendicular - 196"	

Test Results Summary		
Max. Deflection:	6.9	in.
Peak Force:	5.4	k
Initial Linear Stiffness	2.4	k/in.
Total Energy:	25.1	k-in.

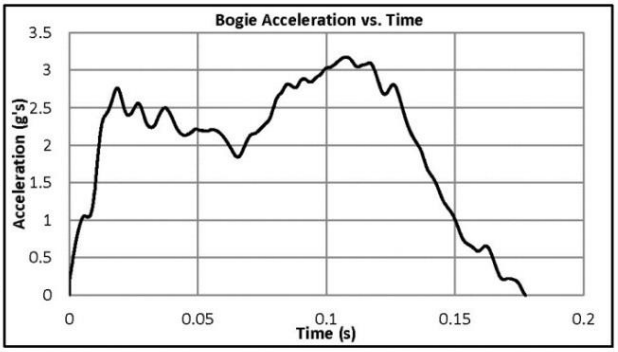

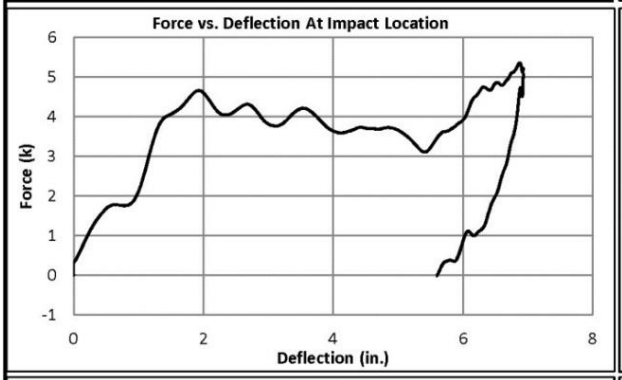

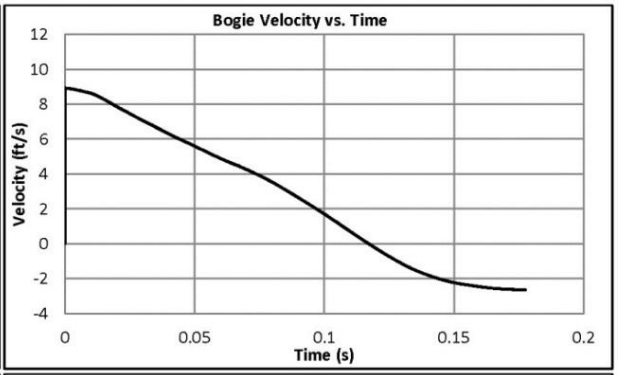

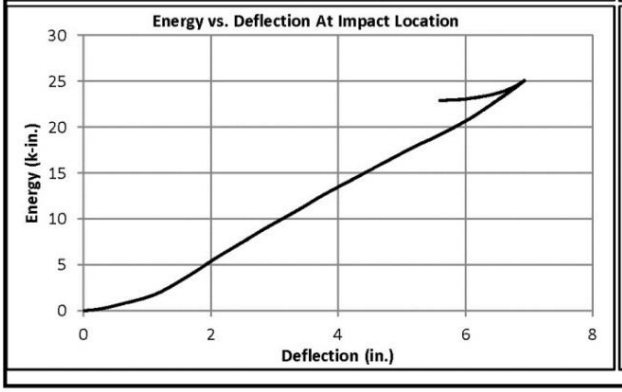

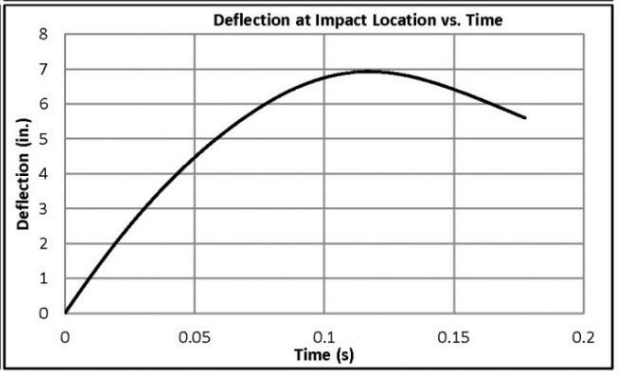

Figure C-8. Results of Test No. EPDM-8

MIDWEST ROADSIDE SAFETY FACILITY

Bogie Test Summary

Test Information	Dynamic Crush Test	
Test Number:	EPDM-9	
Test Date:	2-Sep-2011	
Failure Type:	Rubber Deformation	
Cylinder Properties		
Material:	80 Dur. Rubber	
Outer Diameter:	11.625 in.	29.5 cm
Thickness:	1 in.	2.5 cm
Length:	6.9375 in.	17.6 cm
Orientation:	longitudinal axis parallel to impac	
Soil Properties		
Gradation:	NA	
Moisture Content:	NA	
Compaction Method:	NA	
Soil Density, γd:	NA	
Bogie Properties		
Impact Velocity:	5.73 mph (8.4 fps)	2.56 m/s
Impact Height:	24.875 in.	63.2 cm
Bogie Mass:	1686 lbs	764.8 kg
Data Acquired		
Acceleration Data:	EDR-3	
Camera Data:	AOS-6 Perpendicular - 196"	

Test Results Summary		
Max. Deflection:	6.3	in.
Peak Force:	5.1	k
Initial Linear Stiffness	2.2	k/in.
Total Energy:	22.3	k-in.

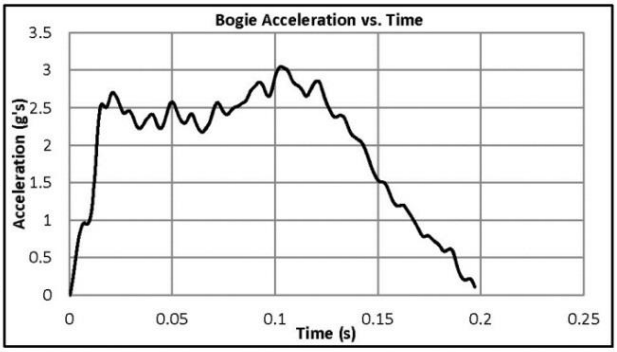

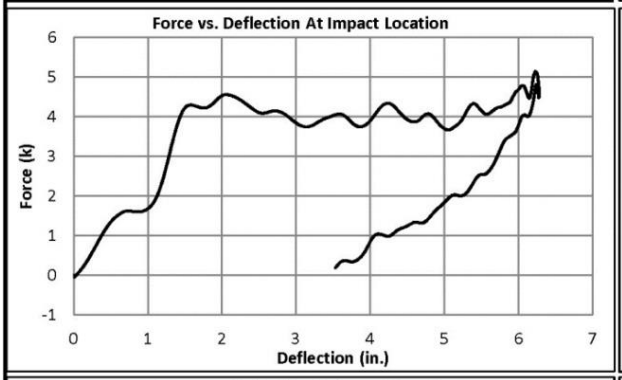

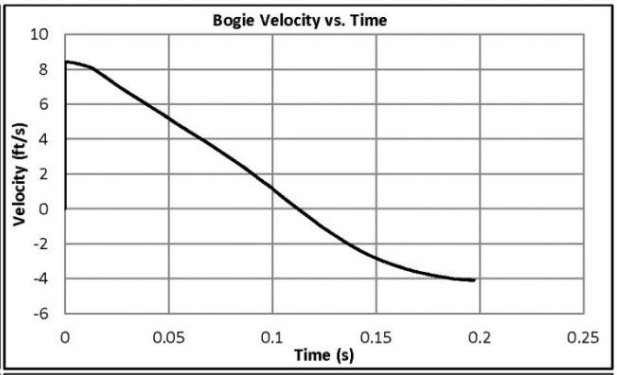

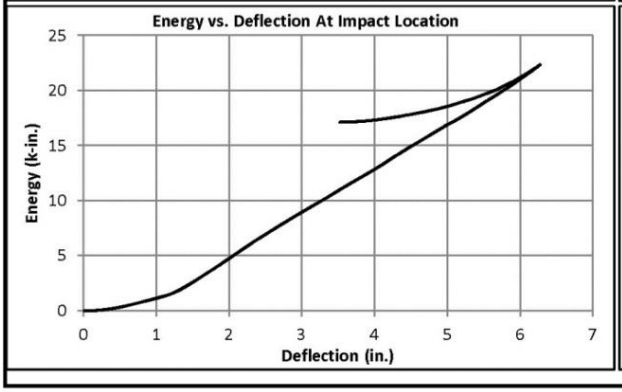

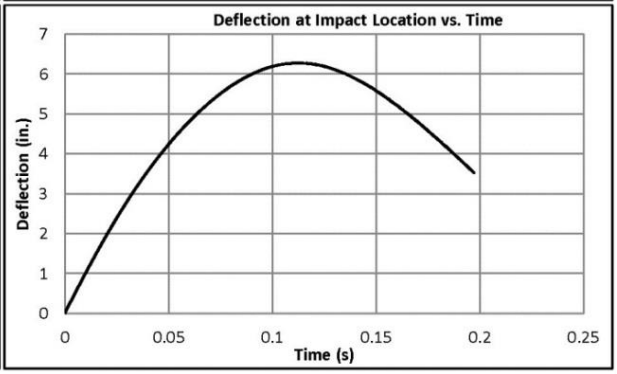

Figure C-9. Results of Test No. EPDM-9

MIDWEST ROADSIDE SAFETY FACILITY

Bogie Test Summary

Test Information	Dynamic Crush Test	
Test Number:	EPDM-10	
Test Date:	2-Sep-2011	
Failure Type:	Rubber Deformation	
Cylinder Properties		
Material:	80 Dur. Rubber	
Outer Diameter:	11.625 in.	29.5 cm
Thickness:	1 in.	2.5 cm
Length:	9.9375 in.	25.2 cm
Orientation:	longitudinal axis parallel to impac	
Soil Properties		
Gradation:	NA	
Moisture Content:	NA	
Compaction Method:	NA	
Soil Density, γd:	NA	
Bogie Properties		
Impact Velocity:	6.02 mph (8.8 fps)	2.69 m/s
Impact Height:	24.875 in.	63.2 cm
Bogie Mass:	1686 lbs	764.8 kg
Data Acquired		
Acceleration Data:	EDR-3	
Camera Data:	AOS-6 Perpendicular - 196"	

Test Results Summary		
Max. Deflection:	6.5	in.
Peak Force:	5.5	k
Initial Linear Stiffness	0.8	k/in.
Total Energy:	24.5	k-in.

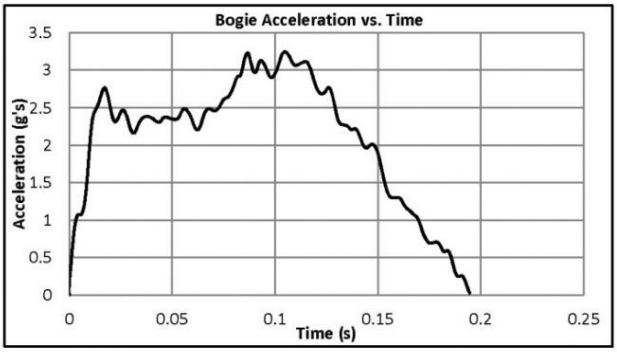

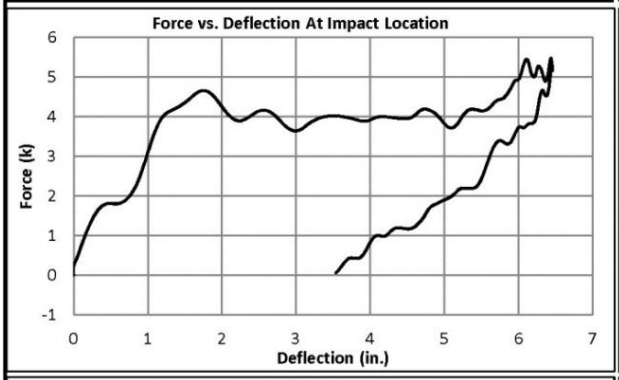

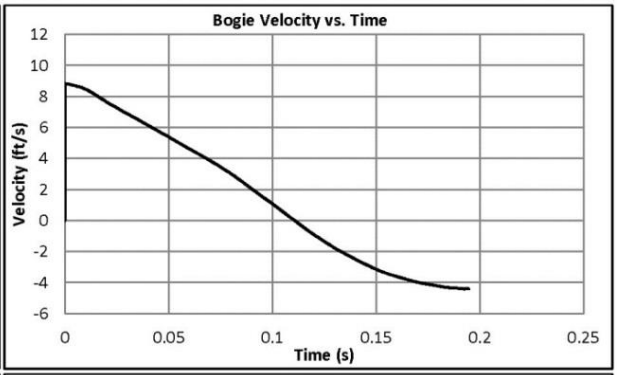

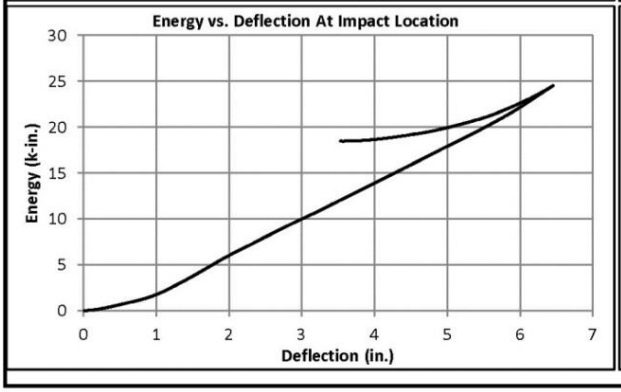

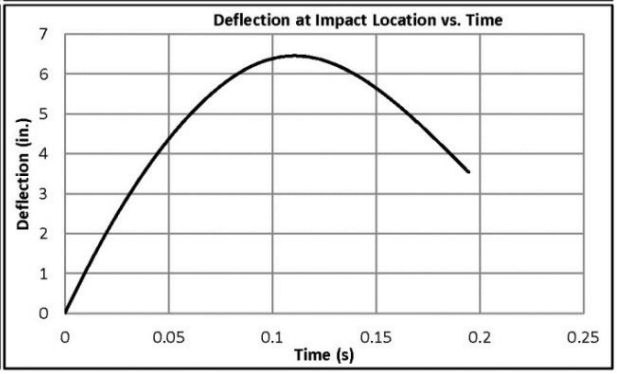

Figure C-10. Results of Test No. EPDM-10

MIDWEST ROADSIDE SAFETY FACILITY

Bogie Test Summary

Test Information	Dynamic Crush Test	
Test Number:	EPDM-11	
Test Date:	2-Sep-2011	
Failure Type:	Rubber Deformation	
Cylinder Properties		
Material:	80 Dur. Rubber	
Outer Diameter:	11.625 in.	29.5 cm
Thickness:	1 in.	2.5 cm
Length:	9.9375 in.	25.2 cm
Orientation:	longitudinal axis parallel to impac	
Soil Properties		
Gradation:	NA	
Moisture Content:	NA	
Compaction Method:	NA	
Soil Density, γd:	NA	
Bogie Properties		
Impact Velocity:	5.3 mph (7.8 fps)	2.37 m/s
Impact Height:	24.875 in.	63.2 cm
Bogie Mass:	1686 lbs	764.8 kg
Data Acquired		
Acceleration Data:	EDR-3	
Camera Data:	AOS-6 Perpendicular - 196"	

Test Results Summary		
Max. Deflection:	5.6	in.
Peak Force:	4.5	k
Initial Linear Stiffness	1.7	k/in.
Total Energy:	19.1	k-in.

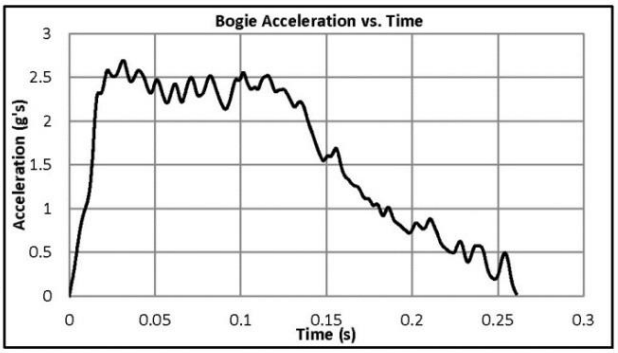

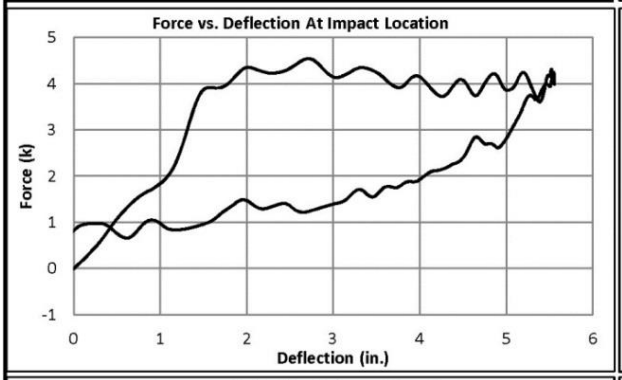

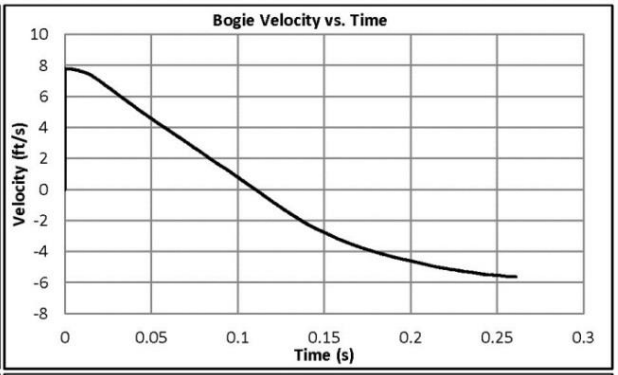

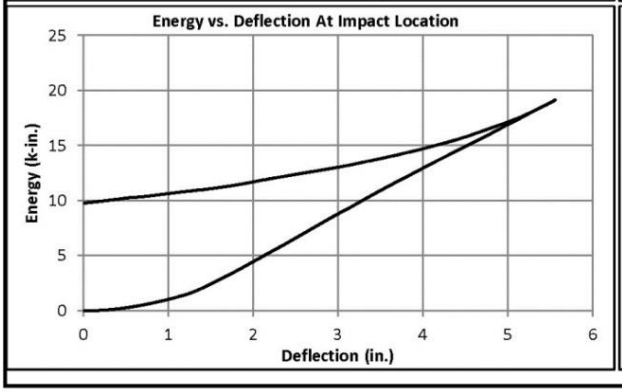

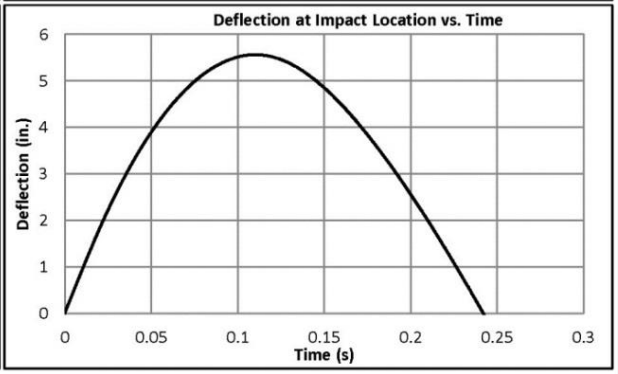

Figure C-11. Results of Test No. EPDM-11

MIDWEST ROADSIDE SAFETY FACILITY

Bogie Test Summary

Test Information	Dynamic Crush Test	
Test Number:	EPDM-12	
Test Date:	2-Sep-2011	
Failure Type:	Rubber Deformation	
Cylinder Properties		
Material:	80 Dur. Rubber	
Outer Diameter:	11.6875 in.	29.7 cm
Thickness:	1 in.	2.5 cm
Length:	9.9375 in.	25.2 cm
Orientation:	longitudinal axis parallel to impac	
Soil Properties		
Gradation:	NA	
Moisture Content:	NA	
Compaction Method:	NA	
Soil Density, γd:	NA	
Bogie Properties		
Impact Velocity:	7.11 mph (10.4 fps)	3.18 m/s
Impact Height:	24.875 in.	63.2 cm
Bogie Mass:	1686 lbs	764.8 kg
Data Acquired		
Acceleration Data:	EDR-3	
Camera Data:	AOS-6 Perpendicular - 196"	

Test Results Summary		
Max. Deflection:	7.6	in.
Peak Force:	10.1	k
Initial Linear Stiffness	0.9	k/in.
Total Energy:	34.4	k-in.

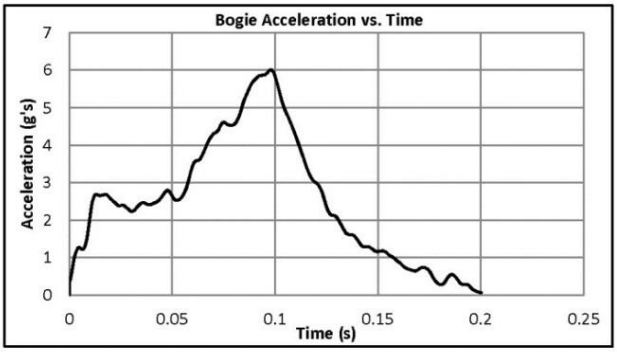

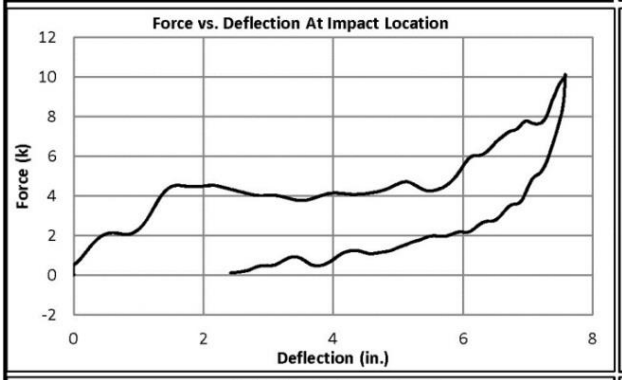

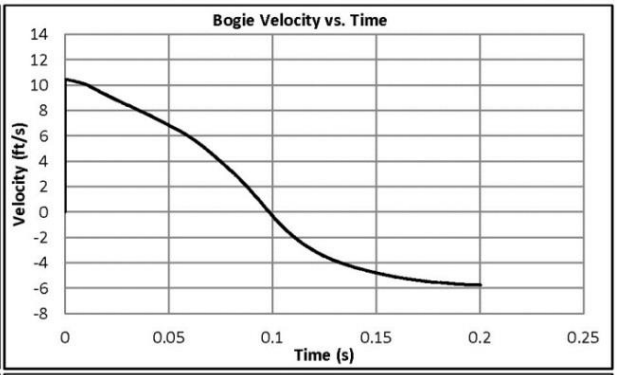

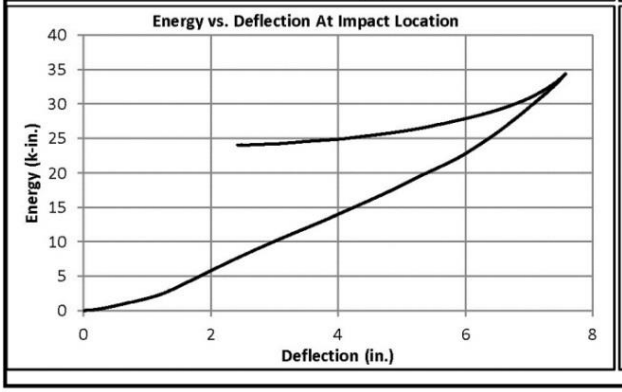

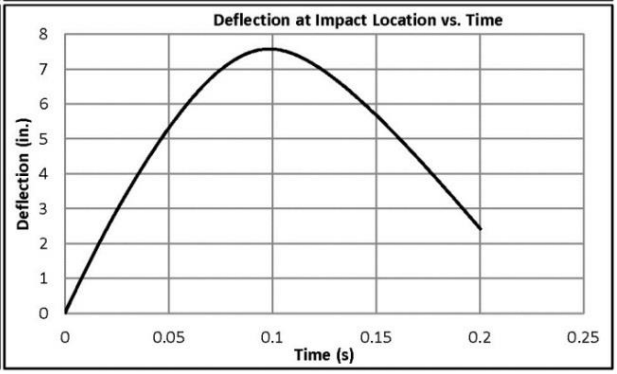

Figure C-12. Results of Test No. EPDM-12

MIDWEST ROADSIDE SAFETY FACILITY

Bogie Test Summary

Test Information SAFER for highways Energy Absorber

Test Number:	HSF14-1
Test Date:	21-Feb-2012
Failure Type:	NA

Energy Absorber Properties

Type:	Maritime Intl HSF14 Shear Fender	
Dimensions:	16" H x 14" W	40.6 cm x 35.6 cm
Length:	22 in.	55.9 cm
Durometer:	NA dur	
Orientation:	perpendicular to hole	

Soil Properties

Gradation:	NA
Moisture Content:	NA
Compaction Method:	NA
Soil Density, γd:	NA

Bogie Properties

Impact Velocity:	4.94 mph (7.3 fps)	2.21 m/s
Impact Height:	17.525 in.	44.5 cm
Bogie Mass:	1818 lbs	824.6 kg

Data Acquired

Acceleration Data:	EDR-3
Camera Data:	AOS-5 Perpendicular -192"

Test Results Summary

Max. Deflection:	6.2	in.
Peak Force:	12.1	k
Initial Linear Stiffness		k/in.
Total Energy:	17.8	k-in.

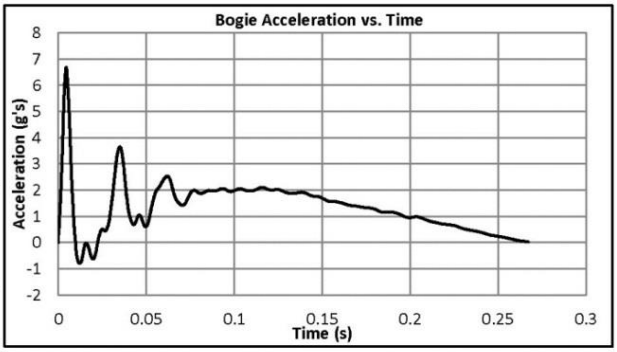

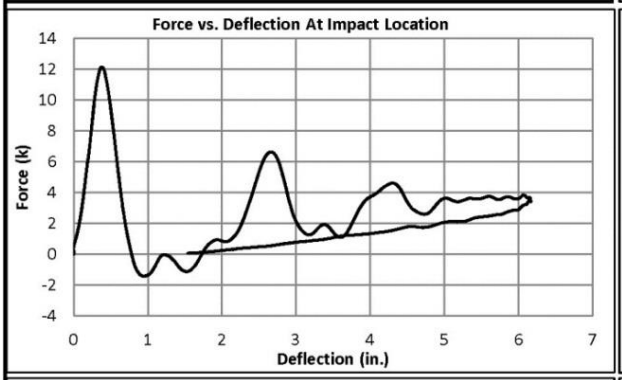

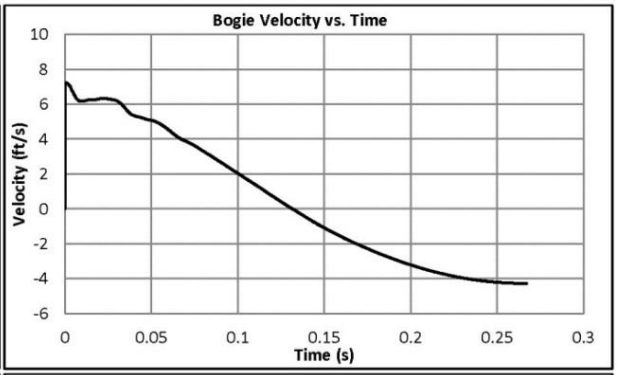

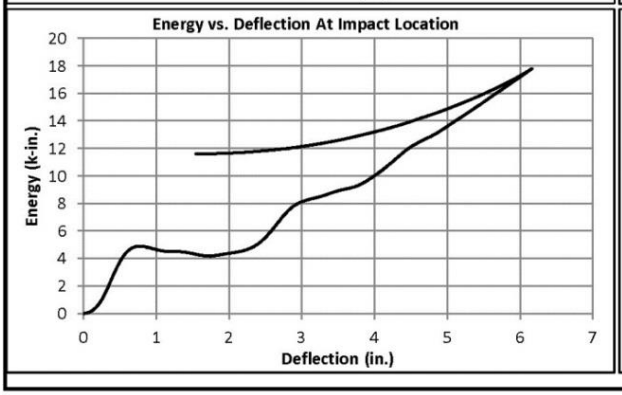

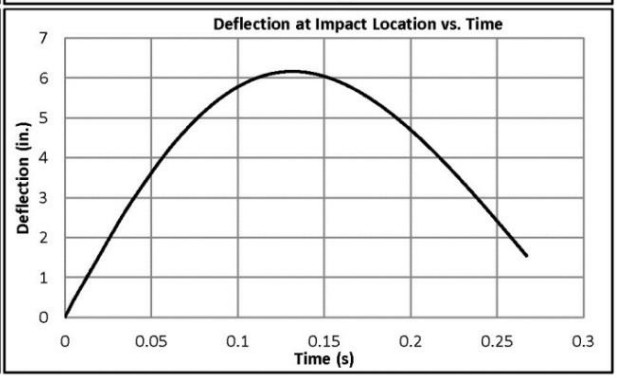

Figure C-13. Results of Test No. HSF14-1

MIDWEST ROADSIDE SAFETY FACILITY

Bogie Test Summary

Test Information	SAFER for highways Energy Absorber	
Test Number:	HSF14-2	
Test Date:	21-Feb-2012	
Failure Type:	NA	
Energy Absorber Properties		
Type:	Maritime Intl HSF14 Shear Fender	
Dimensions:	16" H x 14" W	40.6 cm x 35.6 cm
Length:	22 in.	55.9 cm
Durometer:	NA dur	
Orientation:	perpendicular to hole	
Soil Properties		
Gradation:	NA	
Moisture Content:	NA	
Compaction Method:	NA	
Soil Density, γd:	NA	
Bogie Properties		
Impact Velocity:	4.99 mph (7.3 fps)	2.23 m/s
Impact Height:	17.525 in.	44.5 cm
Bogie Mass:	1818 lbs	824.6 kg
Data Acquired		
Acceleration Data:	EDR-3	
Camera Data:	AOS-5 Perpendicular -192"	

Test Results Summary		
Max. Deflection:	5.3	in.
Peak Force:	13.0	k
Initial Linear Stiffness		k/in.
Total Energy:	18.2	k-in.

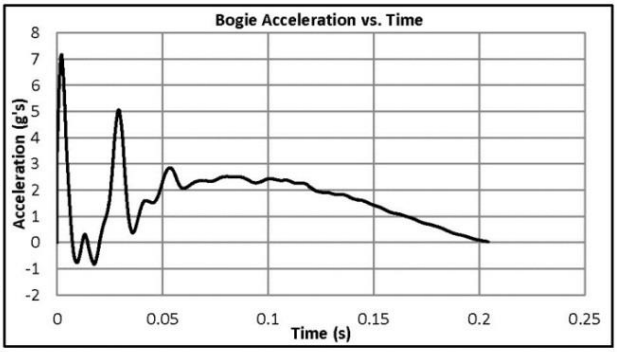

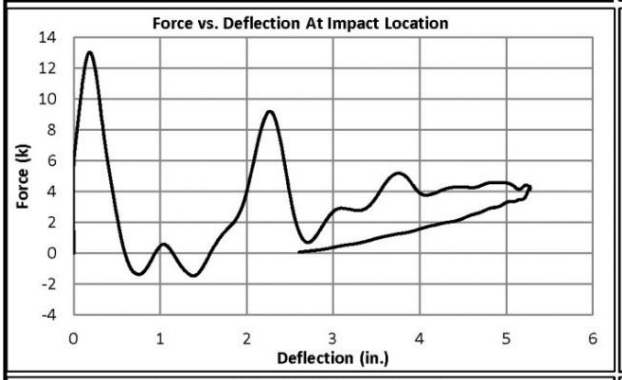

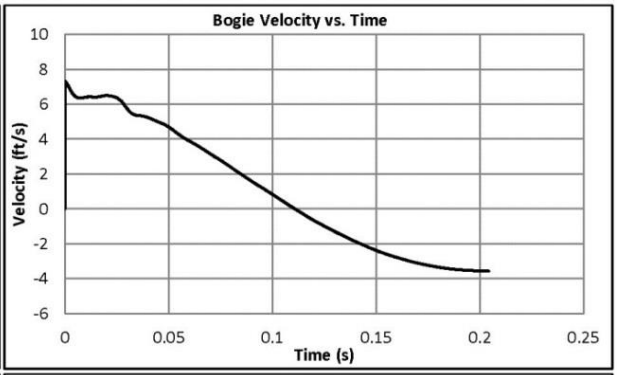

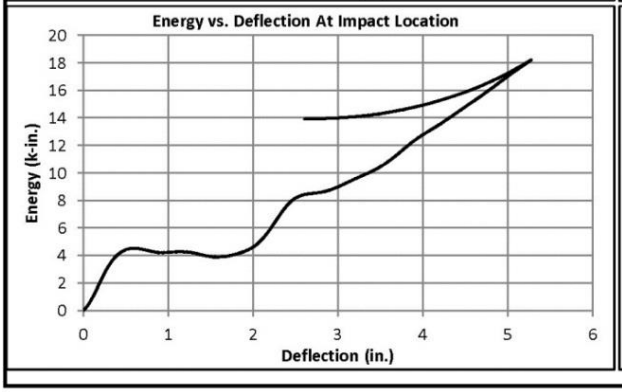

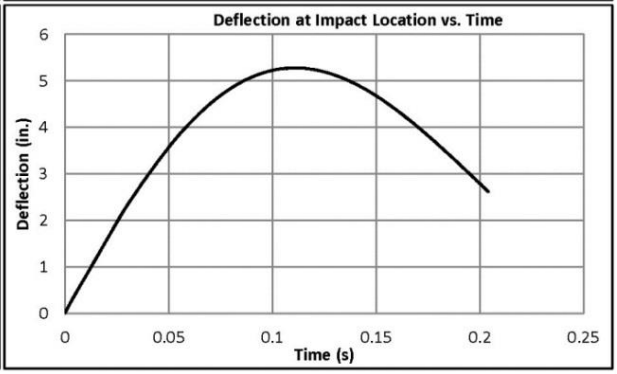

Figure C-14. Results of Test No. HSF14-2

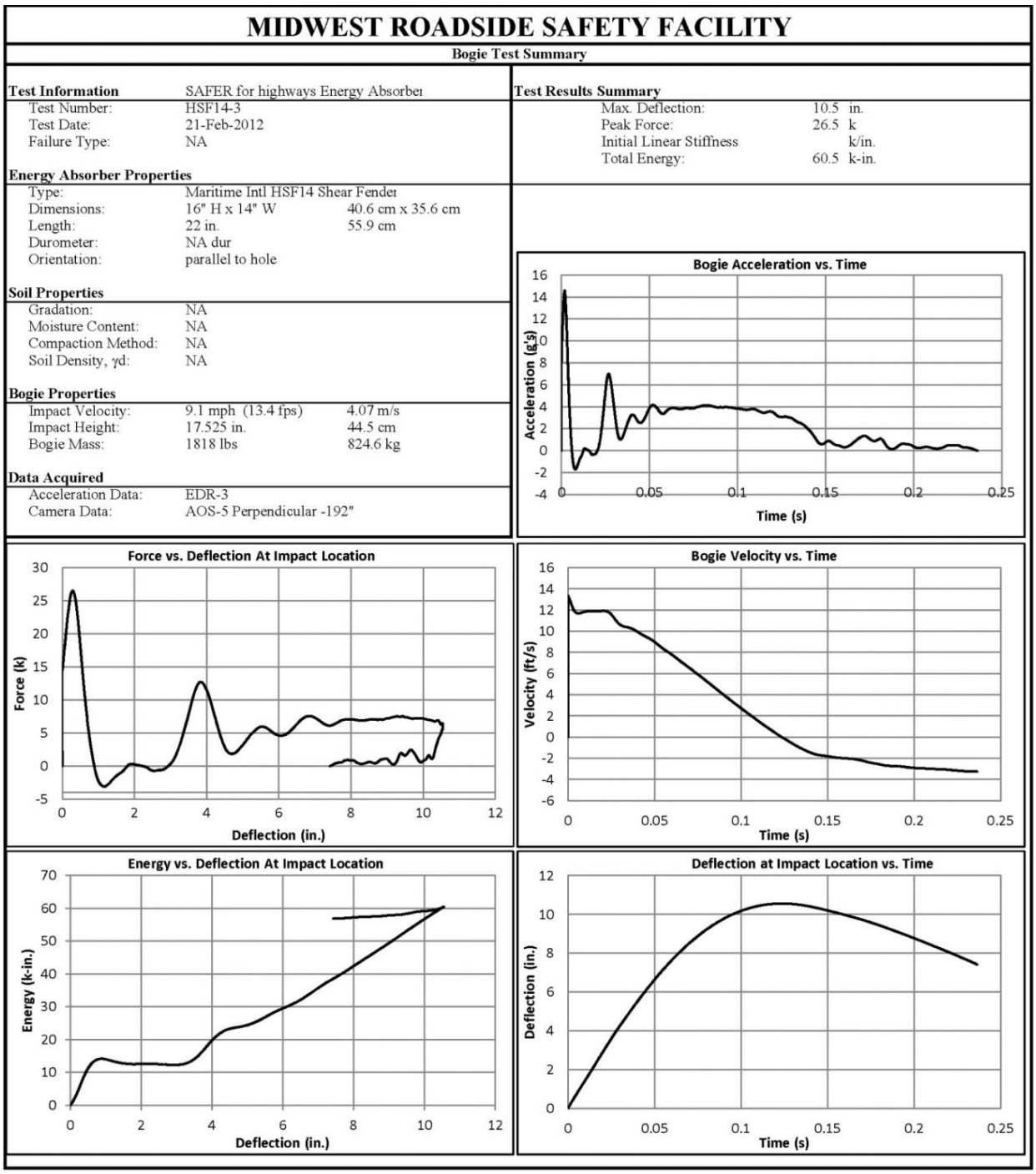

Figure C-15. Results of Test No. HSF14-3

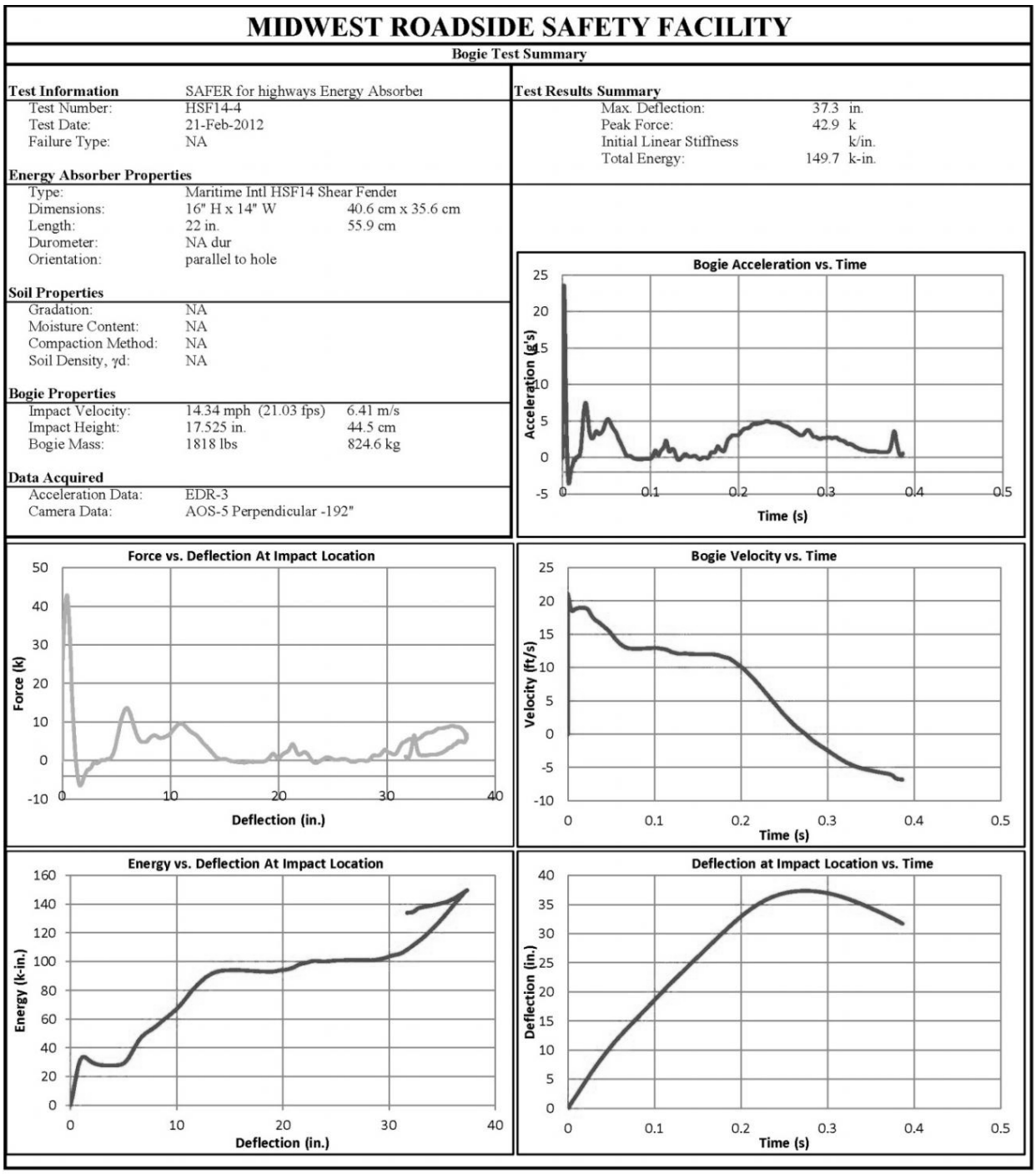

Figure C-16. Results of Test No. HSF14-4

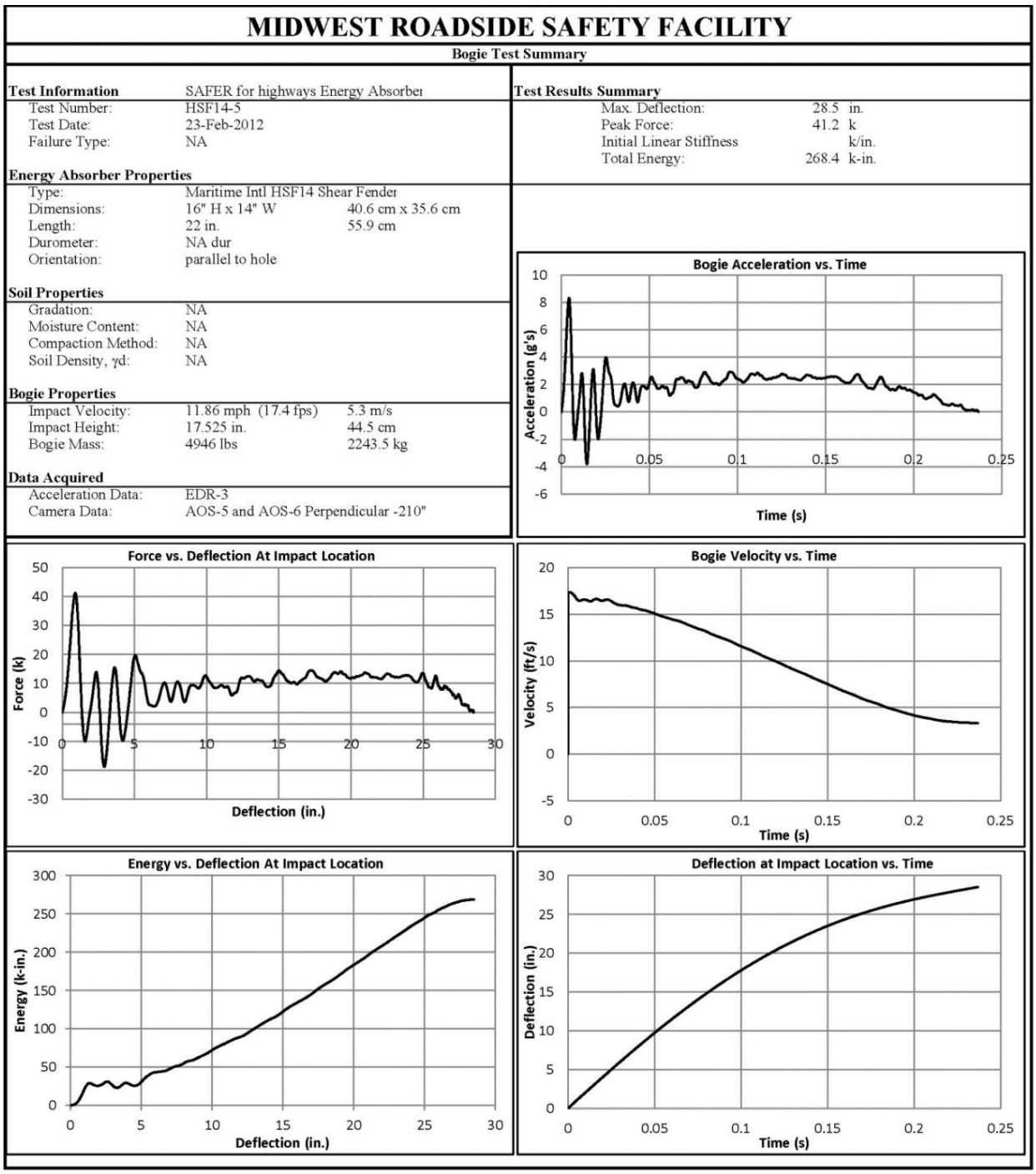

Figure C-17. Results of Test No. HSF14-5

Appendix D. LS-DYNA Models

80 Durometer EPDM Cylinder Rubber – Simplified Material Model (run70)

```
*PART
$      pid       sid       mid     eosid      hgid      grav    adpopt
cylinder
         3         2         2
$
*SECTION_SOLID
$      sid    elform
         2        13
$
*MAT_SIMPLIFIED_RUBBER/FOAM
$
$      mid        ro        km        mu         g      sigf
         2   1.15E-6  0.103422
$
$      sg1        sw        st      lcid
     101.6      38.1      1.96         3
$
*DEFINE_CURVE
$
$     lcid      sidr      scla      sclo      offa      offo
         3                25.4  .0026689
$........>.........1.........>.........2
$               [in]                [lb]
              0.0000              0.0000
              0.0040              0.4531
              0.0100              1.1951
              0.0190              1.4282
              0.0220              1.9272
              0.0250              2.2194
              0.0340              2.9089
              0.0370              3.5655
              0.0430              4.5078
              0.0460              4.9478
              0.0520              5.2301
              0.0580              5.6504
              0.0670              6.2971
              0.0790              6.9833
              0.0910              7.8961
              0.0940              8.0274
              0.1030              8.6216
              0.1060              8.9959
              0.1181              9.7084
              0.1240             10.0039
              0.1330             10.6966
              0.1360             11.2285
              0.1570             12.1379
              0.1750             13.2181
              0.1840             13.6351
              0.1959             14.2884
              0.2110             14.7349
              0.2139             15.0304
              0.2259             15.9366
              0.2408             16.2124
              0.2529             16.7803
              0.2558             17.1382
              0.2708             17.6767
              0.2829             17.9689
              0.2858             18.1593
              0.3038             18.9111
              0.3128             19.5875
              0.3217             19.8665
```

0.3428	20.7038
0.3667	21.9645
0.3877	22.6211
0.4206	23.9968
0.4296	24.8077
0.4595	25.8255
0.4864	26.8893
0.5374	28.9150
0.5883	30.9965
0.6332	32.5298
0.6811	34.4406
0.7530	36.8078
0.7949	38.2918
0.8758	40.6360
0.9386	42.6190
1.0135	44.9927
1.0674	46.7525
1.1483	48.9851
1.2201	50.7974
1.2800	52.7378
1.3698	54.8653
1.4567	56.7630
1.5404	58.9233
1.6124	60.8440
1.7920	65.4043
1.8039	65.8147
2.0555	70.8774
2.2950	75.8186
2.5465	80.9338
2.7621	85.1198
2.7741	85.2610
2.7861	85.6878
3.0497	90.9081
3.3257	95.6293
3.5897	100.4424
3.8417	105.4887
4.1538	110.9913
4.4418	115.8471
4.7302	120.9919
5.0341	125.9692
5.2772	129.9714
5.6962	136.9022
5.9672	141.2458

80 Durometer EPDM Cylinder Rubber – Blatz-Ko Material Model (run71)

```
*PART
$      pid       sid       mid     eosid      hgid      grav    adpopt
cylinder
         3         2         2
$
*MAT_BLATZ-KO_RUBBER
$
$      mid        ro         g
         2   1.15E-6  0.003100
$
*SECTION_SOLID
$      sid    elform
         2        13
```

Shear Fender Rubber – Blatz-Ko Material Model (run55)

```
*PART
$      pid       sid       mid     eosid      hgid      grav    adpopt
rubbershearfender
      1004      1004      1004
$
*SECTION_SOLID
$       sid    elform
      1004        13

*MAT_BLATZ-KO_RUBBER
$
$       mid        ro         g
      1004   1.15E-6  0.000616
```

Shear Fender Rubber – Simplified Material Model (run51)

```
*PART
$      pid       sid       mid     eosid      hgid      grav    adpopt
rubbershearfender
      1004      1004      1004
$
*SECTION_SOLID
$      sid    elform
      1004        13
$
*MAT_SIMPLIFIED_RUBBER/FOAM
$
$
$
$      mid        ro         km         mu          g      sigf
      1004   1.15E-6  0.103422           1.453E-3  1.453E-6
$      sfl        sw         st      lcidi      data     lcid2    bstart     tramp
         1         1          1         52
$
*DEFINE_CURVE
$
$     lcid      sidr       sfa       sfo      offa      offo    dattyp
        52                          0.001
$              Strain         Stress[MPa]
                    0                   0
             0.011124            0.024186
             0.045619            0.081962
             0.075763            0.132146
             0.105624            0.175900
             0.134391            0.216042
             0.162475            0.251671
             0.189974            0.283984
             0.217989            0.313766
             0.246563            0.341020
             0.274056            0.365868
             0.302288            0.389434
             0.329956            0.410984
             0.357987            0.431574
             0.385382            0.450599
             0.413344            0.469271
             0.440653            0.486198
             0.468811            0.503297
             0.496800            0.518873
             0.524863            0.534060
             0.553232            0.548776
             0.580618            0.563281
             0.608560            0.577243
             0.636471            0.591450
             0.664894            0.604672
             0.691339            0.617806
             0.719639            0.631196
             0.746714            0.643873
             0.775760            0.656947
             0.803674            0.669824
             0.831957            0.682602
             0.858732            0.695424
             0.886498            0.708463
             0.914852            0.720750
             0.941977            0.734158
             0.970399            0.747121
             0.997741            0.760687
             1.025748            0.773900
             1.054594            0.787890
             1.081613            0.801306
             1.091784            0.806289
             1.100804            0.811395
```

1.110281	0.816134
1.118951	0.820961
1.128728	0.825975
1.137573	0.830751
1.146860	0.835620
1.156233	0.840787
1.165603	0.845692
1.175083	0.850786
1.184251	0.855876
1.192793	0.860909
1.202345	0.866383
1.211703	0.871536
1.220922	0.876954
1.230135	0.882338
1.239466	0.887369
1.248130	0.893232
1.257800	0.899034
1.266769	0.904468
1.276614	0.910373
1.285934	0.916263
1.295203	0.921883
1.304933	0.927792
1.313273	0.933856
1.322756	0.940143
1.331978	0.946055
1.340728	0.952309
1.350240	0.958792
1.359210	0.965531
1.368443	0.971945
1.377434	0.978845
1.387222	0.985552
1.395744	0.992351
1.404321	0.999343
1.413751	1.006440
1.423115	1.013784
1.432236	1.021058

END OF DOCUMENT